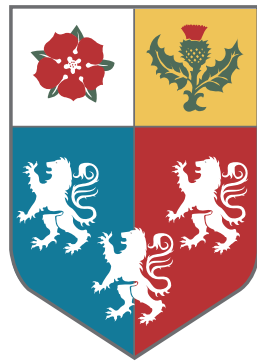


# Supersymmetry searches at the LHC and their interpretations

William James Fawcett  
of Pembroke College, Oxford



A thesis submitted to the University of Oxford  
for the degree of Doctor of Philosophy  
Trinity 2017



# Abstract

One of the primary goals of the CERN Large Hadron Collider is to search for new physics. Many such searches have been carried out, in particular searches for supersymmetry, yet no new physics beyond the Standard Model has been found. With a large number of free parameters introduced by frameworks such as supersymmetry, it can be difficult to interpret the null results of searches. The first analysis presented in this thesis attempts to tackle this difficulty head-on, and gives a summary of the constraints from the Run-1 ATLAS searches. A combination of 22 searches were used, with integrated luminosities of up to  $20.3\text{ fb}^{-1}$  of 7 and 8 TeV data. The results are interpreted in the context of the 19-dimensional phenomenological MSSM, and are presented in terms of the masses of supersymmetric particles. Constraints from dark matter, heavy flavour and precision electroweak measurements were incorporated, and results are also interpreted in terms of these observables. Properties of models missed by the Run-1 searches are also shown. The second analysis presented in this thesis documents a direct search for new physics, using  $18.2\text{ fb}^{-1}$  of 13 TeV data collected during 2015 and 2016 by the ATLAS detector. The search targets final states with large jet multiplicity (at least 7 to at least 10 jets), which can arise from the pair production of gluinos decaying via a cascade. Further requirements are imposed on the sum of masses of reclustered large-radius jets. No evidence for new physics is found, and the results are interpreted in both a model-independent way and in terms of two simplified supersymmetric models, one of which was inspired by the results of the first study. Limits on the gluino mass of up to 1600 GeV are set at the 95% confidence level, extending previous limits.



## Declaration

This dissertation is the result of the author's own work, except in the few cases where explicit reference is made to the work of others, and has not been submitted for another qualification to this or any other university. This dissertation does not exceed the page limit.

William James Fawcett

## Acknowledgements

First, I would like to thank my supervisor, Professor Alan Barr, a true aficionado of supersymmetry and one of the best scientists I have ever met. It has certainly been a privilege to be a part of the Oxford SUSY group, where I have met so many excellent students. Your unique style and contagious enthusiasm have been inspirational throughout my DPhil.

Getting to a place where you can study for a DPhil in particle physics isn't just the work of one person, it's the work of many who have inspired you over years of work. My first real taste of what it was like to work as a particle physicist came while working at Rutherford Appleton Laboratory, and I'd like to thank Stefania Riccardi and Raja Nandakumar for their careful tutelage and supervision whilst I was a very inexperienced summer student. I owe a huge amount to my Master's supervisor, Professor Chris Parkes, for all the inspiration and teaching, and giving me the academic freedom to independently work on my own project. I also had a great deal of support from the other members of the group, including Marco Gersabeck, Mika Vesterinen and Stefaine Riechert, and I would not have progressed so much without your help.

At Oxford, students are fortunate to be surrounded by so many hard working and inspiring people. Nowhere is that more true than in the Oxford SUSY group. I would like to extend a special thanks to the students in the years above me, Alex Dafinca, Mirea Crispín-Ortuza and Will Kalderon. Alex and Mireia, although you may not know it, I am incredibly grateful for the kindness you showed me in helping me during those early days of my DPhil. And Will, who acted as a mentor through several years of my DPhil, without your technical advice (and keen eye for any kind of grammatical error, I really do appreciate that) I would not nearly have accomplished so much. Thanks also to Claire Gwenlan and Koichi Nagai for their help and advice. My experience wouldn't have

been the same without my officemates, Will Kalderon, Mark Pickering and Jon Burr. I'd also like to thank Mike Nelson and Jesse Liu, for reinvigorating my own interest in physics with their seemingly endless enthusiasm for the subject. At Oxford, I was also fortunate to share my DPhil adventure with an amazing cohort of students: Feng-Ting, Jack, Kathryn, Lydia, Peter, Raj, Steve and Tim. Our lunchtime conversations always gave me something to look forward to.

At CERN, I was again surrounded by many wonderful and inspiring people. I am indebted to Chris Young for all his help, and I am grateful to Brian Petersen for answering my endless questions on the pMSSM. I also had the good fortune to work with Anna Sfyrla and Teng Jian Khoo on the multijet analysis and Dave Robinson on the SCT. While working in the SUSY group, I have learned a lot from Jeanette Lorentz, Geert-Jan Besjes, Zach Marshall and Kerim Suruliz, especially with regards to HistFitter. I'd also like to thank my colleagues at SLAC Tom Rizzo and Matthew Cahill-Rowley, from whom I learned a great deal about the pMSSM.

My time at Oxford was also enriched by my experience in College, and I would like to thank all the staff at Pembroke who work tirelessly to make it wonderful. Especially I would like to thank my college adviser, Professor Alfons Weber, who provided a source of support and encouragement throughout the years.

I'd also like to thank the IT staff at Oxford, in particular Sean Brisbane who went far beyond the call of duty to save the multijet analysis from batch-queue related disasters on multiple occasions. Furthermore, the administration staff at Oxford are also exceptional, especially Sue Geddes and Kim Proudfoot.

There is also another important group of people I need to thank. Malte, Daniela, Johnny and Friederike, my housemates who kept me sane throughout the last year of my DPhil. Without a doubt, my time living with you was the happiest during my days at Oxford. You kept me (mostly) sane throughout this year. Thank you for all of the memories (and the pancakes).

Finally, I would like to thank my parents, who nurtured my interest in science from a young age, and taught me the value of hard work.

## Preface

The work presented in this thesis was completed by myself as part of the ATLAS collaboration. In a collaboration like ATLAS no publication is created alone, and the work I have produced is no exception. What follows is a list in reverse chronological order of publications that I have made a leading contribution to, some of which I cover in detail in this thesis.

- **Search for new phenomena with large jet multiplicities and missing transverse momentum using large-radius jets and flavour-tagging at ATLAS in 13 TeV pp collisions.** I was the lead author for this analysis, coordinating the analysis team and performing many aspects of the analysis and producing the majority of the results. The analysis is currently the most comprehensive iteration of the multijet analysis, and is published as a paper [1]. Prior to the release of the paper, the analysis was also published as a conference note [2].
- **Pursuit of new phenomena in final states with high jet multiplicity, high jet masses and missing transverse momentum with ATLAS at  $\sqrt{s}=13$  TeV.** I also lead the majority of aspects for this analysis, which is discussed in detail in chapter 5 of this thesis. The analysis was published as a conference note [3], in which I created all of the plots and tables.
- **Search for new phenomena in final states with large jet multiplicities and missing transverse momentum with ATLAS using  $\sqrt{s}=13$  TeV proton-proton collisions.** I carried out many of the analysis tasks for this study, such as trigger studies, and investigation into pileup effects. My most significant contribution was the statistical analysis and interpretation of the results. The analysis was published as a paper [4], and was the first supersymmetry search to be released from

the LHC with 13 TeV data. Prior to the release of the paper, the analysis was also published as a conference note [5].

- **Summary of the ATLAS experiment’s sensitivity to supersymmetry after LHC Run 1 – interpreted in the phenomenological MSSM.** I was responsible for the interpretation of the results, which was no small endeavour given the 19 dimensional pMSSM. This involved the creation of almost all of the plots that featured in the publication and their interpretation. I also created a framework to re-implement existing analyses and process the 300,000 pMSSM points, implementing 2 of the 22 analyses myself, with the remainder being performed by collaborators. The analysis was published as a paper [6], and is the subject of chapter 4 of this thesis.

In addition to creating publications, I also contributed to the running of the detector and performance work. For my service task, which was required to join the ATLAS collaboration, I performed monitoring of optical links for the semiconductor tracker. I took shifts operating the detector, as both Run Controller and as the Inner Detector shifter, and was involved in SCT operations through hardware replacement and DAQ/DCS expert on-call shifts. I also contributed to the performance of ATLAS simulation, by validating many of the jet triggers in Monte Carlo simulations before the start of Run-2.

My DPhil took place at an exciting time in particle physics. I witnessed, and was actively involved in, the start of Run-2 of the LHC programme that saw an almost doubling of the centre of mass energy of the proton–proton collisions from 8 TeV to 13 TeV. This opened a new energy frontier, hitherto completely unexplored, with which to potentially discover new physics. It has been a great privilege to be one of the first people to probe this new frontier.

Throughout this thesis, if a diagram, plot or other figure has not been produced by me, then this is stated in the caption with a reference to the source. Plots that I created that have been published by the ATLAS collaboration are also labelled **ATLAS** or **ATLAS Preliminary**. Other contributions by collaborators are acknowledged in the text.

# Contents

<b>1. Introduction</b>	<b>1</b>
<b>2. Theoretical overview</b>	<b>3</b>
2.1. The Standard Model . . . . .	3
2.1.1. Particle content of the Standard Model . . . . .	3
2.1.2. Gauge invariance and symmetry . . . . .	7
2.1.3. Theoretical description of the Standard Model . . . . .	8
2.1.4. Renormalisation . . . . .	17
2.2. Problems with the Standard Model . . . . .	18
2.2.1. The dark matter problem . . . . .	20
2.2.2. The hierarchy problem . . . . .	21
2.3. Supersymmetry . . . . .	23
2.3.1. Foundations of supersymmetry . . . . .	24
2.3.2. The Minimal Supersymmetric extension to the Standard Model	28
2.3.3. Implications of supersymmetry . . . . .	31
2.3.4. Maintaining naturalness . . . . .	33
2.3.5. Experimental signatures . . . . .	34
2.4. Summary . . . . .	36
<b>3. The ATLAS experiment</b>	<b>37</b>
3.1. The Large Hadron Collider . . . . .	37
3.2. The ATLAS detector . . . . .	42
3.2.1. Coordinate system . . . . .	43
3.2.2. Magnet system . . . . .	45

3.2.3.	Tracking	47
3.2.4.	Calorimetry	51
3.2.5.	Muon spectrometer	55
3.2.6.	Forward detectors	59
3.3.	Trigger	60
3.3.1.	The Level-1 trigger	63
3.3.2.	The high-level trigger	64
3.4.	Object reconstruction	65
3.4.1.	Tracks and primary vertices	65
3.4.2.	Muons	66
3.4.3.	Electrons and photons	67
3.4.4.	Jets	68
3.4.5.	$b$ -jets	72
3.4.6.	Tau leptons	73
3.4.7.	Missing transverse momentum	74
3.4.8.	Overlap removal	75
3.5.	Summary	75
<b>4.</b>	<b>The Impact of 8 TeV ATLAS Searches on the pMSSM</b>	<b>77</b>
4.1.	The phenomenological MSSM	78
4.2.	Analysis Details	81
4.2.1.	Overview	81
4.2.2.	Model selection	81
4.2.3.	Non-ATLAS constraints	82
4.2.4.	Sampling by LSP type	87
4.3.	Resulting model set	87
4.4.	The ATLAS searches	89
4.5.	ATLAS constraints on the pMSSM	91
4.5.1.	Sparticle masses	93
4.5.2.	Production cross-section	103
4.5.3.	Dark matter	105
4.5.4.	Higgs boson and precision observables.	109

4.5.5. Electroweak precision observables . . . . .	111
4.5.6. Fine-tuning in the model set . . . . .	112
4.6. Conclusions . . . . .	116
<b>5. Search for new phenomena in events with many jets</b>	<b>122</b>
5.1. Analysis overview . . . . .	124
5.2. Signal models . . . . .	125
5.2.1. The two-step model . . . . .	125
5.2.2. The pMSSM slice . . . . .	127
5.3. Analysis strategy . . . . .	130
5.3.1. Trigger . . . . .	130
5.3.2. Physics object definition . . . . .	132
5.3.3. Kinematic variable definition . . . . .	134
5.3.4. Event cleaning . . . . .	136
5.3.5. Event selection . . . . .	140
5.4. Leptonic background estimation . . . . .	145
5.4.1. Description of the leptonic $t\bar{t}$ and $W$ + jets backgrounds . . . . .	147
5.4.2. Monte Carlo simulation . . . . .	149
5.4.3. Control regions . . . . .	151
5.4.4. Theoretical systematic uncertainties . . . . .	152
5.4.5. Experimental systematic uncertainties . . . . .	155
5.5. Multijet background estimation . . . . .	158
5.5.1. Description of the background . . . . .	158
5.5.2. The template method . . . . .	159
5.5.3. Closure tests of the template method . . . . .	161
5.5.4. Heavy-flavour systematic . . . . .	161
5.5.5. Additional systematic uncertainties . . . . .	164
5.6. Results and interpretation . . . . .	168
5.6.1. The background only fit . . . . .	169
5.6.2. Model-independent fit . . . . .	178
5.6.3. Model-dependent limits . . . . .	182
5.6.4. Comparison with the CMS experiment . . . . .	182



---

5.7. Conclusions . . . . .	186
<b>6. Summary and outlook</b>	<b>187</b>
<b>A. Additional theoretical background</b>	<b>190</b>
A.1. Quantum Electrodynamics . . . . .	190
A.2. Quark mixing and CP-violation . . . . .	191
A.3. Higgs vacuum and cosmology . . . . .	192
A.4. The WIMP Miracle . . . . .	193
A.5. Particle masses in unbroken supersymmetry . . . . .	193
<b>B. Additional multijet systematic uncertainties</b>	<b>195</b>
B.1. Leptonic theory systematics . . . . .	195
B.2. $H_T$ binning of the template . . . . .	195
B.3. Complete breakdown of SR and CR yields . . . . .	197
<b>Bibliography</b>	<b>207</b>
<b>List of figures</b>	<b>230</b>
<b>List of tables</b>	<b>241</b>

*“If it disagrees with experiment, it’s wrong.*

*In that simple statement is the key to science.”*

— Richard Feynman, The Character of Physical Law

# 1 | Introduction

What is the universe made of? The pursuit of the answer to this question is the subject of particle physics. Not only that, but the particle physicist desires knowledge of the fundamental building blocks of the universe: the simplest and indivisible pieces from which everything else is successively composed of.

One of the earliest known attempts to describe the universe in terms of elementary building blocks was provided by Anaximenes of Miletus, who proposed that there be only four elements: earth, air, fire and water. While this theory is beautifully simple, it cannot reproduce the universe we observe. The periodic table of elements is another attempt to answer our question, but since each element can be broken down into simpler constituents, this does not represent the fundamental answer that particle physicists are searching for.

Our best answer to this puzzle is the Standard Model of particle physics. The Standard Model is a theory describing all known elementary particles and their interactions, but there are numerous reasons why we acknowledge it is incomplete, and why it cannot fully describe the universe we observe. As a result we continue to search for new physics *beyond* the Standard Model.

Modern day particle physics carries out searches with particle accelerators. As technology progresses, colliders are able to smash particles together with higher and higher energies, allowing the experiments built around the collision points – such as ATLAS – to probe progressively higher energy scales. It is hoped that in a high energy collision, new fundamental particles will be created which will further our understanding of the constituents of the universe.

However, it is one thing to create such a new particle, and another to find it. This thesis documents my contribution to searching for new particles, particularly in the form of supersymmetric particles. Chapter 5 documents a search for the gluino – the supersymmetric partner of the gluon – which is pursued in cases where it decays via a cascade of other particles. This results in final states with a large amount of hadronic activity, which is both difficult to measure accurately and difficult to predict theoretically. A special background estimation technique is employed to overcome these issues. No evidence of new physics was found and strong limits were set on a variety of new physics models.

This thesis also documents the interpretation of the null results of searches for supersymmetry. There are a large number of unknown parameters introduced by supersymmetry, and as a result there is no single way to get an idea of the impact of these searches on the parameter space. Furthermore, there is also limited understanding of the interplay between limits on new physics models set by direct searches at colliders and other measurements, such as the dark matter relic density. The study in chapter 4 attempts to address these issues by combining the results of many Run-1 new physics searches and assessing their impact on a large class of supersymmetric models taken from a scan of the phenomenological MSSM.

Chapters 2 and 3 lay out the theoretical and experimental framework used to carry out the studies in this thesis. A summary of this thesis is provided in chapter 6.

## 2 | Theoretical overview

The Standard Model of particle physics contains our current knowledge of fundamental particles and their interactions – save the masses of the neutrinos and their oscillations. Deeply embedded within the Standard Model is the concept of *symmetry*. Symmetries; either intact or broken, have proved to be at the heart of how matter interacts.

This thesis will focus mostly on experimental aspects of particle physics and some of the implications of the results. To understand this, a basic understanding of the underlying theory is essential. This chapter will cover the fundamental concepts used in later chapters, and is split into three main parts. Section 2.1 will lay out the theoretical framework of the Standard Model, introducing the particle content and then covering the strong and electroweak interactions, as well as the origin of mass. Some of the known problems with the Standard Model will be described in section 2.2 which motivate searches for physics not described by the Standard Model. Supersymmetry, a theoretical framework that could address some of the shortcomings of the Standard Model is introduced in section 2.3, and is the topic of both chapter 4 and chapter 5.

In writing this chapter, I used the excellent references [7–11].

### 2.1. The Standard Model

#### 2.1.1. Particle content of the Standard Model

The two elementary building blocks of the universe, *forces* and *matter* can be described in terms of quantum fields, with the notable exception of gravity. Fundamental particles are

the quantisation of these fields, being point-like, structureless and carrying internal angular momentum (spin). All other entities are then successively constructed as composites of these elementary building blocks. Before going into the details of the interactions, this section will describe the elements that are most widely used from an experimental perspective: the different particles, their charges and main interactions.

We categorise particles according to whether their spin is an integer or half-integer (in units of  $\hbar$ ). The *fermions* comprise the matter particles and have spin one-half. The *bosons*, with integer spin, mediate the interactions of fermions, giving rise to forces and mass of fundamental particles. The particle content of the Standard Model is summarised in table 2.1. In addition to the symbols listed in the table, typically  $f$  is used to denote any type of fermion, with  $\bar{f}$  representing the antiparticle. Similarly  $q$  and  $\ell$  denote a quark and lepton of any flavour.

The fermions are further sub-divided into two categories, depending on whether they have strong interactions or not: if they do they are called *quarks*; if not they are called *leptons*. There are six types (or flavours) of lepton in the Standard Model that come in three generations of charged and neutral doublets, each doublet appearing to be identical in all properties other than mass. Neutral leptons are called neutrinos, and are massless in the Standard Model, however experiments have found that they have a small but non-zero mass [35–39]. The neutrinos only have weak interactions (making them difficult to detect experimentally); whereas the charged leptons, the electron, muon and tau, have both electromagnetic and weak interactions. Similarly to the leptons, there are also six flavours of quarks, again coming in three generations of doublets. Each doublet consists of an up- and down-type quark, named after the quarks of the first generation. The quarks differ from the leptons as, in addition to the weak and electromagnetic, they also carry colour charge and thus have strong interactions. Furthermore, for each flavour of quark there are three ‘colour’ versions. Both the quarks and leptons have an antimatter counterpart, anti-quarks and anti-leptons respectively, which have the same mass but opposite charges. For example, the antiparticle of the electron is the positron. It is theorised that the neutrino may be its own antiparticle [40], however, this has not yet been verified experimentally.

Name	Spin	Mass	Charge	Discovery
Quarks				
$u$ (up)	$\frac{1}{2}$	2.3 MeV	$+2/3$	1968 [12, 13]
$d$ (down)	$\frac{1}{2}$	4.8 MeV	$-1/3$	1968 [12, 13]
$c$ (charm)	$\frac{1}{2}$	1.3 GeV	$+2/3$	1974 [14, 15]
$s$ (strange)	$\frac{1}{2}$	95 MeV	$-1/3$	1968 [12, 13]
$b$ (bottom)	$\frac{1}{2}$	4.2 GeV	$-1/3$	1977 [16]
$t$ (top)	$\frac{1}{2}$	173 GeV	$+ 2/3$	1995 [17, 18]
Leptons				
$e$ (electron)	$\frac{1}{2}$	0.511 MeV	-1	1896 [19]
$\nu_e$ ( $e$ neutrino)	$\frac{1}{2}$	$< 2 \text{ eV}$	0	1956 [20]
$\mu$ (muon)	$\frac{1}{2}$	105.7 MeV	-1	1936 [21, 22]
$\nu_\mu$ ( $\mu$ neutrino)	$\frac{1}{2}$	$< 0.19 \text{ MeV}$	0	1962 [23]
$\tau$ (tau)	$\frac{1}{2}$	1.777 GeV	-1	1974-7 [24]
$\nu_\tau$ ( $\tau$ neutrino)	$\frac{1}{2}$	$< 18.2 \text{ MeV}$	0	2000 [25]
Gauge Bosons				
$\gamma$ (photon)	1	0	0	1932 [26]
$W^\pm$	1	80.34 GeV	$\pm 1$	1983 [27, 28]
$Z$	1	90.12 GeV	0	1983 [29, 30]
$g$ (gluon)	1	0	0	1979 [31]
Higgs Boson				
$h$ (Higgs)	0	125.1 GeV	0	2012 [32, 33]

**Table 2.1.:** The known fundamental particles comprising the Standard Model and some of their properties. Not listed in the table are the antiparticles of the quarks and leptons, which have identical mass and opposite electric charge. Furthermore, for each flavour of quark there are 3 colour versions, and there are 8 different coloured gluons. Masses are from the Review of Particle Physics [34].

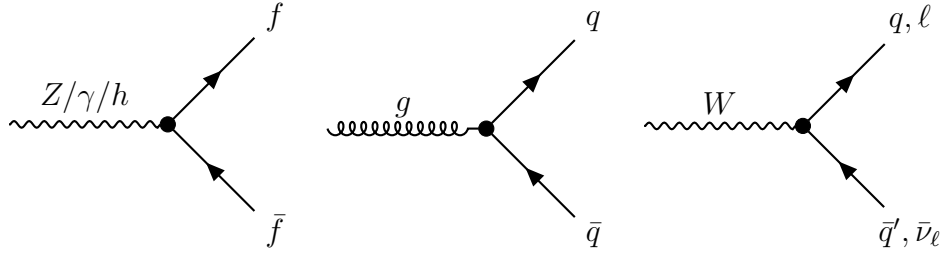


**Figure 2.1.:** Feynman diagrams showing the interactions between fermions and bosons.

Forces in the Standard Model are generated via interactions of the *gauge bosons*. The neutral photon is the carrier of the electromagnetic interaction, which has infinite range due to the massless nature of the photon. The weak interaction is mediated by the charged  $W^\pm$  and neutral  $Z$  bosons; their massive nature giving rise to the short range and hence apparent “weakness” of the weak force. The strong force is mediated by *gluons*, of which there are eight types with different colour combinations. Finally, the neutral, scalar, massive Higgs boson gives rise to the masses of particles in the Standard Model.

Some of the main interaction vertices are depicted in figures 2.1, 2.2 and 2.3, which show the interaction of fermions with bosons, the self-interactions of gauge bosons, and the interactions of the Higgs boson respectively. Neutrino oscillations are not shown.

With the notable exception of the top quark, quarks are never observed outside of bound states known as hadrons. Each hadron contains a number of “valence” quarks that together carry the quantum numbers of the hadron, and “sea” quarks, which are virtual quark-antiquark pairs. The quarks are bound in hadrons by the gluons of the strong force. Each hadron must be arranged such that the overall state is colourless, and hadrons are classified by the number of valence quarks they contain. Mesons are quark-antiquark pairs, for example the  $\pi^+$  ( $u\bar{d}$ ). Baryons are bound states of three quarks, and include the proton ( $uud$ ) and neutron ( $udd$ ). Further states also exist, including the recently discovered pentaquarks [41], containing four quarks and an antiquark (and vice-versa). The top quark is never found inside a hadron due to its large mass; even though it decays weakly the energy released is so great that its lifetime is approximately two orders of magnitude smaller than typical strong interaction time-scales, meaning the top quark decays before any hadron can be formed.



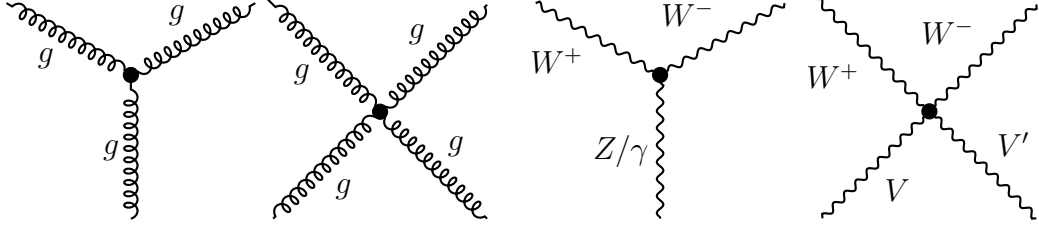


**Figure 2.2.:** Feynman diagrams representing self-interactions between gauge bosons.  $V$  and  $V'$  correspond to any two gauge bosons such that the total electric charge is conserved.

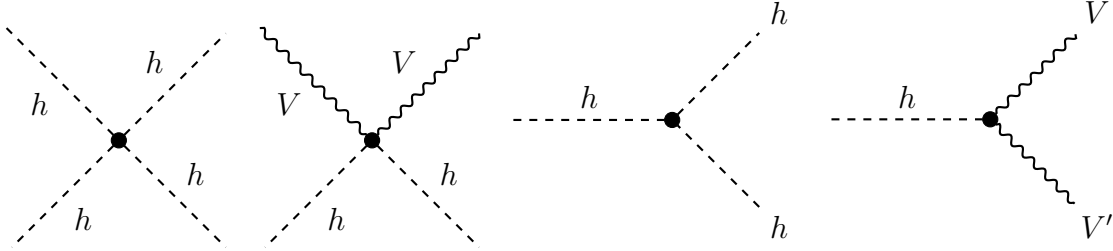


**Figure 2.3.:** Feynman diagrams for the interaction of the Higgs boson with the gauge bosons, and also the self-interactions of the Higgs boson.  $V$  and  $V'$  correspond to any two gauge bosons such that the total electric charge is conserved.

### 2.1.2. Gauge invariance and symmetry

Fundamental to the Standard Model is the concept of gauge symmetry. A field theory is said to be gauge symmetric if the Lagrangian (and therefore any physically measurable quantity) is invariant under a gauge transformation. The simplest example of a gauge symmetry comes from electromagnetism, where Maxwell's equations remain invariant under the transformation of the 4-potential  $A^\mu \rightarrow A'^\mu = A^\mu - \partial^\mu \chi$ .

In quantum field theories, we are interested in the transformation of fields, and due to the unitary nature of the symmetry groups of the Standard Model we are restricted to transformations of the form

$$\psi(x) \rightarrow \psi'(x) = e^{i\alpha} \psi(x), \quad (2.1)$$

where here,  $\alpha$  may mean one of two things: either  $\alpha$  is a real scalar corresponding to *global* gauge transformations, or  $\alpha$  is a real-valued function of the space-time coordinates  $x$ , corresponding to a *local* gauge transformation. In both cases  $\psi$  and  $\psi'$  must describe

the same physics, and imposing this requirement has important consequences. Indeed, as shown by Emmy Noether [42], every continuous symmetry results in conserved quantities. Quantum electrodynamics (QED) provides a starting point to outline some of the relevant principles of gauge invariance, and how symmetry properties are related to dynamics – an account is given in appendix A.1 for the interested reader.

### 2.1.3. Theoretical description of the Standard Model

The Standard Model Lagrangian describes the dynamics of particles and their interactions. It arises from the requirement that all interactions be invariant under local gauge transformations, as well as the Poincaré group transformations (translations, rotations and Lorentz boosts). It is a unified framework to describe the electromagnetic and weak interactions between quarks and leptons, together with the strong interactions between quarks and gluons. There are three generations of left- and right-handed chiral fields<sup>1</sup>, both for the quarks and leptons. The left-handed fermions form  $SU(2)_L$  doublets whereas the right-handed fermions form singlets. The fermion content of the Standard Model is summarised in table 2.2. The left- and right-handed quarks are triplets under  $SU(3)_c$ , while all leptons are colour singlets. In the electroweak sector, the field  $B_\mu$  corresponds to the  $U(1)_Y$  group and the three fields  $W_\mu^i$  ( $i = 1, 2, 3$ ) correspond to the  $SU(2)_L$  group. Furthermore there is also an octet of gluon fields  $G_\mu^a$  ( $a = 1, \dots, 8$ ) which correspond to the colour  $SU(3)_c$  group. The Standard Model Lagrangian *without* mass terms for fermions and gauge bosons is given by

$$\begin{aligned} \mathcal{L}_{\text{SM}} = & -\frac{1}{4}G_{\mu\nu}^a G_a^{\mu\nu} - \frac{1}{4}W_{\mu\nu}^i W_i^{\mu\nu} - \frac{1}{4}B_{\mu\nu}B^{\mu\nu} \\ & + \bar{L}_j i D_\mu \gamma^\mu L_j + \bar{e}_{Rj} i D_\mu \gamma^\mu e_{Rj} + \bar{Q}_j i D_\mu \gamma^\mu Q_j + \bar{d}_{Rj} i D_\mu \gamma^\mu d_{Rj} + \bar{u}_{Rj} i D_\mu \gamma^\mu u_{Rj}, \end{aligned} \quad (2.2)$$

where the summation index  $j$  runs over the three fermion generations,  $\gamma^\mu$  are the Dirac matrices and:

- $G_{\mu\nu}^a = \partial_\mu G_\nu^a - \partial_\nu G_\mu^a + g_s f^{abc} G_\mu^b G_\nu^c,$

---

<sup>1</sup>  $f_{L,R} = \frac{1}{2}(1 \mp \gamma_5)f$

- $W_{\mu\nu}^i = \partial_\mu W_\nu^i - \partial_\nu W_\mu^i + g_2 \epsilon^{ijk} W_\mu^j W_\nu^k$ ,
- $B_{\mu\nu} = \partial_\mu B_\nu - \partial_\nu B_\mu$ ,

are the field strength tensors,

- $D_\mu = \partial_\mu - ig_s T_a G_\mu^a - ig_2 T_i W_\mu^i - ig_1 \frac{Y}{2} B_\mu$

is the gauge covariant derivative, coupling the matter fields to the gauge fields, and

- $T_a = \frac{1}{2} \lambda_a$  are the generators of  $SU(3)_c$ , with  $\lambda_a$  being the Gell-Mann matrices, and  $f^{abc}$  are the structure functions. They satisfy the algebra  $[T_a, T_b] = if_{abc} T_c$ .
- $T_i = \frac{1}{2} \tau_i$  are the generators of  $SU(2)_L$ , with  $\tau_i$  being the Pauli matrices, and  $\epsilon^{ijk}$  is the anti-symmetric tensor. They satisfy the algebra  $[T_i, T_j] = i\epsilon_{ijk} T_j$ .
- $Y$  is the weak hypercharge and is the generator of  $U(1)_Y$ .
- $g_s, g_2$  and  $g_1$  are the coupling constants of  $SU(3)_c, SU(2)_L$  and  $SU(1)_Y$  respectively.
- $L_j, e_{R_j}, Q_j, d_{R_j}, u_{R_j}$  correspond to the fermion fields, listed in table 2.2 (with, for example,  $\bar{L}_j = L_j^\dagger \gamma^0$  representing the anti-fermions).

This Lagrangian is invariant under local  $SU(3)_c \times SU(2)_L \times U(1)_Y$  gauge transformations for the fields. For instance, the electroweak sector has:

$$L(x) \rightarrow e^{i\alpha_i(x)T^i + i\beta(x)\frac{Y}{2}} L(x), \quad R(x) \rightarrow e^{i\beta(x)\frac{Y}{2}} R(x), \quad (2.3)$$

$$\mathbf{W}_\mu(x) \rightarrow \mathbf{W}_\mu(x) + \frac{1}{g_2} \partial_\mu \boldsymbol{\alpha}(x) - \boldsymbol{\alpha}(x) \times \mathbf{W}_\mu(x), \quad B_\mu(x) \rightarrow B_\mu(x) + \frac{1}{g_1} \partial_\mu \beta(x). \quad (2.4)$$

Here,  $\beta(x)$  specifies the local  $U(1)$  gauge transformation, and  $\boldsymbol{\alpha}(x) = (\alpha_1(x), \alpha_2(x), \alpha_3(x))$  specifies the local  $SU(2)$  gauge transformation.  $L$  and  $R$  correspond to any of the left- or right-handed spinors of table 2.2. We are allowed to add any terms to this Lagrangian as long as they leave it gauge invariant.

There are many problems with this theory, some of which will be outlined in section 2.2, but most notably there are no mass terms for the fermions and gauge bosons. Furthermore, the  $W^3$  and  $B$  fields have not mixed to form the more familiar  $Z$  and photon. This is of course due to the lack of the Higgs field and electroweak symmetry breaking, which will

Weak interaction spinor			$Q$	$Y$	$I_3$	$I$
$Q_1 = \begin{pmatrix} u \\ d \end{pmatrix}_L$	$Q_2 = \begin{pmatrix} c \\ s \end{pmatrix}_L$	$Q_3 = \begin{pmatrix} t \\ b \end{pmatrix}_L$	$\begin{pmatrix} +\frac{2}{3} \\ -\frac{1}{3} \end{pmatrix}$	$\begin{pmatrix} \frac{1}{3} \\ \frac{1}{3} \end{pmatrix}$	$\begin{pmatrix} \frac{1}{2} \\ -\frac{1}{2} \end{pmatrix}$	$\begin{pmatrix} \frac{1}{2} \\ \frac{1}{2} \end{pmatrix}$
$d_R^{(1)} = d_R$	$d_R^{(2)} = s_R$	$d_R^{(3)} = b_R$	$-\frac{1}{3}$	$-\frac{2}{3}$	0	0
$u_R^{(1)} = u_R$	$u_R^{(2)} = c_R$	$u_R^{(3)} = t_R$	$\frac{2}{3}$	$\frac{4}{3}$	0	0
$L_1 = \begin{pmatrix} \nu_e \\ e^- \end{pmatrix}_L$	$L_2 = \begin{pmatrix} \nu_\mu \\ \mu^- \end{pmatrix}_L$	$L_3 = \begin{pmatrix} \nu_\tau \\ \tau^- \end{pmatrix}_L$	$\begin{pmatrix} 0 \\ -1 \end{pmatrix}$	$\begin{pmatrix} -1 \\ -1 \end{pmatrix}$	$\begin{pmatrix} \frac{1}{2} \\ -\frac{1}{2} \end{pmatrix}$	$\begin{pmatrix} \frac{1}{2} \\ \frac{1}{2} \end{pmatrix}$
$e_R^{(1)} = (e^-)_R$	$e_R^{(2)} = (\mu^-)_R$	$e_R^{(3)} = (\tau^-)_R$	-1	-2	0	0

**Table 2.2.:** The fermion content of the Standard Model with their associated charges. There are three generations of both right- and left-handed quarks and leptons.  $Q$  refers to the electric charge,  $Y$  to the weak hypercharge, and  $I$  and  $I_3$  to isospin and the third component of isospin respectively. They are related by  $Y = 2(Q - I_3)$ . Right-handed neutrinos are not present in the Standard Model and so are not included.

be discussed later. We will see that the gauge bosons gain mass as a natural consequence of the addition of the Higgs field, which simultaneously also allows one to add fermion mass terms without breaking the gauge invariance. Without the Higgs field, it is not possible to add mass terms for fermions or bosons without breaking the gauge invariance of the Standard Model.

The Lagrangian in eq. (2.2) can be completely broken into separate parts describing the electroweak and strong interactions,

$$\mathcal{L}_{\text{SM}} = \mathcal{L}_{\text{QCD}} + \mathcal{L}_{\text{EW}} \quad (2.5)$$

which will be done in what follows to illuminate some concepts.

## Quantum Chromodynamics

We can extract the relevant parts of eq. (2.2) related to the interactions of quarks with gluons to form the Lagrangian of Quantum Chromodynamics (QCD):

$$\mathcal{L}_{\text{QCD}} = -\frac{1}{4}G_{\mu\nu}^a G_a^{\mu\nu} + i\bar{\psi}\gamma^\mu(\partial_\mu - ig_s G_\mu^a T^a)\psi, \quad (2.6)$$

where the notation has been changed slightly and  $\psi(x)$  denotes the quark fermion field.<sup>2</sup> The quark fermionic field  $\psi(x)$  is an  $\text{SU}(3)_c$  triplet comprising the  $\psi_R(x)$ ,  $\psi_G(x)$   $\psi_B(x)$  fields corresponding to the three colours of QCD, (denoted  $R, G, B$ ). Correspondingly, antiquarks carry anti-colour (denoted  $\bar{R}, \bar{G}, \bar{B}$ ). One important feature of QCD is that the force carriers, the gluons, *also* carry colour charge – each a combination of colour and anti-colour described by the Gell-Mann matrices. This results in self-interactions of gluons, which has important consequences for the theory. This self-interaction is represented mathematically as the non-commutation of the generators  $T^a$ , and in the field-strength tensor  $G_{\mu\nu}^a$  this results in the term  $g_s f^{abc} G_\mu^b G_\nu^c$  giving rise to the three- and four-point self-interactions of gluons, as shown in figure 2.2.

One crucial result of the self-interaction of gluons is that the apparent coupling strength of the strong interaction changes as a function of energy scale – the coupling strength is said to “run”. At high momentum scales, the coupling tends to zero (which is the opposite of what happens with the electromagnetic coupling strength). This is the origin of one of the most peculiar properties of QCD, namely *asymptotic freedom*, which refers to the fact that at short distances quarks and gluons are essentially free due to the coupling strength being very small. Conversely, at low momentum scales the coupling strength blows up. This other extreme results in another important feature known as *confinement*, and corresponds to the phenomenon that coloured particles are never seen in isolation. As two coloured particles separate, the potential energy increases until it becomes energetically favourable to produce a new quark-antiquark pair. This continues until the original energy supply (from, for example, a particle collision) is exhausted, and the quarks and gluons form colourless bound states – the hadrons. The new particles

---

<sup>2</sup>Often in texts a fermion mass term  $-m\bar{\psi}\psi$  is added to the QCD Lagrangian – it is omitted here as mass generation will be discussed later.

travel in approximately the same direction of the originally separating particles, and empirically we see roughly conical sprays of hadrons. In high-energy physics experiments, this is the origin of jets.

### The Electroweak sector

We can pick out the terms corresponding to the interactions of leptons and the electroweak bosons from eq. (2.2):

$$\mathcal{L}_{\text{EW}}^{\text{int}} = \bar{L}_j \gamma^\mu \left[ \frac{g_2}{2} \tau_i W_\mu^i + \frac{g_1}{2} (-1) B_\mu \right] L_j + \bar{e}_{R_j} \left[ \frac{g_1}{2} (-2) B_\mu \right] e_{R_j}, \quad (2.7)$$

where the  $(-1)$ , and  $(-2)$  are respectively the weak isospin of the  $Y(e_L)$  and  $Y(e_R)$  fields. This can further be decomposed into a charged current (denoted CC) part and a neutral current part (denoted NC),  $\mathcal{L}_{\text{EW}}^{\text{int}} = \mathcal{L}_{\text{CC}} + \mathcal{L}_{\text{NC}}$ .

Firstly, we identify the charged vector fields,  $W_\mu^\pm = \frac{1}{\sqrt{2}}(W_\mu^1 \mp iW_\mu^2)$  and define

$$\mathcal{L}_{\text{CC}} = \bar{L}_j \gamma^\mu \left[ \frac{g_2}{\sqrt{2}} (\tau^+ W_\mu^+ + \tau^- W_\mu^-) \right] L_j \quad (2.8)$$

where  $\tau^\pm = \frac{1}{2}(\tau^1 \pm i\tau^2)$ . Expanding the Pauli matrices, one obtains terms such as  $\frac{g_2}{\sqrt{2}} (\bar{\nu}_L \gamma^\mu W_\mu^+ e_L + \bar{e}_L \gamma^\mu W_\mu^- \nu_L)$ , corresponding to the experimentally observed charged currents only interacting on left-handed fermions.

Secondly, we identify the neutral gauge bosons as mixtures of the remaining  $W_\mu^3$  and  $B_\mu$  fields:

$$\begin{pmatrix} W_\mu^3 \\ B_\mu \end{pmatrix} = \begin{pmatrix} \cos \theta_w & \sin \theta_w \\ -\sin \theta_w & \cos \theta_w \end{pmatrix} \begin{pmatrix} Z_\mu \\ A_\mu \end{pmatrix} \quad (2.9)$$

where  $Z_\mu$  and  $A_\mu$  correspond to the  $Z$  and the photon respectively. The mixing is governed by the weak mixing angle  $\theta_w$ , where  $\tan \theta_w = g_1/g_2$ .

The neutral current part of the interaction Lagrangian is

$$\mathcal{L}_{\text{NC}} = \bar{L}_j \gamma^\mu \left[ \frac{g_2}{2} \tau_3 W_\mu^3 - \frac{g_1}{2} B_\mu \right] L_j - g_1 \bar{e}_{R_j} \gamma^\mu B_\mu e_{R_j}, \quad (2.10)$$

which after substituting in the physical fields and using the relation  $g_2 \sin \theta_w = g_1 \cos \theta_w$  becomes

$$\begin{aligned} \mathcal{L}_{\text{NC}} = & g_2 \sin \theta_w (\bar{e}_L \gamma^\mu e_L + \bar{e}_R \gamma^\mu e_R) A_\mu \\ & + \frac{g_2}{2 \cos \theta_w} [\bar{\nu}_L \gamma^\mu \nu_L - \bar{e}_L \gamma^\mu e_L - 2 \sin^2 \theta_w (\bar{e}_L \gamma^\mu e_L + \bar{e}_R \gamma^\mu e_R)] Z_\mu \end{aligned} \quad (2.11)$$

for a single generation of leptons (the expression is repeated for the other generations). The coefficient of  $(\bar{e}_L \gamma^\mu e_L + \bar{e}_R \gamma^\mu e_R) A_\mu$  implies that  $e = g_2 \sin \theta_w$ , the electric charge. Hence both the electromagnetic and weak forces are encompassed in this description.

Finally, we consider the electroweak kinetic terms of eq. (2.2),

$$\mathcal{L}_{\text{EW}}^{\text{kin}} = -\frac{1}{4} W_{\mu\nu}^i W_i^{\mu\nu} - \frac{1}{4} B_{\mu\nu} B^{\mu\nu}. \quad (2.12)$$

After re-writing eq. (2.12) in terms of the physical fields  $W_\mu^\pm$ ,  $Z_\mu$  and  $A_\mu$  we find cubic and quartic terms, corresponding to  $WWZ$ ,  $WWA$ ,  $WWWW$ ,  $WWZZ$  and  $WWAA$  – the weak-boson self-interaction terms.

Throughout this section, there has been no mention of mass, and there are no mass terms in the electroweak Lagrangian. Yet, simply adding mass terms to the Lagrangian such as  $\frac{1}{2} m_B^2 B_\mu B^\mu$  would break the  $\text{SU}(2)_L \times \text{U}(1)_Y$  gauge invariance and so is forbidden. A Dirac mass term for the leptons is also forbidden since terms of the form  $m(\bar{\psi}_R \psi_L + \bar{\psi}_L \psi_R)$  would also break the global gauge invariance (the left and right hand fields belong to different  $\text{SU}(2)$  representations and have different charges under  $\text{U}(1)$ , see eq. (2.3)). A more subtle mechanism is needed to generate masses, namely the Higgs mechanism, which is discussed in the next section.

## The origin of mass

A mass generation mechanism is needed for three gauge bosons ( $W^\pm$ ,  $Z$ ) and the fermions, while simultaneously leaving the photon massless. The problem of mass generation was originally solved by Brout, Englert, Guralnik, Hagen, Higgs and Kibble [43–45] by

introducing a complex  $SU(2)$  doublet of scalar fields

$$\Phi = \begin{pmatrix} \phi^+ \\ \phi^0 \end{pmatrix} = \frac{1}{\sqrt{2}} \begin{pmatrix} \phi_1 + i\phi_2 \\ \phi_3 + i\phi_4 \end{pmatrix}, \quad (2.13)$$

where  $\phi_i$  ( $i = 1, \dots, 4$ ) are real scalar fields. We add this field into the Standard Model Lagrangian in the most general way by adding a kinetic term, a mass term of the new field and a self-interaction term with a coupling strength,  $\lambda$ . This gives the following terms in the Higgs Lagrangian:

$$\mathcal{L}_{\text{Higgs}} = (D^\mu \Phi)^\dagger (D_\mu \Phi) - V(\Phi), \quad \text{with} \quad V(\Phi) = \mu^2 \Phi^\dagger \Phi + \lambda (\Phi^\dagger \Phi)^2. \quad (2.14)$$

For  $\mu^2 < 0$ , the potential  $V(\Phi)$  has a minimum at

$$\Phi^\dagger \Phi = -\frac{\mu^2}{2\lambda} \quad (2.15)$$

which has an infinite number of solutions. One must choose a solution and, in order to conserve electric charge and keep the photon massless, it is convenient to choose  $\phi_1 = \phi_2 = \phi_4 = 0$ . By making this choice, the neutral component ( $\phi_3$ ) of the doublet field  $\Phi$  develops a non-zero vacuum expectation value

$$\langle 0 | \Phi | 0 \rangle = \frac{1}{\sqrt{2}} \begin{pmatrix} 0 \\ v \end{pmatrix} \quad \text{with} \quad v = \sqrt{\frac{-\mu^2}{\lambda}}. \quad (2.16)$$

By picking this vacuum we have spontaneously broken the  $SU(2)_L \times U(1)_Y$  symmetry. This process is known as *electroweak symmetry breaking*.

Expanding around this point and writing in exponential form yields

$$\Phi(x) = \frac{1}{\sqrt{2}} e^{i\theta_a(x)\tau^a(x)/v} \begin{pmatrix} 0 \\ v + h(x) \end{pmatrix} \quad (2.17)$$

with three circular  $\theta_{1,2,3}(x)$  and one radial  $h(x)$  degrees of freedom. The circular fields, known as Goldstone bosons, can be absorbed by a gauge choice known as the unitary



gauge ( $\Phi \rightarrow e^{-i\theta_a(x)\tau^a(x)/\nu}\Phi$ ). This leaves

$$\Phi \rightarrow \frac{1}{\sqrt{2}} \begin{pmatrix} 0 \\ v + h(x) \end{pmatrix}. \quad (2.18)$$

With  $\Phi$  in the unitary gauge one can expand the kinetic term of the Higgs Lagrangian,  $(D_\mu\Phi)^\dagger(D^\mu\Phi)$ , which, after using the physical fields  $W_\mu^\pm$ ,  $Z_\mu$  and  $A_\mu$  and ignoring strong interaction terms, becomes

$$\frac{1}{2}(\partial_\mu h)^2 + \frac{g_2^2}{8}(v+h)^2 W_\mu^+ W^{\mu-} + \frac{1}{8}(v+h)^2(g_1^2 + g_2^2)Z_\mu Z^\mu, \quad (2.19)$$

where  $Y_H = 1$ , the Higgs hypercharge, has been used. Immediately, we can read off mass terms for the  $W$  and  $Z$  bosons:

$$M_W = \frac{g_2 v}{2} \quad m_Z = \frac{1}{2}v\sqrt{g_1^2 + g_2^2}, \quad (2.20)$$

and, crucially, we see there are no terms of the form  $\frac{1}{2}M_A^2 A_\mu A^\mu$  – the photon has remained massless. Therefore, by spontaneously breaking of the symmetry  $SU(2)_L \times U(1)_Y \rightarrow U(1)_Q$ , three Goldstone bosons have been absorbed by the  $W^\pm$  and  $Z$  bosons to form their longitudinal components and get their masses. Since the  $U(1)_Q$  symmetry is still unbroken, the photon which is its generator remains massless. Furthermore, from eq. (2.19) we also see interaction terms between the gauge bosons and the Higgs boson of the form  $hhWW$ ,  $hhZZ$ ,  $hWW$  and  $hZZ$ , with the coupling strength proportional to the square of the gauge boson mass.

The Higgs potential can also be expanded in terms of the unitary  $\Phi$ , giving

$$V(\Phi) = -\frac{2\lambda v^2}{2}h^2 - \lambda v h^3 - \frac{\lambda}{4}h^4 + \frac{\lambda v^4}{4}, \quad (2.21)$$

from which we conclude the Higgs boson mass is

$$m_h^2 = 2\lambda v^2. \quad (2.22)$$

From eq. (2.21), we also see there are cubic and quartic terms in  $h$ , corresponding to three- and four-point Higgs self-interactions shown in figure 2.3, with the coupling strength proportional to the square of the Higgs mass.

We now turn our attention to the fermion masses. Amazingly, this can be solved by the same field. Due to the arrangement of the scalar Higgs field  $\Phi$  in the complex  $SU(2)$  doublet, one can construct interactions of the Higgs field with fermions that do not break the  $SU(2)_L \times U(1)_Y$  gauge symmetry. For example, for leptons of the first generation, the invariant Lagrangian has the form

$$\mathcal{L}_e = \lambda_e (\bar{L}_1 \Phi e_R + \Phi^\dagger \bar{e}_R L_1). \quad (2.23)$$

After electroweak symmetry breaking when the Higgs field obtains a non-zero vacuum expectation value and with the Higgs field in the unitary gauge, one obtains

$$\mathcal{L}_e = \frac{\lambda_e v}{\sqrt{2}} (\bar{e}_L e_R + \bar{e}_R e_L) (1 + h). \quad (2.24)$$

Since  $\bar{\psi}_L \psi_R + \bar{\psi}_R \psi_L = \bar{\psi} \psi$  we can read off the electron mass  $m_e = \lambda_e v / \sqrt{2}$ . Furthermore we see terms such as  $eeh$ , the coupling of the Higgs to pairs of electrons, with the coupling strength proportional to the mass of the electron (or rather, the mass of the electron proportional to the coupling strength). The mathematics is identical for the other generation of leptons, giving  $m_\mu = \lambda_\mu v / \sqrt{2}$  and  $m_\tau = \lambda_\tau v / \sqrt{2}$  and corresponding couplings.

Similarly for the leptons, interaction terms can be added giving rise to quark masses,

$$\mathcal{L}_q = -\lambda_d (\bar{Q}_1 \Phi d_R + \Phi^\dagger \bar{d}_R Q_1) - \lambda_u (\bar{Q}_1 \tilde{\Phi} u_R + \tilde{\Phi}^\dagger \bar{u}_R Q_1) \quad (2.25)$$

$$= -\frac{\lambda_d(v+h)}{\sqrt{2}} (\bar{d}_L d_R + \bar{d}_R d_L) - \frac{\lambda_u(v+h)}{\sqrt{2}} (\bar{u}_L u_R + \bar{u}_R u_L) \quad (2.26)$$

where  $\tilde{\Phi} = i\tau_2 \Phi^*$  and only the first generation of quarks is considered. Again we see mass terms for the  $u$  and  $d$  quarks ( $m_u = \lambda_u v / \sqrt{2}$ ;  $m_d = \lambda_d v / \sqrt{2}$ ) and interaction terms  $uuh$  and  $ddh$ . However, the situation becomes more complex when three generations of quarks are included. Cross-generation transitions between quarks are observed experimentally in weak-force mediated processes. This suggests that the weak quark eigenstates are a superposition of the mass eigenstates, which gives rise to CP-violation, as described further in appendix A.2.

That neutrinos oscillate between flavours, and therefore have mass has now been well established [35–39]. However, in this formalism there are no mass terms for the neutrinos.

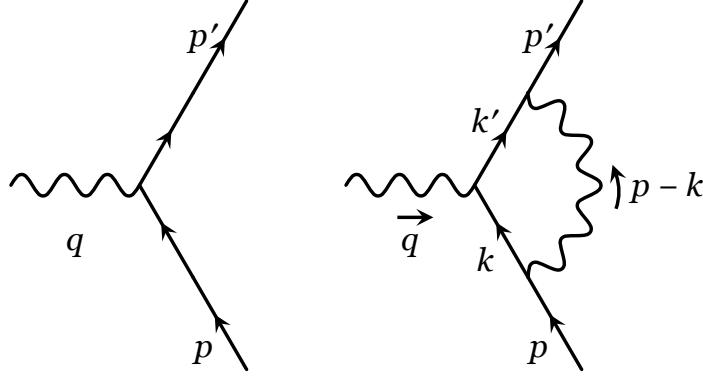


**Figure 2.4.:** A photon–fermion interaction at tree-level (left) and one-loop (right). As long as momentum is conserved at each vertex and  $q = p' - p$ , the momenta around the loop  $k$  and  $k'$  are unconstrained. Diagrams from [46].

It is possible to generate mass terms for the neutrinos by adding  $\nu_R$  fermions, and after electroweak symmetry breaking, terms similar to eq. (2.24) emerge. This approach does not explain the very low experimentally observed masses, as intuitively the Dirac masses should be at the electroweak symmetry breaking scale.

#### 2.1.4. Renormalisation

When considering quantum corrections to calculable properties in the Standard Model, such as coupling strengths, the effect of loops such as the one shown in figure 2.4 must be taken into account. However, one finds that the momenta of internal particles in the loops are unconstrained, which can lead to divergences in calculations at low or high momenta, known as “infra-red” and “ultra-violet” respectively. These divergences correspond to missing information in the theory – the Standard Model is not expected to work at all scales, and new heavy particles may enter the loops changing the divergence. In order to make our theory consistent with measurements these divergences must be removed, and are done so via a process called *renormalisation*.

From a technical perspective, renormalisation is the process in which the divergences can be absorbed by adding scale-dependence to various parameters such as coupling strengths or particle masses. The result is that one can subtract counter-terms from the

“bare” Lagrangian  $\mathcal{L}_0$  in order to remove the divergences

$$\mathcal{L}_{\text{phys}}(\mu) = \mathcal{L}_0 - \mathcal{L}_{\text{CT}}(\mu) \quad (2.27)$$

where  $\mathcal{L}_{\text{CT}}$  contains the counter-terms. The new Lagrangian,  $\mathcal{L}_{\text{phys}}$  contains the physical couplings comparable to experimental measurements. These counter-terms, although they remove the divergences from the calculation, introduce a dependence on the momentum scale  $\mu$ , which is characteristic of the process considered.<sup>3</sup> Therefore the physically measured value of a quantity also depends on  $\mu$ . This outlines the important consequence of renormalisation: that the (renormalised) coupling strength – as well as other physical observable – is not constant. For example, in the case of QED, the coupling constant  $\alpha_{EM}$  becomes a running coupling  $\alpha_{EM}(\mu)$  varying with the momentum scale  $\mu$ .

For QED, the coupling strength increases with  $\mu$ . This is equivalent to the charge screening effect in QED, whereby the closer one approaches an electron with an electromagnetically-interacting probe (increasing  $\mu$ ), the larger one measures the charge. The opposite occurs in QCD, as the coupling strength decreases with increasing  $\mu$ , leading to the phenomenon of asymptotic freedom and confinement.

## 2.2. Problems with the Standard Model

While the Standard Model can accurately predict many processes, the theory is far from a “theory of everything”. Firstly, the Standard Model fails to explain a range of observed physical phenomena. Most strikingly, the gravitational force is not taken into account. Furthermore, astronomical observations suggest that 95.1% [47] of the energy density of the universe is made from a mixture of dark matter and dark energy, of which there is no candidate source in the Standard Model, discussed in section 2.2.1. Even within the observable matter sector, the Standard Model does not provide enough CP-violation to explain the origin of matter-antimatter asymmetry that must have existed to provide the matter dominated universe we inhabit. Another important example is that the Standard

---

<sup>3</sup>For example,  $\mu$  can be understood as a measure of the momentum transfer in an interaction, however the exact choice of value is arbitrary.

Model does not provide a mechanism to generate neutrino masses (although this can be incorporated), nor why the neutrino masses are on such a different scale to other particle masses.

Secondly, although the Standard Model may explain the interactions of matter and forces, it does not explain *why* they interact in that way. The Standard Model has 19 free parameters, whose values have no theoretical motivations and must be determined experimentally. In an ultimate theory, one hopes to have a dynamic mechanism that generates the values of the free parameters. There is also no justification for the orders of magnitude difference between the masses of the fermions, or that there are three generations of fermions. Furthermore, the transition rates between different quark flavours (the elements of the CKM matrix) are also not predicted.

Thirdly, there are inconsistencies within the Standard Model, although some argue that these are more aesthetical in nature. For example, in order to create a “theory of everything” one would expect that the forces unify at some high scale, however this is not the case in the Standard Model, as can be seen in figure 2.5. The non-zero vacuum expectation value of the Higgs is potentially at odds with the observed total energy density of the universe by over 50 orders of magnitude (see appendix A.3 for a discussion). CP-violation has also only been observed in the weak sector, yet there is no reason a priori why there shouldn’t be an additional term in the Standard Model that breaks CP symmetry in the strong sector. Such a term would provide a source of CP-violation from the strong interaction. Experimentally, no such violation has been found, implying that the coefficient of this term is very close to zero. The coefficient is said to be “finely tuned”, and is considered to be unnatural. Another example is the hierarchy problem, further described in section 2.2.2.

There are also a small number of experimental measurements that have some tension with the Standard Model, though there is currently no  $5\sigma$  discrepancy. Notably, the experimentally measured value of muon’s anomalous magnetic dipole moment (“muon  $g - 2$ ”) is between  $3-4\sigma$  away from the Standard Model prediction [48].

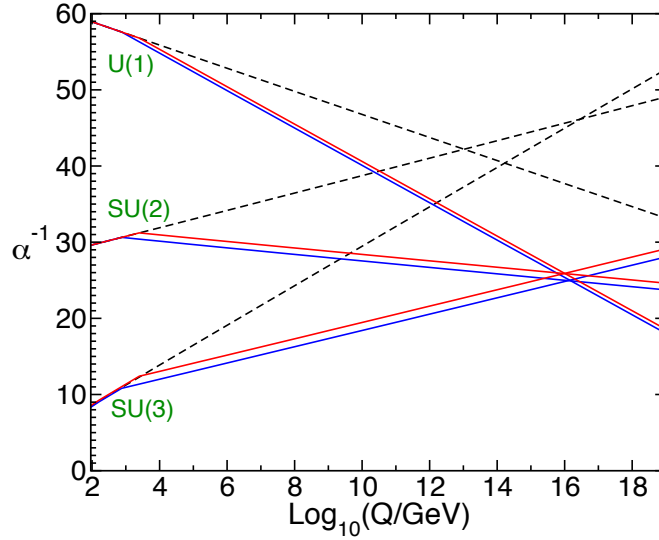


**Figure 2.5.:** Renormalisation group evolution of the inverse gauge couplings  $\alpha^{-1}$  as a function of the energy scale  $Q$  in the Standard Model (dashed lines) and the MSSM (solid lines). In the MSSM case, the sparticle masses are treated as a common threshold varied between 500 GeV and 1.5 TeV, and  $\alpha_S(m_Z)$  is varied between 0.117 and 0.121 giving rise to the red and blue solid lines. Image taken from reference [10].

### 2.2.1. The dark matter problem

A major problem with the Standard Model comes from cosmology. Measurements of the power spectrum of the cosmic microwave background (CMB) suggest that there exists a type of matter that interacts gravitationally, but not luminously. This is supported by a host of other astronomical observations, including galactic rotation curves, gravitational lensing and collisions of galactic nuclei (for a review of the evidence for dark matter, see reference [49, 50]). However, to date no convincing evidence of direct detection of dark matter has been found. Recent measurements by the Planck collaboration [47] suggest the energy density of the universe is split into the following fractions:

$$\Omega_{\Lambda} = 0.69 \quad (2.28)$$

$$\Omega_{\text{CDM}} = 0.26 \quad (2.29)$$

$$\Omega_{\text{baryons}} = 0.04 \quad (2.30)$$

where  $\Omega_{\Lambda}$ ,  $\Omega_{\text{CDM}}$  and  $\Omega_{\text{baryons}}$  refer to the fractions of dark energy, cold dark matter (CDM) and baryonic matter respectively.

The identity of dark matter (and dark energy) remains mysterious, however it is assumed to have a particle nature<sup>4</sup>. In order to be consistent with cosmological observations and particle physics, dark matter must be stable (or long-lived) and have no electromagnetic or strong interactions. This rules out every particle in the Standard Model with the exception of the neutrinos, however CMB measurements suggest that the majority of dark matter must be “cold” (that is, non-relativistic). As a result, although Standard Model neutrinos are dark matter particles, they cannot explain the observed dark matter abundance in the universe.

Several proposed solutions to the dark matter problem exist, including axions, sterile neutrinos, or additional generations of heavy neutrinos. One of the leading candidates is the proposed existence of weakly interacting massive particles (WIMPs), due to the coincidence that WIMPs have the velocity-weighted mean annihilation cross-section with the right order of magnitude to yield the observed dark matter abundance (see appendix A.4 for more details). However, as already mentioned there is no such candidate particle for a WIMP in the Standard Model, and so a new physics theory is required.

### 2.2.2. The hierarchy problem

The bare mass of the Higgs boson,  $m_{h,0}$  depends on the curvature of the Higgs potential at its vacuum minimum. The physical mass squared is the sum of the bare mass squared and the sum of corrections from radiative corrections squared,  $m_h^2 = m_{h,0}^2 + \delta m_h^2$ .

A problem arises when considering radiative corrections to the Higgs mass. Large corrections appear when considering loops such as those shown in figure 2.6. At 1-loop, the corrections have the form

$$\delta m_{h,f}^2 \propto -g_f^2 \left[ \Lambda^2 + m_f^2 \ln \left( \frac{\Lambda}{m_f} \right) \right], \quad \delta m_{h,b}^2 \propto +g_b^2 \left[ \Lambda^2 + m_b^2 \ln \left( \frac{\Lambda}{m_b} \right) \right], \quad (2.31)$$

---

<sup>4</sup>Alternative hypotheses exist, for example that the universe is permeated with astronomical bodies such as primordial black holes or brown dwarfs that are non luminous, or that modified forms of Newtonian gravity or general relativity provide a more accurate description. However, it is difficult to account for either all of the dark matter, or all of the experimental observations with these approaches.

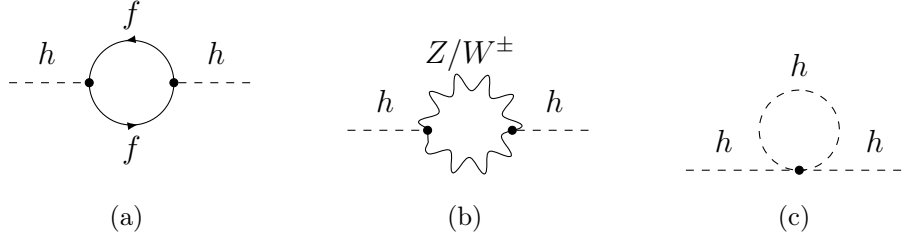


**Figure 2.6.:** Corrections to the Higgs mass from (a) fermions, (b) gauge bosons and (c) scalars at 1-loop.

from a fermion  $f$  and a boson  $b$ . All of the  $\Lambda$  terms come from the regularisation of the loop integral and are unphysical, and after renormalisation the corrections become

$$\delta m_{h,f}^2(\mu) \propto -g_f^2 m_f^2 \ln\left(\frac{m_f}{\mu}\right), \quad \delta m_{h,b}^2(\mu) \propto +g_b^2 m_b^2 \ln\left(\frac{m_b}{\mu}\right), \quad (2.32)$$

where  $\mu$  is the momentum scale. These corrections will hold for any fermion or boson as long as they couple to the Higgs, including any new physics particle that could be very heavy<sup>5</sup>.

Given that new physics is expected at the Planck scale,  $M_{pl} = \sqrt{\frac{\hbar c}{G_N}} \approx 10^{19}$  GeV at which the gravitational interaction becomes important at the quantum scale, eq. (2.32) implies there are potentially enormous corrections to the mass of the Higgs from any new particle. This is at odds with the experimentally measured value of 125 GeV.

This can be resolved if  $m_{h,0}^2$  is also  $\mathcal{O}(M_{pl}^2)$  however, in order to achieve  $m_h^2 = (125 \text{ GeV})^2$ , one would require a cancellation between  $m_{h,0}^2$  and  $\delta m_h^2$  through over 30 orders of magnitude. Such a cancellation, or *fine-tuning*, is widely regarded as unlikely. The apparent need for fine-tuning defines the hierarchy problem, which is not actually a problem with the Standard Model itself, but rather that the Higgs mass has a disturbing sensitivity to new physics at high scales.

There are several possible approaches to the addressing hierarchy problem, including that there is a new physics scale well below the Planck scale [51], close enough to the electroweak scale that the level of fine-tuning is no longer an issue; or that the Planck

<sup>5</sup>Even if new physics particles don't couple to the Higgs, as long as these couple to Standard Model particles with Higgs couplings, then they will contribute via 2-loop corrections.



scale is actually closer to the electroweak scale, as is in the case of models with large extra dimensions.

It is interesting to note that none of the other particles in the Standard Model suffer from such a divergence. This is because they are all protected by a symmetry [11, 52]. This raises the question, is the Higgs mass protected by a new symmetry not found in the Standard Model? From eq. (2.32) we see a sign difference between the correction from fermions and bosons which raises a tantalizing possibility: if every boson was accompanied by a fermion partner of equal mass and coupling (and vice versa), then the dangerous divergences would be systematically removed. In other words, if there was a new symmetry between bosons and fermions then the Higgs mass would be protected from the radiative divergences. Such fermion–boson partners are an essential consequence of *supersymmetry*, which is explored in the next section.

## 2.3. Supersymmetry

Supersymmetry (SUSY) is a proposed symmetry between bosons and fermions. As will be discussed in this section, the result of such a symmetry is that for every particle in the Standard Model there is an additional *supersymmetric* partner particle, or *superpartner*. This results in the particle content of the universe increasing by at least a factor of two, which is somewhat at odds with any desire for a theoretically simple universe. However, the theory has many attractive phenomenological qualities which make this increase in particle content worthwhile. For example, both the hierarchy problem and dark matter problems can be elegantly solved with SUSY.

The idea of SUSY was born out of the need to extend the Standard Model, driven by searches for solutions to the hierarchy problem. Since the Standard Model is built upon symmetry principles, it is natural to attempt to extend it by finding a larger symmetry group that envelopes the Poincaré symmetries of special relativity (translations, rotations and boosts) and the internal symmetries of the Standard Model. However, the Coleman-Mandula theorem [53] severely restricts the possible ways in which this can be done. In fact, it was later shown [54] that the *only* possible extension of symmetries beyond Lie

algebra and groups was to directly link the matter and gauge fields. This results in the *super*-Poincaré group, which includes transformations of bosons into fermions and vice versa, as well as the Poincaré symmetries. The transformations between bosons and fermions are known as *supersymmetric* transformations.

This section will explore the properties of such a symmetry, and its implications. First, the theoretical foundations of SUSY will be laid out in section 2.3.1. Then the particle content of the Minimal Supersymmetric extension to the Standard Model will be discussed in section 2.3.2, with section 2.3.3 exploring the implications of these new particles. Conditions required to maintain low fine-tuning are given in section 2.3.4, and finally experimental signatures will be discussed in section 2.3.5.

### 2.3.1. Foundations of supersymmetry

A supersymmetric transformation is one which transforms a fermionic state into a bosonic one. The generators of the SUSY transformation  $Q$  and  $Q^\dagger$  are constrained [53, 54] and must satisfy the algebra

$$\{Q_\alpha, Q_{\dot{\alpha}}^\dagger\} = -2\sigma_{\alpha\dot{\alpha}}^\mu P_\mu \quad (2.33)$$

$$\{Q_\alpha, Q_\beta\} = \{Q_{\dot{\alpha}}^\dagger, Q_{\dot{\beta}}^\dagger\} = 0 \quad (2.34)$$

$$[P^\mu, Q_\alpha] = [P^\mu, Q_{\dot{\alpha}}^\dagger] = 0 \quad (2.35)$$

where  $P^\mu$  are the generators of space-time translations,  $\mu$  is a Lorentz index,  $\alpha, \dot{\alpha}$  are spinor indices, and  $\sigma^{\mu\nu} = \frac{1}{4}[\gamma^\mu, \gamma^\nu]$ . It is possible to define  $N$  such pairs of SUSY generators, however cases with  $N > 1$  are only of mathematical interest, and only a single ( $N = 1$ ) SUSY is considered in this thesis.

Single particle states are organised into *supermultiplets*. Each supermultiplet contains both fermion and boson states which are superpartners of one another. The supermultiplets themselves must contain the same number of degrees of freedom. Two of the main categories of supermultiplet are *chiral* and *gauge*. Chiral multiplets comprise a two-component Weyl fermion and a complex scalar field. Gauge multiplets consist of a spin-1 vector boson and a spin-1/2 Weyl fermion which are both massless, at least

before electroweak symmetry breaking.<sup>6</sup> In a supersymmetric extension of the Standard Model, each of the known fundamental particles is therefore in either a chiral or gauge supermultiplet, and must have a superpartner with spin differing by  $1/2$  unit.

Since the SUSY operators  $Q, Q^\dagger$  commute with the generators of gauge transformations, particles in the same supermultiplet must have the same electric charges, weak isospin, and colour degrees of freedom. Furthermore, as the  $Q$  operators commute with the generators of translations  $P^\mu$ , they also commute with the mass squared operator  $P^\mu P_\mu$ , from which it follows that particles within the same supermultiplet must have the same mass, as is shown in appendix A.5. This provides an elegant solution to the hierarchy problem discussed in section 2.2.2 as, if SUSY exists, then the quadratic divergences of the radiative corrections to the Higgs mass exactly cancel out. This cancellation is not just possible, but is an unavoidable consequence of SUSY. However, if the masses of bosons and fermions were identical, then the SUSY partner particles would have been discovered along with the Standard Model counterparts. As this is not the case, then this symmetry must be broken.

### Supersymmetry breaking

The fact that superpartners have not been observed experimentally means that SUSY, should it exist, cannot be an exact symmetry of nature. Therefore there must be some mechanism to break the symmetry. The nature of this mechanism is unknown, however it is desirable that the mechanism preserves as many of the attractive qualities of SUSY as possible (otherwise one may as well abandon the introduction of the symmetry in the first place). In particular, we should not want to re-introduce the quadratic divergences associated with the corrections to the Higgs mass.

This can be achieved by the addition of “soft” SUSY breaking parameters to the Lagrangian of the supersymmetric Standard Model. These soft parameters are not invariant under SUSY transformations, and so break the symmetry, however maintain the property that

---

<sup>6</sup>Gravity may also be included, in which case the spin-2 graviton would share a “supergravity” multiplet with the spin-3/2 gravitino.

the loop corrections to the Higgs mass from superpartners cancel out the quadratic divergences.

A general model including the soft terms is known as the *Minimal Supersymmetric extension to the Standard Model* (MSSM). However, the new terms added to the Lagrangian leads to over 100 free parameters. With so many parameters, the MSSM is no longer a predictive theory, but instead a framework from which specific theories can be generated, corresponding to choices of these parameters.

In a theory in which SUSY was exact and unbroken, the dynamics of the superpartners would be precisely determined. Therefore the method by which SUSY is broken has important consequences for the properties of any models generated. Concrete mechanisms for soft SUSY breaking have been proposed, including gravity mediated SUSY breaking [55], Gauge Mediated SUSY Breaking (GMSB) [56–58] and Anomaly Mediated SUSY Breaking (AMSB) [59,60]. Each of these methods results in a different phenomenology of the models possible, for example mass splitting between sparticles and the nature of the lightest SUSY particle (LSP), resulting in different signatures at collider experiments.

## R-Parity

Supersymmetric theories are constructed by specifying the particle content and the associated symmetries, from which the dynamics can be calculated. This approach often gives rise to lepton or baryon number violating terms in the supersymmetric Lagrangian that has the key consequence of allowing rapid proton decay, for example  $p \rightarrow \pi^0 e^+$  may occur as shown in figure 2.7. However, powerful constraints on the proton lifetime have been set by experiments [61,62], with a lower bound on the proton lifetime of  $10^{34}$  years.

One solution to this problem is to introduce a new symmetry to protect the proton from decaying, coined “ $R$ -symmetry”. The corresponding quantum number  $R$ -parity is multiplicatively conserved, and is defined for each particle as

$$P_R = (-1)^{3(B-L)+2s}, \quad (2.36)$$

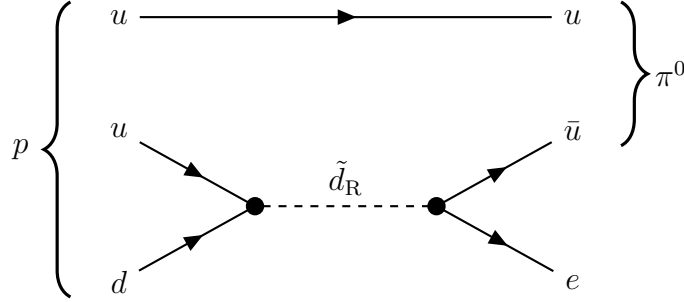


**Figure 2.7.:** Example of a Feynman diagram depicting proton decay, in the case non-zero  $R$ -parity violating couplings.

where  $B$  is baryon number,  $L$  is lepton number and  $s$  is spin of the particle. All Standard Model particles have  $P_R = +1$  and SUSY partners have  $P_R = -1$ . Conservation of this quantum number has several important consequences. Firstly, that Standard Model and sparticles cannot mix, meaning that there must be two sparticles at every interaction vertex and therefore all sparticles must be produced in pairs at a collider experiment. Secondly, that the LSP cannot decay to a Standard Model particle, meaning it must be stable. Since the LSP has not been found it must also be neutral and weakly interacting.

If the LSP is massive<sup>7</sup> then there are further consequences. A massive LSP is an ideal cold dark matter candidate, and SUSY models then have the potential to solve the dark matter problem. Furthermore, each of the LSPs produced in a SUSY event will, as they only have weak interactions, escape detection and potentially generate a large amount of missing transverse momentum ( $E_T^{\text{miss}}$ ). This signature provides a clean separation between SUSY events and the Standard Model background, and has been exploited in many searches, including the one discussed in chapter 5.

The imposition of  $R$ -parity conservation is rather *ad hoc*, and alternative solutions exist. For example, the couplings between the sparticles and particles allowing proton decay could be very small, such that proton decay is not explicitly forbidden but allowing for an extremely long-lived proton. Such theories are called  $R$ -parity violating and have very different collider signatures to RPC scenarios.

<sup>7</sup>It is possible for the LSP to be massless [63].

### 2.3.2. The Minimal Supersymmetric extension to the Standard Model

After soft SUSY breaking, the simplest extension to the Standard Model is known as the Minimal Supersymmetric extension to the Standard Model. This section describes the particle content of the MSSM and some of its properties.

Before discussing the additional particles introduced via SUSY, it is natural to ask if any of the Standard Model particles are already superpartners of one another? As described above, superpartners must have the same gauge quantum numbers, but differ by spin a half. The only candidates are the Higgs boson and the neutrino, however, if these were superpartners of one another many phenomenological problems would result, including a mass for at least one of the neutrinos that is beyond experimental bounds, and lepton number non-conservation. Therefore, in any supersymmetric extension to the Standard Model, each known particle must exist in a multiplet alongside a genuinely new particle.

The MSSM is most conveniently described in terms of its interaction eigenstates, at a high energy scale where SUSY breaking is small. At low energies, all of the MSSM particles gain mass through a supersymmetric version of the Higgs mechanism.

The Standard Model particles are grouped into chiral and gauge multiplets. The fermions are placed into chiral multiplets, such that their partners are scalars. If the fermions were placed into gauge multiplets, this would yield additional gauge bosons and corresponding gauge interactions. The gauge bosons are placed into gauge multiplets, such that their partners are fermions. The particle content of the MSSM is summarised in table 2.3, and is described below.

The superpartners of the quarks and leptons are called *squarks* and *sleptons* respectively, with the “s” that has been prepended standing for scalar. Collectively the squarks and sleptons are referred to as sfermions. The left and right handed pieces of the quarks and leptons form separate two-component Weyl spinors, with different gauge transformations, and so each piece must have a scalar partner. For a fermion  $f$ , the supermultiplets are then  $(f_L, \tilde{f}_L)$  and  $(f_R, \tilde{f}_R)$ , where the new scalar partner of the fermion is denoted with

Names	Spin 0	Spin 1/2	Spin 1
Chiral multiplets			
Squark, quarks	$(\tilde{u}_L \ \tilde{d}_L)$	$(u_L \ d_L)$	
( $\times 3$ generations)	$\tilde{u}_R$ $\tilde{d}_R$	$u_R$ $d_R$	
Sleptons, leptons	$(\tilde{\nu}_e \ \tilde{e}_L)$	$(\nu_e \ e_L)$	
( $\times 3$ generations)	$\tilde{e}_R$	$e_R$	
Higgs, Higgsinos	$(H_u^+ \ H_u^0)$	$(\tilde{H}_u^+ \ \tilde{H}_u^0)$	
	$(H_d^0 \ H_d^-)$	$(\tilde{H}_d^0 \ \tilde{H}_d^-)$	
Gauge multiplets			
Gluino, Gluon		$\tilde{g}$	$g$
Wino, $W$ bosons		$\tilde{W}^\pm \ \tilde{W}^0$	$W^\pm \ W^0$
Bino, $B$ boson		$\tilde{B}^0$	$B^0$

**Table 2.3.:** Particle content of the MSSM before electroweak symmetry breaking.

a tilde on top of the symbol (note the tilde notation is used for all SUSY particles). The scalar partners have also maintained the  $L$  and  $R$  subscripts, however there is of course no “handedness”, and the subscript refers to the handedness of the superpartner. Within a supermultiplet, the gauge interactions are the same, for example the  $\tilde{u}_L$  will interact with the  $W$  boson, but the  $\tilde{u}_R$  will not. Neutrinos in the Standard Model are only left-handed, and so the scalar partner is denoted  $\tilde{\nu}_\ell$  for neutrino flavour  $\ell$ .

The vector particles of the Standard Model are arranged into the eponymous gauge multiplets.<sup>8</sup> These are the SUSY equivalent of the Standard Model gauge bosons, and contain the minimal additional fields necessary to create a theory that is both

<sup>8</sup>One may consider that the gauge bosons may have been placed in a “higher” multiplet, and have spin-3/2 superpartners. However, such a theory would be not be renormalisable [10].

supersymmetric and gauge invariant. The spin-1/2 partners of the gauge bosons are collectively referred to as *gauginos*. The gauginos corresponding to the unbroken  $SU(3)_c \times SU(2)_L \times U(1)_Y$  are called the gluinos, winos and binos respectively.

### Higgs Mechanism in the MSSM

As a scalar, the Higgs must be placed into a chiral multiplet. In the Standard Model, only a single Higgs boson is necessary to give mass to the quarks of different hypercharge. However, this is not the case in SUSY and a second doublet is required, with opposite hypercharge, to give mass to the up and down quarks. The new complex doublet fields are denoted  $H_u$  and  $H_d$ , named so because they give rise to the masses of the up-type and down-type quarks respectively,  $H_d$  also giving rise to the lepton masses. Each of the fields has two weak isospin components  $(H_u^+ \ H_u^0), (H_d^0 \ H_d^-)$ . The corresponding fermion superpartners are the *Higgsinos*, denoted  $(\tilde{H}_u^+ \ \tilde{H}_u^0), (\tilde{H}_d^0 \ \tilde{H}_d^-)$ .

The addition of two complex  $SU(2)$  doublets spontaneously breaks the electroweak gauge symmetry in a similar way to the Standard Model. Both  $H_u^0$  and  $H_d^0$  obtain vacuum expectation values, satisfying  $v_u^2 + v_d^2 = v^2$ , with  $v$  as in eq. (2.20). The ratio of the vacuum expectation values is traditionally written as  $\tan \beta \equiv v_u/v_d$ . At the tree-level, the Standard Model fermion masses become

$$m_u = \frac{\lambda_u}{\sqrt{2}}v_u, \quad m_d = \frac{\lambda_d}{\sqrt{2}}v_d, \quad m_\ell = \frac{\lambda_\ell}{\sqrt{2}}v_d \quad (2.37)$$

which, for the quarks, has the knock-on effect that the mixing angles in the CKM matrix not only depend on the Yukawa couplings, but also  $\beta$ .

With two complex doublets, there are eight degrees of freedom. Three of these become the longitudinal components of the massive vector bosons,  $W^\pm, Z$ , with masses still given by eq. (2.20). The remaining five Higgs scalars become the following physical fields:

- 2 CP-even scalars,  $h^0$  and  $H^0$ ,
- 1 CP-odd scalar,  $A^0$
- A pair of oppositely charged scalars,  $H^\pm$ .



By convention,  $h^0$  is the lighter CP-even scalar, and is identified with the Standard Model Higgs boson.

### Sparticle mixing

The superpartners listed in table 2.3 are not necessarily the mass eigenstates. After electroweak symmetry breaking, mixing between the gauginos and Higgsinos, and within the various sets of squarks and sleptons can occur. The neutral gauginos and Higgsinos mix to form the *neutralinos*, denoted  $\tilde{\chi}_i^0$ , with  $i = 1, 2, 3, 4$ , while the charged winos and Higgsinos mix to form the *charginos*, denoted  $\tilde{\chi}_j^\pm$ , with  $j = 1, 2$ , in both cases ordered from lightest to heaviest. Typically, it is assumed that the lightest neutralino  $\tilde{\chi}_1^0$  is the lightest SUSY particle, unless there is a lighter gravitino or  $R$ -parity is not conserved.

The gluinos are unique among MSSM particles, as they cannot mix. As for the squarks and sleptons, in principle, any scalars with the same electric charge,  $R$ -parity and colour quantum numbers can mix with each other. For example, the up-type squarks ( $\tilde{u}_L, \tilde{c}_L, \tilde{t}_L, \tilde{u}_R, \tilde{c}_R, \tilde{t}_R$ ) can all mix, likewise for the down-type squarks, charged sleptons and neutral sleptons. However, this leads to flavour changing neutral currents from SUSY loop diagrams, which are heavily constrained by experiment. What is still allowed is mixing between the sfermions within the same generation. This is only significant for the third generation, and as a result the  $\tilde{t}_L$  and  $\tilde{t}_R$  mix to form the  $\tilde{t}_1$  and  $\tilde{t}_2$ , with  $\tilde{t}_1$  being the lighter squark. Similarly, the sbottoms and staus mix to form  $(\tilde{b}_1, \tilde{b}_2)$  and  $(\tilde{\tau}_1, \tilde{\tau}_2)$  respectively. A summary of the gauge and mass eigenstates is given in table 2.4.

### 2.3.3. Implications of supersymmetry

Many beyond the Standard Model theories exist, yet SUSY has ranked among particle physicist's favourites for several decades. There are several reasons for this, some of which have already been alluded to. Firstly, SUSY provides an elegant solution to the hierarchy problem in its unbroken form, automatically cancelling out the quadratic divergences to the Higgs mass from radiative divergences. Secondly, in the case of  $R$ -parity conserving

Names	Gauge Eigenstates	Mass Eigenstates
Higgs bosons	$H_u^0 \ H_d^0 \ H_u^+ \ H_d^-$	$h^0 \ H^0 \ A^0 \ H^\pm$
Squarks	$\tilde{u}_L \ \tilde{u}_R \ \tilde{d}_L \ \tilde{d}_R$	(same)
	$\tilde{s}_L \ \tilde{s}_R \ \tilde{c}_L \ \tilde{c}_R$	(same)
	$\tilde{t}_L \ \tilde{t}_R \ \tilde{b}_L \ \tilde{b}_R$	$\tilde{t}_1 \ \tilde{t}_2 \ \tilde{b}_1 \ \tilde{b}_2$
Sleptons	$\tilde{e}_L \ \tilde{e}_R \ \tilde{\nu}_e$	(same)
	$\tilde{\mu}_L \ \tilde{\mu}_R \ \tilde{\nu}_\mu$	(same)
	$\tilde{\tau}_L \ \tilde{\tau}_R \ \tilde{\nu}_\tau$	$\tilde{\tau}_1 \ \tilde{\tau}_2 \ \tilde{\nu}_\tau$
Neutralinos	$\tilde{B}^0 \ \tilde{W}^0 \ \tilde{H}_u^0 \ \tilde{H}_d^0$	$\tilde{\chi}_1^0 \ \tilde{\chi}_2^0 \ \tilde{\chi}_3^0 \ \tilde{\chi}_4^0$
Charginos	$\tilde{W}^\pm \ \tilde{H}_u^\pm \ \tilde{H}_d^\pm$	$\tilde{\chi}_1^\pm \ \tilde{\chi}_2^\pm$
Gluino	$\tilde{g}$	(same)

**Table 2.4.:** The undiscovered particle content of the MSSM (with the exception of  $h^0$ ), before and after electroweak symmetry breaking. Mixing within the first two generations is assumed to be negligible.

SUSY, the LSP is an ideal dark matter candidate, with the potential to either saturate the observed dark matter relic density, or make up a component thereof. The additional CP-violating phases also provide mechanisms to provide the observed matter-antimatter imbalance in the universe. The third reason is purely aesthetic in nature, and is related to the speculation that all three Standard Model forces might eventually be described in terms of a single grand unified theory (GUT).

## Grand unified theories

The idea of a GUT is to embed the  $SU(3) \times SU(2) \times U(1)$  gauge groups into a larger group that is spontaneously broken at some scale. Above this scale, the three forces of the Standard Model would have equal couplings, and would have become unified into a single force. Below this scale, the couplings would run according to the renormalisation group equation. This “grand unification” is not only borne out of a desire for theoretical

simplicity, but it would also automatically predict the quantized nature and values of all elementary particle charges, which is not done in the Standard Model [64].

The nature of the running depends on the particle content at a given scale. With the known content of the Standard Model, the gauge couplings do not appear to be on a trajectory such that they would unify at a high scale, as shown by figure 2.5. However, adding SUSY particles provides a significant improvement to the unification as is also shown by figure 2.5.

#### 2.3.4. Maintaining naturalness

The Standard Model is considered *unnatural* since a large degree of fine-tuning is required to account for the divergences associated with radiative corrections to the Higgs mass. One of the motivating principles behind SUSY is the automatic cancellations of these divergent terms. However, since SUSY is a broken symmetry the cancellation is not exact and there is some inherent fine-tuning in any SUSY model, albeit less than in the Standard Model. Requiring low fine-tuning for a model therefore has consequences on sparticle masses.

In the MSSM, the contribution to the Higgs mass from radiative corrections depends on the difference in mass between superpartners. This suggests that a particle and its superpartner shouldn't have too large a separation in mass, otherwise the problems of fine-tuning would re-emerge. In particular, the largest correction to the Higgs mass (at 1-loop) comes from the stop quark [65], which itself receives large corrections from the gluino. Other sparticle masses do not contribute significantly. Furthermore, the mass of the  $Z$  is also dependent on masses of the Higgsinos. This implies that in order to avoid a SUSY theory that is largely fine-tuned, the stop, gluino and Higgsino shouldn't be too heavy [65, 66].

Exactly how heavy is “too heavy” is a subject of debate, which is related to the subjective nature of quantifying naturalness. However, it is often stated that if the masses of the superpartners are very much larger than the TeV scale, then the radiative corrections

to the Higgs mass again become problematic [67]. This motivates searches at the LHC, which can probe the TeV scale.

### 2.3.5. Experimental signatures

The existence of SUSY can be inferred indirectly through the effects of quantum corrections affecting, for example, branching ratios of certain decays, particle masses, or additional CP-violation. However, the most striking evidence for SUSY would be the production, and subsequent detection, of SUSY particles at a collider experiment such as ATLAS. The most frequently produced particles would be those with the largest production cross-section, and therefore the most likely to be seen first. As we can see from figure 2.8, which summarises the sparticle pair-production cross-section at a centre-of-mass energy of 13 TeV, it is the gluino and the squarks that have the largest cross-section for a given mass, due to their direct coupling to the quarks and gluons of the proton via the strong force. The production modes for squarks and gluinos are shown in figure 2.9. Given their large cross-section, and that naturalness arguments suggest these particles could be in the TeV range, it seems prudent to search for these particles at the LHC.

How might one search for squarks and gluinos if they are produced at the LHC? If the squark is lighter than the gluino, then dominant decay modes of the gluino would be  $\tilde{g} \rightarrow g\tilde{q}$  or  $\tilde{g} \rightarrow q\tilde{q}$ , if not, the gluino may decay directly to the LSP and a quark or gluon. Squarks would decay similarly, typically  $\tilde{q} \rightarrow q\tilde{\chi}$ , but again depending on the mass hierarchy of the SUSY particle spectrum. In both cases, many jets would be produced from the hadronisation of the quarks, especially if they are top quarks. The charginos and heavier neutralinos will typically decay to the lighter neutralinos and charginos via  $h/W/Z$  (depending on the charge), or possibly a squark or gluino if heavy enough. In all cases, the end of the decay chain results in the LSP, which escapes the detector resulting in a key signature of SUSY: missing transverse momentum. However, the amount of missing transverse momentum depends on the mass splitting between the different SUSY particles in the chain and the mass of the LSP, resulting in scenarios where any missing

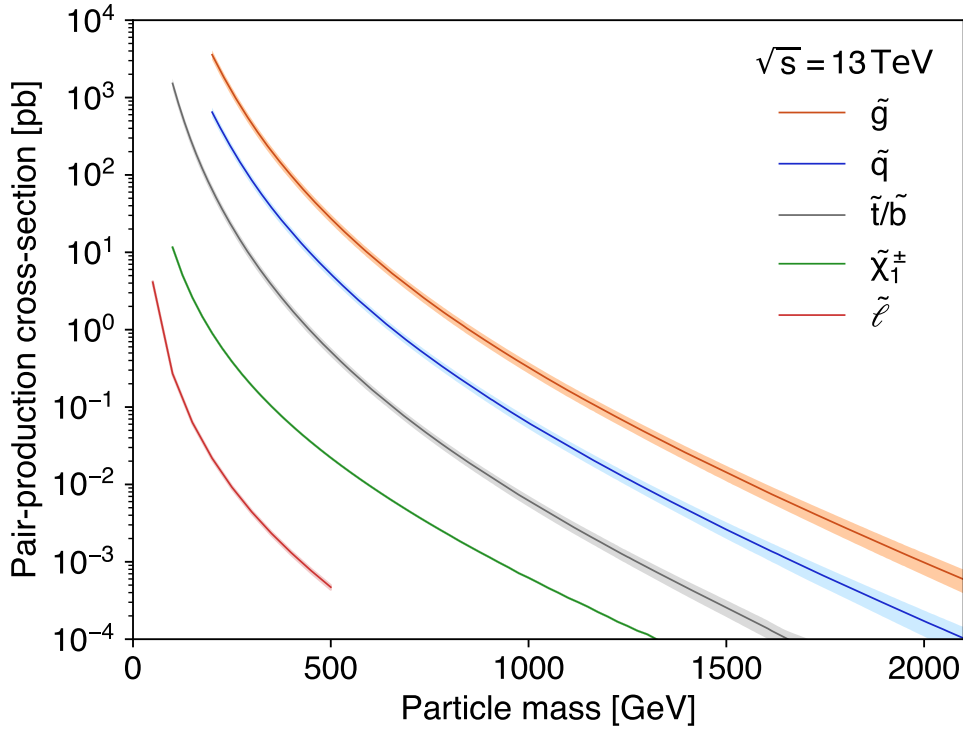


**Figure 2.8.:** Sparticle pair-production cross-sections at 13 TeV as a function of sparticle mass, calculated from ref. [68]. The gluino cross-section assumes all squarks are decoupled, the squark cross-section assumes the gluino and the stop are decoupled with the remaining squarks degenerate (meaning a 10-fold squark degeneracy), and the stop/sbottom cross-section assumes the gluino and the first and second generation squarks are decoupled.

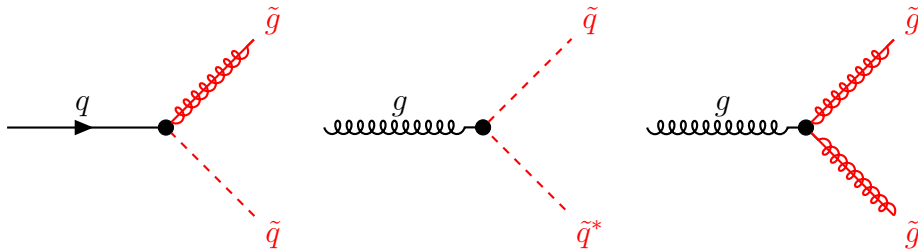


**Figure 2.9.:** Feynman diagrams for strong production of SUSY particles.

transverse momentum becomes difficult to measure above experimental noise. A search for the gluino in such a scenario is presented in chapter 5.

## 2.4. Summary

This chapter has introduced the Standard Model, the theory describing the interactions between the known bosons and fermions which give rise to the macroscopic concepts of forces and matter, and also the origin of mass. Yet, for all of the precise verification provided by particle physics experiments, the Standard Model has many shortcomings and there are too many unanswered questions to consider the theory a complete one.

The possible extensions to the Standard Model are severely limited by the Coleman-Mandula theorem. One exception is supersymmetry. Not only is it certainly a fundamental question to ask whether there exists a symmetry unifying matter and forces, but there are strong theoretical reasons to suppose there is. Many of the problems with the Standard Model can be resolved simultaneously by the introduction of supersymmetry.

Despite the strong motivation, there is currently no experimental evidence that SUSY is realised in nature. Yet few would argue that it is not worth searching for. However, the fact that after soft SUSY breaking the theoretical framework has over 100 free parameters raises the question of how to even begin to search for SUSY. Furthermore, how might one interpret the null results of such searches? Possible answers to these questions are explored in the following chapters of this thesis.

## 3 | The ATLAS experiment

ATLAS [69] – “A Toroidal LHC Apparatus” – is one of the four major experiments at the Large Hadron Collider at the European Centre for Nuclear Research (CERN), situated near Geneva, Switzerland. The name is shared by both the detector with which all of the data used in this thesis was collected and the collaboration of over 3000 scientists that operate the detector and analyse the data. This chapter describes the Large Hadron Collider and then the ATLAS detector, focusing on the individual sub-components and algorithms used to reconstruct and identify physics objects used in this thesis.

### 3.1. The Large Hadron Collider

The Large Hadron Collider (LHC) [70] is the most powerful particle accelerator ever built, and also the most complex and largest single scientific machine ever created. It is used to accelerate and collide protons together (as well as provide heavy ion collisions such as lead-lead and proton-lead), such that new physics may be explored from the particles created during the collision. It is roughly circular in shape with a perimeter of approximately 27 km, and is situated across the Swiss–French border, at a mean depth of 100 m underground (with a maximum depth of 175 m). The LHC was built over a period of 10 years, from 1998 to 2008, and resides in a tunnel which was previously occupied by the Large Electron Positron Collider (LEP).

Around 9300 magnets are used to control the beam of protons in the LHC, including 1232 dipole magnets to bend the beam in a circular direction, and 858 quadrupoles to focus the beams. The remaining magnets are of higher orders, up-to dodecapoles, which are used

for cleaning and more precision tuning of the beam. The dipole magnets were designed to bend a beam of 7 TeV protons, which requires a magnetic field of 8.3 T. In order to accomplish this, superconducting wires, cooled to 1.9 K, carry a current of 11800 A.

The LHC programme has operated in several phases. The first, Run-1, took place between the 30<sup>th</sup> March 2010 to the 13<sup>th</sup> February 2012, with a nominal beam energy of 3.5 TeV, rising to 4 TeV in 2012.<sup>1</sup> The second, Run-2, began on the 20<sup>th</sup> May 2015<sup>2</sup> with a beam energy of 6.5 TeV, and is scheduled to finish at the end of 2018. In-between these phases, the LHC entered a shut down phase for maintenance and upgrade work, to enable the increase in the beam energy. Run-3 of the LHC is planned to begin in 2021, lasting for at least three years, finally reaching the design beam energy of 7 TeV.

The LHC beam itself has humble beginnings as gaseous hydrogen inside a pressurised bottle. Protons are produced by ionising hydrogen inside a *duoplasmatron*, which generates a plasma of electrons, protons and molecular ions. Protons are then extracted and injected into the first of a series of accelerators which act like gears to progressively increase their energy up to 450 GeV, after which they are injected into the LHC in two counter-rotating beams. A schematic of the LHC injector chain is shown in figure 3.1. The LHC beam is not continuous, but is arranged into bunches of  $\mathcal{O}(10^{11})$  protons. These bunches are injected into the LHC from the Super Proton Synchrotron in “trains” of bunches. A summary of a selection of beam parameters during the major data-taking periods of Run-1 and Run-2 are shown in table 3.1. After the LHC is filled with bunches of protons, the beam energy is ramped up to the desired energy by 400 MHz radio frequency (RF) cavities. The beam is then squeezed and then finally stable beams are announced and collisions occur. The beam itself loses intensity over time, mainly due to the collisions in the interaction regions.

The proton beams are brought to collision at four interaction points along the LHC ring. At each point, a detector has been built to measure the particles produced in

<sup>1</sup>The beginning of LHC running was delayed for over a year after the completion of the construction due to a catastrophic magnet quench. The quench caused localised heating, causing the liquid helium to vaporise resulting in an explosion of the LHC beam pipe. About 100 bending magnets were damaged.

<sup>2</sup>The author had the good fortune to be the run-controller for the ATLAS experiment on the first day of stable beams, which saw collisions in the ATLAS detector at a centre-of-mass energy of 13 TeV.



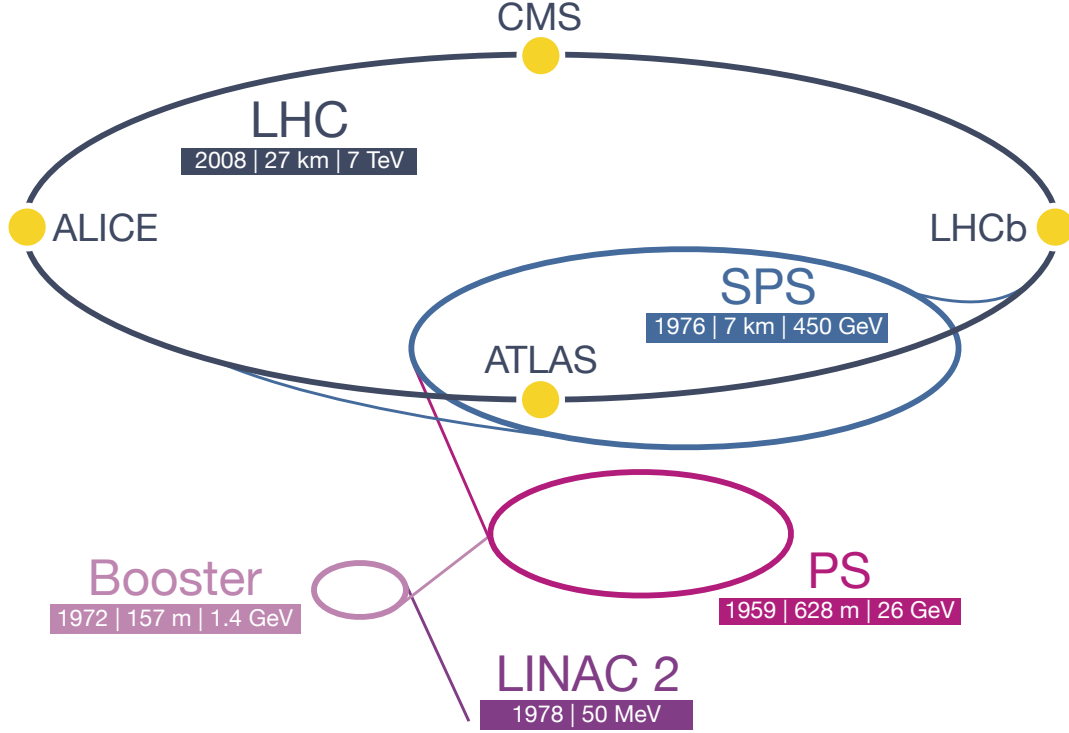


**Figure 3.1.:** A schematic of the LHC ring and accelerator complex at CERN. The successively higher energy accelerators are: Linear Accelerator 2 (LINAC 2), Proton Synchrotron Booster, Proton Synchrotron (PS), Super Proton Synchrotron (SPS) and finally the Large Hadron Collider. Image reproduced with permission from [71].

the collisions. The ATLAS experiment is one of two general-purpose detectors situated around the ring, the other being the Compact Muon Solenoid (CMS) [72]. The other two experiments are more specialised: the LHC-beauty experiment (LHCb) [73], a forward-arm spectrometer designed specifically to study the properties of heavy-flavour hadrons; and ALICE (A Large Ion Collider Experiment) [74], designed to study lead-lead collisions. The interaction point (IP) in ATLAS is approximately 10 mm long and 0.005 mm wide in the traverse plane [75].

An important figure of merit for the LHC is the luminosity of the beams it can deliver to the experiments. The luminosity  $L$  is defined as the proportionality factor between the rate of events of a given process  $i$  with cross-section  $\sigma_i$ :

$$\frac{dN_i}{dt} = L \cdot \sigma_i. \quad (3.1)$$

Parameter	2012	2016	Design
Centre-of-mass energy (TeV)	8	13	14
Bunches / beam	1380	2208	2808
Protons / bunch ( $\times 10^{11}$ )	1.48	1.10	1.15
Minimum bunch spacing (ns)	50	25	25
Peak luminosity ( $10^{33}$ ) $\text{cm}^{-2}\text{s}^{-1}$	7.7	13.8	10

**Table 3.1.:** Summary of LHC beam parameters through the major data-taking years to-date, and also the design specification. Data were also recorded in 2011 and 2015, however these years provided a significantly smaller fraction of the total data recorded.

In order to be sensitive to rare processes (with small cross-sections), such as the production of supersymmetric particles, the LHC must provide as large luminosity as possible. For a collider experiment such as the LHC, with two counter-rotating colliding beams, the instantaneous luminosity is given by:

$$L = \frac{N_b n^2 f}{4\pi\sigma_x\sigma_y} F, \quad (3.2)$$

after assuming two equal sized beams, Gaussianly distributed in  $x$  and  $y$ . In the above expression,  $N_b$  is the number of bunches per beam,  $n$  is the number of protons per bunch,  $f$  is the revolution frequency,  $\sigma_{x,y}$  are the Gaussian widths in the  $x$  and  $y$  directions respectively and  $F$  is a reduction factor due to the crossing angle of the beams at the interaction point. Using the design parameters of the LHC given in table 3.1 with  $f = 11.25 \text{ kHz}$  and  $\sigma_{x,y} = 16.7 \mu\text{m}$  yields the design maximum luminosity of  $L \approx 10^{34} \text{ cm}^{-2}\text{s}^{-1}$  [76]. The luminosity can be improved by optimising these parameters.

A consequence of higher instantaneous luminosity is a larger number of additional proton-proton interactions per bunch crossing, known as pile-up. Although a rare interesting event will trigger the detector readout, these common low momentum transfer events will simultaneously be recorded, obscuring the interesting physics and degrading detector performance. Increasing  $n$  or decreasing  $\sigma_{x,y}$  gives more interactions within the same bunch crossing, known as *in-time pile-up*.

For example, at the peak instantaneous luminosity recorded in 2016 of  $13.8 \times 10^{33} \text{cm}^{-2}\text{s}^{-1}$  translates to an average of about 47 simultaneous proton-proton interactions per bunch crossing.<sup>3</sup> For large  $N_b$ , the bunch spacing can be shorter than the detector latency, and interactions from other bunch crossings can affect the measurement; this is known as *out-of-time pile-up*. The distribution of the mean number of interactions per bunch crossing during Run-2 is shown in figure 3.2.

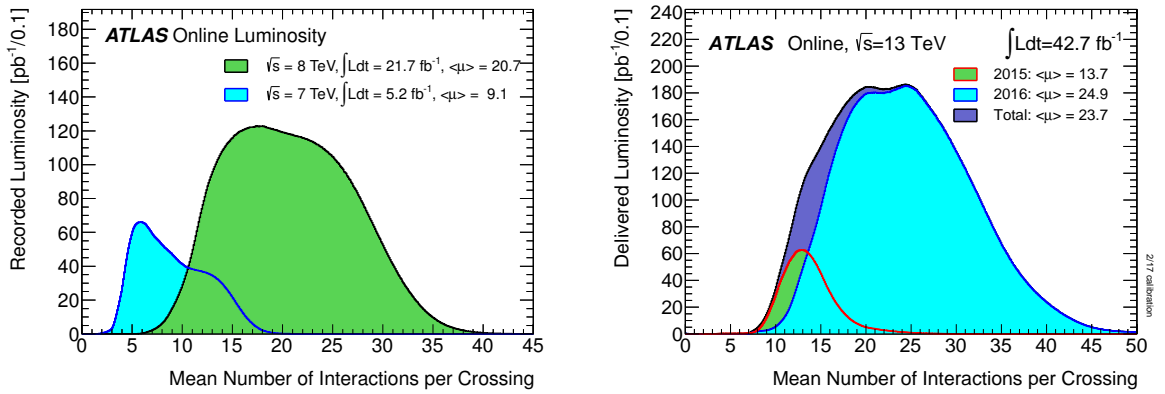


**Figure 3.2.:** Distribution of the mean number of proton–proton interactions per bunch crossing, commonly referred to as in-time pile-up, for the Run-1 (left) and Run-2 (right) datasets, taken from reference [77] and reference [78] respectively.

Equations 3.1 and 3.2 both refer to the *instantaneous* luminosity, which decreases over time as protons are lost from the beam. The *integrated* luminosity,  $\mathcal{L} = \int L dt$ , provides a convenient way to describe the total size of a dataset, and is directly related to the total number of observed events, simply  $N_i = \mathcal{L}\sigma_i$ . In 2012,  $23.3 \text{fb}^{-1}$  of 8 TeV data were delivered to ATLAS by the LHC machine, and in 2015 and 2016  $42.7 \text{fb}^{-1}$  of 13 TeV data were delivered.

<sup>3</sup>The mean number of interactions per bunch crossings is calculated as  $\frac{L_{\text{bunch}}\sigma_{\text{total}}}{f}$ , where  $L_{\text{bunch}}$  is the instantaneous luminosity of each bunch in the LHC,  $\sigma_{\text{total}} = 80 \text{mb}$  is the total inelastic cross-section,  $f$  is the LHC revolution frequency 11.245 kHz. During the 2016 LHC runs where instantaneous luminosity was at its maximum, there was nominally 2200 bunches in the LHC. The instantaneous luminosity is calculated in discrete time intervals over a *luminosity block*, which is approximately one minute of data taking.

## 3.2. The ATLAS detector

The ATLAS detector is a general purpose particle detector. Its primary objectives are to investigate the Standard Model and search for new phenomena beyond that. To do this, many particle detector technologies are combined to measure all kinds of Standard Model particles to high precision. Neutrinos are the only kind of known particle that cannot be detected directly by ATLAS, however due to the hermetic design of the detector the transverse momentum of these particles can be inferred. This principle also extends to the measurement of supersymmetric particles, which may escape ATLAS undetected if weakly interacting.

Overall the ATLAS detector is cylindrical in shape, and at 46 m long and 25 m in diameter it is physically the largest of the detectors at the LHC. With a mass of 7000 tonnes it is also one of the heaviest, second only to its companion detector – CMS. Around 100 million electronic channels read out the detector, which is similar in number to that of a modern digital camera, except that the detector must respond to particle collisions at a rate of 40 MHz and withstand the intense radiation produced for many years.

The detector is generally divided in three regions: the so-called barrel region consists of concentric cylinders centred around the beam axis, the end-cap regions provide the circular faces of the cylinder, and forward regions are those closest to the beam direction which receive the largest particle flux. The exact boundaries of these regions vary according to context, and will be discussed below. ATLAS comprises a magnet system, described in section 3.2.2, to bend the trajectories of charged particles such that their momenta can be measured, and several sub-detectors. The Inner Detector (ID), described in section 3.2.3, is located closest to the beam interaction point – itself consisting of three further subsystems. The purpose of the ID is to detect the primary interaction point of proton-proton collisions, measure displaced or secondary vertices from long-lived particles such as those containing  $c$  or  $b$  quarks, and measure the tracks of charged particles with high precision such that their momentum can be calculated. The calorimeter system surrounds the ID, and consists of two subdetectors. It measures the energies and positions of electrons, taus, photons and hadrons; further details are given in section 3.2.4. The

muon system surrounds the calorimeter and is responsible for triggering and providing space-point measurements of muons that traverse the system, it makes use of four detector technologies and is described in section 3.2.5. Additionally, there are also a three forward detectors, positioned close to the beam-line and further away from the interaction point than the rest of the ATLAS detector. The three forward detectors, LUCID, the ZDC and ALFA have the primary purpose of measuring the luminosity and detecting forward neutrons ( $|\eta| > 8.3$ ) from heavy ion collisions, brief details are given in section 3.2.6. A schematic of the ATLAS detector is shown in figure 3.3.

### 3.2.1. Coordinate system

The coordinate system employed by ATLAS is a right handed one with its origin at the nominal interaction point in the centre of the detector. The  $x$ -axis points from the origin to the centre of the LHC ring, and the  $y$ -axis vertically upwards. The  $z$ -axis points down the LHC beam pipe. Circular coordinates  $(r, \phi)$  can be used in the plane transverse to the beam direction with  $\phi$  being the azimuthal angle around the  $z$ -axis such that  $\phi$  increases in a anticlockwise direction looking into the positive  $z$ . The positive  $x$ -direction defines  $\phi = 0$ , such that  $x = r \cos \phi$  and  $y = r \sin \phi$ . This  $(r, \phi)$  plane, or equivalently the  $(x, y)$  plane, will be referred to as the transverse plane throughout the rest of this thesis.

Positions in the detector are given with cylindrical coordinates  $(r, \phi, z)$ , however particle trajectories are often given with spherical coordinates  $(r, \phi, \theta)$ , introducing the polar angle  $\theta$ . The polar angle is defined from the  $z$ -axis, with  $\theta = 0, \pi$  corresponding to the positive and negative  $z$ -axes respectively. It is sometimes preferential to describe detector components in spherical polar coordinates.

When describing the trajectory of a particle, it is common to replace  $\theta$  with the pseudo-rapidity  $\eta$ , defined as  $\eta = -\ln \tan(\theta/2)$ , which itself is an approximation to the rapidity,  $y$ , where their equivalence is in the ultra-relativistic limit,

$$y = \frac{1}{2} \ln \frac{E + p_z}{E - p_z} \quad (3.3)$$

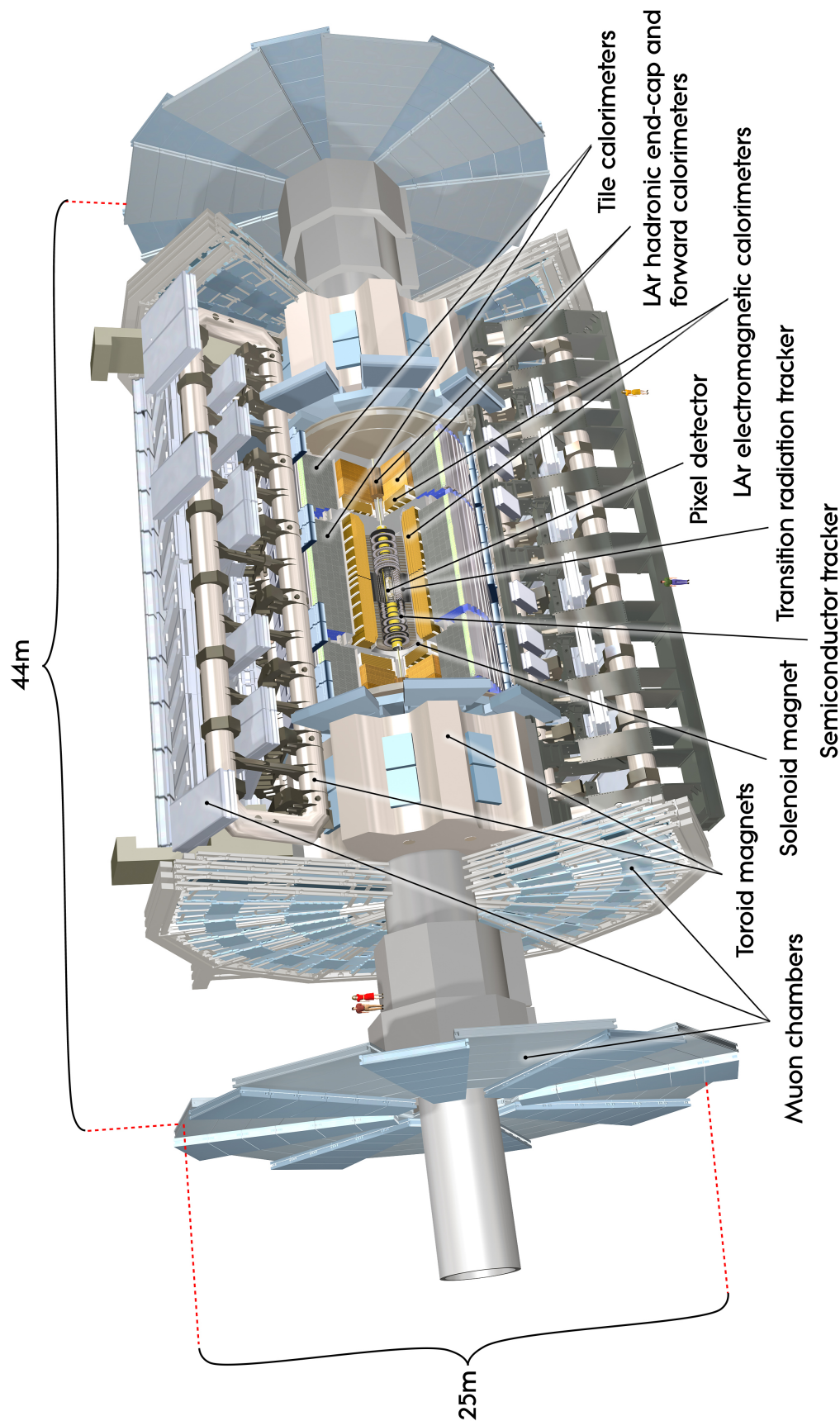


**Figure 3.3.:** A cut-away drawing of the ATLAS detector at the LHC, showing the separate subsystems. Image from reference [69]. Note that LUCID and the other forward detectors are not pictured.

for a particle with energy  $E$  and  $z$ -component of momentum  $p_z$ . The pseudorapidity is 0 anywhere in the  $z = 0$  plane and tends towards  $\pm\infty$  in the forward and backward directions, respectively. The difference between the rapidity of two particles has the useful property that it is invariant under Lorentz boosts in the  $z$ -direction, which is suitable for the LHC as the centre-of-mass frame of a pair of particles from a decay is rarely coincident with the rest frame of the detector due to the composite nature of protons. Pseudorapidity is favoured over rapidity because it is difficult to measure the  $z$ -component of the momentum for highly-boosted particles.

### 3.2.2. Magnet system

The magnets of ATLAS play a critical role in the measurement of particle momenta. Charged particles are bent by a electromagnetic fields according to the Lorentz Force Law:

$$\mathbf{F} = q(\mathbf{E} + \mathbf{v} \times \mathbf{B}), \quad (3.4)$$

where  $\mathbf{F}$  is the force acting on the particle,  $q$  is the charge,  $\mathbf{v}$  is the velocity, and  $\mathbf{E}$  and  $\mathbf{B}$  are the electric and magnetic fields respectively. In ATLAS, only magnetic fields are used to bend the trajectories of charged particles, the degree of bending being proportional to the velocity of the particle allowing its momentum to be extracted.

Magnetic fields in ATLAS are provided by four superconducting magnet systems: a solenoid and three toroidal magnet systems. The solenoid resides in-between the inner detector and calorimeters. The toroids, of which there are 24, are arranged into three groups of 8: one in the barrel region around the calorimeters and two in the end-cap regions. A schematic of the magnet system is show in figure 3.4.

#### The solenoid magnet

The ATLAS solenoid is approximately 2.5 m in diameter and 5.8 m in length. It resides inside the calorimeter systems, and surrounds the Inner Detector. A 2 T axial field is generated by 7.73 kA of current, which winds through 9 km of wire. To withstand the

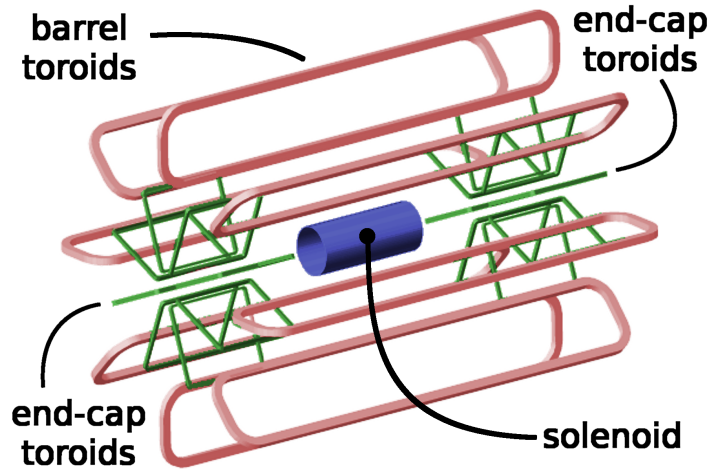


**Figure 3.4.:** A schematic of the ATLAS magnet system. Image taken from reference [79].

high current, the coil is cooled to 4.5 K such that it is superconducting. As the magnet is before the calorimeter, it has been designed to be as thin as possible to reduce the amount of material that particles can interact with. To this end, the magnet and the LAr calorimeter (see section 3.2.4) share the same vacuum vessel, eliminating the need for two additional walls. The total stored energy stored in the magnetic field produced by the solenoid magnet (both inside and outside of the solenoid) is approximately 40 MJ.

### The toroidal magnets

There are three sets of toroidal magnets inside ATLAS: one for the barrel and one each for the two end-caps. Each toroid consists of 8 coils encased in individual racetrack-shaped stainless-steel vacuum vessels, with the coils of the barrel toroid interleaved with those of the end-cap toroids, as shown in figure 3.4. Both the barrel and end-cap toroids are superconducting, cooled to about 4.5 K, and carry a current of 20.5 kA.

The barrel toroid is large, at 25.3 m long and stretching from an inner radius of 9.4 m and extending to 20.1 m. It stores 1.1 GJ of energy during operation, and provides a magnetic field of approximately 0.5 T to the barrel muon detectors.

The end-cap toroids are both 5 m long and have an inner-to-outer diameter of 1.7–10.7 m. They provide an approximate 1 T magnetic field to the end-cap muon detectors, and store an energy of 0.25 GJ each.



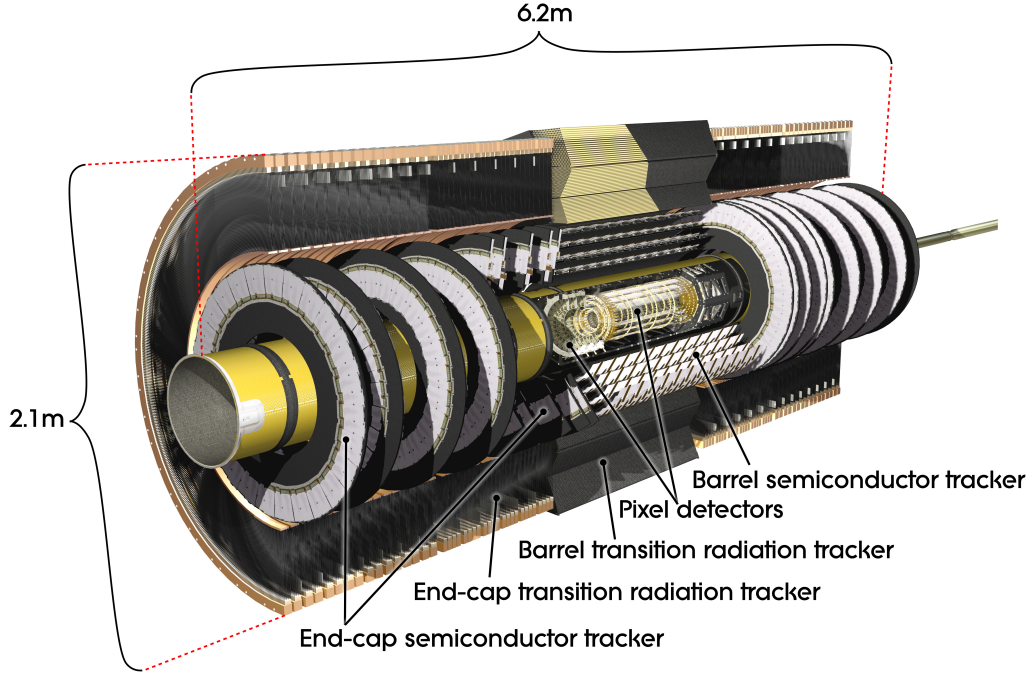


**Figure 3.5.:** A cut-away view of the ATLAS inner detector used in Run-1. The Insertable B-Layer was added in-between Run-1 and Run-2 and is not shown here. Image taken from reference [69].

### 3.2.3. Tracking

The tracking of charged particles through the ATLAS detector is necessary for the measurement of particle momentum. Tracking is provided by the Inner Detector (ID), the subsystems of which are shown together in figure 3.5 and split into barrel and end-cap in figure 3.6. The ID is immersed in a 2 T magnetic field, which allows the momentum of a particle to be measured from the curvature of its track. Momentum and vertex measurements both require an excellent spatial resolution, which is achieved through the fine granularity of the detector subsystems. The three subsystems are the pixel detector, the semiconductor tracker (SCT) and the transition radiation tracker (TRT) which are described below. During the shut down period between Run-1 and Run-2, the pixel detector was augmented with an additional subsystem, the Insertable B-Layer (IBL).

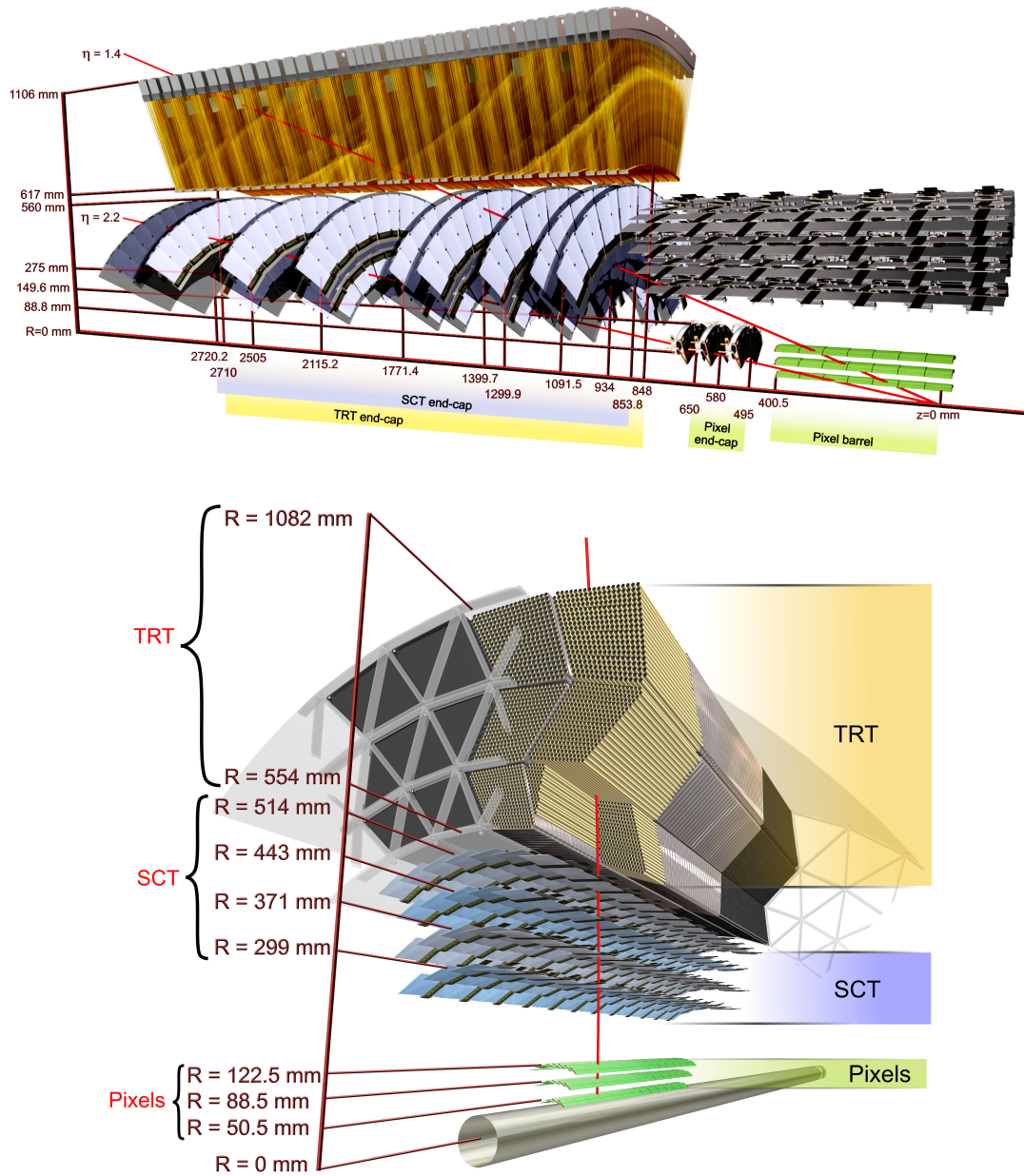


**Figure 3.6.:** Cross-sectional views of the ATLAS inner detector. The end caps are shown in the upper panel, and the barrel is shown in the lower panel. Images taken from reference [69].

## The pixel detector and IBL

The pixel detector [80] was originally the innermost subdetector of ATLAS and therefore has fine granularity to deal with large particle fluxes. It consists of 1744 silicon pixel modules, arranged in the following geometry: three barrel layers of concentric cylinders around the beam axis, at radii of 50.5, 80.5 and 122.4 mm, each with length 801.0 mm; and two sets of three disks perpendicular to the beam axis – one set for each end-cap – located at  $z$ -positions of 495, 580 and 650 mm. This arrangement is such that any particle within  $|\eta| < 2.5$  will traverse through at least three pixel layers. Each pixel sensor module is  $19 \times 63 \text{ mm}^2$  and contains 47268 pixels, the majority of which have an area of  $50 \times 400 \text{ }\mu\text{m}^2$  and a thickness of 250  $\mu\text{m}$ . This gives a total of approximately 80 million pixel sensors.

A silicon particle detector consists of a reverse-biased p-n junction. When a charged particle passes through the depletion region it creates electron-hole pairs, which drift to the respective electrodes. The charge is collected and amplified to produce a signal current. The precision of charged particle measurement is  $\sim 10 \text{ }\mu\text{m}$ , determined largely by pixel size.

As the pixel detector was closest to the interaction point during Run-1, it received the largest fluency of particles and therefore the most damage from radiation. It was originally planned to replace the innermost layer of the pixel detector after 5 years of operation, however this was later realised to be infeasible [81]. To maintain the overall performance of the ATLAS detector, a new pixel layer was installed in May 2014 – the “Insertable B-Layer” (IBL) [82]. This new layer is attached to the Beryllium beam pipe of the LHC itself and consists of 14 staves of 3D silicon pixels. Each staff is  $64 \times 2 \text{ cm}^2$  and contains 32 chips. Each chip contains 26880 3D pixels arranged in a matrix of 80 columns by 336 rows. The mean sensor distance from the centre of the beam pipe is an impressively small 33 mm.

### Semiconductor tracker

The semiconductor tracker (SCT) [83] is the intermediate subdetector of the ATLAS ID. It is a silicon strip particle detector that provides precision three-dimensional space-point measurements for charged particle tracks. The SCT therefore plays an essential role in track reconstruction, charged particle identification and  $b$ -tagging. It consists of a total of 4088 separate silicon strip modules in a similar geometry to that of the pixel detector: four concentric cylindrical barrel layers, and 9 end-cap disks on each side. The geometry is arranged such that a particle emerging from the IP with  $|\eta| < 2.5$  will traverse at least four layers of the SCT.

Each SCT module is double sided and segmented into strips  $80\text{ }\mu\text{m}$  wide and  $\sim 13\text{ cm}$  long (for the barrel modules, the end-cap modules are segmented radially and have varying pitch), resulting in around 6.2 million channels, providing position measurements in  $\phi$  to a precision of  $16\text{ }\mu\text{m}$ . The halves of each module are offset by a small stereo-angle of  $40\text{ mrad}$  in order to provide  $z$  (in the barrel) and  $r$  (in the end-cap) measurements to a precision of  $580\text{ }\mu\text{m}$ .

### Transition radiation tracker

The transition radiation tracker (TRT) [84, 85] is a straw drift tube detector filling the majority of the volume of the ID. It provides two functions: to provide a large number of space-point measurements of charged particles for use with tracking, and to discriminate between different types of particles. The detector makes use of transition radiation: as a charged particle traverses the boundary between two media with different dielectric constants, soft X-rays are emitted in the direction of the motion of the particle, the intensity of the radiation being proportional to the energy of the particle.

The detector consists of hundreds of thousands of straws [86], each of which is a  $4\text{ mm}$  diameter thin-walled cylindrical tube with an aluminium coating on the inner surface to act as a high voltage cathode. In the middle of the tube there is a  $31\text{ }\mu\text{m}$  diameter gold-plated tungsten anode wire, which collects the charge and reads the signal out. The straws are filled with a  $\text{Xe}/\text{CF}_4/\text{CO}_2$  gas mixture, chosen for high absorption probability

of transition radiation. As a charged particle traverses the material surrounding the straws, transition radiation photons are produced that enter the tube and ionise the gas, liberating electrons that are collected on the anode wire forming the signal. The probability of emitting a transition radiation photon at any boundary is small, and so volume around each straw is filled with polypropylene fibres or strips to provide many such boundaries. Electrons will produce more photons than a pion for the same particle energy, giving a larger signal and allowing the two to be distinguished.

The TRT provides coverage of  $|\eta| < 2.0$  and is segmented into three major sections: a barrel region and two end caps. The barrel region covers the range  $|\eta| < 1.0$  and consists of 52,544 straws, each 144 cm long arranged parallel to the beam axis. The straws are stacked radially from 563–1066 mm and split into 32 groupings in  $\phi$  such that there are no gaps which a particle could traverse undetected – see figure 3.6. Each of the anode wires is split in the middle with insulating material, such that each end is read out separately, resulting in 105,088 channels. Some of the innermost wires are split twice to create three regions, the centre of which is not read out, in order to deal with the high occupancy at the LHC. The straws in the end-caps are 37 cm long and are arranged radially in wheels covering  $1.0 < |\eta| < 2.0$ . Each end-cap contains 122,880 straws. The geometry of the TRT ensures that a particle with  $|\eta| < 2.0$  will cross about 35 straws.

Due to ozone production and resulting localised corrosion, some of the straws developed leaks in Run-1 that could not be fixed during LS1. The gas mixture in the straws with the highest leak rate was changed from xenon to argon in Run-2 to reduce the cost of replenishing the leaked gas. As a result, the electron identification efficiency was reduced, however the tracking performance was not affected.

### 3.2.4. Calorimetry

The ATLAS calorimetry system is designed to measure the energies of both charged and neutral particles. It consists of two subsystems: the liquid argon calorimeter (LAr) [87], which is primarily used for the measurement of electrons and photons and also hadrons in the end-cap regions; and the tile calorimeter [88] used for measurements of hadrons in

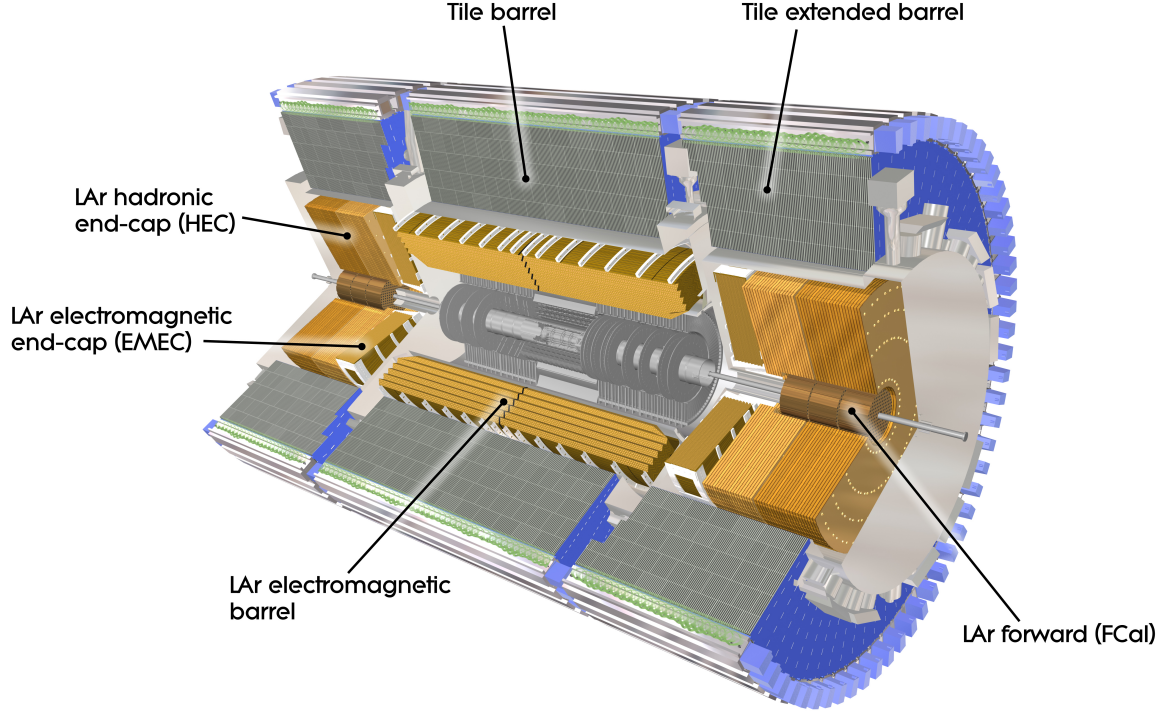


**Figure 3.7.:** A cut-away diagram of the ATLAS calorimeter system. Image taken from reference [69].

the barrel region. A layout of the system is shown in figure 3.7, with the LAr calorimeter built around the solenoid surrounding the ID, and the tile calorimeter surrounding the LAr calorimeter. The calorimeters cover up to  $|\eta| = 4.9$  and combine different techniques to cover the characteristics of the different physics processes of interest. As particles are incident upon the calorimeters they create ionising showers of other particles. The energy of the showers is collected and used to measure the energy of the incident particles, and the shape of the shower can be used to aid particle identification. The ATLAS calorimeters are sampling detectors, which means that the active material providing the signal is different from the medium responsible for absorbing the particle energy.

### The liquid argon calorimeter

The primary purpose of the LAr calorimeter is to measure the energies of electrons and photons, and also hadrons in the higher  $\eta$  regions. In the barrel, the LAr is made

from lead sheets, coated with stainless steel that act as absorber material. These sheets are immersed in a bath of liquid argon, chosen for its intrinsic radiation hardness and linear and stable responses, at a temperature of around 88 K. As particles strike the lead sheets they shower producing a cascade of other electrons, positrons and photons. These particles then ionise the liquid argon, and the resulting electrons are drawn to a copper anode in-between the lead sheets which is read out as a signal. In the end-caps, the lead is exchanged for copper and tungsten.

A fine granularity is required to make precise electron and photon energy measurements, and to distinguish single photons from  $\pi^0 \rightarrow \gamma\gamma$ . Thus, the LAr is typically segmented into three layers with a minimum  $\Delta\eta \times \Delta\phi$  granularity of  $0.003 \times 0.025$ .

The LAr is arranged into several sub-systems. The barrel region, covering  $|\eta| < 1.475$  employs an accordion geometry of the sampling material, in order to ensure uniform  $\phi$ -coverage. This is split into two half-barrels, as shown in figure 3.7, and is referred to as the electromagnetic barrel calorimeter (EMB). Each end-cap is segmented into three: first the LAr electromagnetic end-cap (EMEC) from  $1.375 < |\eta| < 3.2$ , then further out is the hadronic end-cap (HEC) from  $1.5 < |\eta| < 3.2$ , and finally the forward end-cap calorimeters (FCAL) [89] from  $3.1 < |\eta| < 4.9$ . Both the EMEC and HEC are made from two co-axial wheels each, with outer radius approximately 2 m. As with the barrel the EMEC employs an accordion geometry, whereas the HEC has a flat-plate design. The FCAL resides inside the wheels of the HEC and at 4.7 m from the IP and at high  $\eta$  is designed to withstand high particle fluxes. Each FCAL end-cap is split into three modules of parallel plates, the first designed for electromagnetic calorimetry and mostly made from copper, and the other two designed for hadronic calorimetry made from a mixture of tungsten and copper.

The transition between the barrel and the end-cap LAr,  $1.37 < |\eta| < 1.52$ , is used for detector services. Since this material is difficult to model, this “crack” region is usually excluded when reconstructing electrons. For  $|\eta| < 1.8$ , a LAr pre-sampler is installed before the first lead layer. This enables estimation of the energy lost by electrons and photons before encountering the calorimeter.

### The tile calorimeter

The tile calorimeter [88] is used for the measurement of the energies of hadrons. It is an array of interleaved steel and scintillator sheets, spanning the pseudorapidity region  $|\eta| < 1.7$ . The tile calorimeter comprises three cylinders around the LAr calorimeter: the central cylinder, known as the “long barrel” extends to  $|\eta| = 1.0$  and is flanked on both sides by an “extended barrel”, as shown in figure 3.7. There is no “end-cap”, as this is provided by the LAr calorimeter. Both the barrel and extended barrel are segmented into 64 wedges (or modules) in  $\phi$ , corresponding to a  $\Delta\phi$  granularity of  $\sim 0.1$  radians. Each wedge is made of dozens of steel plates that act as absorber material and plastic scintillator tiles as the active material. The light produced from the interactions of charged particles is collected and transmitted by wavelength-shifting optical fibres and turned into signals by photomultiplier tubes.

### Calorimeter energy resolution

The energy resolution of calorimeters can be parameterised as:

$$\frac{\sigma(E)}{E} = \frac{a}{\sqrt{E}} \oplus \frac{b}{E} \oplus c, \quad (3.5)$$

where  $a$ ,  $b$  and  $c$  are  $\eta$ -dependent parameters;  $a$  is the *sampling* or *stochastic* term,  $b$  is the *noise* term and  $c$  is the *constant* term. The noise term parameterises external noise contributions that are not dependant on energy, for example electronic noise or contributions from pile-up. The constant term characterises fluctuations that are constant as a function of energy, for example from energy lost in passive material such as the cryostat or the solenoid.

For the electrons, positrons and photons, whose energies are measured by the LAr calorimeter, the sampling term is dominant at low energies with a value of around  $10\%/\sqrt{E[\text{GeV}]}$  at low  $|\eta|$ , which worsens as the amount of material in front of the calorimeter increases at larger  $|\eta|$  [90,91]. The noise term is  $350 \times \cosh \eta$  MeV for a pile-up of  $\mu = 20$  [90]. At higher energies the relative energy resolution tends asymptotically to the constant term,  $c$ , which has a design value of 0.7% [90].



The energies of hadrons (and hence jets) are measured primarily by the tile calorimeter, their energy resolution is given by [88]

$$\frac{\sigma(E)}{E} = \frac{50\%}{\sqrt{E[\text{GeV}]}} \oplus 3\%. \quad (3.6)$$

### 3.2.5. Muon spectrometer

The muon spectrometer is designed to measure the momentum of particles that escape the calorimeters in the region  $|\eta| < 2.7$ . Such particles are typically muons, but in rare cases highly energetic jets of hadrons may punch through the calorimeter into the muon spectrometer. Muons traverse the entire ATLAS detector and can do so because they don't interact strongly, so they very rarely undergo hard collisions with atomic nuclei where they could lose significant energy. Muons also lose very little energy via electromagnetic interactions due to being much more massive than electrons<sup>4</sup>. The huge air-core toroid magnet system generates a 0.5 T (1 T) field in the barrel (end-caps), enabling momentum to be inferred from track curvature measurements. Four types of tracking chamber are installed in several layers (see figure 3.8): monitored drift tubes and cathode strip chambers are used to provide precise hit coordinates of muons, but have relatively slow readout times. They are complemented by resistive plate chambers and thin gap chambers that provide less precise measurements but have faster readout times making them useful for triggering.

#### Monitored drift tubes

The largest subsystem of the muon spectrometer are the monitored drift tube chambers (MDTs), which provide precision measurements of charged particle hits. There are 1150 chambers inside the ATLAS detector, covering a total area of 5520 m<sup>2</sup>. Three layers of chambers are arranged cylindrically around the barrel, with a further three wheels in each end-cap (though at high  $|\eta|$  only two layers of MDTs are used due to the higher

---

<sup>4</sup>In any muon-electron interaction, the muon will only lose a small fraction of its energy due to its much larger mass. Furthermore, because of their high mass, muons don't radiate as much energy during passage through the electromagnetic fields of nuclei as electrons do.

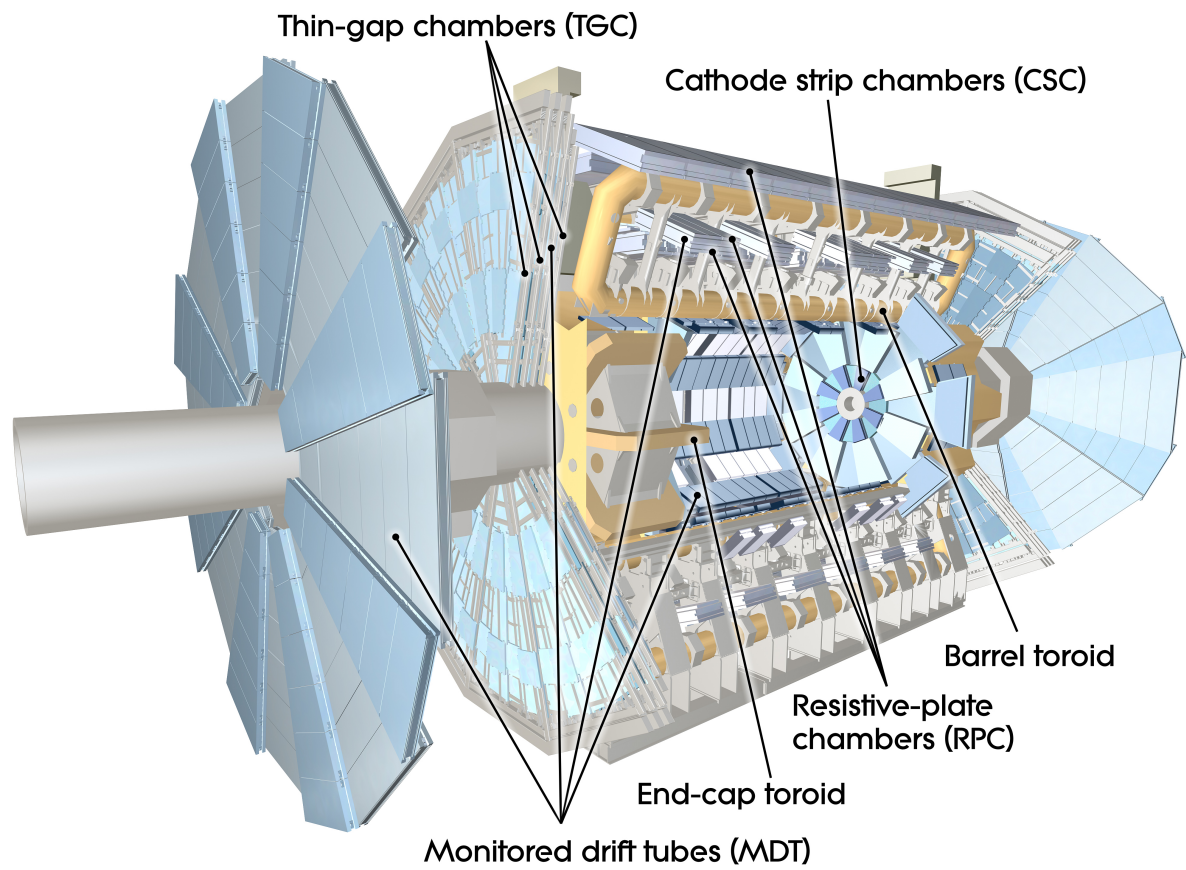


**Figure 3.8.:** A cut-away diagram of the ATLAS muon spectrometer. Image taken from reference [69].

particle flux). Each chamber consists of two multilayers of eponymous tubes, separated by the chamber support structure, with three or four layers of tubes per multilayer. The tubes are 3 cm diameter aluminium alloy proportional drift chambers, filled with Ar/CO<sub>2</sub> gas in a 97%/3% mixture under almost 3 atmospheres of pressure. At the centre of each wire is a gold-plated tungsten-rhenium wire at a potential of 3080 V to collect ionisation electrons which are read out as a signal. A muon will typically cross 20 tubes as it traverses the detector.

The MDTs provide a typical resolution of 35  $\mu\text{m}$  in the  $z$  direction, which is superior to measurements provided by the other muon systems. This comes at the cost of a longer response time of 700 ns (the maximal drift time from wall to wire) that requires the readout system to implement a dead-time after the first detection of charge.

### Cathode strip chambers

The cathode strip chambers (CSCs) are multiwire proportional chambers used in the end-cap region,  $2.0 < |\eta| < 2.7$ , where only two layers of MDTs are present. Each chamber consists of four planes of wires arranged perpendicular to one another, providing four independent measurements and two coordinates of each track. The wires act as anodes and are held at a potential of 1900 V, and positional information is obtained by having the cathodes segmented into strips perpendicular to the wires. The chambers are filled with a Ar/CO<sub>2</sub> mixture in a 80%/20% ratio. For each end-cap there are two segmented disks both containing 8 chambers each, arranged so the innermost chambers cover the gaps between the outermost chambers. The CSCs provide fewer hits than the MDT, however make up for this with a smaller electron drift time of less than 40 ns allowing for fewer readout inefficiencies. The fine segmentation of the cathodes allows for accurate position measurements, allowing for typical resolutions of 40  $\mu\text{m}$  in  $r$  and 5 mm in  $\phi$ .

### Resistive plate chambers

Triggering on muons in the barrel region is provided by resistive plate chambers (RPCs). These are gas-filled parallel plate detectors with a fast readout speed. Each chamber consists of two resistive parallel plates separated by a distance of 2 mm by insulating spacers. The electric field between the plates of 4.9 kV/mm allows avalanches to form along the ionising tracks of muons, which travel towards the anode and are read out as signal. The short timing resolution of 5 ns makes these ideal for triggering.

The chambers are arranged in three concentric cylindrical layers around the barrel, as shown in figure 3.8. The innermost two layers of RPCs sandwich the second layer of MDTs (they are constructed together), and are separated by about 0.5 m. The third layer alternates in  $\phi$  between being above and below the outermost MDT layer and are about 2 m further away from the other two RPC layers. Each of the cylindrical layers consists of two sets of chambers, so that an infinite momentum muon will traverse 6 RPCs, each providing independent  $\eta$  and  $\phi$  measurements.

The large separation between the first two layers and the third layer of RPCs acts as a high- $p_T$  (9–35 GeV) muon trigger, whereas the smaller distance in-between the first and second layers acts as a low- $p_T$  (6–9 GeV) trigger.

### Thin gap chambers

The thin gap chambers (TGCs) perform a similar function to the RPCs, except they are mounted in the end-cap regions. Their primary purpose is to provide triggering and an azimuthal coordinate to complement the MDTs in the end-cap. They are multiwire proportional chambers, similar to the CSCs: a series of anode wires are arranged perpendicular to cathode strips in a gas chamber. The wires are held at a potential of 2900 V.

There are a total of 9 wheels of TGCs, located in the end-cap as shown in figure 3.8 and interspersed between the three wheels of MDTs. The innermost layer of MDTs are complemented by two TGCs, and the middle layer of MDTs is complemented by 7 TGCs.

The TGCs have a typical hit resolution of 2–6 mm in  $r$  and 3–7 mm in  $\phi$ , and a time resolution better than the minimum LHC bunch spacing of 25 ns.

### 3.2.6. Forward detectors

In addition to the main ATLAS detector systems described in the previous section, three smaller sets of detectors are installed to provide coverage in the very forward regions. The three systems, LUCID, the ZDC and ALFA are described below.

The first system LUCID (LUminosity measurement using Cherenkov Integrating Detector), consists of two sets of 20 aluminium tubes arranged in a cylinder such that each tube points towards the interaction point when placed around the beam line. The cylinders are located  $\pm 17$  m in  $z$  from the interaction point and placed at a radial distance of 10 cm from the beam line ( $|\eta| \approx 5.8$ ). The main purpose of LUCID is to detect inelastic  $pp$  scattering in the forward direction, such that the instantaneous luminosity can be measured on-line, and the integrated luminosity can also be measured. On-line monitoring of beam conditions are also provided by LUCID. Each of the aluminium tubes is filled with pressurised  $C_4F_{10}$  gas; as particles traverse the gas, Cherenkov light is emitted which is collected by photomultiplier at the end of the tube. Counting the number of tubes with a signal above a pre-defined noise threshold provides a measurement for online monitoring.

The zero degree calorimeter (ZDC) is a forward detector located  $\pm 140$  m from the interaction point. The primary purpose of the ZDC is to detect very forward neutrons ( $|\eta| > 8.3$ ) from heavy-ion collisions, however it can also be used to reduce backgrounds from beam gas and beam halo effects. These can be greatly reduced by requiring a tight coincidence from the two arms of the ZDCs, located symmetrically with respect to the interaction point. This coincidence is found to be 9% of the total  $pp$  inelastic scattering rate. Therefore, the ZDC is also important for initial beam tuning. The timing resolution of the ZDC is approximately 100 ps, which is sufficient to locate the interaction point to about 3 cm in  $z$ , and can therefore provide some knowledge of the primary vertex location without inner detector information.

ALFA (Absolute Luminosity measurement For ATLAS) is another device for measuring the luminosity in ATLAS, however it can only be used during special LHC beam conditions giving low luminosity (at high  $\beta^*$ , where  $\beta^*$  parameterises the size of the beam at the interaction point). The ALFA detector is designed to measure the elastic scattering rate in the forward region. Via the optical theorem, the elastic-scattering amplitude in the forward direction is connected to the total cross-section, which can be used to extract the luminosity. The detector consists of a scintillating fibre tracker, located physically inside the LHC beam tube  $\pm 240$  m away from the interaction point. It can be moved a few millimetres from the beam line, which is required to measure the small scattering angles ( $3\text{ }\mu\text{rad}$ ) from the elastic collisions.

### 3.3. Trigger

The collision rate at the LHC is so large that it is infeasible for ATLAS to record all of the data. With an event size of approximately 1.3 Mbytes, the 40 MHz collision rate of the LHC in Run-2 would correspond to a data rate of 60 Tbytes/s, which is far in excess of the read-out and storage capabilities of ATLAS.<sup>5</sup> However, the vast majority of collisions at the LHC produce well known physics studied at earlier colliders and therefore are “uninteresting” to the LHC programme. The majority of proton-proton collisions produce mainly hadrons with low transverse momentum, with only around 2% of charged particle tracks carrying  $p_{\text{T}} > 2\text{ GeV}$  [92]. The contribution of a variety of different processes to the total proton-proton cross-section is shown in figure 3.9 and we see that any “interesting” physics has a cross-section several orders of magnitude smaller than the total. For example, a Higgs boson will be produced in only about 1 in every  $10^{10}$  collisions, and the production of supersymmetric particles is predicted to be several orders of magnitude rarer than that (depending on the mass).

The ATLAS trigger system [94, 95] is designed to identify interesting physics events and give the signal to read out the detector so that the event can be stored for more detailed analysis. Between Run-1 and Run-2 the trigger system was redesigned to deal with the

---

<sup>5</sup>Compare this to a contemporary transatlantic network, the largest bandwidth variants carrying up to 10 Tbits/s.

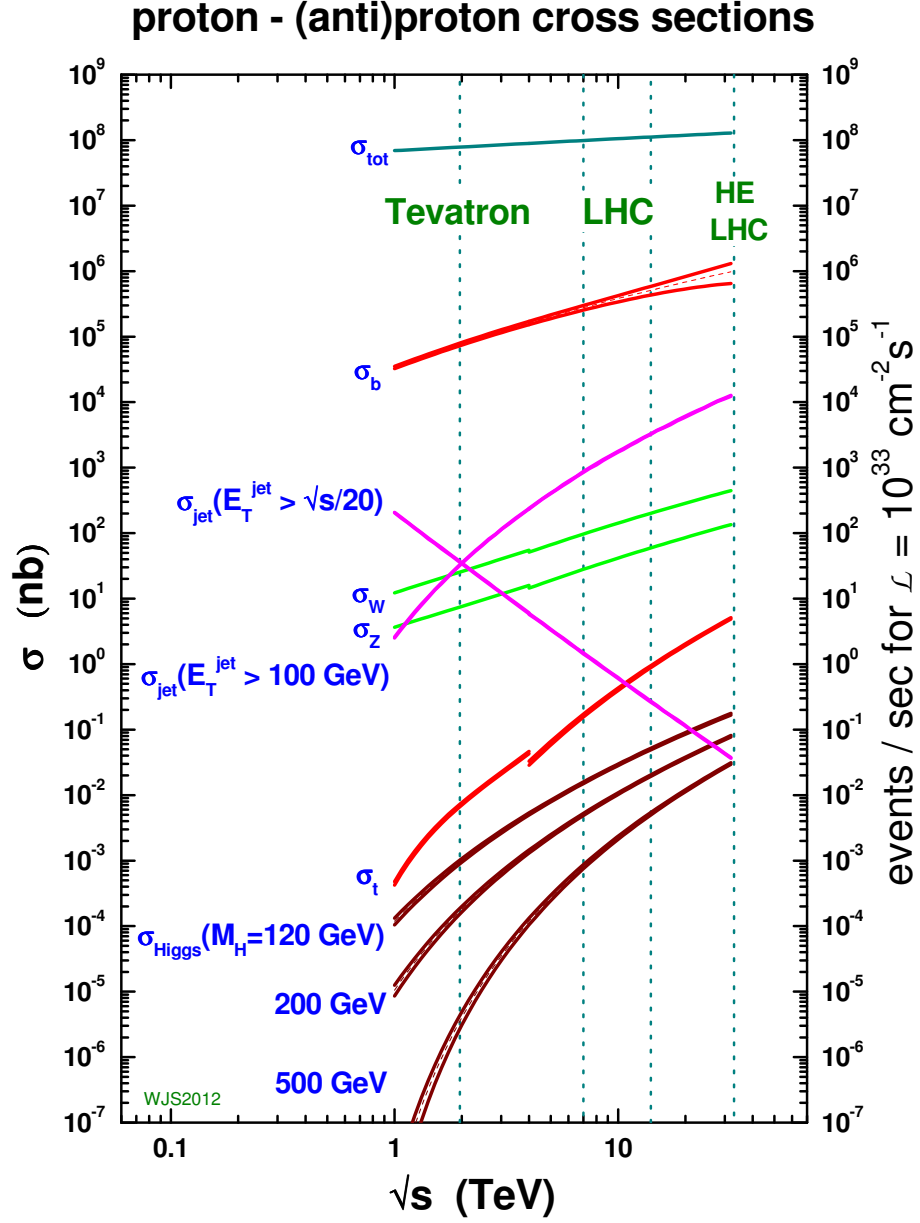


**Figure 3.9.:** Inclusive cross-section values for several important processes as a function of centre of mass energy. The right vertical axis reports the number of events for an instantaneous luminosity of  $L = 10^{33} \text{ cm}^{-2} \text{ s}^{-1}$ . The cross-sections on the left hand side of the discontinuity at  $\sqrt{s} = 4 \text{ TeV}$  are calculated for the proton-antiproton initial state, while the cross-sections on the right hand side are calculated for the proton-proton initial state. Image from reference [93].

higher rate due to the decreased bunch spacing. Originally, the trigger system was a three-level system, however the latter two levels were merged to allow better resource sharing and overall improved performance. As a result, in Run-2, the trigger operated with an input rate of 40 MHz and an output rate of 1 kHz whereas in Run-1 the input rate was 20 MHz for an output rate of 0.7 kHz. The two levels of the Run-2 trigger system are Level-1 (L1) and the high-level trigger (HLT). Level-1 is purely hardware-based, with the electronics located in the ATLAS cavern to reduce the latency in the trigger decision. In 2015 and 2016, the L1 trigger operated with an input rate of 40 MHz and an output rate of 100 kHz, with an allowed decision time of up-to 2.5  $\mu$ s. The HLT has enough processing time available per event (300 ms) to use software based algorithms, and reduces the event rate from 100 kHz to 1 kHz.

For every kind of physics object – electrons, photons, muons, taus, jets and  $E_T^{\text{miss}}$  – there are dedicated triggers, some specialised for specific analysis needs. There are also random triggers which record events randomly to provide an unbiased dataset. The HLT decision is said to be “seeded” by a L1 decision.

For certain physics objects that ATLAS triggers on, the production rate might be too high to record every single event passing the trigger. In such cases, prescaled triggers exist, which record only a certain fraction of the events that would normally pass the trigger, effectively reducing the luminosity recorded. Usually searches for new physics need to employ the full dataset to boost their sensitivity, for which an unprescaled trigger with the lowest possible thresholds should be employed. In the search described in chapter 5 of this thesis for example, the HLT\_6j45\_0eta240 trigger was used, which requires at least 6 jets each with  $p_T > 45$  GeV and  $|\eta| < 2.4$  at HLT, and is seeded by a trigger at L1 requiring 4 jets with  $p_T > 20$  GeV.

The Run-1 trigger system is described fully in reference [94] and the Run-2 system in reference [95].



### 3.3.1. The Level-1 trigger

#### Level-1 Calo

The Level-1 calorimeter trigger “L1-calo” is designed for triggering on electrons, photons, jets and taus, and also global event quantities such as missing transverse energy. Calorimeter cells are summed into “trigger towers” each  $0.1 \times 0.1$  in  $\Delta\eta \times \Delta\phi$ , and a sliding window algorithm is used to identify regions of interest (RoIs) [96]. The trigger towers for the electromagnetic (EM) and hadronic calorimeters are grouped separately.

To identify  $e/\gamma$  showers or  $\tau$ /hadron showers a similar algorithm is used. For both cases a  $2 \times 2$  window of EM trigger towers are considered. Within this  $2 \times 2$  window, the energies within the four possible  $2 \times 1$  and  $1 \times 2$  rectangles are summed and compared to some threshold, and at least one of the four sums is required to pass. In the  $\tau$ /hadron case, the sum of the energies in the hadronic trigger towers behind the  $2 \times 2$  window are included in the threshold comparison, whereas in the  $e/\gamma$  case, the shower is required to have not penetrated into the hadronic calorimeter. In both cases, an isolation requirement is also imposed: the  $E_T$  values in the 12 EM trigger towers surrounding the  $2 \times 2$  window are summed and required to be less than an isolation threshold.

The L1 jet algorithm is similar to the  $e/\gamma$  and  $\tau$ /hadron, except that a lower granularity is needed, and there is no need to separate the EM and hadronic calorimeters. As a result, the most basic unit considered is the “jet element”, which is the sum of the  $2 \times 2$  trigger towers added to the  $2 \times 2$  hadronic towers. To identify an RoI, the total transverse energy  $E_T$  of  $2 \times 2$ ,  $3 \times 3$  and  $4 \times 4$  windows of jet elements is summed and compared to a threshold. The different sized windows perform different purposes, with the larger windows capturing the most energy and thus having the greatest efficiency, and the smaller windows better for resolving more jets.

L1-calo also provides triggering for  $E_T$  and  $E_T^{\text{miss}}$ . The trigger towers are summed to calculate  $E_T$  and  $E_T^{\text{miss}}$ ,<sup>6</sup> using the calorimeter information only. These sums are compared to thresholds.

---

<sup>6</sup>The scalar sum is performed for  $E_T$ , and the vector sum for  $E_T^{\text{miss}}$ .

### Level-1 muon

Muon triggering at L1 is provided via identification of the spatial and temporal coincidence of hits in either the RPCs or TGCs pointing to the beam interaction region [97]. Triggering in the barrel ( $|\eta| < 1.05$ ) is provided by the RPCs. A trigger is generated by a coincidence of three hits in the RPC layers for the high  $p_T$  muons, and a coincidence of two hits for low  $p_T$  muons. In the end-cap region ( $1.05 < |\eta| < 2.4$ ), triggering is provided by the TGCs, and a coincidence of three hits is required. The differences in L1 muon triggering between Run-1 and Run-2 are described in reference [95] and largely correspond to extra layers of muon detectors being installed or brought online in some areas. One of the main differences is that in Run-2, a hit coincidence with the innermost layer of the TGCs was required, to prevent triggering on low momentum tracks originating far ( $z \approx 10$  m) from the interaction point. The muon's momentum is not measured at Level-1, and only the coincidence thresholds are passed.

### 3.3.2. The high-level trigger

After an event is accepted at L1, it is processed by the HLT with additional information not available at L1. Finer granularity calorimeter information, tracking information from the ID and precision information from the muon spectrometer are included. Any RoI that has been identified at L1 is passed to the HLT, and as needed the HLT reconstruction can either be executed within the RoI or for the full detector. In both cases the data are retrieved on demand from the readout system.

### Jet triggers

The primary trigger used in the analysis presented in chapter 5 is a multi-jet trigger.

Jets are reconstructed at the HLT using the anti- $k_t$  clustering algorithm with radius parameter  $R = 0.4$  or  $R = 1.0$ . The inputs to the algorithm are so-called calorimeter topological clusters “topo-clusters”, which are topologically connected groups of calorimeter cells with a signal above some threshold [98]. The entire calorimeter is scanned, allowing

pileup subtraction to be performed and low energy jets to be reliably extracted in a selection that is close to that used offline, although no tracking information is available.

## 3.4. Object reconstruction

A physics object is any identifiable phenomenon that is useful for study in high energy physics; including particles, groups of particles, or information on all of the particles produced in a collision. As particles traverse the ATLAS detector, they leave behind energy deposits which are read out as electronic signals. This information from the various detector components must be collated to attempt to reconstruct the original particle, or other physics object, that produced the signal. In this section, the reconstruction algorithms used to identify the different physics objects are described.

When performing physics analysis, only a subset of the objects described here may be used, and additional selection criteria are typically imposed based on the specific needs of the analysis.

### 3.4.1. Tracks and primary vertices

The tracks of charged particles with  $p_T > 0.5 \text{ GeV}$  and  $|\eta| < 2.5$  are reconstructed with information from the ID [69]. Though not used directly as standalone objects in most physics analysis, they are necessary inputs to many of the objects that follow. They are formed via a three-stage procedure. Firstly, a pre-processing step in which the raw information from the pixel and SCT detectors are translated into clusters and then space-point measurements. Secondly, a track-finding stage in which a seed track is formed with hits in the pixel layer, which is then extended to the SCT. During this stage many ambiguities are resolved and fakes are rejected. Quality criteria such as requiring only a limited number of tracks to share the same cluster, and tracks do not pass through too many holes<sup>7</sup>, are imposed. The tracks are then extended to include information from the TRT, and afterwards the track is re-fitted using information from all of the ID

---

<sup>7</sup>A hole is defined as a silicon sensor crossed by a track without generating any associated cluster.

subsystems. A complementary track finding algorithm is then used “backwards” from the TRT inwards, which improves the efficiency for secondary tracks from (for example) long lived particles or conversions ( $\gamma \rightarrow e^+e^-$ ). Finally, a dedicated vertex-finding algorithm is used to locate the Primary Vertex (PV), which is the vertex with the largest  $\sum p_T^2$  of the tracks associated to it. Only one PV is identified per bunch crossing, and an “event” is defined as all of the reconstructed objects that are associated with that vertex.

### 3.4.2. Muons

Muons are identified using information from the ID and muon spectrometer, and to a lesser extend also the calorimeters. The identification is performed according to several reconstruction criteria, resulting in four different “types” [99].

**Combined Muon** Reconstruction is performed independently in the ID and muon spectrometer. If the tracks from each system can be successfully combined, then the track is identified as a combined track. The track is then re-fitted to take into account the information from both systems. This is the most common type of muon used in analyses and has the best performance in terms of sample purity and momentum resolution.

**Stand Alone** The trajectory of the muon is reconstructed only in the muon spectrometer, and extrapolated back to the point of closest approach with the beam line. The estimated energy loss from the muon traversing the calorimeter is taken into account. This type of muon is used for  $2.5 < |\eta| < 2.7$ , which is not covered by the ID.

**Segment-Tagged** ID tracks can be classed as a muon if once extrapolated to the muon spectrometer, it can be associated with at least one local track segment in the MDT or CSC chambers. Segment-tagged muons can be used to increase acceptance in cases in which the muon crossed only one layer of muon spectrometer chamber, potentially due to the low  $p_T$  of the muon or it falling into a low acceptance region.

**Calorimeter-Tagged** ID tracks can be classed as a muon if once extrapolated to the calorimeter they can be associated to an energy deposit consistent with a minimum

ionising particle. The muons have the lowest purity, but this method improves acceptance in regions of the muon spectrometer that are not instrumented.

### 3.4.3. Electrons and photons

The reconstruction of electrons and photons is performed in parallel. Brief details are given here, but more information can be found in reference [100] and reference [101]. In the forward region ( $2.5 < |\eta| < 4.9$ ) no tracking information is available and so electrons and photons are indistinguishable from one another. Nonetheless, a topo-clustering algorithm [98] is used to identify electromagnetic clusters of energy deposits in the EMEC, the energies of which are corrected for expected energy losses in the material in-between the IP and the calorimeter. These forward objects are typically not used directly in physics analyses.

In the central region,  $|\eta| < 2.5$ , tracking information can be used to distinguish electron and photons. Firstly, electromagnetic energy clusters are identified, starting from seeds with  $E_T > 2.5$  GeV, then a sliding window algorithm is used with window size  $3 \times 5$  in units of  $0.025 \times 0.025$  in  $(\eta, \phi)$  to fully locate the cluster. The cluster finding is close to 100% efficient for clusters with  $E_T > 20$  GeV. Next, it is attempted to match clusters with tracks. Tracks with  $p_T > 0.5$  GeV are extrapolated from their last-measured point in the ID to the middle of the LAr calorimeter. The extrapolated  $\eta$  and  $\phi$  coordinates of the track's impact point in the calorimeter are compared to a corresponding seed cluster position. A track and a cluster are considered to be successfully matched if the distance between the track impact point and the EM cluster barycentre have  $|\Delta\eta| < 0.05$ . In the absence of a track, the cluster is identified as an unconverted photon. Electrons are distinguished from converted photons by looking for two close-by oppositely-charged tracks originating from a vertex displaced from the IP.

After cluster and track matching, the cluster sizes are further optimised to take into account the overall energy distribution [100]. The total reconstructed energy is then the sum of four contributions: an estimate of the energy deposited in the material in-between the calorimeter and the IP, the measured energy of the cluster corrected for the fraction of

energy measured by the sampling calorimeter, and the estimated energy deposit outside the cluster (both in and outside the LAr).

### 3.4.4. Jets

It is not possible to measure the position and energy of every particle produced in ATLAS. As a result, we are led to group together particles into artificial composite objects known as jets. The algorithms used to cluster particles into jets are designed to take advantage of the fact that particles produced from the hadronisation of a quark or gluon are typically produced in collimated streams, emerging in approximately conical shaped bundles from the IP, and in so doing capture as much of the hadronic activity produced from that initial quark or gluon. Indeed, jets of hadrons are the observable counterparts of the perturbative concepts of quarks and gluons.

There is no unique way of grouping particles into a jet, however the different options are classified according to two considerations: the set of rules which govern how the particles are grouped into a jet, or the *jet algorithm*; and how the momenta of particles inside the jet are combined, or *recombination scheme*. These two properties define the jet. Jets are used ubiquitously at hadron colliders, and the clustering algorithm is among the main tools used for analysing data at the LHC.

### Jet reconstruction

There are many types of jet algorithm, such as cone algorithms and sequential-combination algorithms. It is desirable that the definition of a jet should be such that if an event is modified through soft and collinear radiation, the set of reconstructed jets stays the same. Many algorithms do not satisfy these criteria, and will not be described here. ATLAS uses a sequential-combination algorithm, which attempts to construct a jet via a bottom up approach in which the sequence of parton splittings is reversed.

The algorithm predominantly used in ATLAS is the anti- $k_t$  [102, 103] jet clustering algorithm. An important characteristic of the anti- $k_t$  algorithm is that it can be applied

in exactly the same way to several different categories of “entity”. These entities can be from simulation, such as individual hadrons or partons, or detector-level quantities such as tracks or groups of calorimeter cells; and that they are treated in the same way aids the comparison between experimental results and theoretical calculations. Furthermore, the anti- $k_t$  algorithm is both infrared and collinear safe, and produces jets of roughly conical shape in the  $\eta$ - $\phi$  plane.

The algorithm is defined as follows. The distance metric  $d_{ij}$  between two entities (e.g particles, clusters)  $i$  and  $j$  is defined by

$$d_{ij} = \min \left( \frac{1}{p_{T,i}^2}, \frac{1}{p_{T,j}^2} \right) \frac{\Delta_{ij}^2}{R^2}, \quad (3.7)$$

where  $\Delta_{ij}^2 = (y_i - y_j)^2 + (\phi_i - \phi_j)^2$  and  $y_i$  and  $\phi_i$  are the rapidity and azimuth respectively of entity  $i$ . The radius parameter,  $R$ , is a number that characterises the radius of the jet in the  $(\eta, \phi)$  plane, and is usually set to 0.4, however in some cases “large-radius” jets are defined with  $R = 1.0$ . For each entity, a beam distance is also defined,

$$d_{iB} = \frac{1}{p_{T,i}^2}. \quad (3.8)$$

A set of distances is then compiled

$$\mathcal{D} = \{d_{iB}, d_{ij}\}, \quad (3.9)$$

for all entities  $i$  and pairs  $i, j$ . The clustering algorithm then proceeds as follows:

- If  $\min(\mathcal{D}) = d_{ij}$  then entities  $i$  and  $j$  are clustered together by adding their four-momentum, and  $\mathcal{D}$  is recompiled with the remaining entities.
- If  $\min(\mathcal{D}) = d_{iB}$  then the entity  $i$  is labelled as a jet and removed from  $\mathcal{D}$ .
- The steps are repeated until there are no more entities in  $\mathcal{D}$ .

As  $d_{ij}$  is weighted by the reciprocal of the momentum of the particle pairs, then the  $d_{ij}$  between a hard and soft particle will be small, whereas the  $d_{ij}$  between two soft particles will be larger. As a result, soft particles will be clustered with a hard particle before clustering with themselves. This continues until all of the particles are separated by  $\Delta_{ij} > R$ , after which the smallest of the distances in  $\mathcal{D}$  will be a beam distance, and

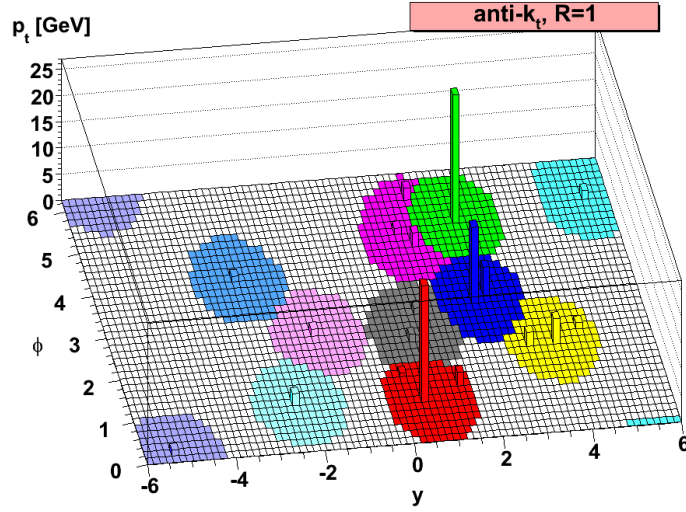


**Figure 3.10.:** Jets clustered with the anti- $k_t$  algorithm with radius parameter  $R = 1$ . Image from reference [102].

all the remaining particles are labelled as jets. In the case that there are no other hard particles within  $2R$  then this will result in perfectly conical jets of radius  $R$ , as shown in figure 3.10. If there are two hard particles such that  $R < \Delta_{ij} < 2R$  then there will be two hard jets and one of them will be clipped, missing the overlapping part of the harder jet, which is also shown in figure 3.10.

## Jets in ATLAS

In ATLAS, the first step is to create *topoclusters*, which are topologically connected clusters of calorimeter cells above a noise threshold [98]. The energy of each topocluster is calculated by summing the energy of its constituent cells, taking into account cases where the energy from cells was split between two topoclusters. The direction of the topocluster (relative to the geometric centre of the ATLAS detector) is calculated as the energy-weighted barycentre of the cell directions, using the absolute value of the cell energies. In the jet clustering algorithm, the topoclusters are treated as massless, such that the jet four-vector is then defined only by the energy and direction of the topocluster. These jets must then be combined with tracks, which is described in the next section. Jets can also be created solely from tracks, however these “track-jets” are not used in this thesis and so are not described further.



## Jet recombination

After application of the jet algorithm, the next step is to choose a method for calculating energies and momenta of the resulting jet objects, known as a *recombination scheme* [104]. In ATLAS the *four-vector* recombination scheme is used, in which the four-vectors of the jet constituents (e.g. the topoclusters) are added together. The jet then has “mass” even though the constituent topoclusters are massless, the jet mass being a function of energies and the angular separation of the topoclusters within the jet. Next is to associate tracks with the jet, which is done via the *ghost association* method. Tracks are assigned infinitesimal  $p_T$  and added to the list of jet inputs. The jet clustering algorithm is then applied again, and any tracks which are clustered into a jet are then associated to it.

## Jet calibration

The goal of the calibration is to correct the jet four-momentum as measured by the calorimeter to the jet four-momentum at the particle level [105]. In order to do this several detector effects must be accounted for including; energy deposited in inactive material or material before the calorimeter, leakage of the hadronic shower outside of the calorimeter, energy losses due to noise thresholds or energy deposited outside of a jet, and additional energy entering a jet from pile-up. The calibration is known as the *Jet Energy Scale* (JES)

The calibration of jets and topoclusters varied between Run-1 and Run-2; the common details are briefly described here, and a full description can be found in references [105,106] respectively. The topoclusters are first calibrated assuming that all the energy was deposited by electromagnetic showers. This is then corrected for the hadronic shower contribution – the calorimeter response to hadrons is approximately 75% of that for electrons due to energy losses from e.g. nuclear break-up, spallation or the emission of soft neutrons. The procedure includes a classification of the clusters as electromagnetic or hadronic, based mostly on the energy density and longitudinal shower depth. The four-vectors of the topoclusters are corrected to originate from the PV, instead of the

detector co-ordinate origin. Next, the effects of pile-up on jet energies are accounted for by an event-by-event  $p_T$ -density correction [107]. Then, a residual pile-up correction is applied to remove any additional  $p_T$  dependence on the number of interaction vertices in the event. A correction, derived in Monte Carlo from the average of the ratio of reconstructed jet energy to particle level jet energy, is then applied (the correction varying as a function of the jet energy and  $\eta$ ). Afterwards, a residual correction derived from measurements of benchmark processes measured in data (e.g. jets balancing against a well-measured object) is applied.

An extra calibration stage was applied in Run-2, to improve the jet energy resolution and reduce the sensitivity of the calibration to the flavour of the jets. The corrections are based on several jet properties, including the number of muon segments behind a jet or the fraction of energy deposited in different layers of the detector.

### 3.4.5. $b$ -jets

Flavour-tagging is the process by which the flavour of a specific quark inside a hadron can be identified and “tagged”. The technique is used by many experiments in high energy physics, but in ATLAS this is mostly done for  $B$ -hadrons. If a jet is found to contain such a particle the jet is said to be “ $b$ -tagged”. Jets containing charmed hadrons or light-flavour quarks can also be tagged, however this is done to a lesser extent in ATLAS. A common misconception is that a  $b$ -tagged jet is one which originated from the decay of a  $B$ -hadron, but it is simply the identification of a jet that contains a  $B$ -hadron. The identification of the flavour of particles within a jet is particularly useful to many measurements in ATLAS and  $b$ -tagged jets are widely used in new physics searches.

The algorithms used to identify a  $B$ -hadron in a jet make use of its relatively long lifetime. The lifetime of a  $B$  meson is approximately 1.5 ps, resulting in an average transverse flight distance of  $\beta\gamma c\tau \approx 3$  mm for a  $p_T = 50$  GeV particle. This is large enough that the tracks of charged particles coming from the decay of the  $B$ -hadron can be identified as not originating from the PV, and can therefore be used to reconstruct a secondary vertex.

ATLAS uses an artificial neural network to classify the flavour of jets. For  $b$ -tagging, the inputs to the classifier include longitudinal and transverse impact parameters of tracks, and also information about the secondary vertex. The weak decays of  $B$ -hadrons are often semileptonic, and so the fraction of electromagnetic energy in the jet, or the presence of a muon is also taken into account. Furthermore, the  $b$ -tagging algorithm is designed to reject the identification of similar particles, such as tau leptons and  $D$ -mesons, which have similar lifetimes and flight distances<sup>8</sup>. As tracking information is required, only jets within the acceptance of the ID can be  $b$ -tagged. The algorithms used for Run-1 are described in detail in reference [108], and were upgraded for use in Run-2 [109].

### 3.4.6. Tau leptons

Taus are unique among leptons in that they are heavy enough to decay into hadrons as well as other leptons. They are short-lived enough to decay within the detector volume, and so specialised chambers that are used to detect muons cannot be used to identify taus, but also long-lived enough to travel far enough from their production point for their flight distances to be similar to that of a  $B$ -hadron decay, allowing them to be potentially confused with  $b$ -jets. These properties present a unique challenge to the identification and reconstruction of taus. The leptonic decay modes of the tau ( $\tau \rightarrow \mu\nu\nu$ ,  $\tau \rightarrow e\nu\nu$ ) cannot be directly distinguished from prompt electron or muons in ATLAS, as the neutrinos cannot be detected. Therefore, only taus that have decayed hadronically, which comprises around 65% of tau decays [34], can be identified in ATLAS.<sup>9</sup>

In the hadronic case, the virtual  $W^\pm$  boson produced from the tau decay can itself decay directly into a single charged pion but more often decays into a resonance such as a  $\rho^\pm$  or  $a^\pm$  meson. The  $\rho^\pm$  decays to a charged and neutral pion, whereas the  $a^\pm$  decays into three or four pions, which are a mix of either one or three charged pions accompanied

---

<sup>8</sup>The lifetime of the tau is approximately 0.3 ps, the lifetime of a  $D$  meson is approximately 0.4 ps. While these lifetimes are shorter than that of the  $B$ , they are lighter and are therefore more boosted for the same  $p_T$ .

<sup>9</sup>It is possible to infer the presence of a tau that has decayed leptonically if it is produced as a tau pair, with the other tau decaying hadronically, for example in  $Z \rightarrow \tau\tau$ .

with neutral pions. Thus, hadronic tau decays are categorised as either “one-prong” or “three-prong” depending on the number of charged tracks detected.

Taus are not initially reconstructed directly but instead identified from the collection of anti- $k_t$  jets with  $R = 0.4$ . Jets with  $p_T > 10 \text{ GeV}$  and  $|\eta| < 2.5$  are used as seed candidates for taus. A Boosted Decision Tree is used to classify jets as originating from taus. The input variables exploit the different characteristics of jets produced by the hadronic decays of taus to those initiated by a quark or a gluon. For example, taus produce jets that are typically more collimated, have a different EM fraction due to the presence of  $\pi^0$ , contain specific number of tracks pointing to a displaced vertex [110].

### 3.4.7. Missing transverse momentum

Momentum conservation transverse to the beam axis implies that the transverse momenta of all particles in the final state should sum to zero. However, some particles, such as neutrinos and the LSP predicted by RPC supersymmetry, are invisible to ATLAS and escape the detector without their momentum being measured. Their presence can be inferred from any imbalance of the transverse momentum sum. Therefore, an important variable in many new physics searches is the missing transverse momentum vector  $\mathbf{E}_T^{\text{miss}}$ , which is the negative vector sum of the  $\mathbf{p}_T$  of the reconstructed objects. As the direction of this variable is often unimportant, the magnitude of  $\mathbf{E}_T^{\text{miss}}$  is often used, denoted here and throughout this thesis as  $E_T^{\text{miss}}$ . In addition to particles escaping ATLAS undetected,  $E_T^{\text{miss}}$  is also generated by the mismeasurement and imperfect calibration of physics objects. Furthermore, pile-up has to be taken into account, as particles emanating from one interaction point can be confused with those emanating from another during the same bunch crossing.

The  $E_T^{\text{miss}}$  is calculated using the components along the  $x$  and  $y$  axes:

$$E_{x(y)}^{\text{miss}} = E_{x(y)}^{\text{miss}, e} + E_{x(y)}^{\text{miss}, \gamma} + E_{x(y)}^{\text{miss}, \tau} + E_{x(y)}^{\text{miss}, \mu} + E_{x(y)}^{\text{miss}, \text{jets}} + E_{x(y)}^{\text{miss}, \text{soft}}. \quad (3.10)$$

This is calculated only for the physics objects that are associated with the PV of the event so that, for example, jets not associated with the PV will not be included. The final

term in eq. (3.10) is the so-called soft term, which accounts for the signals in the detector not associated with any other physics object. There are two methods of calculating the soft term: using unassociated calorimeter deposits to create the “calorimeter soft term”; or using tracks originating from the primary vertex that are not associated to any objects to create the “track soft term”. In Run-1, the calorimeter soft term was used for many analyses. However, this variable was found to be sensitive to pile-up, and so with the increased pile-up conditions realised during Run-2, the track soft term was favoured.

### 3.4.8. Overlap removal

The reconstruction of different objects is performed independently. As a result, the same calorimeter energy cluster could be identified as both an electron and a jet, and be double counted. An overlap removal procedure is then required to resolve these ambiguities, which can be unique to each analysis depending on the set of objects used.

## 3.5. Summary

The LHC is the world’s largest particle accelerator, capable of smashing protons together at a centre of mass energy of up to 14 TeV. Surrounding one of the interaction points is the ATLAS detector, designed to measure the properties of the Standard Model and search for physics beyond. ATLAS has many specialised subsystems to precisely measure the properties of the particle collisions: the inner detector measures the tracks of charged particles, the calorimeter systems measure the energies of particles, and the muon system provides additional tracking information for muons. A powerful magnet system provides a field for bending the trajectories of charged particles as they traverse the detector. Crucial for the operation of the detector is the trigger system, which uses information from several of the ATLAS subsystems to select interesting events for later analysis. Information from the subsystems is combined to reconstruct and potentially identify the particles produced from the initial collision. From this, event-level information such

as missing transverse momentum can be inferred – a key variable in searches for new physics.

## 4 | The Impact of 8 TeV ATLAS Searches on the pMSSM

One of the main challenges faced by the theoretical and experimental communities is the interpretation of the null results of searches for new physics. This is particularly acute in the context of the searches for SUSY, given that the full MSSM has over 100 free parameters.

A popular method of presenting the results of searches is to use *simplified models* [111–113]. These models consider only two free parameters, typically sparticle masses, with a fixed branching fraction of one sparticle decaying into another. No attempt is made to satisfy the various indirect constraints that would apply to a viable physical model, such as dark matter relic density, and all SUSY particles other than the directly relevant ones are assigned an arbitrarily large mass. One example is the so-called “Gtt” model, in which it is assumed that only gluinos are pair produced, with each gluino decaying with a 100% branching fraction to a  $t\bar{t}$  pair and a neutralino,  $\tilde{g} \rightarrow t\bar{t}\tilde{\chi}_1^0$ . In the model, all of the other sparticles are assigned arbitrarily large masses, and the only two parameters considered is the gluino mass and the neutralino mass. The use of these models has several benefits: it allows analysis teams to optimise their searches, compare the relative strength of one search to another, and publish the results on a 2-dimensional piece of paper in a way easy for people to interpret. However, the simplified model approach can fail to capture the complexity of more “realistic” SUSY scenarios, in which many different sparticles have competing production and decay mechanisms. As a result, different analyses can publish different exclusion limits on the same sparticle when considering a slightly different simplified model. In the context of the broader MSSM it is less clear

what sparticle masses have been excluded, and where the limits on SUSY really lie. Part of the motivation for simplified models is they can show the best possible discovery reach for searches, but conversely this means that they also show aggressive limits for exclusion, which can result in overly-simplified views on the constraints of sparticle masses from both the experimental and theoretical communities.

The simplified model approach and the full MSSM lie at extremes, the former being somewhat an over-simplification and the latter being far too complex to explore directly. How can one attempt to get a sense of what regions of the SUSY parameter space are more tightly constrained than others? One solution is to use an intermediary between the simplified model approach and that of the full MSSM, being the *phenomenological Minimal Supersymmetric extension to the Standard Model* (pMSSM) [114, 115], a 19 parameter subset of the full MSSM described in the next section.

Our approach has been to sample a large number of points in the pMSSM space and test their validity after considering all relevant dark matter, heavy flavour and electroweak constraints, and then consider further constraints from a combination of 22 ATLAS searches to assess their impact. This was the first time such a large scale study of this kind was carried out by an LHC collaboration.

This chapter is based on the publication in reference [6], which I created with collaborators. I have indicated which parts were carried out by my collaborators, but note that the interpretation of the results was done by me. Many of the plots in this chapter also feature in the publication, but they have been visually improved for this thesis.

## 4.1. The phenomenological MSSM

The majority of the 120 parameters of the  $R$ -parity conserving MSSM are associated with flavour changing neutral currents or CP-violating phases, both of which are tightly constrained by experiment. Therefore by applying a series of experimentally motivated constraints, (and a desire for theoretical simplicity) one can reduce the parameter space of the MSSM to the more tractable 19 parameter pMSSM. These assumptions are:



*(i) No new sources of CP-violation.*

New sources of CP-violation are tightly constrained by the experimental limits on the electron and neutron electric moments [114] as well as in the  $K$ ,  $B$ ,  $B_s$  and the  $D$  system [116]. By assuming that the soft-SUSY breaking parameters are real (i.e. that all soft-SUSY breaking phases are zero), all sources of CP-violation beyond the CKM matrix are eliminated.<sup>1</sup>

*(ii) No flavour changing neutral currents.*

The off-diagonal terms in the sfermion mass matrices and the trilinear coupling matrices can induce large flavour violations, which are tightly constrained by experimental data. Minimal Flavour Violation [117] is imposed at the electroweak scale, by taking all sfermion mass matrices and trilinear couplings to be diagonal in flavour.

*(iii) Universality of the first and second generation sfermions.*

Experimental data, for example from  $K^0-\bar{K}^0$  mixing, severely limit the splitting between the masses of the first and second generation squarks, unless squarks are significantly heavier than 1 TeV. Therefore, we assume that the soft-SUSY breaking scalar masses are the same for the first and second generation. This results in, for example, the  $\tilde{u}_L$  and  $\tilde{c}_L$  being degenerate in mass, but the left- and right-handed superpartners are not necessarily degenerate, nor are the up- and down-type squarks. There is no experimental constraint on the third generation masses.

In addition to the three general constraints listed above, a further two conditions are imposed for this study:

*(a)  $R$ -parity is exactly conserved.**(b) The LSP is the lightest neutralino.*

This leaves 19 real weak-scale parameters defining the pMSSM, which are defined in table 4.1.

---

<sup>1</sup>As there are many phases in the MSSM, it is possible for a cancellation to occur between them such that little CP-violation would be observable. However, this introduces something of a fine-tuning problem.

Parameter	Definition
$m_{\tilde{L}_1} (\equiv m_{\tilde{L}_2})$	LH slepton mass (first two generations)
$m_{\tilde{e}_1} (\equiv m_{\tilde{e}_2})$	RH slepton mass (first two generations)
$m_{\tilde{L}_3}$	LH stau doublet mass
$m_{\tilde{e}_3}$	RH stau mass
$m_{\tilde{Q}_1} (\equiv m_{\tilde{Q}_2})$	LH squark mass (first two generations)
$m_{\tilde{u}_1} (\equiv m_{\tilde{u}_2})$	RH $u$ -type squark mass (first two generations)
$m_{\tilde{d}_1} (\equiv m_{\tilde{d}_2})$	RH $d$ -type squark mass (first two generations)
$m_{\tilde{Q}_3}$	LH squark mass (third generation)
$m_{\tilde{u}_3}$	RH top squark mass
$m_{\tilde{d}_3}$	RH bottom squark mass
$M_1$	Bino mass parameter
$M_2$	Wino mass parameter
$M_3$	Gluino mass parameter
$A_t$	Trilinear top coupling
$A_b$	Trilinear bottom coupling
$A_\tau$	Trilinear $\tau$ lepton coupling
$\mu$	Bilinear Higgs mass parameter
$M_A$	Pseudoscalar Higgs boson mass
$\tan \beta = v_u/v_d$	Ratio of the Higgs vacuum expectation values

**Table 4.1.:** The definition of the 19 pMSSM parameters, in addition to those of the Standard Model. LH and RH refer to left- and right-handed respectively.

It is interesting to note that many of the generic properties of the mass spectra of sparticles in the pMSSM are also found in the wider MSSM. For example, in the first and second generation the super-partner of the left-handed up-type quarks are nearly mass degenerate with the corresponding super-partner of the down-type quarks. Similarly the left-handed sleptons are near-degenerate with the sneutrinos. Furthermore, the nature of the neutralino mass spectrum is dictated by the relative separation and magnitude of the bino, wino and Higgsino mass parameters. If well separated, the mass eigenstates will split into a bino-like singlet of mass approximately  $|M_1|$ , containing a single neutralino, a wino-like triplet of two oppositely charged charginos and a neutralino of mass approximately  $|M_2|$  and a Higgsino-like quartet of two charginos and two neutralinos with mass approximately  $|\mu|$ . If not well separated then the LSP can be a mixture of the neutral states.

## 4.2. Analysis Details

### 4.2.1. Overview

The goal of the study is to find how ATLAS searches have impacted the pMSSM parameter space, and what constraints exist on SUSY particles. Like throwing darts, millions of “points” were generated by randomly selecting parameters in the pMSSM space. These points were then tested with all relevant dark matter, electroweak, Higgs mass and heavy flavour constraints; those that failed were discarded, and the remainder kept, of which there were around 300,000. Each surviving model point was then tested with a combination of 22 ATLAS searches. The selection and generation of models described in this section was performed by collaborators.

### 4.2.2. Model selection

The generation of the model set is detailed in reference [6], but the key details will be described here. Firstly, the scan range of each parameter was restricted, with each

parameter and its range listed in table 4.2. Notably, a 4 TeV upper bound on the mass parameters was chosen to make most sparticles kinematically accessible at the LHC. Reducing this limit would increase the relative fraction of models that the ATLAS searches are sensitive to, so care must be taken when interpreting the results. Conversely, increasing this threshold has little effect on LHC phenomenology, until the limit is increased so much that either no sparticles are kinematically accessible, or those that are collapse to the simplified model cases, which have already been studied elsewhere. An exception to this is when decays proceed via virtual heavy sparticles, when increasing that sparticle mass would lead to further suppression of those decays, such as in the case of “split-SUSY” [118–120]. Lower limits on some mass parameters were chosen to avoid existing constraints from existing LHC searches and also the LEP experiments, for example the requirement that charged sparticles must have mass larger than 100 GeV. Additionally, a large range for  $|A_t|$  is permitted, which is a parameter that affects loop corrections to the mass of the Higgs boson, with a larger  $|A_t|$  leading to a greater chance that the mass of the Higgs boson is close to the experimentally measured value for a given model point.

The large dimensionality of the pMSSM renders a grid sampling technique at regular intervals inappropriate. Therefore, a point is chosen by generating a random value for each parameter within the scan ranges listed in table 4.2. A flat probability distribution is chosen for each parameter. Some of the parameters are relevant for a given observable, and therefore the scan is effectively more comprehensive within the subspace of relevant parameters.

### 4.2.3. Non-ATLAS constraints

Once a model point is chosen, a variety of public codes are used to calculate observables predicted by the model as described in the appendices of reference [6]. Further experimental constraints, shown in table 4.3, which indirectly affect the parameter space are applied and described below. For each model point, the observables described here were calculated with `micrOMEGAS` 3.5.5 [121], unless specified otherwise.

Parameter	Minimum value	Maximum value
$m_{\tilde{L}_1}(=m_{\tilde{L}_2})$	90 GeV	4 TeV
$m_{\tilde{e}_1}(=m_{\tilde{e}_2})$	90 GeV	4 TeV
$m_{\tilde{L}_3}$	90 GeV	4 TeV
$m_{\tilde{e}_3}$	90 GeV	4 TeV
$m_{\tilde{Q}_1}(=m_{\tilde{Q}_2})$	200 GeV	4 TeV
$m_{\tilde{u}_1}(=m_{\tilde{u}_2})$	200 GeV	4 TeV
$m_{\tilde{d}_1}(=m_{\tilde{d}_2})$	200 GeV	4 TeV
$m_{\tilde{Q}_3}$	100 GeV	4 TeV
$m_{\tilde{u}_3}$	100 GeV	4 TeV
$m_{\tilde{d}_3}$	100 GeV	4 TeV
$ M_1 $	0 GeV	4 TeV
$ M_2 $	70 GeV	4 TeV
$M_3$	200 GeV	4 TeV
$ A_t $	0 GeV	8 TeV
$ A_b $	0 GeV	4 TeV
$ A_\tau $	0 GeV	4 TeV
$ \mu $	80 GeV	4 TeV
$M_A$	100 GeV	4 TeV
$\tan \beta$	1	60

**Table 4.2.:** Scan ranges used for each of the 19 pMSSM parameters (as defined in table 4.1). Where the parameter is written with a modulus sign both the positive and negative values are permitted.

Parameter	Minimum value	Maximum value
$\Delta\rho$	$-0.0005$	$0.0017$
$\text{BR}(b \rightarrow s\gamma)$	$2.69 \times 10^{-4}$	$3.87 \times 10^{-4}$
$\text{BR}(B_s \rightarrow \mu^+\mu^-)$	$1.6 \times 10^{-9}$	$4.2 \times 10^{-9}$
$\text{BR}(B^+ \rightarrow \tau^+\nu_\tau)$	$66 \times 10^{-6}$	$161 \times 10^{-6}$
$\Delta(g_\mu - 2)$	$-17.7 \times 10^{-10}$	$43.8 \times 10^{-10}$
$\Omega_{\tilde{\chi}_1^0} h^2$	—	$0.1208$
$\Gamma_{\text{invisible}(\text{SUSY})}(Z)$	—	$2 \text{ MeV}$
Masses of charged sparticles	$100 \text{ GeV}$	—
$m(\tilde{\chi}_1^\pm)$	$103 \text{ GeV}$	—
$m(\tilde{u}_{1,2}, \tilde{d}_{1,2}, \tilde{c}_{1,2}, \tilde{s}_{1,2})$	$200 \text{ GeV}$	—
$m(h)$	$124 \text{ GeV}$	$128 \text{ GeV}$

**Table 4.3.:** Constraints on acceptable pMSSM points from considerations of precision electroweak and flavour results, dark matter relic density, and other collider measurements. A long dash (—) indicates that no requirement is made. Further details may be found in the text.

### Electroweak and heavy-flavour constraints

The electroweak parameter,  $\Delta\rho$  (see section 2.4 of reference [122] for a detailed description) is constrained by the limit on  $\Delta T$  (the parameter describing the radiative corrections to the total  $Z$  boson coupling strength, the effective weak mixing angle, and the  $W$  boson mass) from the electroweak fit to the Standard Model [123], where  $\Delta\rho = \alpha\Delta T$  with  $\alpha = 1/128$ .

The allowed branching ratios (BR) of  $b \rightarrow s\gamma$ ,  $B_s \rightarrow \mu^+\mu^-$  and  $B^+ \rightarrow \tau^+\nu_\tau$  all lie within the union of the two standard deviation ( $2\sigma$ ) intervals around the respective experimental measurements and theoretical predictions. For  $b \rightarrow s\gamma$ , the theoretical prediction and experimental measurement are both taken from reference [124]. For  $\text{BR}(B_s \rightarrow \mu^+\mu^-)$ , the value calculated by `micrOMEGAS 3.5.5` was scaled by  $1/(1 - 0.088)$  for comparison with experiment, as proposed in reference [125]. It is the scaled value that is required

to lie within the  $2\sigma$  interval described above, which is the combined result from the CMS and LHCb Collaborations [126].<sup>2</sup> For each model point, the branching ratio of  $B^+ \rightarrow \tau^+ \nu_\tau$  is calculated using **SuperIso v2.3** [127] (which includes  $\tan\beta$ -enhanced corrections). The experimental result is from references [128–131] and the Standard Model prediction from reference [132].

For the SUSY contribution to the anomalous magnetic moment of the muon,  $\Delta(g_\mu - 2)$ , the  $2\sigma$  uncertainty intervals for the experimental result and theoretical prediction do not overlap. Therefore, a larger range of  $3\sigma$  is used to allow a continuous interval. The Standard Model prediction  $(0.0 \pm 5.9) \times 10^{-10}$  is the combination [133] of the results of references [134–136]. The experimental measurement [137, 138] is corrected using an updated value of the muon to proton magnetic moment ratio [139, 140] giving  $\Delta(g_\mu - 2)_{\text{exp}} = (24.9 \pm 6.3) \times 10^{-10}$ .

### Dark matter constraints

Since  $R$ -parity is assumed to be exactly conserved, the LSP is stable and therefore can contribute to the total matter density observed in the universe. Additionally the LSP is both neutral and weakly interacting and so provides an ideal dark matter candidate. No assumption is made as to whether the LSP is the sole constituent of dark matter, but it is assumed that any other non-SUSY particle carrying positive  $R$ -parity cannot annihilate with the LSP (should such a particle exist). Therefore, the observed cold dark matter (CDM) is used as an upper limit on the LSP abundance. At the time of publication, the latest result was the combined measurement from the Planck Collaboration,  $\Omega_{\text{CDM}} h^2 = 0.1188 \pm 0.0010$  (table 4 of reference [47]), and the upper limit was set to the central value plus  $2\sigma$  of the experimental uncertainty.

Limits are also imposed on the interaction cross section of a neutralino with a nucleus. In the spin-independent case, the limit is taken from the LUX experiment [141]. For the spin-dependent cases, the proton–neutralino and neutron–neutralino cross-section limits are taken from the COUPP [142] and XENON100 [143] Collaborations, respectively. All

---

<sup>2</sup>The uncertainty on the theoretical prediction for the Standard Model,  $(3.20 \text{ to } 4.12) \times 10^{-9}$ , lies within the experimental uncertainty.

of these cross-sections depend on the neutralino mass, and so a single number for these limits cannot be quoted. As it is not assumed that the neutralino accounts for 100% of the observed dark matter relic density, these cross-sections are scaled down by the ratio of the expected relic density from the LSP to the observed relic density to obtain the effective dark matter cross-sections (assuming the remaining non-LSP dark matter is invisible to the direct detection experiments). To account for nucleon form-factors, the calculated value of the neutralino–nucleon cross section is allowed to be up to a factor of four higher than the limits obtained by the experiments [115].

### Collider constraints

Model points are rejected if they do not correctly predict the mass of any Standard Model particle, within the uncertainties of the theoretical calculation and experimental measurement. This is particularly important in the case of the mass of the Higgs boson. The mass of the lightest Higgs boson  $h$ , as calculated by `FeynHiggs 2.10.0` [122, 144], was required to be in the range  $124 < m(h) < 128$  GeV. This range was centred on the known mass of the Higgs boson at the time of model generation, with a 2 GeV window reflecting the uncertainty on the theoretical calculation.<sup>3</sup>

Finally, constraints from LEP are also taken into account. Model points are discarded if their additional contribution to the invisible width of the  $Z$  boson is greater than 2 MeV [145]. The lightest charged sparticle is required to be heavier than 100 GeV, except in the case of the chargino where this bound is increased provided that all sneutrinos are heavier than 160 GeV and the mass splitting between the chargino and the LSP is at least 2 GeV [146]. First- and second-generation squarks are required to be heavier than 200 GeV, although this only has a very small effect given the scan range and the assumption of negligible first- and second-generation mixing.

---

<sup>3</sup>The most recent measurement of the mass of the Higgs boson is  $125.09 \pm 0.24$  GeV [34]. It is shown later in section 4.5.5 that results involving physical observables do not depend on the exact mass of the Higgs boson.



#### 4.2.4. Sampling by LSP type

Low mass SUSY models typically over-produce dark matter, unless there is a particularly effective neutralino annihilation mechanism available. The relic density constraint in table 4.3 therefore strongly influences the distribution of the allowed model points. Model points with a wino or Higgsino-like LSP always have a near-degenerate chargino, which can act as a co-annihilator reducing the relic abundance for these types of models. However, models with a bino-like LSP do not necessarily have such a mechanism and therefore generally tend to produce too much dark matter [147]. This results in bino-LSP models being infrequently accepted in a random scan employing flat priors. The model points are therefore partitioned into three categories: bino-like, wino-like and Higgsino-like; with the categorisation being made according to the dominant contribution to the LSP within the neutralino mixing matrix  $N_{ij}$  as shown in table 4.4. In order to sample approximately equal numbers of models with each LSP type, two scans of the parameter space (within the ranges listed in table 4.2) were performed. Sampling 20 million points yielded 206,917 models with either a wino-like or Higgsino-like LSP and satisfied all of the constraints of table 4.3. A further 480 million points were sampled to obtain a sufficiently high number of models with bino-like LSP, resulting in 103,410 that satisfied all of the constraints in table 4.3. Generally models have an LSP dominated by one particular type, with over 87% of models having an LSP which is at least 90% pure. The phenomenology of the wino, bino and Higgsino LSP models can be explored separately due to the large number of model points in each category.

### 4.3. Resulting model set

The gluino and LSP mass distributions (for all of the simulated models) are shown in figure 4.1, separately for models with a bino-, wino- or Higgsino-like LSP. For both distributions the behaviour of models with a Higgsino or wino-like LSP is similar, with the number of models increasing with increasing gluino mass, and conversely the number of models decreasing with increasing LSP mass. However, we see some differences between

LSP type	Definition	Sampled	Simulated	
			Number	Fraction
‘Bino-like’	$N_{11}^2 > \max(N_{12}^2, N_{13}^2 + N_{14}^2)$	$480 \times 10^6$	103,410	35%
‘Wino-like’	$N_{12}^2 > \max(N_{11}^2, N_{13}^2 + N_{14}^2)$	$\left. \vphantom{\begin{matrix} N_{11}^2 > \max(N_{12}^2, N_{13}^2 + N_{14}^2) \\ (N_{13}^2 + N_{14}^2) > \max(N_{11}^2, N_{12}^2) \end{matrix}} \right\} 20 \times 10^6 \left\{$	80,233	26%
‘Higgsino-like’	$(N_{13}^2 + N_{14}^2) > \max(N_{11}^2, N_{12}^2)$		126,684	39%
<b>Total</b>		$500 \times 10^6$	310,327	

**Table 4.4.:** Categorisation of the 310,327 model points by the type of the LSP (assumed to be the  $\tilde{\chi}_1^0$ ) according to the neutralino mixing matrix parameters  $N_{ij}$ , where the first index indicates the neutralino mass eigenstate and the second indicates its nature in the lexicographical order ( $\tilde{B}^0, \tilde{W}^0, \tilde{H}_u^0, \tilde{H}_d^0$ ). For example,  $N_{12}$  is the amplitude for the LSP to be  $\tilde{W}^0$ . The final two columns indicate the total number of viable models in each of the LSP categories, and the fraction relative to the total 310,327 models.

the models with a bino-LSP and the others; firstly there are a greater proportion of bino-LSP models with lighter gluinos and secondly there is a sharp concentration of models with  $m(\tilde{\chi}_1^0) < 70 \text{ GeV}$ . Both of these effects are due to the constraint on the relic density: light gluinos can act as co-annihilators if close in mass to the LSP, and the neutralino can resonantly annihilate to either a Higgs or  $Z$  boson if the mass of the LSP is roughly half of one of the aforementioned bosons. Either form of annihilation, which would occur in the early universe, can reduce the LSP relic density to a level that satisfies the constraint on  $\Omega_{\tilde{\chi}_1^0} h^2$ .

Distributions of the  $\tilde{t}_1$ ,  $\tilde{b}_1$ ,  $\tilde{\tau}_1$  and  $\tilde{q}$  masses are shown in figure 4.1, where  $\tilde{q}$  here (and throughout this chapter) refers to the lightest of any of the eight first- or second-generation squarks<sup>4</sup>. Unlike the gluino and neutralino, these sparticles have similar distributions for the bino-, wino- and Higgsino-LSP model sets, and so are shown altogether. One can see that the lightest stop is generally heavier than the other sparticles plotted, with only 7.7% of models having  $m(\tilde{t}_1) < 1 \text{ TeV}$  and the peak of the stop mass distribution being around 2.5 TeV. The paucity of light stops is a result of the constraint on the Higgs mass: at tree level in the MSSM,  $m(h) < m(Z)$  and therefore to get the correct Higgs boson

<sup>4</sup>That is, the lightest of the following set:  $\{\tilde{u}_L, \tilde{u}_R, \tilde{d}_L, \tilde{d}_R, \tilde{c}_L, \tilde{c}_R, \tilde{s}_L, \tilde{s}_R\}$ .

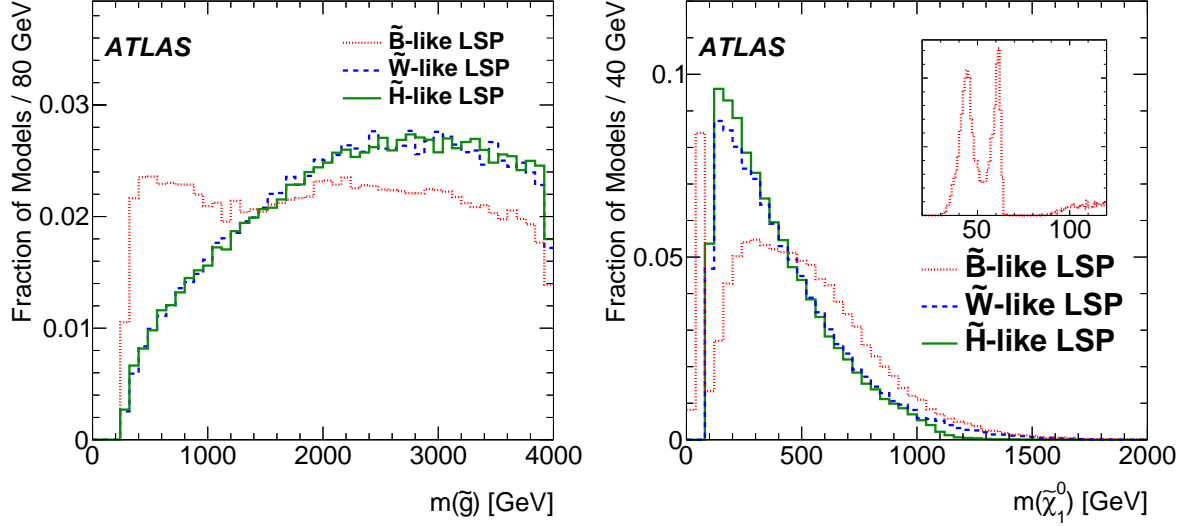


**Figure 4.1.:** Distributions of the gluino (left) and LSP (right) masses, shown separately for models with a bino-like (dotted red), wino-like (dashed blue) or Higgsino-like (solid green) LSP. The constraints listed in table 4.3 have been applied, but not the constraints from the ATLAS searches. The distributions are normalised to unit area. The inset in the plot on the right shows in more detail the region of low neutralino mass for the models with bino-like LSP.

mass large loop-level corrections are needed. At 1-loop, the correction to  $m_h^2$  from the stop is approximately [66],

$$m_h^2(\text{one loop, stop}) \propto \left[ \ln \frac{M_S^2}{m_t^2} + \left( \frac{X_t}{M_S} \right)^2 \left( 1 - \frac{X_t^2}{12M_S^2} \right) \right] \quad (4.1)$$

where  $m_t$  is the top mass,  $M_S^2 = m_{\tilde{t}_1} m_{\tilde{t}_2}$  and  $X_t = A_t - \mu/\tan\beta$ . The 1-loop correction is maximised when *both*  $M_S^2$  is large and  $X_t/M_S \sim \sqrt{6}$ . This implies reasonable mixing (large  $A_t$ ) and that both  $m_{\tilde{t}_1}$  and  $m_{\tilde{t}_2}$  be reasonably large (large  $m_{\tilde{Q}_3}$  and  $m_{\tilde{U}_3}$ ), hence depleting light stops.

## 4.4. The ATLAS searches

The 22 ATLAS searches for new physics implemented for this study are listed in table 4.5. Each search is briefly summarised in reference [6] and described in full in the references listed in the table 4.5. Instead of summarising each search, common features of the searches in each group will be briefly described here.

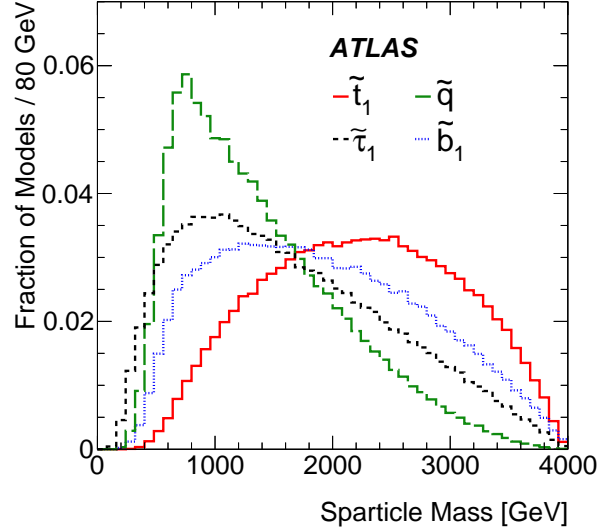


**Figure 4.2.:** Normalised distribution of sparticle masses for the lightest stop (solid red), sbottom (dashed blue), first- or second-generation squark (dashed green) and stau (dot-dashed black) for all LSP types combined. The constraints listed in table 4.3 have been applied, but not the constraints from the ATLAS searches.

Searches in the *strong production* category target, or are sensitive to, scenarios where gluinos or first and second generation squarks are produced. These scenarios typically yield final states with many jets, and  $E_T^{\text{miss}}$  from the undetected LSP. Leptons and  $b$ -jets can also be produced from the decays of the initial SUSY particles.

*Third generation* searches are similar to those of strong production, however they instead target the direct production of third generation squarks. This typically leads to a greater proportion of final states containing heavy-flavour particles, and so these searches are tailored specifically for those types of event.

The *electroweak* searches target cases where sleptons or electroweakinos are pair produced, which typically yield final states with several leptons.

One search worth special mention is the Disappearing Track analysis, which targets charginos with small ( $\lesssim 200$  MeV) mass splitting with the LSP. This results in the chargino becoming long lived and decaying away from the primary vertex. The decay products are a neutralino and a soft charged pion, both of which are missed by the detector, giving the signature of a *disappearing* charged track.

The final category, *other*, contains analyses that don't fit into any of the above categories. The long-lived particle search targets only the direct production of pairs of long-lived stops, sbottoms, squarks, gluinos, staus or charginos. The  $H/A \rightarrow \tau^+\tau^-$  search is designed to detect the heavy, neutral Higgs bosons predicted in the MSSM decaying to  $\tau$ -pairs.

## 4.5. ATLAS constraints on the pMSSM

It can be particularly challenging to quantify the impact of experimental searches on multidimensional parameter spaces such as the pMSSM. One of the most straightforward methods is to project onto one- or two-dimensional subspaces of the full 19 parameter pMSSM space; the most relevant parameters onto which to project are typically the sparticle masses. These projections of the distribution of models for a given variable can be shown before and after the ATLAS searches, or as the fraction of models excluded, indicating their impact.

Production cross-sections for sparticles decrease rapidly when their masses are increased. When those initial sparticles decay, the masses of other sparticles affect the types of visible decay products and their kinematics. Of particular importance is the mass of the LSP, since a decay to a high-mass LSP results in less energy being available for the observable decay products. Furthermore, by the nature of the other sparticles having to be heavier than the LSP, they also have a correspondingly smaller production cross-section.

It is important to note that the fraction of surviving model points in the projected space necessarily depends both on the prior distribution of model points in the parameters that have been projected out, and on experimental constraints on sparticle masses other than those plotted. Thus, some care is needed in their interpretation. In particular the fractions of model points excluded can depend, in some cases sensitively, on the non-collider constraints shown in table 4.3, the choice of scan ranges shown in table 4.2, and on the choice of a flat prior. Nevertheless, some general features of the impact of the ATLAS Run-1 searches are clear.

Analysis	Ref.	Category
0-lepton + 2–6 jets + $E_T^{\text{miss}}$	[148]	Strong production
0-lepton + 7–10 jets + $E_T^{\text{miss}}$	[149]	
1-lepton + jets + $E_T^{\text{miss}}$	[150]	
$\tau(\tau/\ell)$ + jets + $E_T^{\text{miss}}$	[151]	
SS/3-leptons + jets + $E_T^{\text{miss}}$	[152]	
0/1-lepton + 3 $b$ -jets + $E_T^{\text{miss}}$	[153]	
Monojet	[154]	
0-lepton stop	[155]	Third generation
1-lepton stop	[156]	
2-leptons stop	[157]	
Monojet stop	[158]	
Stop with $Z$ boson	[159]	
2 $b$ -jets + $E_T^{\text{miss}}$	[160]	
$t\bar{b}$ + $E_T^{\text{miss}}$ , stop	[161]	
$\ell h$	[162]	Electroweak
2-leptons	[163]	
2- $\tau$	[164]	
3-leptons	[165]	
4-leptons	[166]	
Disappearing Track	[167]	
Long-lived particle	[168, 169]	Other
$H/A \rightarrow \tau^+\tau^-$	[170]	

**Table 4.5.:** The 22 different ATLAS searches considered. The term ‘lepton’ ( $\ell$ ) refers specifically to  $e^\pm$  and  $\mu^\pm$  states, except in the cases of the electroweak 3-leptons and 4-leptons analyses where  $\tau$  leptons are also included.

In the following section, many plots contain all three LSP model types (wino, bino and Higgsino) and are referred to as “combined”. When making this combination, the bino-LSP models were weighted by a factor of  $1/24$  to account for the fact that bino models were sampled by a factor of 24 more than the wino- and Higgsino-LSP models. It is stated in the caption if a plot contains only one type of LSP.

### 4.5.1. Sparticle masses

#### Squarks and gluinos

The sensitivity of the combined ATLAS searches to gluinos and squarks is shown in figure 4.3. These plots show the distribution of all models generated<sup>5</sup>, both before ATLAS searches and afterwards. Additionally, the ratio showing the fraction of models excluded by ATLAS is shown. Gluinos are tightly constrained for masses below 1 TeV and all models that have gluinos with mass less than 500 GeV are excluded, as shown in figure 4.3a. The fraction of models excluded continues to decrease until around 3 TeV showing that the searches have sensitivity to gluinos with this mass (either via direct production of gluinos, or the influence of virtual gluinos on the production cross-section of other sparticles). Squarks are less tightly constrained than gluinos, as show by figure 4.3b, which is unsurprising given their smaller production cross-section. The ATLAS searches are more sensitive to lighter squarks, with the fraction of models excluded decreasing monotonically until about 1.5 TeV. Beyond this, the sensitivity of the ATLAS searches is related to other sparticles and so the fraction of models excluded as a function of mass becomes flat.

More information can be gained by projecting the pMSSM onto the  $\tilde{g}-\tilde{\chi}_1^0$  and  $\tilde{q}-\tilde{\chi}_1^0$  mass planes, as shown in figure 4.4. Overlaid are the 95% CL exclusion limits on simplified models from the 0-lepton + 2–6 jets +  $E_T^{\text{miss}}$  [148] search. In the case of figure 4.4(a) the simplified model assumes pair production of gluinos, which decay to quarks and a neutralino,  $\tilde{g} \rightarrow q\bar{q}\tilde{\chi}_1^0$ . We see that the simplified model limit has a good congruence with the exclusion in the pMSSM. This is surprising given increased complexity of the

---

<sup>5</sup>The generated models passed all the constraints in table 4.3.

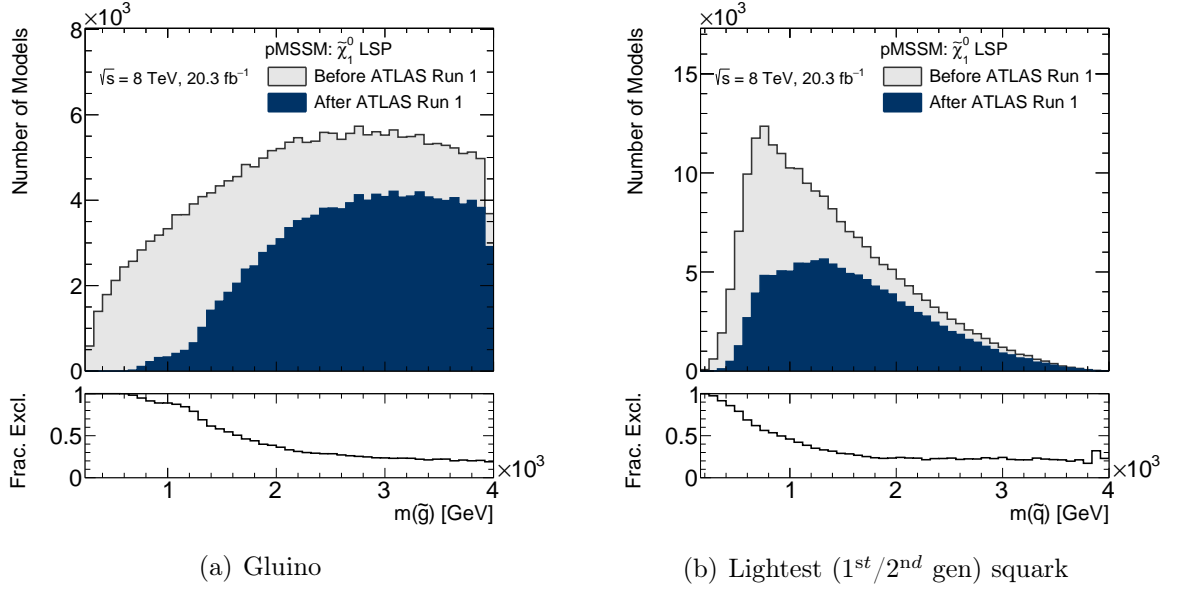


**Figure 4.3.:** Distributions of all simulated pMSSM models before and after the combination of ATLAS searches for gluinos (left) and the lightest squark (right). The ratio plot shows the fraction of models excluded by the searches.

pMSSM where other particles compete for production mechanisms and other particles are permitted with masses lying in between the gluino and the LSP, which can lead to cascade decays. In general, such cascade decays can lead to different final states from those considered in the simplified model, with different jet  $p_T$  and  $E_T^{\text{miss}}$  spectra, additional leptons or photons with different acceptances. There are cases where the sensitivity does differ in detail from the simplified model limit. For example in the “compressed” region, where the gluino mass is only a little larger than the LSP mass the simplified model limit underestimates the sensitivity of the ATLAS searches. Here the  $\tilde{g} \rightarrow q\bar{q}\tilde{\chi}_1^0$  decay produces low-energy quarks which typically fail to meet the kinematic requirements on jets. In this region, the sensitivity is instead due to the monojet analyses [154, 159], which target the recoil of LSPs (or other, slightly heavier, SUSY particles) against initial-state QCD radiation. Furthermore, in the region with lighter neutralinos ( $m(\tilde{\chi}_1^0) \lesssim 300 \text{ GeV}$ ) and gluinos with mass greater than 1200 GeV, we see only around 80 % of the models have been excluded, showing the overoptimistic nature of simplified models.

The solid line overlaid on figure 4.4(b) corresponds to a simplified model that assumes only the LSP and all eight of the first and second generation squarks are kinematically



accessible, with the squarks having identical mass and decaying to the LSP and a quark. This limit overestimates the sensitivity of the ATLAS searches, with around 30% of models within the limit remaining viable. This is primarily because in the pMSSM the squarks are not necessarily eight-fold degenerate, reducing the production cross-section. The exclusion has a closer correspondence with the dashed line, in which the simplified model production cross-section was reduced by a factor of 4, emulating the case where a single pair of squarks are kinematically accessible. Another feature that is visible in this figure is the horizontal band that are excluded for models with  $m(\tilde{\chi}_1^0) \lesssim 200$  GeV, even for very high squark masses. This is the effect of the Disappearing Track analysis which is sensitive to models with wino-dominated LSPs, with masses up to approximately 200 GeV, regardless of the other sparticle content of the model.

The sensitivity of the ATLAS searches is projected onto the  $\tilde{g}$ – $\tilde{q}$  mass plane in figure 4.5(a), where the LSP mass may take on any value within the range defined in table 4.2. Gluinos are almost completely excluded up to 700 GeV and tightly constrained up to 1200 GeV. Squarks are also tightly constrained up to around 200 GeV, however, the sensitivity to squarks weakens as the gluino mass increases. This is due to the suppression of direct squark production via  $t$ -channel gluino exchange and also the suppression of associated production of  $\tilde{g} + \tilde{q}$  exchange. The simplified model limit, which assumes strong production of gluinos and eight-fold degenerate first- and second-generation squarks that directly decays to quarks and massless neutralinos, lies at the upper-limit of the ATLAS sensitivity. This is as expected because the pMSSM allows non-degenerate squarks and massive LSPs, however this does highlight one case where the simplified model limit shows the best-possible scenario. Figure 4.5(b) shows the same plane except that only the models with a bino-dominated LSP are shown. For these models, there is a sharp cut-off in the sensitivity at around  $m(\tilde{g}) \sim 600$  GeV and  $m(\tilde{q}) \sim 600$  GeV, whereas the decrease in sensitivity is more gradual for the wino- and Higgsino-LSP models (as shown in figure 4.5(a)). This is a result of the relic-density constraint, as described in section 4.3. Many of these models have an LSP with a mass splitting less than 100 GeV with a squark or a gluino (or both), in which case either sparticle can act as a coannihilator, reducing the relic density. As a result, models with both a heavy squark and a heavy gluino are more likely to have a heavy LSP, and hence the sensitivity is reduced in these regions.

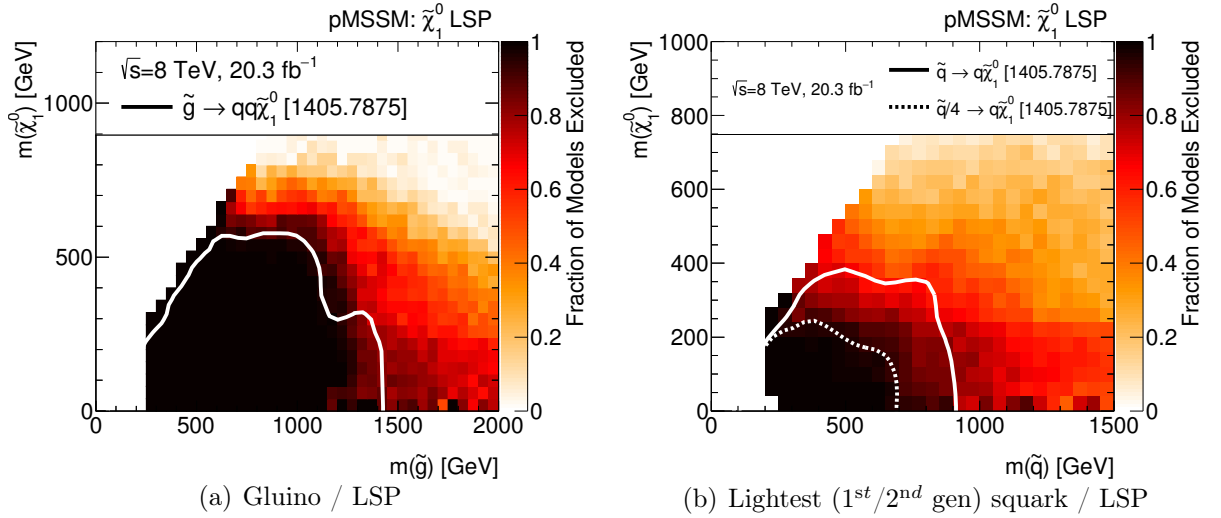


**Figure 4.4.:** Fraction of pMSSM points excluded by the combination of 8 TeV ATLAS searches in the (a)  $\tilde{g}$ - $\tilde{\chi}_1^0$  and (b) the  $\tilde{q}$ - $\tilde{\chi}_1^0$  mass planes. These plots are binned projections of the pMSSM onto a 2D plane. Many models may populate each bin, and the colour scale indicates the fraction of models excluded, with black squares indicating 100% of model points being excluded. The white regions indicate places where no model points were sampled, due to the constraints of table 4.2 and table 4.3. In both cases, the solid white lines overlaid are observed simplified-model limits from the 0-lepton + 2-6 jets +  $E_T^{\text{miss}}$  search [148] at 95% CL. In the  $\tilde{g}$ - $\tilde{\chi}_1^0$  case, the simplified-model limit is set assuming direct production of gluino pairs and that the squarks are decoupled, with gluino decaying to quarks and a neutralino,  $\tilde{g} \rightarrow q\bar{q}\tilde{\chi}_1^0$ . In the  $\tilde{q}$ - $\tilde{\chi}_1^0$  plane, both lines are drawn assuming directly produced first/second-generation squark pairs, with each squark decaying to a quark and a neutralino,  $\tilde{q} \rightarrow q\tilde{\chi}_1^0$ . The solid line corresponds to the case where all eight squarks from the first two generations are assumed to be mass degenerate. The dashed line has the squark production cross-section scaled down by a factor of four to emulate the effect of only two of those eight squarks being kinematically accessible.

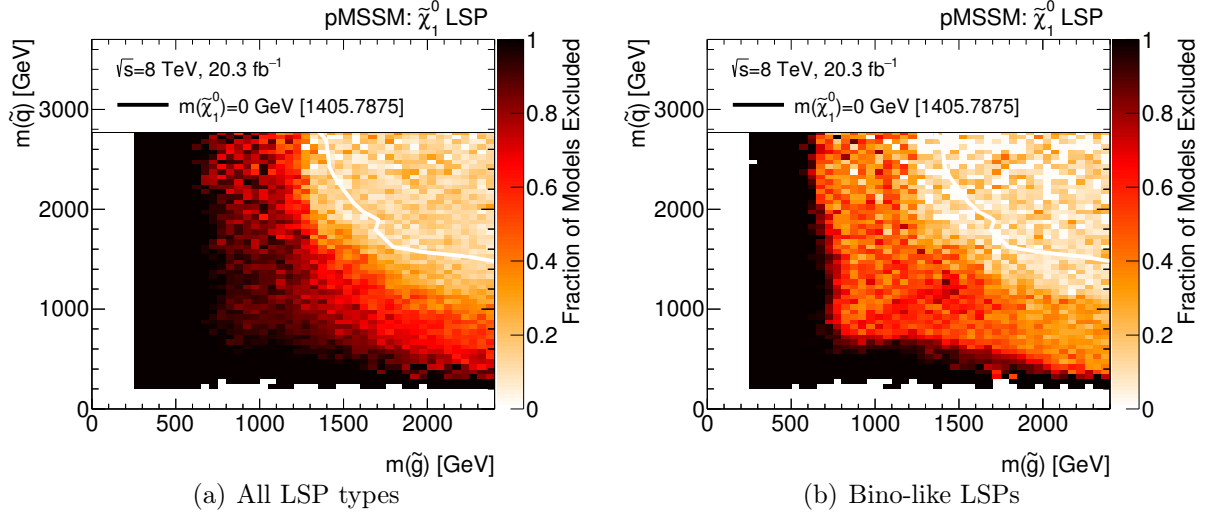


**Figure 4.5.:** Fraction of pMSSM points excluded in the  $\tilde{g}$ – $\tilde{q}$  mass plane, where  $\tilde{q}$  represents the lightest squark from the first two generations. The overlaid line shows a limit for a simplified model from the 0-lepton + 2–6 jets +  $E_T^{\text{miss}}$  search [148] which assumes strong production of gluinos and eight-fold degenerate first- and second-generation squarks, with direct decays to quarks and massless neutralinos.

### Third generation squarks

One of the major motivations for SUSY is that it provides a natural solution to the hierarchy problem, provided the super-partners of third generation quarks have masses close to the TeV-scale [67]. The decays of stops and sbottoms also typically involve top and/or bottom quarks, which have distinctive decay patterns. As a result, the ATLAS collaboration has produced a suite of dedicated searches for third generation sparticles.

The distribution of the mass of the lightest stop and lightest sbottom ( $\tilde{t}_1$  and  $\tilde{b}_1$  respectively) before and after the ATLAS searches is shown in figure 4.6. We see that the ATLAS searches are directly sensitive to stops and sbottoms up a mass of about 1 and 0.8 TeV respectively as the fraction of models excluded ceases to decrease after this point.

The sensitivity of the ATLAS searches in the  $\tilde{t}_1$ – $\tilde{\chi}_1^0$  mass plane is shown in figure 4.7, now with three simplified model limits overlaid for comparison. Figure 4.7(a) shows the combined exclusion of all the ATLAS searches. Again the impact of the Disappearing Track analysis is clear as the horizontal band of excluded models, independent of stop mass. Promisingly for natural solutions to the hierarchy problem, many models with sub-

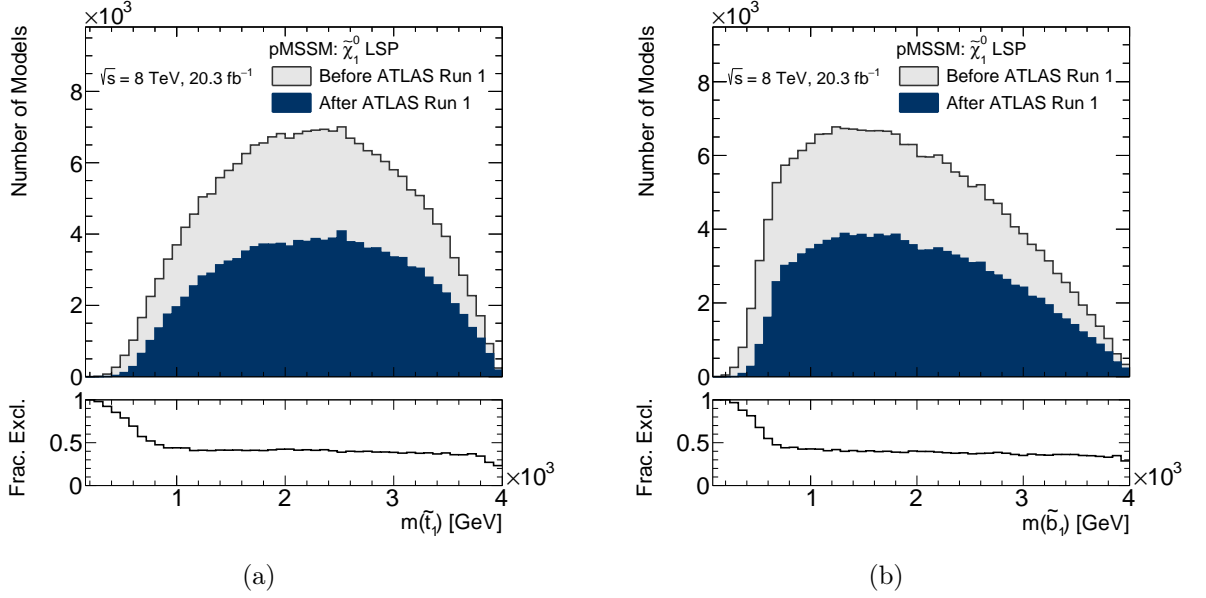


**Figure 4.6.:** Distribution of the mass of the lightest stop (left) and sbottom (right) before and after the combined ATLAS searches.

TeV stops are still viable, however, stops are tightly constrained up to around 500 GeV for  $\tilde{\chi}_1^0$  masses below 500 GeV, and are completely excluded below  $m(\tilde{t}_1) = 250$  GeV. Models with  $m(\tilde{t}_1) \approx 300$  GeV can evade the ATLAS searches in the compressed region. The sensitivity to stops is mainly driven by the third-generation searches (defined in table 4.5), as shown by figure 4.7(b) which shows the impact of just those searches.

Another feature shown by figure 4.7 is the lack of light stops. Although stops are permitted by the constraints in table 4.3 to be as light as 100 GeV, there are no models with  $m(\tilde{t}_1) < 200$  GeV and for models with  $m(\tilde{\chi}_1^0) < 50$  GeV this bound increases to 400 GeV. As discussed in section 4.3, this is a result of requiring a Higgs boson with mass in the range  $124 < m(h) < 128$  GeV.

The simplified model limit indicated by the solid line on figure 4.7 assumes direct production of stop pairs, with the decay  $\tilde{t}_1 \rightarrow t\tilde{\chi}_1^0$ , and over-predicts the exclusion of models in the kinematically allowed region. This is partly because in the pMSSM multi-step decays of the stop are permitted, for example  $\tilde{t}_1 \rightarrow b\tilde{\chi}_1^\pm$  with  $\tilde{\chi}_1^\pm \rightarrow W^{(*)}\tilde{\chi}_1^0$ , and the sensitivity of the  $\tilde{t}_1$  search analyses depends on the branching ratio of the top squark to the LSP. In fact, the 95% CL limit for this multi-step process does not extend

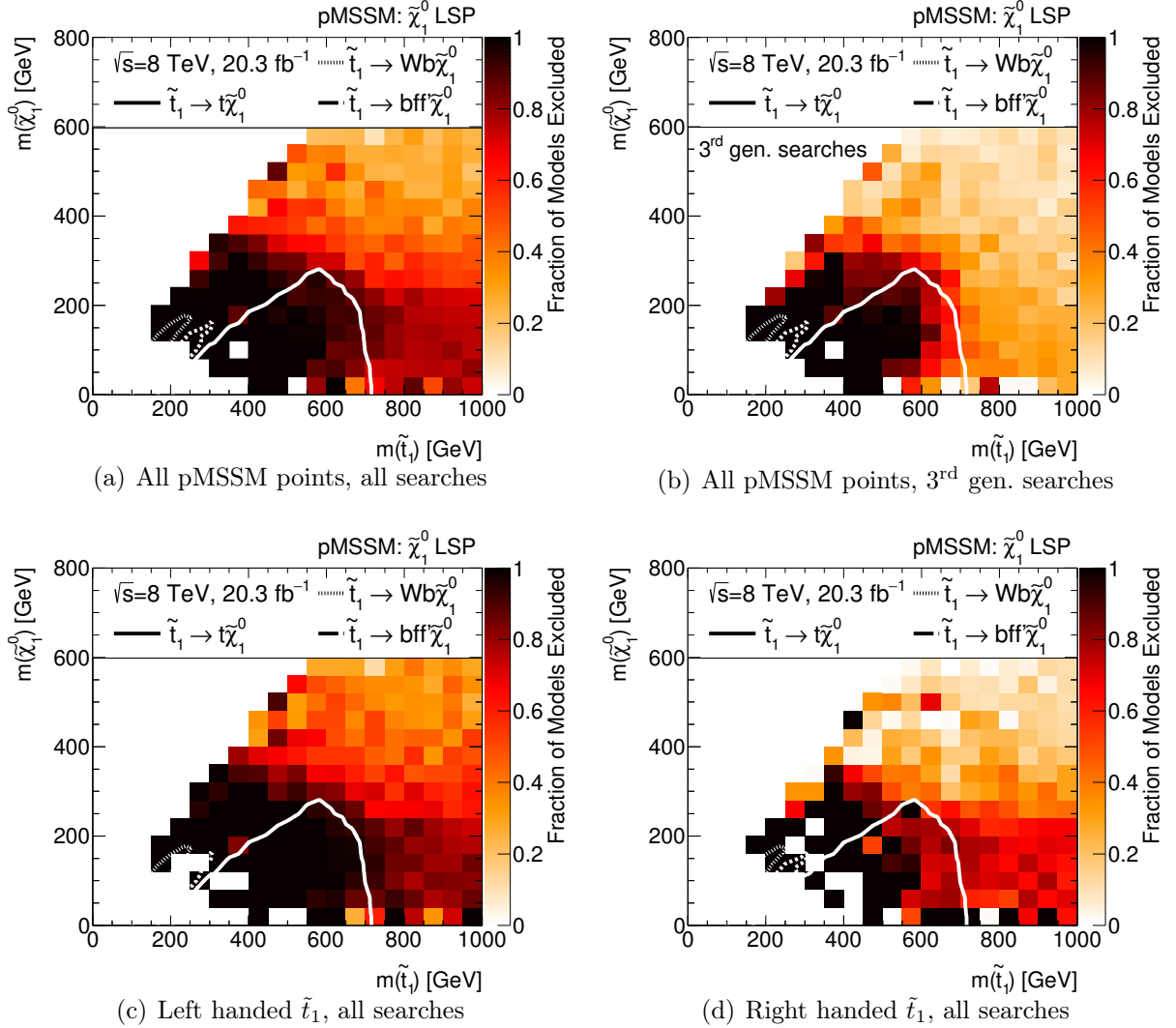


**Figure 4.7.:** Fraction of pMSSM points excluded in the  $\tilde{t}_1$ - $\tilde{\chi}_1^0$  plane in various cases. The top two plots show the full model set, with impact of all searches on the left and only the third-generation searches on the right. The bottom row of plots separates the models according to whether the  $\tilde{t}_1$  is either mostly (c)  $\tilde{t}_L$  or (d)  $\tilde{t}_R$ . There are relatively few pMSSM points at low  $\tilde{t}_1$  mass for the reasons described in the text. Three simplified-model limits are overlaid [156, 161]. The solid line represents the limit set assuming directly produced top squark pairs, with each decaying to a top quark and neutralino,  $\tilde{t}_1 \rightarrow t \tilde{\chi}_1^0$ . The dashed and dotted lines correspond to limits assuming decays of  $\tilde{t}_1 \rightarrow \tilde{\chi}_1^\pm b$  with the chargino decaying via an off- or on-shell  $W$  to the neutralino, respectively.

beyond  $m(\tilde{t}_1) = 540 \text{ GeV}$  [161], which is closer to the exclusion in the pMSSM. The other two simplified model limits, indicated by the dashed and dotted lines, assume decays of  $\tilde{t}_1 \rightarrow \tilde{\chi}_1^\pm b$  with the chargino decaying via an off- or on-shell  $W$  to the neutralino, respectively. Both of these limits fail to describe the exclusion of models in the pMSSM, this time underestimating the sensitivity in the pMSSM.

The stop mass eigenstates,  $\tilde{t}_1$  and  $\tilde{t}_2$  are mixtures of left and right chiral superpartners of the top,  $\tilde{t}_L$  and  $\tilde{t}_R$ . The mass eigenstates are defined through the mixing angle  $\theta_{\tilde{t}}$

$$\begin{pmatrix} \tilde{t}_1 \\ \tilde{t}_2 \end{pmatrix} = \begin{pmatrix} \cos \theta_{\tilde{t}} & -\sin \theta_{\tilde{t}} \\ \sin \theta_{\tilde{t}} & \cos \theta_{\tilde{t}} \end{pmatrix} \begin{pmatrix} \tilde{t}_L \\ \tilde{t}_R \end{pmatrix}. \quad (4.2)$$

The degree to which the lightest stop is mostly  $\tilde{t}_L$  or  $\tilde{t}_R$  can affect the sensitivity of searches in a non-trivial way that is not captured by the simplified model approach. Figure 4.7(c) and figure 4.7(d) show the exclusion of the combined ATLAS searches for models where the lightest stop was mostly  $\tilde{t}_L$  and  $\tilde{t}_R$  respectively. Immediately we see that the ATLAS searches are more sensitive to models where the  $\tilde{t}_1$  is mostly  $\tilde{t}_L$ , compared to models where the  $\tilde{t}_1$  is mostly  $\tilde{t}_R$ . Furthermore, models where the  $\tilde{t}_1$  is mostly  $\tilde{t}_L$  are more common, and such stops are typically lighter than when mostly  $\tilde{t}_R$ . The improved sensitivity to  $\tilde{t}_L$  is due to both the  $\tilde{t}_L$  and  $\tilde{b}_L$  masses being set by the  $m_{\tilde{Q}_3}$  parameter and so their masses are typically split by no more than 50 GeV. Therefore if the lightest sbottom is mostly  $\tilde{b}_L$  then analyses targeting sbottom production become relevant in constraining the models. On the other hand, if the lightest stop is  $\tilde{t}_R$ , there is no correlation between the right-handed stop and the lightest sbottom masses. The  $\tilde{t}_L$  tend to be lighter than the  $\tilde{t}_R$  due to the two-loop correction to the mass of the Higgs boson from the stop, which needs to be significant in order to get the correct mass. Here  $X_t$  appears as a odd power, favouring one direction in mixing over the other [171].

The sensitivity to sbottoms of the combined ATLAS searches and just the third generation searches are show in figure 4.8(a) and (b) respectively. There is a good correspondence between the exclusion in the pMSSM and the simplified model limit, and again we see that the third generation searches are dominating the sensitivity. Sbottoms are completely excluded up to 250 GeV, and are tightly constrained up to about 450 GeV for models with

neutralinos lighter than 205 GeV. The dependence on the handedness of the sbottom is weaker than in the stop case, as shown by figure 4.8 (c) and (d). Interestingly, opposite to the stop case, the lightest sbottom mass eigenstate is more likely to be right-handed than left-handed. Again this is due to the Higgs boson mass, which requires a large  $m_{\tilde{Q}_3}$  and hence drives up the left-handed sbottom mass. As there is no similar requirement on  $m_{\tilde{d}_3}$ , then the  $\tilde{b}_R$  is more likely to be the lightest state.<sup>6</sup>

### Electroweak bosons and sleptons

If the masses of the gluinos and squarks are large, then the direct production of neutralinos, charginos, sleptons and sneutrinos through the electroweak interaction may dominate SUSY particle production. ATLAS had produced a dedicated array of searches targeting these scenarios. The sensitivity to selectrons, smuons and sneutrinos counterparts, the lightest of which is denoted by  $\tilde{\ell}$  (here and throughout this chapter), is displayed in figure 4.9 for both the combination of all searches and just the electroweak searches, as defined in table 4.5. Comparing the two figures we see that at higher masses, the sensitivity to sleptons comes from non-electroweak searches except for and also the familiar band of exclusion due to the Disappearing Track search. However, there is a good core of sensitivity from the electroweak searches that tallies well with the simplified model limit, which in this case assumes direct production of slepton pairs assuming that the left- and right-handed selectrons and smuons are all mass-degenerate, and that each decays via  $\tilde{\ell} \rightarrow \ell \tilde{\chi}_1^0$ . The limit is still an overestimate however, as in the pMSSM the left- and right-handed sleptons are not necessarily degenerate, reducing their production cross-section.

Figure 4.10 shows the sensitivity of the electroweak searches to the  $\tilde{\ell}_L$  and  $\tilde{\ell}_R$  (which represent the lightest of the left- or right-handed selectrons or smuons). Here, the assumptions of the simplified model limits have been relaxed, and now assume directly pair-produced left (right) handed selectrons/smuons, decaying to an electron/muon and neutralino. Here, there is particularly good agreement with the simplified model case

---

<sup>6</sup>The same argument does not apply to the stop case, as  $m_{\tilde{u}_3}$  is required to be large by the Higgs boson mass constraint.

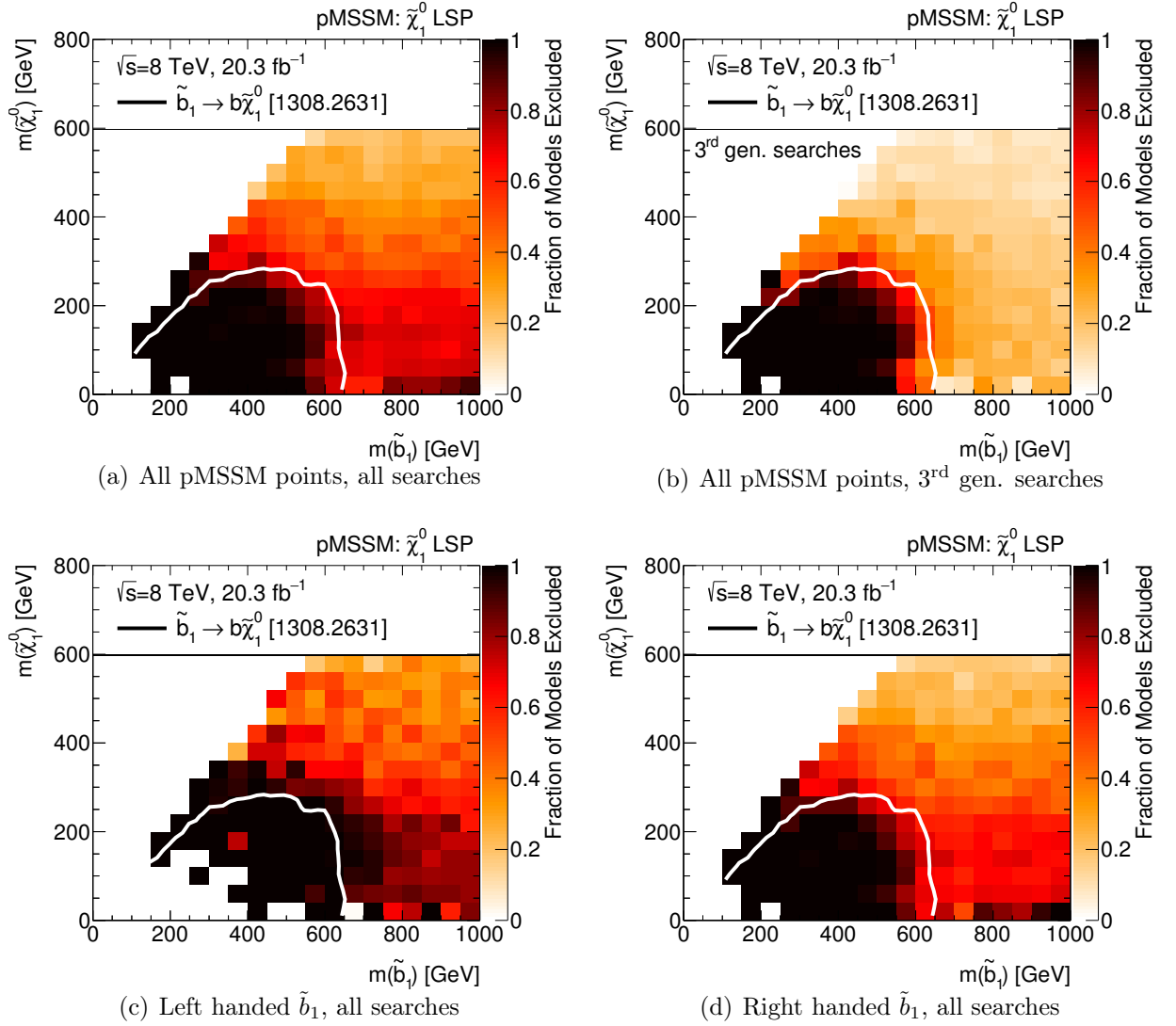


**Figure 4.8.:** Fraction of pMSSM points excluded in the  $\tilde{b}_1$ – $\tilde{\chi}_1^0$  plane after the combination of all ATLAS searches (a) and just the third generation searches (b). In both cases, the white line corresponds to the simplified model limit from [160] which assumes direct production of sbottom pairs, with the decay  $\tilde{b} \rightarrow b\tilde{\chi}_1^0$ . The bottom row of plots separates the models according to whether the  $\tilde{b}_1$  is either mostly (c)  $\tilde{b}_L$  or (d)  $\tilde{b}_R$ .



and the region that is 100% excluded by ATLAS. We also see that the ATLAS searches are more sensitive to left-handed sleptons than their right-handed counterparts, which can be understood from the lack of  $SU(2)$  couplings of the  $\tilde{\ell}_R$  reducing their production cross-section. In addition to this, there is also a pocket of extra sensitivity beyond the simplified model limit in the  $\tilde{\ell}_L$  case, approximately in the region  $300 < m(\tilde{\ell}_L) < 400$  GeV and  $100 < m(\tilde{\chi}_1^0) < 200$  GeV. Here, the majority of models have either a wino- or Higgsino-dominated LSP. We find that ATLAS is more sensitive to left-handed sleptons in models where the Higgsino is the LSP than when the wino is the LSP, whereas this is not the case for right handed sleptons. As this difference is seen in LSP type, it cannot be driven by production mechanisms, and therefore is related to the decays of the sleptons. In both wino and Higgsino cases, the right-handed slepton decays to a lepton and a neutralino (hence the similar sensitivity). Left-handed decays differ for the LSP types: for Higgsino models, approximately 100% of the left handed slepton decay is to leptons and a neutralino, however for wino models only around 2/3 of decays are of this form. The remaining 1/3 are to a chargino and a neutrino. The result is there are fewer leptons produced from the decays of left handed sleptons when the wino is the LSP than when the Higgsino is the LSP, and so fewer events pass the selections of the electroweak searches, explaining the difference in sensitivity.

#### 4.5.2. Production cross-section

One of the most generic ways to interpret the result of the ATLAS searches is by examining their effect on the overall production cross-section,  $\sigma_{\text{total}}$ , which is shown in figure 4.11. It should be noted that this distribution is sculpted by the lower and upper limits on sparticle masses applied during model selection. The most likely value of the production cross-section is around 100 fb, which drops by around an order of magnitude after the ATLAS searches are considered. Furthermore, the fraction of models excluded in the lower pad of the figure show that the direct searches are sensitive to models with cross-sections as low as 1 fb and that no models with cross-section above 30,000 fb evade the searches. Interestingly, there are around 90 models with large cross-section,  $\sigma_{\text{total}} > 10,000$  fb, that do evade the searches. Around 2/3 of these models have a

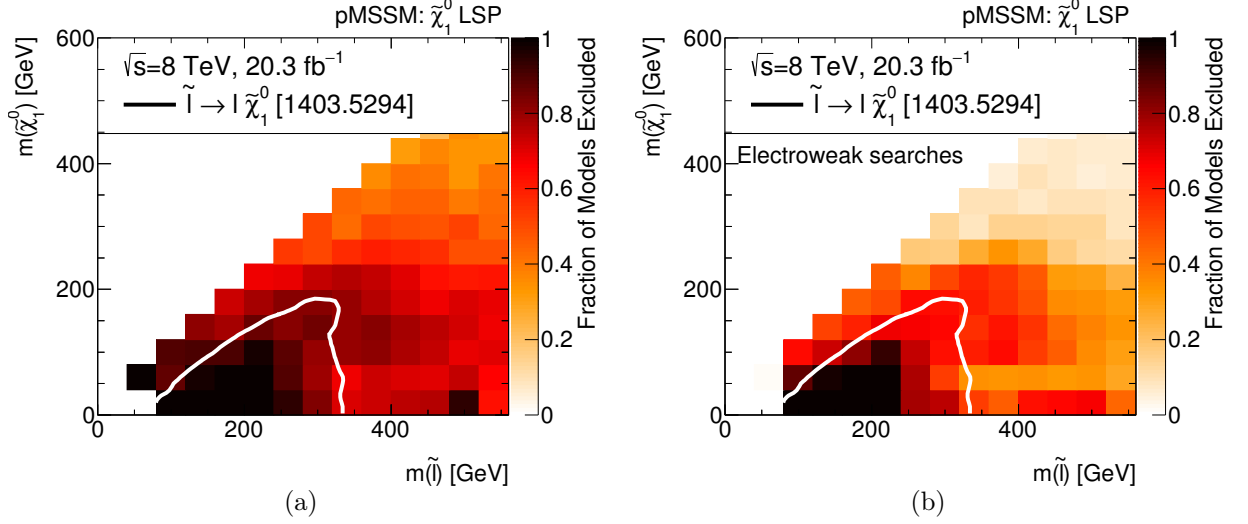


**Figure 4.9.:** Fraction of pMSSM points excluded in the  $\tilde{l}$ - $\tilde{\chi}_1^0$  plane after the combination of all ATLAS searches (a) and just the electroweak searches (b). Here  $\tilde{l}$  corresponds to the lightest of any first or second generation slepton or sneutrino. In both cases, the white line corresponds to the simplified model limit from [163] which assumes direct production of slepton pairs assuming that the left- and right-handed selectrons (or smuons) are mass-degenerate and that each decays via  $\tilde{\ell} \rightarrow \ell \tilde{\chi}_1^0$ .

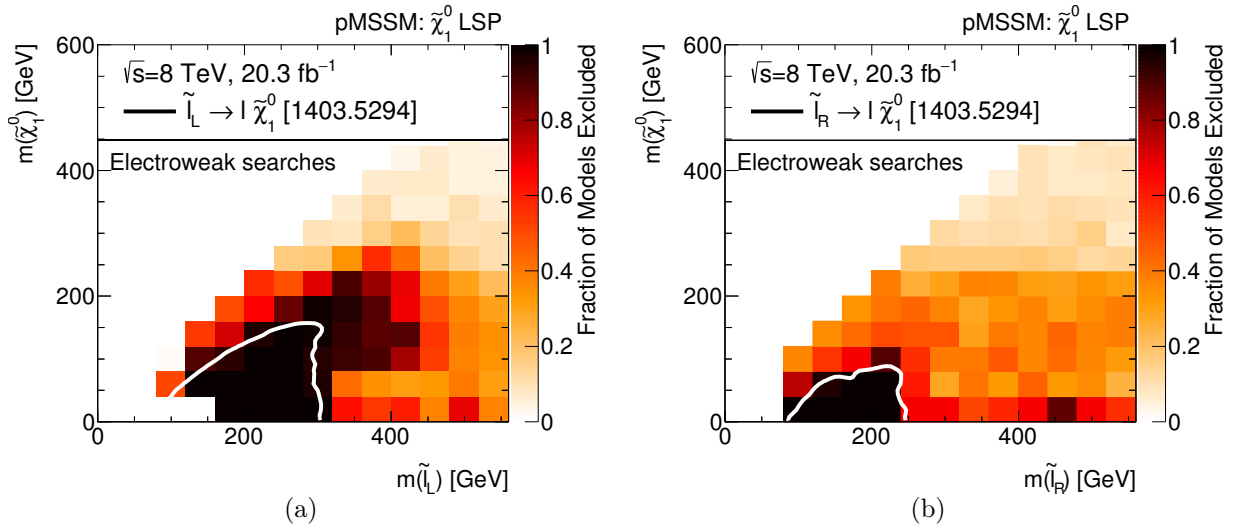


**Figure 4.10.:** Fraction of pMSSM points excluded in the  $\tilde{\ell}_L$ - $\tilde{\chi}_1^0$  plane (left) and  $\tilde{\ell}_R$ - $\tilde{\chi}_1^0$  plane (right) after the combination of the electroweak searches as defined in table 4.5. The simplified model limit in the  $\tilde{\ell}_L$  ( $\tilde{\ell}_R$ ) case is set assuming directly pair-produced left (right) handed selectrons/smuons, decaying to an electron/muon and neutralino [163].

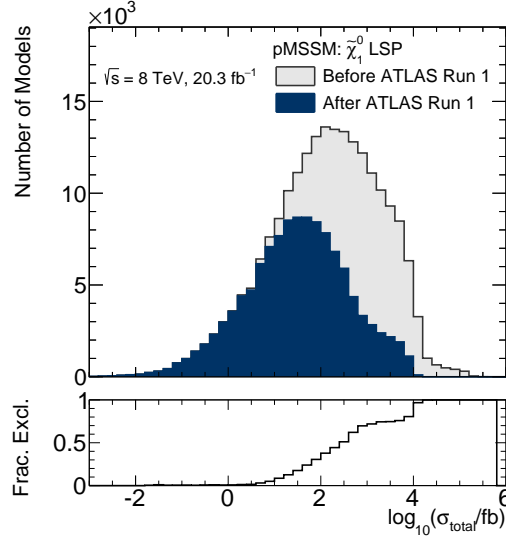


**Figure 4.11.:** Distribution of the total production cross-section for the production of SUSY particles before and after the combined ATLAS searches.

wino-dominated LSP with some Higgsino mixture, and the remaining 1/3 having a mixed bino-wino LSP, with the only kinetically accessible sparticles are the electroweakinos in both cases. This combination allows the charginos in these models to decay quickly enough to evade the Disappearing Track analysis, have light winos with a high production cross-section, but heavy enough winos to evade the direct electroweak searches. Many of these models will be discoverable by 13 TeV searches.

### 4.5.3. Dark matter

The nature of the LSP has a strong influence on the predicted relic density. SUSY models typically produce too much dark matter, unless there is some mechanism to reduce it. Therefore, imposing the constraint that the predicted relic density be smaller than the observed sculpts the initial mass spectrum of the LSP and also imposes the requirement that a mechanism exists for controlling the predicted relic density.

The effect of the relic density constraint can be seen in figure 4.13, which shows each of the pMSSM points projected onto the plane of the neutralino relic density,  $\Omega_{\tilde{\chi}_1^0} h^2$  versus the neutralino mass, colour coded by the dominant LSP contribution. This plot has several striking features. Firstly, the models with a wino- or Higgsino-dominated LSP

lie within two bands that are approximately straight on the logarithmic plot, which is cut off at  $m(\tilde{\chi}_1^0) \approx 100$  GeV. Wino- and Higgsino-like neutralinos are accompanied by an almost degenerate chargino, the mass of which was constrained by the LEP experiments to be  $m(\tilde{\chi}_1^\pm) > 103$  GeV [146]. The degenerate chargino acts to co-annihilate with the neutralino to reduce the relic density from the early universe, with the mechanism shown in figure 4.12(a). For both wino and Higgsino LSP models, the thermally averaged annihilation cross-section is expected to be proportional to the inverse square of the LSP mass, resulting in proportionality between relic density and the square of the LSP mass,  $\Omega_{\tilde{\chi}_1^0} h^2 \propto m(\tilde{\chi}_1^0)^2$  [147]. This also effectively limits the maximum mass of the neutralino to approximately 1 (2.5) TeV for models with pure Higgsino (wino) neutralinos; which corresponds to the case where the neutralino is the sole constituent of dark matter. The combined ATLAS searches were not sensitive to models with  $m(\tilde{\chi}_1^0) > 800$  GeV, and so if the neutralino is the sole constituent of dark matter, and is not bino-dominated, then SUSY would not have been discoverable at the 8 TeV LHC.

Equally striking in figure 4.13 are the stalactite-like structures in the region  $m(\tilde{\chi}_1^0) < 65$  GeV and the triangular structures for  $m(\tilde{\chi}_1^0) > 100$  GeV, corresponding to the bino-like LSP models. The reason for all of these structures is revealed by figure 4.14, which shows only the bino-LSP models projected onto the same plane as in figure 4.13 this time colour-coded according to annihilation mechanism. The two stalactite-like structures correspond to models where the neutralino is approximately half the mass of either the  $Z$  or Higgs boson, allowing resonant  $s$ -channel annihilation  $\tilde{\chi}_1^0 \tilde{\chi}_1^0 \rightarrow Z/h$ , in what is known as the  $Z$  and Higgs funnels. A diagram of this reaction is shown in figure 4.12(b). For this reaction to occur, the neutralino cannot be pure bino as some Higgsino component is required for the  $Z$  and  $h$  couplings; the reaction amplitude being proportional to the Higgsino component in the neutralino. Furthermore, the annihilation becomes more efficient as the neutralino mass approaches half the  $Z$  or  $h$  mass. These two effects yield the stalactite-like structure. As these models have the lightest neutralinos, they are also the most tightly constrained by the ATLAS searches. This is shown in figure 4.13 and figure 4.14, but is displayed more clearly in figure 4.15, which shows the mass distribution of the lightest neutralino before and after the ATLAS searches. Figure 4.15

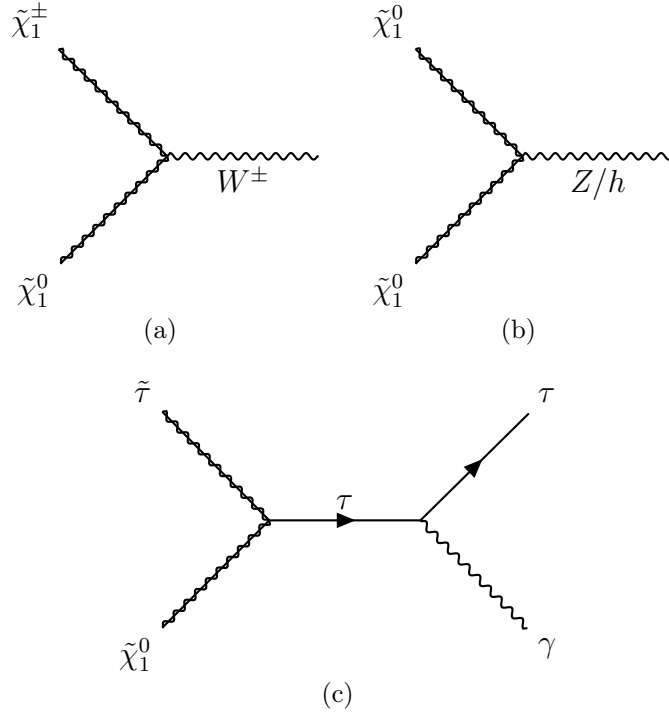


**Figure 4.12.:** Examples of annihilation and co-annihilation mechanisms that can reduce the dark matter relic density. Diagram (a) typically occurs for models with a wino- or Higgsino-dominated LSP as these naturally have a chargino that is degenerate with the neutralino, whereas diagram (b) is only possible for models with a bino-dominated LSP (with some Higgsino component) in the  $Z/h$  funnel. Diagram (c) is an example of stau co-annihilation, which may occur if the stau is sufficiently close in mass to the neutralino. Similar diagrams exist where the stau is replaced with another sfermion.

also highlights the limit of the sensitivity of Run-1 searches to the neutralino, as no models with  $m(\tilde{\chi}_1^0) > 800$  GeV are excluded.

Beyond  $m(\tilde{\chi}_1^0) > 100$  GeV the overlapping, triangular structures correspond to different types of co-annihilation, for example  $\tilde{\chi}_1^0 \tilde{\tau} \rightarrow \gamma \tau$ . The efficiency of the co-annihilation is related to the mass splitting, the coupling strength (the type of co-annihilator sparticle) and the mass of the neutralino [172], so the lower diagonal of the triangular structures are bounded by the maximally efficient annihilation mechanism. The vertical edges are bounded by constraints from previous experimental searches that were imposed during model generation. An example of such a co-annihilation mechanism is given in figure 4.12(c).

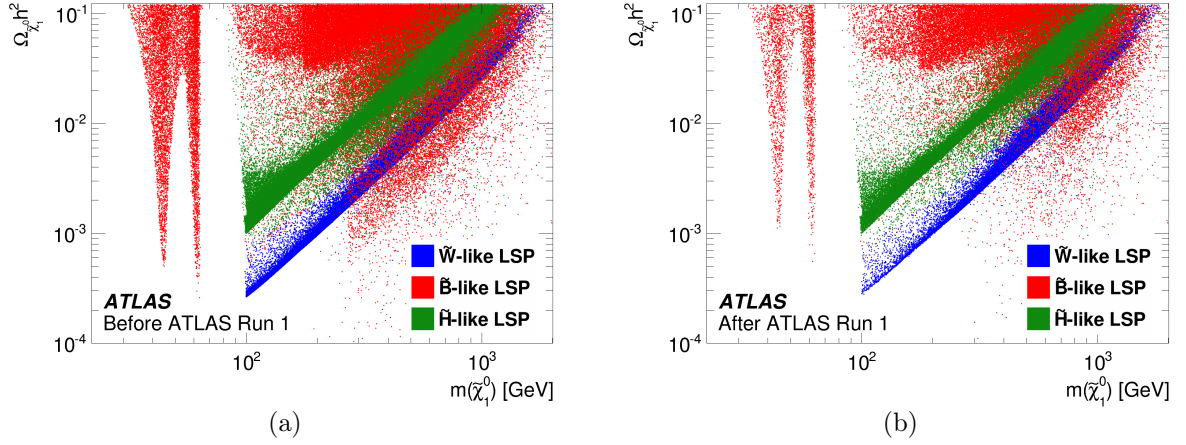


**Figure 4.13.:** The density of pMSSM points projected onto the plane of dark matter relic density versus LSP mass, before and after the constraints from the ATLAS searches. The colours code the dominant LSP type, as defined in table 4.4.

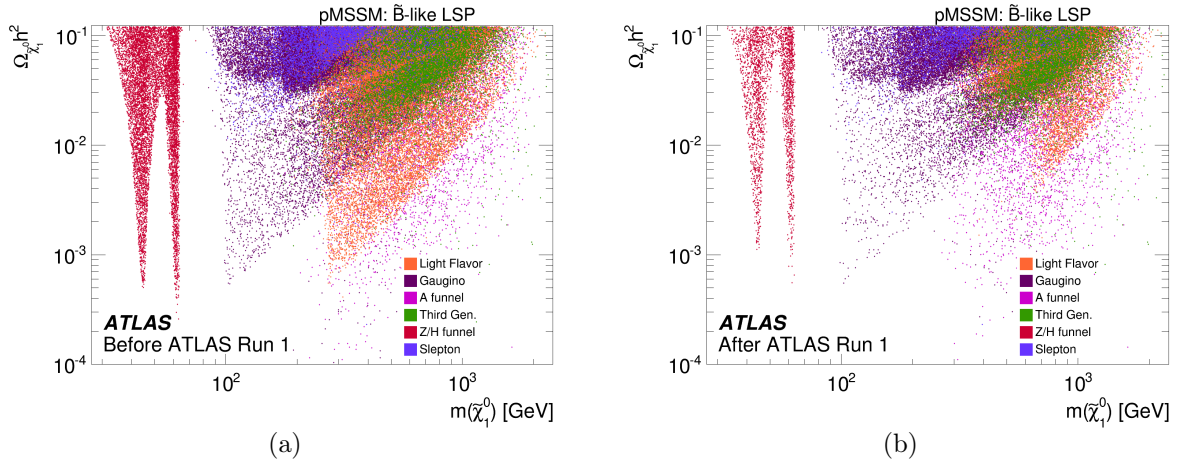


**Figure 4.14.:** The density of pMSSM points with a bino-dominated LSP projected onto the plane of dark matter relic density versus LSP mass, before and after the constraints from the ATLAS searches. The colours code the annihilation mechanism as described in the text. ‘Gaugino’ refers to electroweak gaugino coannihilation, while ‘Light Flavour’ refers to coannihilation either against squarks of the first two generations or against gluinos.

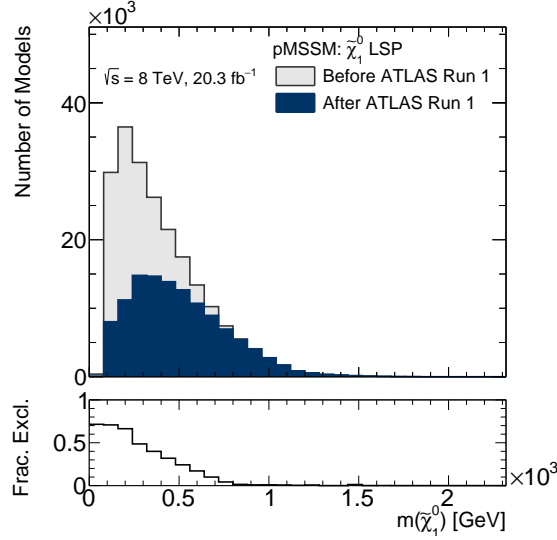


**Figure 4.15.:** The mass distribution of the lightest neutralino (the dark matter candidate) before and after the ATLAS searches.

#### 4.5.4. Higgs boson and precision observables.

The direct searches for new physics can be aided by precision measurements of other Standard Model particles. With the mass of the observed Higgs known, the Standard Model predicts all other properties with no free parameters, so any deviation from the prediction is evidence for new physics. For example, loop-contributions from virtual SUSY particles can alter low-energy observables, such as the coupling of the Higgs boson to other Standard Model particles and Higgs boson decay rates.

One specific example is the invisible decay of the Higgs boson. As the Higgs boson couples to mass, then the decay of the Higgs boson to a pair of new massive particles could occur with a rate discoverable at the LHC. If these particles were both stable and weakly interacting, this would give the signature of an invisible decay.<sup>7</sup> In the case of SUSY, if the LSP is sufficiently light (i.e.  $m(\tilde{\chi}_1^0) < m(h)/2$ ) then the decay  $h \rightarrow \tilde{\chi}_1^0 \tilde{\chi}_1^0$  can occur. As the LEP limits of  $\sim 100$  GeV on the mass of charged sparticles was applied during model generation, this decay is possible only if the LSP is bino-dominated, as the neutral winos, Higgsinos and sneutrinos are accompanied with a charged partner of similar mass.

<sup>7</sup>Note that the expected branching ratio of the Standard Model decay  $h \rightarrow ZZ^* \rightarrow 4\nu$  is  $\mathcal{O}(10^{-3})$ , which is much smaller than present uncertainties and therefore negligible in this context.

However, some Higgsino component is required in the LSP for the Higgs coupling. The invisible decay of the Higgs was not observed in the 8 TeV run of the LHC, and so limits were set on the branching ratio by ATLAS [173]. This in turn can be used to constrain the models in the pMSSM and the limits from the ATLAS search are overlaid on the distribution of  $\text{BR}(h \rightarrow \tilde{\chi}_1^0 \tilde{\chi}_1^0)$  in figure 4.16(a). The observed and expected limits, which are  $\text{BR}(h \rightarrow \tilde{\chi}_1^0 \tilde{\chi}_1^0) < 0.23$  and  $< 0.24$  respectively, disfavour around 1250 models, which corresponds to 14% of the models with a bino-dominated LSP and  $m(\tilde{\chi}_1^0) < 65$  GeV (this selection captures models where the invisible decay is possible). Figure 4.16(a) also shows that the models are more prevalent with smaller values of  $\text{BR}(h \rightarrow \tilde{\chi}_1^0 \tilde{\chi}_1^0)$ , meaning the discovery (or exclusion) of models where the invisible decay is possible will be difficult.

Combined fits by ATLAS to the measured Higgs boson production and decay rates are also used to constrain coupling scale factors

$$\kappa_i = \sqrt{\frac{\Gamma_h}{\Gamma_{h,\text{SM}}} \times \frac{\text{BR}(h \rightarrow ii)}{\text{BR}(h \rightarrow ii)_{\text{SM}}}}, \quad (4.3)$$

where  $\Gamma_h$  and  $\text{BR}$  represent the model prediction in the pMSSM of the total width of the observed Higgs boson and its branching ratio respectively, and a SM subscript indicates the Standard Model prediction. The parameter  $\kappa_b$  corresponds to the coupling of the Higgs field to  $b$ -quarks, with a value of unity for the Standard Model and any significant deviation from that being an indication of new physics. From the ATLAS fit at the time, the expected 95% CL range was  $|\kappa_b| < 1.8$  [174], which contains almost all the pMSSM points not already excluded by the direct searches and therefore the constraint from the expected limit is negligible. However, the corresponding observed 95% CL constrains the range  $|\kappa_b| < 1.2$  disfavouring models with  $\kappa_b > 1.2$ . These models typically have larger values of  $\tan \beta$  and smaller values of  $m(\tilde{b}_1)$ . As shown in figure 4.16(b), only a relatively small proportion of models are disfavoured by the observed limit (around 4% of all models generated), and the majority of models predict a value of  $\kappa_b$  close to unity.

There is no overlap between the models disfavoured by the  $\kappa_b$  measurement and those disfavoured by the Higgs boson invisible branching ratio. Furthermore, the indirect measurements were able to exclude models that the direct searches were not sensitive to.



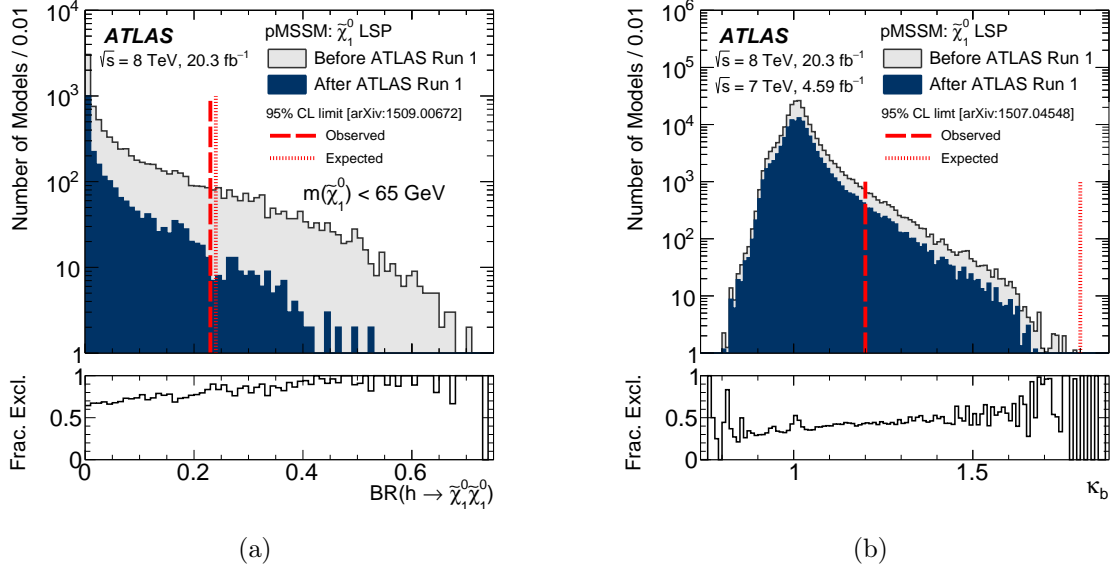


**Figure 4.16.:** Impact of the combined ATLAS searches on observables relating to the decays of the Higgs boson. The branching ratio of the Higgs boson to a pair of neutralinos is shown in (a), and (b) shows the Higgs  $b$ -quark coupling ratio  $\kappa_b$ . Only models with a bino-dominated LSP and  $m(\tilde{\chi}_1^0) < 65 \text{ GeV}$  are included in (a), whereas all models are included in (b). The dashed lines show the observed and expected upper bounds of the 95% confidence limits on those parameters.

This demonstrates that these indirect searches for new physics complement the direct searches in different ways by constraining different parts of the pMSSM space.

#### 4.5.5. Electroweak precision observables

Loop contributions from SUSY particles can also affect lower-energy observables. The measured values of several precision observables were taken as prior constraints on the pMSSM space sampled, as explained in section 4.2.2. Figure 4.17 shows the impact of the ATLAS searches on  $m(h)$ , and the branching ratios of  $B_s \rightarrow \mu\mu$ ,  $b \rightarrow s\gamma$  and  $B \rightarrow \tau\nu$ . The ATLAS searches have little direct sensitivity to  $m(h)$  and  $BR(B_s \rightarrow \mu\mu)$ , the former can be understood as the kinematic selections of SUSY searches will not be sensitive to changes in the mass of the Higgs boson of order 1 GeV. There is some dependence of the ATLAS sensitivity on  $b \rightarrow s\gamma$  and  $B \rightarrow \tau\nu$ , which can be seen as a slight increase in the sensitivity in the tails of the distribution of the former, and the lower-values of the

distribution of the latter. These models typically have lighter neutralinos and charginos, which are important to the loop-corrections to these quantities.

Figure 4.18 shows the number of models generated in the plane showing the difference between the Standard Model value of  $g_\mu - 2$  and the prediction from the pMSSM point, here referred to as  $\Delta(g_\mu - 2)$ , versus the lighter of the  $\tilde{\mu}_L$  or  $\tilde{\mu}_R$  mass. The hatched band overlaid shows the experimentally measured value  $\pm 1\sigma$  of the experimental uncertainty, taken from equations (19) and (1) of reference [133]. If confirmed, this experimentally measured value would be a powerful constraint on the pMSSM (as well as ruling out the Standard Model), as the majority of models have a value of  $g_\mu - 2$  close to the Standard Model expectation. Notably this band only overlaps a region where  $m(\tilde{\mu}) < 1 \text{ TeV}$ , indicating that such a measurement could be interpreted as evidence of a light smuon.

#### 4.5.6. Fine-tuning in the model set

The Barbieri and Giudice [67] measure of fine-tuning is chosen for this study, and is briefly described here. The electroweak symmetry breaking scale chosen was the  $Z$  mass, which is a function of the 19 parameters  $p_i$  ( $i \in \{1, \dots, 19\}$ ) in the pMSSM,  $M_Z^2 = M_Z^2(p_i)$ . We consider the relation

$$M_Z^2 = -2\mu^2 + 2 \frac{m_{H_d}^2 - \tan^2 \beta m_{H_u}^2}{\tan^2 \beta - 1} \quad (4.4)$$

where  $m_{H_{u,d}}^2$  are the doublet mass terms in the Higgs potential. Electroweak symmetry breaking is induced by radiative corrections, and this relationship is assumed to hold beyond tree level and include well-known radiative corrections [175]. These mass terms are functions of the parameters themselves,  $m_{H_{u,d}}^2 = m_{H_{u,d}}^2(p_i)$  and therefore we can calculate

$$Z_i = \frac{p_i}{M_Z^2} \frac{\partial M_Z^2}{\partial p_i} \quad (4.5)$$

directly. The fine-tuning parameter is then defined as  $\Delta = \max(|Z_i|)$ , such that any percentage change of a parameter  $p_i$  does not correspond to a percentage change of  $M_Z^2$

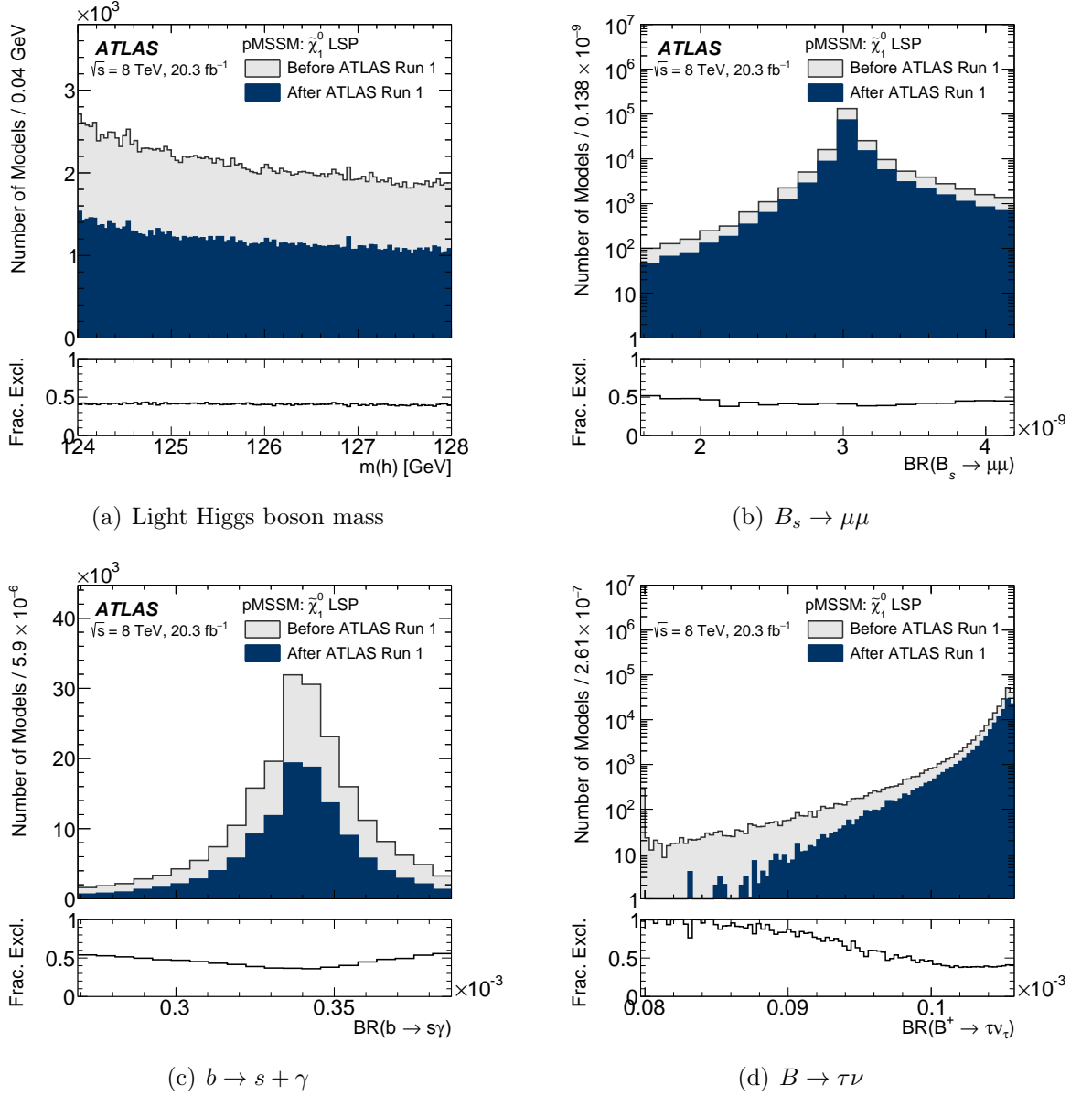


**Figure 4.17.:** Distributions of model points before and after applying ATLAS searches for various precision observables. Figure (a) shows the mass of the light (SM-like) Higgs boson,  $m(h)$ , (b) shows the branching ratio of  $B_s \rightarrow \mu + \mu$ , (c) is the branching ratio of  $b \rightarrow s + \gamma$  and (d) is the branching ratio of  $B \rightarrow \tau\nu$ .

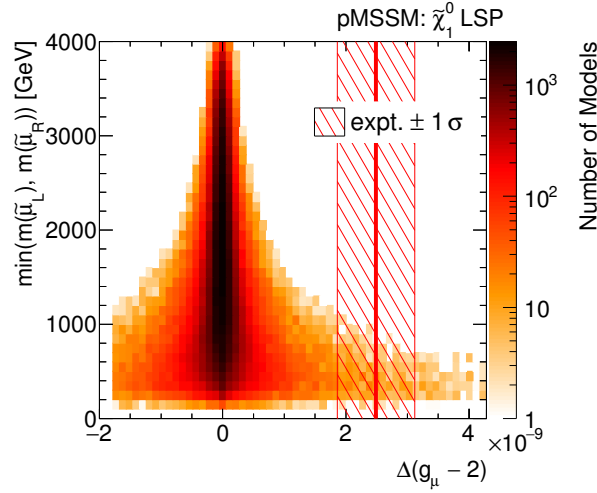


**Figure 4.18.:** Distribution of model points in the plane of the mass of the lightest left- or right-handed smuon versus  $\Delta(g_\mu - 2)$ . The experimental measurement is overlaid as the hatched band [133].

more than  $\Delta$  times larger. This definition does not take into account any correlations between the soft terms which can reduce fine-tuning.

Figure 4.19 illustrates the measure of fine-tuning before and after ATLAS exclusion. Overall, ATLAS searches are not sensitive to the measure of fine-tuning however, there is a tendency for models with smaller values to be rejected, leaving a set of less natural models after exclusion, in particular for bino models. It is the input parameters to the theory which control the shape of the distribution of fine-tuning. Interestingly, the largest contributor to  $\Delta$  in our models is the Higgsino mass parameter,  $\mu$  (which can have a value within the range  $80 < |\mu| < 4000$  GeV). The fine-tuning from this parameter arises at tree level, and is given by [175]

$$Z_\mu = \frac{4\mu^2}{M_Z^2} \left[ 1 + \frac{M_A^2 + M_Z^2}{M_A^2} \tan^2(2\beta) \right] \quad (4.6)$$

and therefore we can expect  $\Delta \propto \mu^2$ . The correlation between  $\Delta$  and  $\mu^2$  is shown in figure 4.20. That models with Higgsino LSPs (and hence small values of  $\mu$  parameter) still have large fine-tuning implies that  $\mu$  is not the only parameter contributing to fine-tuning. As discussed in section 4.3, in order to get a value of the Higgs boson mass within the range required by this study, large loop corrections are required. The dominant correction is from the stop and to maximise this correction (without extremely large stop

masses) significant mixing between the left and right handed stop quarks is required. This translates to large  $A_t$ , and is an additional source of fine-tuning in our models which first enters at leading-log as [175]

$$Z_{A_t} = \text{const } y_t^2 \frac{A_t^2}{M_Z^2} \frac{-\tan^2 \beta}{\tan^2 \beta - 1}, \quad (4.7)$$

where  $y_t$  is the top Yukawa coupling, and therefore we can expect  $A_t^2$  to be correlated with  $\Delta$ . The density of pMSSM models in the  $\Delta$ - $A_t^2$  plane is shown in figure 4.21 displaying correlation between these two variables, particularly for Higgsino-LSP models, although the correlation is not as strong as in the  $\mu^2$  case.

### Models evading searches

A number of model points with particularly low fine-tuning evaded the ATLAS searches, a selection of which are shown in figure 4.22 and figure 4.23. The model with the smallest fine-tuning (figure 4.22(a)) has wino-LSP, light Higgsinos and sub-TeV stops, the latter two features would be expected for a generic model with low fine-tuning. This model evades the Disappearing Track search as the mass splitting between the neutralino and chargino of the wino multiplet is large enough (1.6 GeV) such that the chargino lifetime is short enough ( $< 1$  ps) to be missed by the search. The other strongly interacting sparticles are also too heavy to have been discovered by the Run-1 searches.

The other models with low fine-tuning have similar properties. They all have light Higgsinos (typically a Higgsino LSP) and a stop around or below 1 TeV in mass. Furthermore, the strongly interacting particles are heavy enough to evade the Run-1 searches, in particular the gluino is heavier than 3 TeV in the models shown.

Aside from model points with a wino-dominated or a Higgsino-dominated LSP there also remain model points with low fine-tuning and a mixed LSP. For example, figure 4.23(a) shows a model point with a mixed bino-Higgsino LSP a so-called ‘well-tempered’ neutralino case [147]. This model has a bottom squark with mass of about 650 GeV, not far above the Run 1 direct search sensitivity.

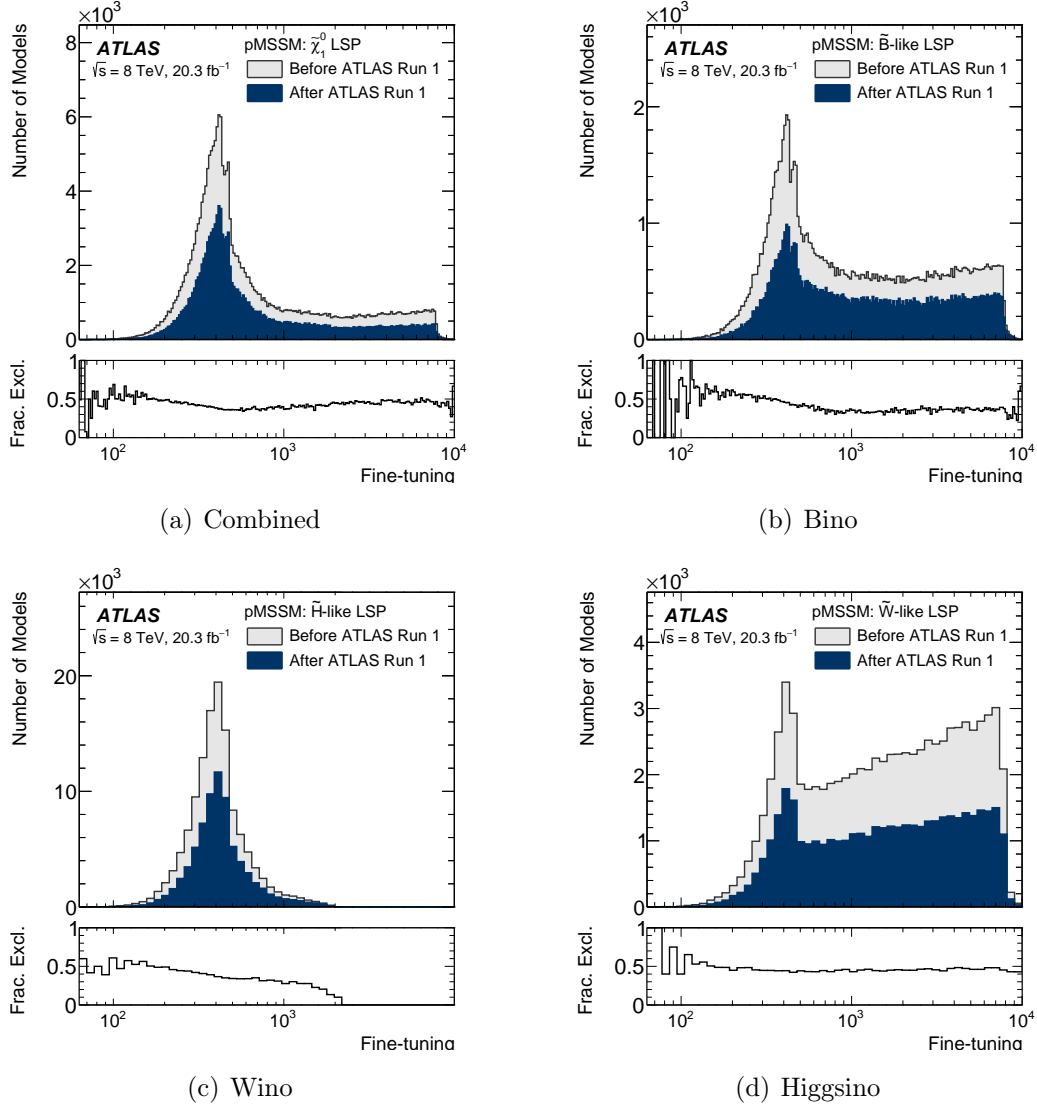


**Figure 4.19.:** Fine-tuning, before and after ATLAS exclusion. The second pad shows the ratio between the two histograms.

## 4.6. Conclusions

This chapter has presented a summary of the impact of the 8 TeV searches for SUSY carried out by the ATLAS collaboration during Run-1 of the LHC operation. The results were interpreted in the context of the 19-parameter pMSSM. The relevant dark-matter, heavy flavour and precision electroweak measurements were taken into account, and results were also presented in terms of those quantities. From an initial sampling of 500

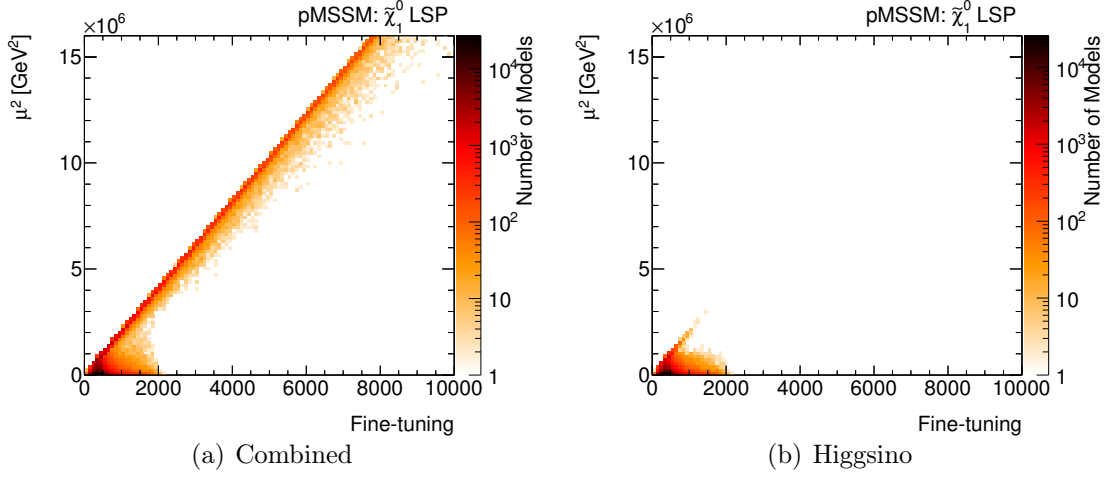


**Figure 4.20.:** Distribution of pMSSM points in the plane showing fine-tuning versus  $\mu^2$  for all models (left) and Higgsino-LSP models (right). The wino- and bino-LSP models have similar distribution to one another and make up the difference between the two plots.

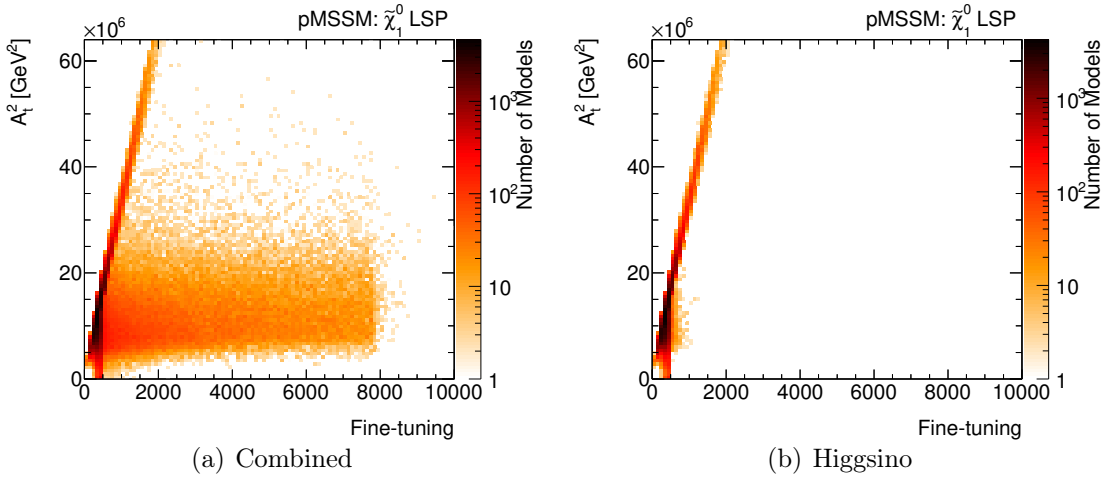
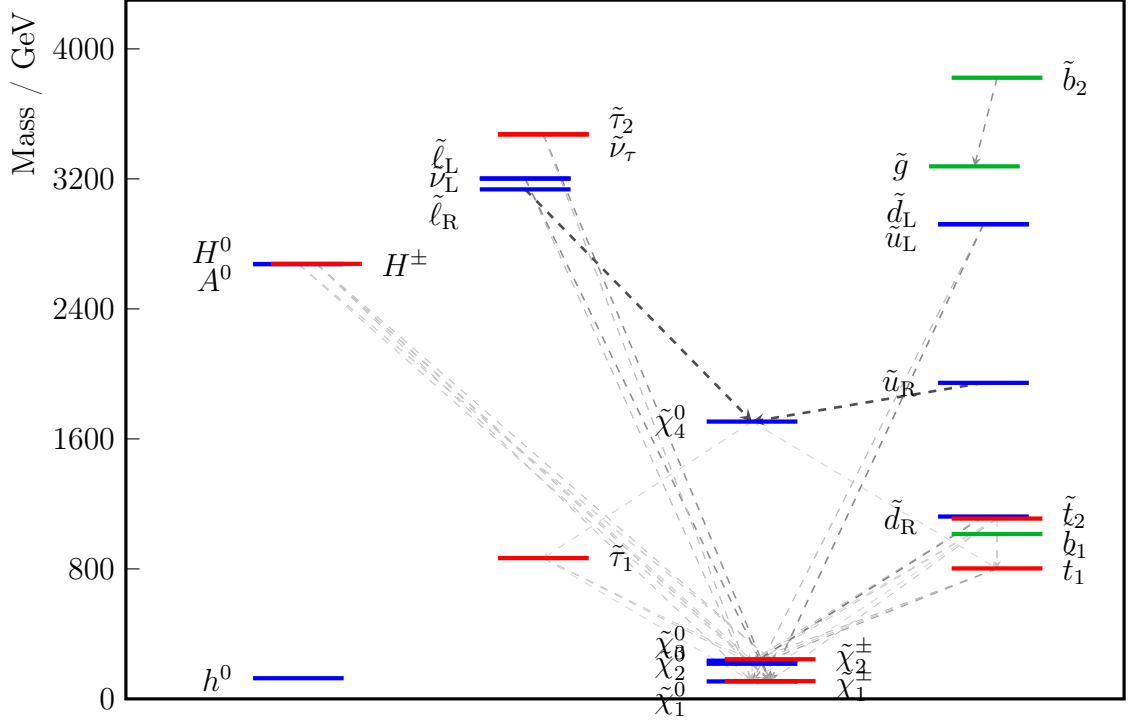


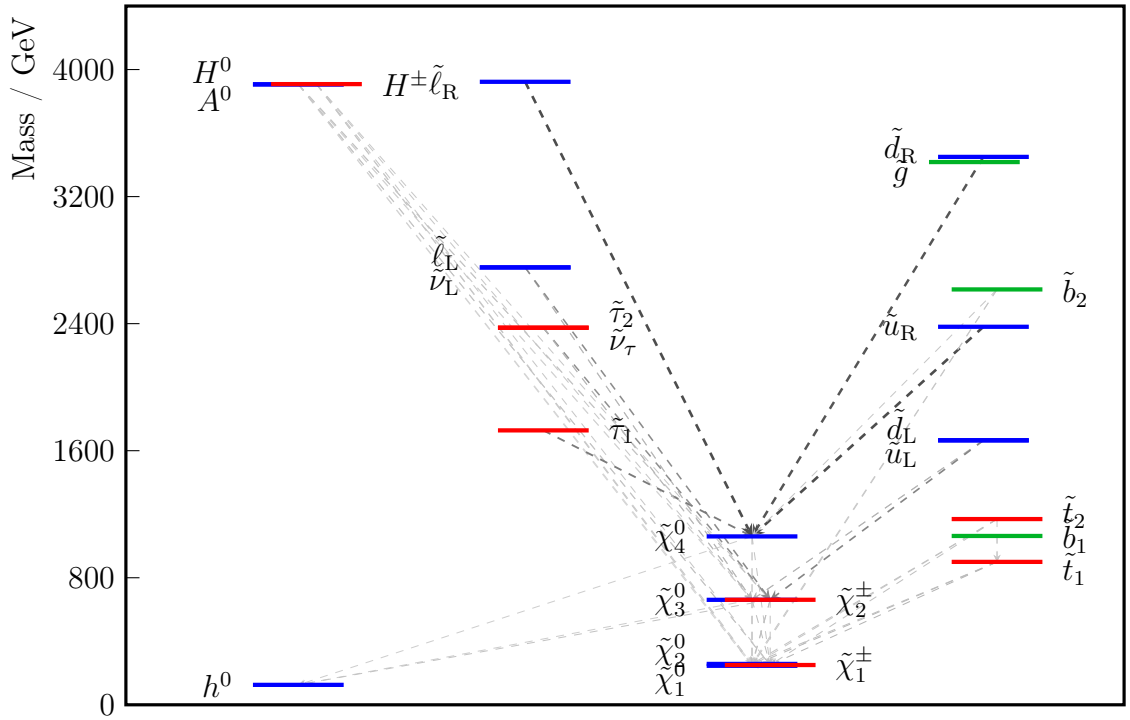
**Figure 4.21.:** Distribution of pMSSM points in the plane showing fine-tuning versus  $A_t^2$  for all models (left) and Higgsino-LSP models (right). The wino- and bino-LSP models have similar distribution to one another and make up the difference between the two plots.

million model points around 300,000 were selected and simulated, and a combination of 22 ATLAS searches for beyond the Standard Model (BSM) Higgs bosons, exotic particles and SUSY were utilised to assess the impact of ATLAS Run-1 on the pMSSM.

Several messages can be extracted from the results. There is a general congruence between simplified model limits and the exclusion in the pMSSM for strongly produced



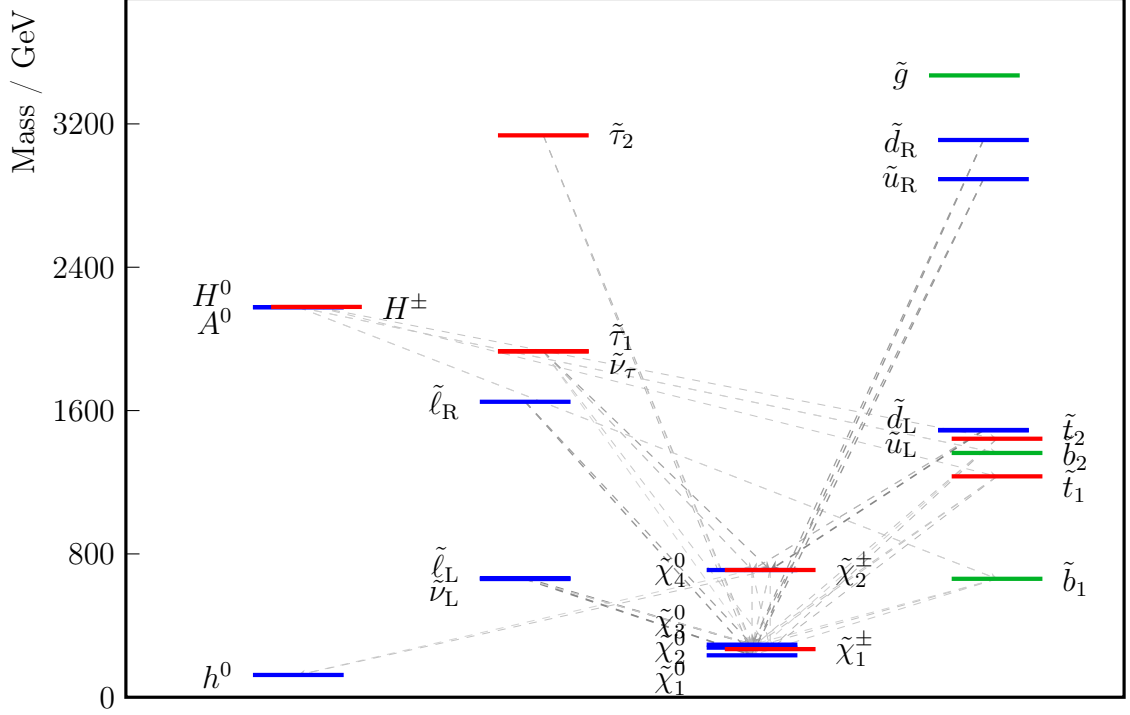
(a) Model point 18898934 (fine-tuning 56)



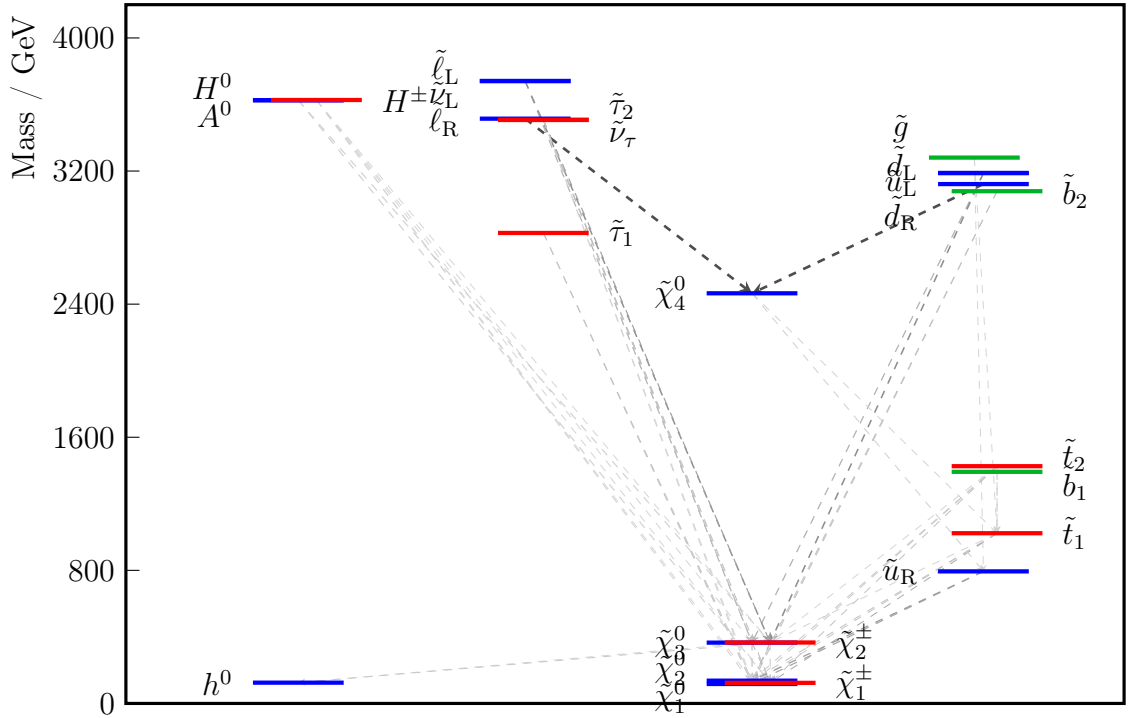
(b) Model point 10407816 (fine-tuning 57)

**Figure 4.22.:** Particle spectra for models with low fine-tuning that evaded the ATLAS searches. Figures produced using PySHLA [176].





(a) Model point 112647893 (fine-tuning 64)



(b) Model point 6755879 (fine-tuning 63)

**Figure 4.23.:** Particle spectra for models with low fine-tuning that evaded the ATLAS searches. Figures produced using PySHLA [176].

sparticles. However, the exclusion limits derived from simplified models are typically an over-estimate of the exclusion in the pMSSM, owing to the more complex production and decay mechanisms available with the increased particle content. In the case of particles with only electroweak interactions, such as sleptons, the agreement between the simplified model limit and the exclusion in the pMSSM is less good than in the strong production case.

Generally, the limits shown in the pMSSM, although not fully model-independent, can provide a more accurate picture of where the limits really lie. One example is for stops, where the simplified model limit excludes stops with masses less than 700 GeV, whereas in the pMSSM the limit is closer to 500 GeV. The nature of the LSP and also the handedness of kinematically accessible sparticles can have influence on the sensitivity of searches, which is often not captured by the simplified model approach. Furthermore, the interplay of indirect searches for SUSY (or BSM physics more generally), such as the search for the Higgs boson decaying invisibly and measurements of  $\kappa_b$ , can also constrain different types of models that are not accessible via direct searches.

Although the results of this study have now been superseded by 13 TeV searches the pMSSM study presented in this thesis will provide a legacy of the 8 TeV searches for several years to come. A summary of the sensitivity of ATLAS Run-1 searches to different particle masses is presented in figure 4.24.

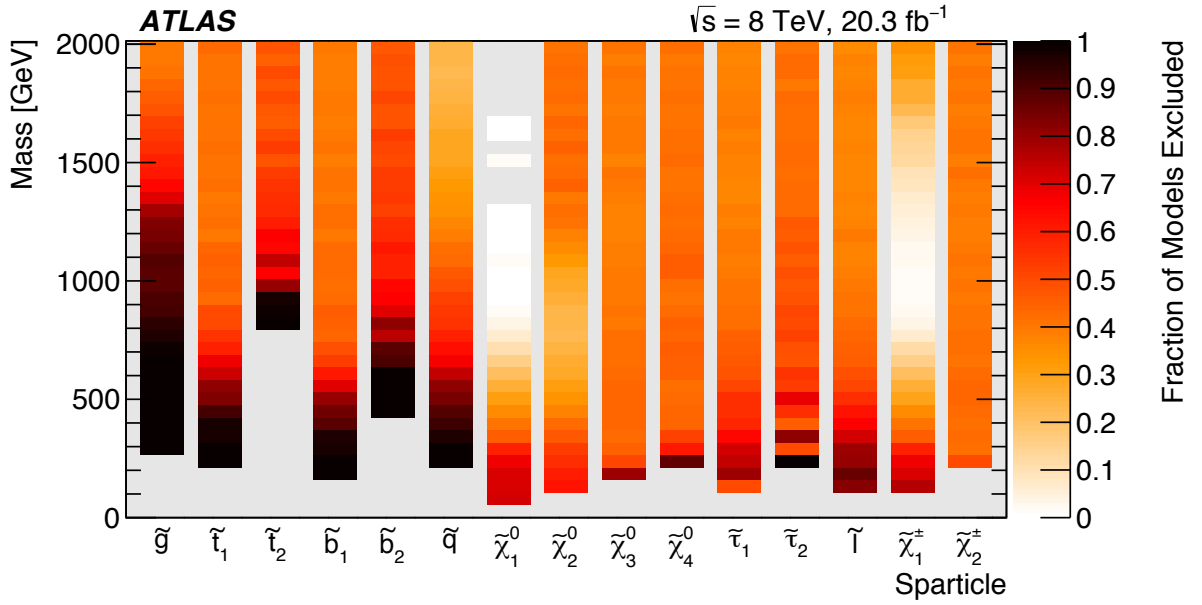


**Figure 4.24.:** The fraction of models excluded for each sparticle in the pMSSM, as a (binned) function of sparticle mass. The combination of models is shown (all LSP types), weighted as described in the text. One interesting feature that can be seen in the case of the  $\tilde{\chi}_1^\pm$ , where the fraction of model points decreases to almost 0 at 1 TeV and then increases again at around 1.5 TeV. This is because the chargino mass and neutralino mass are near degenerate in wino and Higgsino-LSP models, and so a heavy  $\tilde{\chi}_1^\pm$  means a heavy LSP. The decrease in sensitivity to the chargino mass around 1 TeV is an artefact of weighting the bino model points by a factor of  $1/24$ , because in bins around this region there are relatively few bino-LSP model points and so their contribution to the fraction of model points excluded is negligible. As the chargino mass increases, there are fewer model points with wino or Higgsino LSPs and so the fraction of model points excluded is then only representative of the bino-LSP models.

## 5 | Search for new phenomena in events with many jets

The main design goal of the LHC and the ATLAS detector is to search for new physical phenomena; either to solve some of the mysteries left open by the Standard Model, or to broaden the field by finding something new. One such search has already come to fruition, namely the discovery of the Higgs boson in 2012 by the ATLAS and CMS collaborations [32, 33]. However, many questions remain unanswered and currently, no evidence favouring new physics beyond the Standard Model has been found.

The study in this chapter focuses on the search for new physics in events with high jet multiplicity (or simply multi-jet events). Such final states can become relevant when one or more new particles are produced and decay via a cascade of other particles, which can be predicted by SUSY and other BSM theories [177–179]. One realisation of this is when the supersymmetric partner of the gluon, the gluino, is pair produced and each gluino cascade decays into a multitude of particles. A feature of these scenarios with longer decay chains is that they often do not produce large  $E_T^{\text{miss}}$ , which is at odds with the majority of experimental searches for SUSY – large  $E_T^{\text{miss}}$  being a smoking gun signature of many simpler SUSY scenarios. Therefore, the search discussed in this chapter also has a moderate  $E_T^{\text{miss}}$  selection and a different trigger strategy when compared to a more typical SUSY search.

Searching for new physics in events with high jet multiplicity has the benefit that the background from Standard Model processes is small, as high jet multiplicity processes are rare. However, such final states are difficult to predict theoretically and simulate

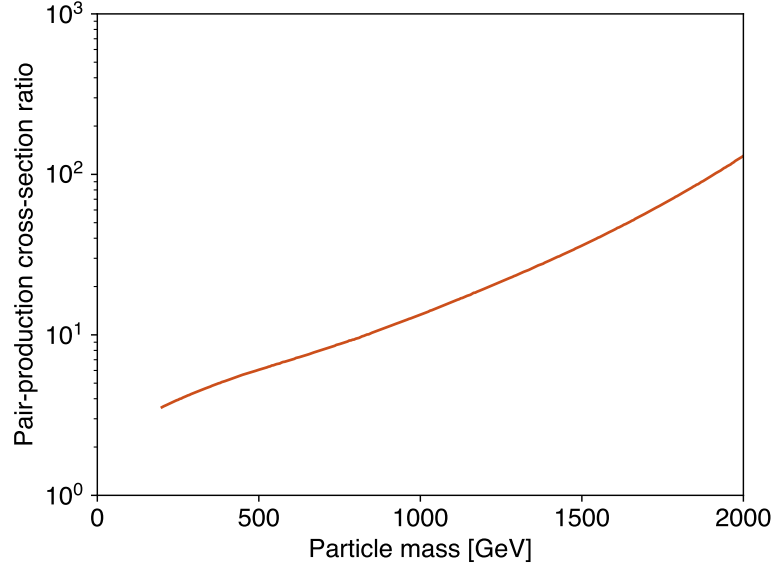


**Figure 5.1.:** Ratio of the gluino production cross-section from 8 to 13 TeV. Cross-sections calculated from reference [68].

with Monte Carlo, which adds extra challenges to the search. The solution is to use a data-driven technique to estimate the majority of the background.

Searching for the gluino was a high priority early in Run-2. It has the highest production cross-section of any SUSY particle for a given mass, as summarised by figure 2.8 on page 35, and so it is the most likely to be produced – given that nothing is known about the SUSY particle spectrum. This also means that limits on this particle from Run-1 were also the most stringent, as discussed in chapter 4 however, the heavier particles gain the largest boost in production cross-section when moving from a centre-of-mass energy of 8 to 13 TeV, as shown by figure 5.1, meaning the gluino is one of the best candidates for early discovery. As such a large increase in the centre of mass energy will not occur again for many decades, and total integrated luminosity doubled on a relatively short timescale, it was important to rapidly analyse the data and search for gluinos. This resulted in three publications with early Run-2 data, with 3.2, 18.2 and 36.1 fb<sup>-1</sup> of integrated luminosity, documented in references [4], [3] and [1] respectively. The second of these will be discussed in this chapter. The analysis strategy also builds upon previous searches carried out during Run-1 [149, 180, 181].

## 5.1. Analysis overview

The basic strategy of the analysis is to create *signal regions* with events containing at least 8, 9 or 10 jets (each with  $p_T > 50$  GeV) and no leptons. Further cuts are also made on the ratio of the missing transverse momentum to the square-root of  $H_T$ ,  $E_T^{\text{miss}}/\sqrt{H_T}$ , where  $H_T$  is the sum of the transverse momenta of the jets in the event, and finally  $M_J^\Sigma$ , which is the sum of masses of large-radius jets. Further details of the kinematic variables are given in section 5.3.3. The main challenge to the analysis is the estimation of the background, which is split into two categories: leptonic and non-leptonic. Once the total Standard Model background prediction is made, the data are compared to check for any statistically significant deviations, which would be evidence for new physics.

Even though events with leptons are vetoed, processes producing many jets and leptons can pollute the signal regions if the lepton is misidentified or falls out of acceptance of the detector. These backgrounds are estimated with Monte Carlo simulations, which are improved through the use of dedicated *control regions*. The control regions are kinematically close to, but distinct from, the signal regions by requiring similar kinematic selections but also exactly one lepton. The Monte Carlo estimate of the background is scaled to the data in the control regions using a fit, which fully takes into account correlations between systematic uncertainties; the results of which are used to scale the leptonic background estimation in the signal regions.

The majority of the background comes from fully hadronic processes, such as QCD multijet production. This cannot be estimated accurately via Monte Carlo techniques and so a bespoke data-driven background estimation technique is employed, first developed in reference [180]. Details of the QCD multijet extrapolation method, called the “template method” is described in section 5.5.

The final selection variable is the sum of the masses of reclustered large radius jets,  $M_J^\Sigma$ , which provides good separation between signal and background. In particular, it has the power to remove some of the  $t\bar{t}$  background, which is the largest of the leptonic backgrounds. Two cuts on this variable were made, optimised for different scenarios, which along with the different jet multiplicity requirement creates six signal regions.

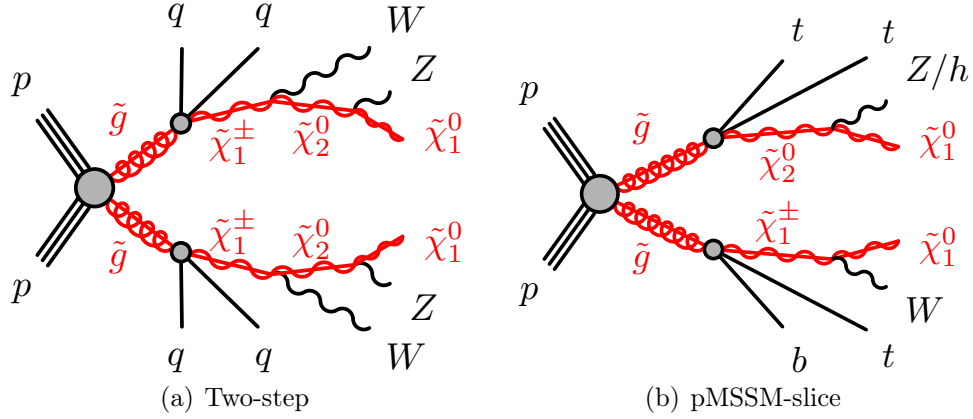


**Figure 5.2.:** Pseudo-Feynman diagrams showing benchmark signal processes used for interpretation and optimisation. No attempt is made to distinguish particles and their corresponding anti-particles. Diagram (a) was produced by collaborators.

## 5.2. Signal models

Many BSM scenarios predict final states with large numbers of jets and missing transverse momentum. The signal models discussed here were chosen to aid in the optimisation of the kinematic selection and also for interpretation of the results. Two models were chosen, both of which are SUSY models, although the analysis can be interpreted in terms of other BSM theories. The two models, named “two-step” and “pMSSM-slice” are shown schematically in figure 5.2 and are described below.

### 5.2.1. The two-step model

This is a classic simplified model, assuming the pair production of gluinos. Each gluino decays in a cascade involving two intermediate steps, hence the name. Both steps in the decay are fixed to occur with a 100% probability, and no other sparticles other than those considered are assumed to be kinematically accessible. The first step is the decay of the gluino via a virtual squark into a pair of first or second generation quarks and the lightest chargino. This is followed by the decay of the chargino to a  $W$  boson and the next-to-lightest neutralino  $\tilde{\chi}_2^0$ , which then subsequently decays to a  $Z$  boson and the

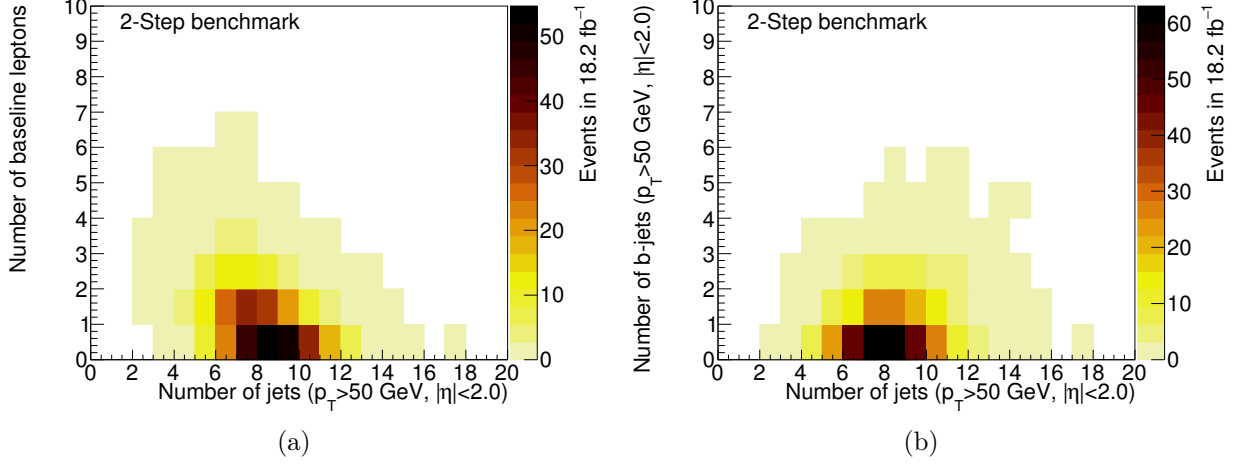


**Figure 5.3.:** Distributions of the number of jets versus (a) the number of baseline leptons, and (b) the number of  $b$ -jets from a benchmark two-step model with  $(m(\tilde{g}), m(\tilde{\chi}_1^0)) = (1400, 200)$  GeV. Basic event cleaning has been applied.

lightest neutralino.

$$\begin{aligned}
 \tilde{g} &\rightarrow q + \tilde{q}^* \\
 \tilde{q}^* &\rightarrow q + \tilde{\chi}_1^\pm \\
 \tilde{\chi}_1^\pm &\rightarrow W + \tilde{\chi}_2^0 \\
 \tilde{\chi}_2^0 &\rightarrow Z + \tilde{\chi}_1^0
 \end{aligned}$$

In this model, the only parameters that are varied are the gluino mass and the lightest neutralino mass. The intermediate masses  $m_{\tilde{\chi}_1^\pm}$  and  $m_{\tilde{\chi}_2^0}$ , are set to  $(m_{\tilde{g}} + m_{\tilde{\chi}_1^0})/2$  and  $(m_{\tilde{\chi}_1^\pm} + m_{\tilde{\chi}_1^0})/2$ , respectively. The Feynman diagram for this decay chain is shown in figure 5.2(a).

As shown in figure 5.3, the model is characterised by high jet multiplicity and low numbers of leptons. There are few  $b$ -jets in the model, due to the lack of heavy-flavour particles produced in the cascade decay.



### 5.2.2. The pMSSM slice

This model was inspired by the results of the large scan of the pMSSM, discussed in chapter 4 and in reference [6]. It was found that the Run-1 version of this analysis (see reference [149]) had unique sensitivity to a class of models with the following properties: a gluino with mass approximately 1.2 TeV, an intermediate Higgsino multiplet and a bino-like neutralino LSP with mass approximately 60 GeV, putting it close to either the Higgs boson or  $Z$  pole. The decay spectra of a representative pair of models from reference [6] are shown in figure 5.4. As the previous multijet analysis was uniquely sensitive, this means that it would be difficult to discover SUSY scenarios of this type by any other means, and therefore a model was created to aid in the study of, and search for, decays of this form. A “slice” of the pMSSM parameter space was formed by varying the gluino and Higgsino mass parameters ( $M_3$  and  $\mu$  respectively) and requiring the LSP to be a bino-dominated neutralino of mass 60 GeV ( $M_1 = 60$  GeV). The rest of the spectrum was set as follows:

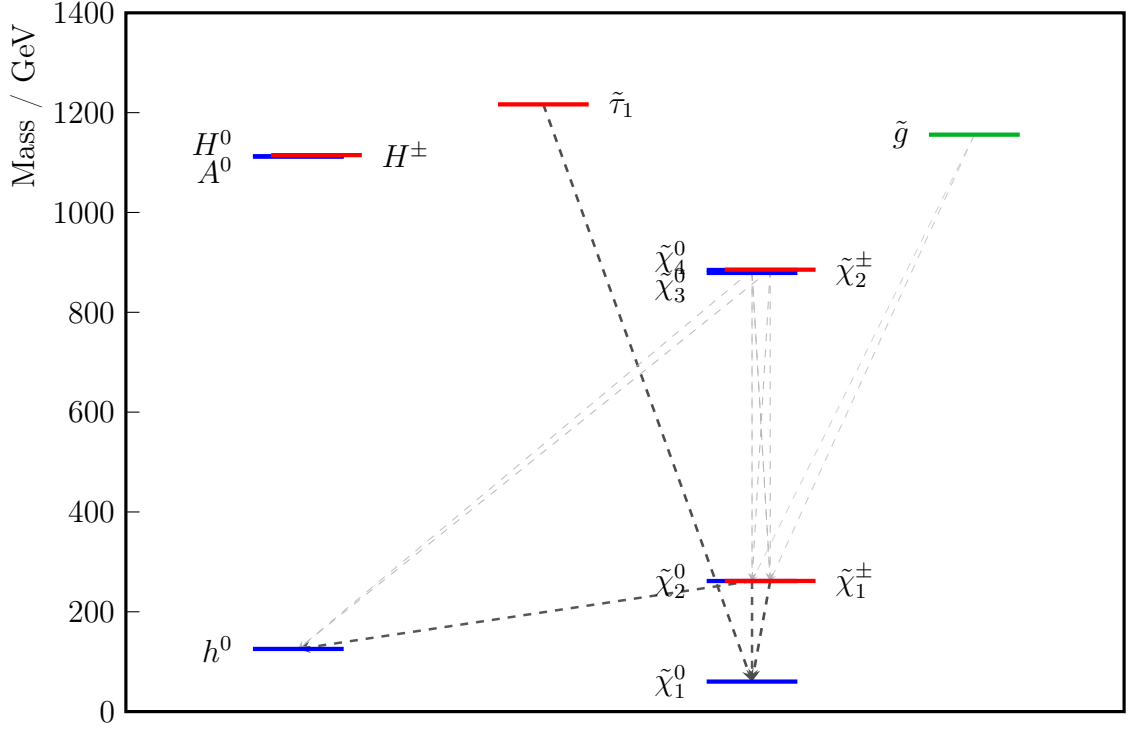
$$M_A = M_2 = 3 \text{ TeV},$$

$$A_\tau = 0,$$

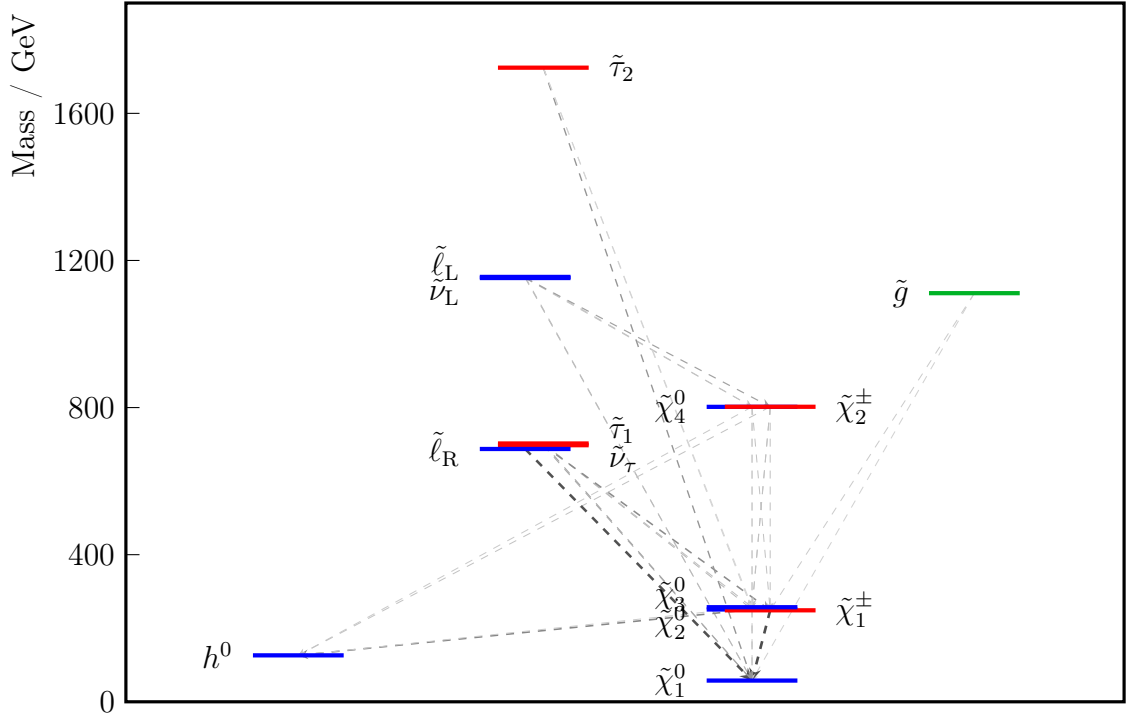
$$\tan \beta = 10,$$

$$A_t = A_b = m_{(\tilde{L}_1, \tilde{L}_2, \tilde{L}_3)} = m_{(\tilde{Q}_1, \tilde{Q}_2, \tilde{Q}_3)} = m_{(\tilde{e}_1, \tilde{e}_2, \tilde{e}_3)} = m_{(\tilde{u}_1, \tilde{u}_2, \tilde{u}_3)} = m_{(\tilde{d}_1, \tilde{d}_2, \tilde{d}_3)} = 5 \text{ TeV},$$

with the symbols defined in table 4.1. As the full set of pMSSM parameters is available in this model, it has predictive properties unavailable to simplified models typically used in ATLAS searches, including the two-step model. For example, the mass of the Higgs boson is correctly predicted at around 125 GeV and the bino-LSP can fully saturate the dark matter relic density (without over-saturation as the model has an LSP in the  $Z$ /Higgs funnel). Furthermore, the decays between the intermediate sparticles do not have fixed branching fractions, resulting in a more varied set of decays than would be found in a standard simplified model. Nevertheless, common features amongst the decays are seen and a typical set of branching ratios for models with chargino masses below



(a) Model point 141010615.



(b) Model point 208013200.

**Figure 5.4.:** The particle spectra for a pair of models taken from the pMSSM study described in chapter 4 and reference [6]. Particles with mass greater than 1.8 TeV are not shown, and decays with branching fraction  $< 0.1$  are not shown. Figures produced using PySLHA [176].

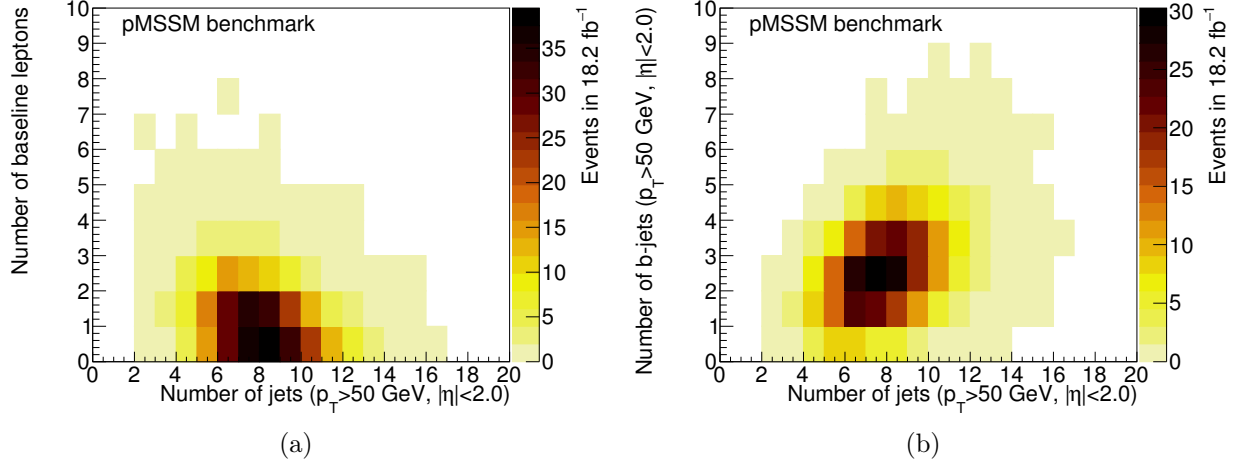


**Figure 5.5.:** Distributions of the number of jets versus (a) the number of baseline leptons, and (b) the number of  $b$ -jets from a benchmark pMSSM model with  $(m(\tilde{g}), m(\tilde{\chi}_1^\pm)) = (1400, 200)$  GeV. Basic event cleaning has been applied.

500 GeV and gluino masses above 1200 GeV are show below:

$\tilde{g} \rightarrow t + b + \tilde{\chi}_1^\pm$	(44%)	$\tilde{\chi}_1^\pm \rightarrow W^\pm + \tilde{\chi}_1^0$	(100%)
$\tilde{g} \rightarrow t\bar{t} + \tilde{\chi}_{2,3}^0$	(36%)		
$\tilde{g} \rightarrow q\bar{q} + \tilde{\chi}_1^0$	(10%)	$\tilde{\chi}_2^0 \rightarrow Z + \tilde{\chi}_1^0$	(58%)
$\tilde{g} \rightarrow t\bar{t} + \tilde{\chi}_1^0$	(3%)	$\tilde{\chi}_2^0 \rightarrow h + \tilde{\chi}_1^0$	(42%)
$\tilde{g} \rightarrow g + \tilde{\chi}_{2,3}^0$	(3%)		
$\tilde{g} \rightarrow b\bar{b} + \tilde{\chi}_1^0$	(1%)	$\tilde{\chi}_3^0 \rightarrow Z + \tilde{\chi}_1^0$	(90%)
$\tilde{g} \rightarrow b\bar{b} + \tilde{\chi}_{2,3}^0$	(1%)	$\tilde{\chi}_3^0 \rightarrow h + \tilde{\chi}_1^0$	(10%)

These branching fractions result in a large number of jets being produced from the gluino cascade decay, with many of these being  $b$ -jets from the direct decays of gluinos to  $b$ -quarks or from the subsequent decays of  $t$ -quarks. As shown in figure 5.5, the model is characterised by very high jet multiplicity and low numbers of leptons, although more leptons are present in this model than for the two-step due to the preponderance of  $Z$  and  $h$  bosons produced. There are additionally large numbers of  $b$ -tagged jets as expected, usually 2 or 3 for events with high jet multiplicity.

I created this model with a collaborator, Christopher Young.

### 5.3. Analysis strategy

Data were recorded between June–November 2015 and April–August 2016 by the ATLAS detector. After passing the selection of a good runs list (GRL), which is list of runs and luminosity blocks with high data-quality criteria as defined by the ATLAS Data Preparation team,  $18.2 \text{ fb}^{-1}$  of data were available for the search.

#### 5.3.1. Trigger

A collision event is only stored if it passes the selection of a trigger. The trigger decision is also simulated in MC, and therefore to maintain a consistent background estimation, the first cut that is applied is the trigger cut. This analysis relies on a single multijet trigger, denoted HLT\_6j45\_0eta240, which firstly requires 4 jets each with  $p_T > 15 \text{ GeV}$  at Level-1 and at HLT requires events to have 6 jets within  $|\eta| < 2.4$  each with  $p_T > 45 \text{ GeV}$ .

There are several advantages to using multijet triggers. Firstly, no  $E_T^{\text{miss}}$  requirement is made by the trigger, which allows this analysis to achieve lower  $E_T^{\text{miss}}$  thresholds than other SUSY searches, which in turn allows greater sensitivity to  $R$ -parity violating and non-SUSY BSM scenarios which produce little or no  $E_T^{\text{miss}}$ . The second advantage is multijet triggers have relatively low rate, which allows for lower  $p_T$  thresholds on the jets. This is important in *compressed* scenarios, where the directly produced SUSY particle (for example the gluino) is close in mass to the LSP, allowing limited phase space for any decay and thus lower  $p_T$  of any produced particles or jets. Such cases are typically difficult to find without dedicated searches.

The trigger is not fully efficient as jets at the HLT are not fully calibrated. Therefore an offline threshold of  $p_T > 50 \text{ GeV}$  is required to ensure the trigger selection is  $> 99\%$  efficient. Figure 5.6 shows the cumulative efficiency curves versus the sixth, seventh and eighth leading jet  $p_T$ . Table 5.1 shows the jet  $p_T$  threshold at which HLT\_6j45\_0eta240 becomes 90, 95, 99 and 99.5% efficient for the sixth, seventh and eighth leading jet. The selection is over 95% efficient for 6 jets, and over 99.5% efficient for 8 jets. The efficiency curves are calculated relative to a data set selected from events passing an orthogonal

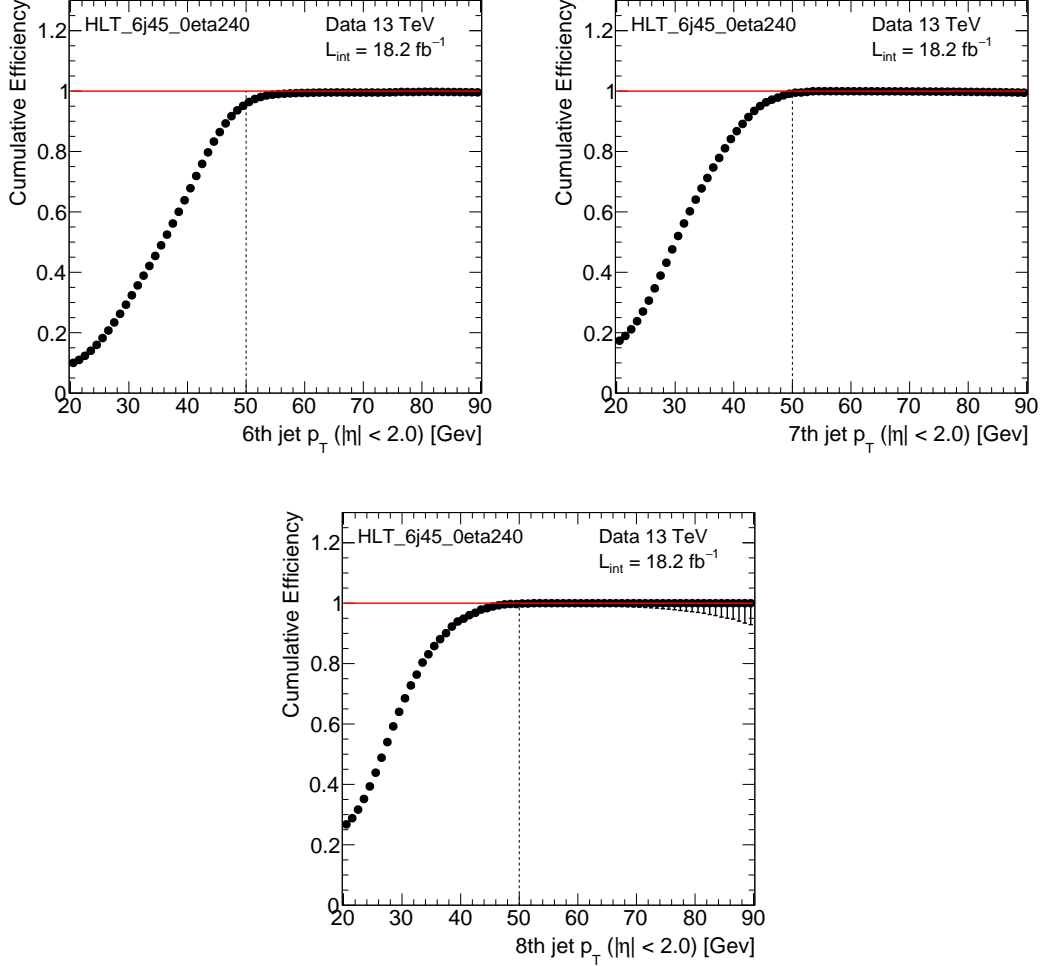


**Figure 5.6.:** Cumulative efficiency curves for HLT\_6j45\_0eta240, shown as a function jet  $p_T$  for various jet multiplicities. The top-left panel shows the sixth leading jet, the top-right panel shows the seventh, and the lower panel shows the eighth. The offline jet  $p_T$  threshold used in the analysis is shown by the vertical dashed line. The efficiencies were derived by

trigger, in this case the logical OR of the lowest unscaled electron and muon triggers, which both require one electron (or muon) at HLT with  $p_T > 26$  GeV.

The same trigger was used for both the signal and control regions, even though the control regions require a lepton. Lepton triggers could have been used, however the inefficiency of the lowest unscaled lepton triggers would have enforced tighter offline  $p_T$  cuts on the leptons, reducing the number of events useful for analysis.

Offline jet multi.	Jet $p_T$ threshold for efficiency [GeV]			
	90%	95%	99%	99.5%
6	46.8	49.4	55.5	62.3
7	41.9	44.5	49.3	50.9
8	37.5	40.6	45.8	47.2

**Table 5.1.:** The jet  $p_T$  threshold at which the trigger HLT\_6j45\_0eta240 becomes 90, 95, 99 and 99.5% efficient for the sixth, seventh and eighth leading jet.

### 5.3.2. Physics object definition

The physics objects used by analysis are designed to match as closely as possible to the physical particles or observables that they represent. The selections described here follow the recommendations of the corresponding ATLAS performance groups, and are designed to ensure they are well calibrated, efficiently triggered and allow high purity selection.

Electromagnetic calorimeter energy depositions will be reconstructed by the ATLAS reconstruction software as both jets and electrons simultaneously. This means the same group of signals can be classified as both a jet and an electron at the same time. First, a set of *baseline* objects are defined, which are used as inputs to an overlap removal procedure described below. After the object overlap removal, further requirements might be imposed to create the *signal* objects used in defining the analysis signal and control regions, as well as kinematic variables.

The Primary Vertex, tracks and the  $E_T^{\text{miss}}$  are as described in chapter 3.

**Jets** are reconstructed using the anti- $k_t$  reclustering algorithm with radius parameter  $R = 0.4$  and calibrated as described in section 3.4.4. Jets are classified as baseline if they have  $p_T > 20$  GeV and  $|\eta| < 2.8$ . The jet is further classed as signal if it passes overlap removal, and has  $JVT > 0.59$  (JVT is defined on page 138). Although this selection allows jets which are outside of the trigger  $\eta$  acceptance, signal region selection is sufficiently tight to ensure events are selected efficiently.

**$b$ -jets** are defined as signal jets with the stricter kinematic criteria  $p_T > 50$  GeV and  $|\eta| < 2.0$ , and have also been identified by the MV2c10 algorithm [182, 183] as containing a  $b$ -hadron. The algorithm produces a multivariate discriminant used for the classification of  $b$ -jets, and the selection used was designed to give a  $b$ -jet selection efficiency of 70% in simulated  $t\bar{t}$  events. This operating point rejects jets containing a  $c$ -quark, jets containing a  $\tau$  or jets originating from light-quark or gluons with rejection rates of 12, 55 and 381 respectively [183].

**Electrons** are classified as baseline if they have  $p_T > 10$  GeV and  $|\eta| < 2.47$ . They must satisfy a series of requirements on the shower shape, track hits and alignment of the tracks and calorimeter clusters, as outlined in reference [184] but optimised for 2015 data [185]; they are collectively referred to as *loose* criteria. To be classified as signal, electrons must pass overlap removal as well as more stringent criteria than above. Signal electrons must have  $p_T > 20$  GeV, satisfy the *tight* quality criteria and the *GradientLoose* isolation criteria, also described in reference [185]. Furthermore, signal electrons are required to have a longitudinal (transverse) impact parameter within 0.5 mm ( $5\sigma$ ) of the primary vertex.

**Muons** pass baseline selection if they have  $p_T > 10$  GeV and lie within  $|\eta| < 2.5$ . Baseline muons are required to pass the *medium* quality criteria requirements outlined in reference [186]. Only *combined* muons are considered that have tracks that were reconstructed independently from hits in the Inner Detector and Muon Spectrometer, as described in section 3.4. Muons are classified as signal if they pass the *GradientLoose* isolation working point [186], have  $p_T > 20$  GeV and have a longitudinal (transverse) impact parameter within 0.3 mm ( $3\sigma$ ) of the primary vertex.

**Large-radius jets** A collection of larger radius  $R = 1.0$  jets is created by feeding the smaller  $R = 0.4$  jets into a second iteration of the anti- $k_t$  algorithm. The jet four-vectors are used as inputs to the algorithm, and only jets passing the “signal” requirement described above are used, with a further restriction on  $|\eta| < 2.0$  being applied. When defining control regions, signal leptons are treated as jets in this

reclustering and their four-momenta are also included, provided they pass the same kinematic criteria as the jets ( $p_T > 20 \text{ GeV}$ ,  $|\eta| < 2.8$ ).

**Overlap removal** is performed using the baseline objects described above. The procedure is described sequentially as follows, and once an object is removed it is not considered further. Photons and taus are treated as jets.

1. If an electron and a muon share an inner-detector track, the electron is removed.
2. If a jet and an electron are within  $\Delta R = \sqrt{\Delta\phi^2 + \Delta\eta^2}$  of 0.2 the jet is removed, unless the jet is  $b$ -tagged (with an operating point of 85%), in which case the electron is removed.
3. If an electron and jet are within  $\Delta R = 0.4$ , the electron is removed.
4. If a muon track is ghost associated<sup>1</sup> to a jet, or a jet and a muon are within  $\Delta R = 0.2$ , then the jet is removed.
5. If a muon and a jet are within  $\Delta R = 0.4$ , the muon is removed.

### 5.3.3. Kinematic variable definition

Variables defined in this section are constructed only from the *signal* objects described in section 5.3.2.

**$H_T$**  The scalar sum of the  $p_T$  of all of the jets in the event that have  $p_T > 40 \text{ GeV}$  and  $|\eta| < 2.8$ ,

$$H_T = \sum p_T^{\text{jet}}. \quad (5.1)$$

In the leptonic control regions, leptons are treated as jets in the calculation of  $H_T$  if they meet the same kinematic criteria as the jets. The  $p_T$  and  $\eta$  thresholds were optimised in a Run-1 version of the analysis as part of the studies to improve the data-driven background estimation technique for the multijet background [187].

---

<sup>1</sup>Ghost association is described in section 3.4.4.



$E_T^{\text{miss}}/\sqrt{H_T}$  Referred to as the “ $E_T^{\text{miss}}$  significance”, this variable is used ubiquitously in this analysis. It is key to both the background estimation and the discrimination of signal from background, and is used in signal, validation and control regions. It has the observed property that the shape of the  $E_T^{\text{miss}}/\sqrt{H_T}$  distribution is invariant under changes in jet multiplicity in events where the  $E_T^{\text{miss}}$  is dominated by jet mis-measurement, which is an accurate assumption for events with many jets, and is the key feature of the background estimation technique, described in section 5.5.

The invariance of the shape under changes in jet multiplicity can be understood as the ratio  $E_T^{\text{miss}}/\sqrt{H_T}$  is closely related to the significance of the  $E_T^{\text{miss}}$ . For Gaussian resolutions, the true  $E_T^{\text{miss}}$  significance is a monotonic function of

$$(E_T^{\text{miss}})^2/2\sigma^2(E_T^{\text{miss}}), \quad (5.2)$$

where  $\sigma(x)$  is the resolution on  $x$  [188]. Given that  $E_T^{\text{miss}} = \left| -\sum \mathbf{p}_T^{\text{jet}} \right|$ , in events where  $E_T^{\text{miss}}$  is dominated by jet mis-measurement, then

$$\sigma^2(E_T^{\text{miss}}) \propto \sum \sigma^2(p_T). \quad (5.3)$$

The resolution of jet momenta,  $\sigma(p_T)$  is derived from the calorimeter energy resolution (given in section 3.2.4) can be approximated by  $\sigma(p_T) \propto \sqrt{p_T}$  over a large range. Combining this with eq. (5.3) then yields  $\sigma^2(E_T^{\text{miss}}) \propto \sum |\mathbf{p}_T^{\text{jet}}|$ , or equivalently:

$$\sigma^2(E_T^{\text{miss}}) \propto H_T, \quad (5.4)$$

which has also been observed empirically [189]. Finally, combining eq. (5.2) and eq. (5.4) we find that the true  $E_T^{\text{miss}}$  significance will be a function of

$$(E_T^{\text{miss}})^2/H_T, \quad (5.5)$$

which can be written as the more familiar  $E_T^{\text{miss}}/\sqrt{H_T}$ .

$M_J^\Sigma$  The sum of the masses all large-radius jets with  $p_T > 100$  GeV and  $|\eta| < 1.5$

$$M_J^\Sigma = \sum_j m_j^{R=1.0}. \quad (5.6)$$

Again, the  $p_T$  and  $|\eta|$  thresholds were optimised for a previous version of the analysis [149] however, optimisation studies performed by collaborators showed that this variable was optimal in extending the sensitivity of the analysis to models with larger gluino masses. The variable can be useful as a discriminating variable to reject  $t\bar{t}$  background.

**$m_T$**  The transverse mass,  $m_T$ , is only used in the 1-lepton control regions and is calculated from the  $p_T$  of the lepton, the  $E_T^{\text{miss}}$  and the angle between the  $E_T^{\text{miss}}$  and the lepton,  $\Delta\phi_{\ell, E_T^{\text{miss}}}$

$$m_T = \sqrt{2p_T^\ell E_T^{\text{miss}} [1 - \cos \Delta\phi_{\ell, E_T^{\text{miss}}}]} \quad (5.7)$$

For a semi-invisible decay of a particle, the distribution of  $m_T$  values has an end point at the mass of the parent particle. As a result, signal contamination in control regions can be effectively reduced by requiring an upper bound on  $m_T$ .

#### 5.3.4. Event cleaning

The cleaning cuts described below were applied to this analysis, and follow the recommendations of the relevant ATLAS performance groups unless stated otherwise. They are designed to ensure that the events analysed are free from detector problems, and that the particles originated from proton-proton collisions in the centre of the ATLAS inner detector. This is particularly important in searches for new phenomena, as some of the exotic features of their decays can easily be faked by detector effects.

Firstly, only runs and luminosity blocks in the GRL are selected. The remaining events are expected to be mostly free from hardware problems however, further cleaning is required on an event-by-event basis to remove any remaining problems. Events are removed where, for example, physics objects stray into regions of the detector that are no longer functioning or became inoperative at different moments of data-taking. These dead regions are small compared to the overall size of the ATLAS detector and so such cases are rare but can have a non-negligible impact on analyses. Other examples include environmental effects, which broadly consists of three subcategories: cosmic rays,

beam induced backgrounds and noise bursts. Cosmic rays are high energy particles, usually muons, that are created in the upper atmosphere by other immensely high energy particles, up-to  $\mathcal{O}(10^{19})$  eV, that can be created from supernovae of massive stars and active galactic nuclei [190, 191]. The particles that reach ATLAS can be coincident (within detector timing) with a beam crossing. Beam induced backgrounds refer to stray particles from the LHC beam traversing regions of the detector. The cuts to reject these backgrounds are discussed below and summarised in table 5.2. They remove around 0.1% of events that pass the GRL selection.

**Primary Vertex** Events with  $\leq 2$  tracks associated with the Primary Vertex are rejected, to reduce the effect of pileup through incorrect identification of the Primary Vertex.

**Cosmic muon** These muons arrive in ATLAS from above, mainly via the two large access shafts used for detector installation and pass through the ID with a rate of several Hz [192]. Events are rejected if they contain a muon passing overlap removal that has  $|z_0| > 1$  mm or  $|d_0| > 0.2$  mm.  $z_0$  is the distance in the  $r - z$  plane between the intersection of the track direction with the beam line and the primary vertex.  $d_0$  is the transverse impact parameter.

**Bad muon** A muon is flagged as bad if the relative errors on the combined muon charge-to-momentum ratio measurement,  $q/p$ , is larger (with some tolerance) than the corresponding measurement from the separate ID and the ME track fits. Such muons have significantly worse momentum resolution than those that pass the veto and in most cases show “pathological” behaviour. Often these are fake muons, which can be reconstructed from high hit multiplicities in the muon spectrometer due to a “punch-through” jet, or from badly measured ID tracks wrongly matched to muon spectrometer segments. This occurs rarely, however, a single mis-reconstructed muon can produce large fake  $E_T^{\text{miss}}$ . Events are vetoed if any baseline muon, before overlap removal, has a relative error on the charge-to-momentum ratio  $\frac{\sigma(q/p)}{|q/p|} > 0.2$ .

**Bad jet** Mis-identified jets from non-collision sources, commonly referred to as “fake jets”, need to be distinguished from “good” jets from  $pp$  collisions. Fake jets originate from three main sources [193]:

- Beam-induced backgrounds, where proton losses upstream of the detector induce cascades, leading to muons that reach the ATLAS detector. These muons can be reconstructed as jets with energies as high as the beam energy.
- Cosmic-ray showers, which mostly produce muons, but the muon is reconstructed as a jet.
- Fake signals in the calorimeter from large-scale coherent noise, or pathological cells.

Fake jets are identified through several methods. Quality criteria on pulse shapes in calorimeter cells and the fraction of jet energy in specific calorimeter regions can distinguish good jet activity from calorimeter noise. Energy ratio variables, such as the fraction of total jet energy deposited in the electromagnetic calorimeter can identify fake jets, which tend to be more longitudinally isolated in the calorimeters than good jets and have smaller electromagnetic fractions. Good jets contain charged hadrons that can be reconstructed by ID tracking system, and track based variables such as the fraction of the jet's  $p_T$  from tracks associated to the primary vertex can be used to identify fake jets.

Events are removed if any jet with  $p_T > 20 \text{ GeV}$  that passes overlap removal<sup>2</sup> meets any of the *LooseBad* criteria listed in reference [193].

**Jet Vertex Tagger and pileup suppression** The JVT is a multivariate discriminant based on the fraction of the total momentum of tracks in the jet which are associated with the primary vertex, and is designed to suppress additional jets from pileup interactions [194]. Events are removed when there is a jet with  $50 < p_T < 70 \text{ GeV}$ ,  $|\eta| < 2.4$ ,  $\text{JVT} < 0.64$  and with  $\Delta\phi(\text{jet}, E_T^{\text{miss}}) > 2.2$ . This selection was designed specifically for this analysis by collaborators, and is designed to remove events where pileup jets would significantly bias the  $E_T^{\text{miss}}$ .

**LAr, Tile and SCT errors** Events affected by LAr noise bursts and data corruption are vetoed. Similarly, events with corrupted information from the Tile calorimeter

---

<sup>2</sup>Overlap removal is required as electrons and photons can be reconstructed as jets, and have similar qualities to bad jets.

Name	Description
Data quality GRL	Events must be in time periods (luminosity blocks) included in the final 2015 or 2016 good runs lists
Good primary vertex	At least 2 tracks associated to the primary vertex
Cosmic muon	Reject events with muons passing overlap removal with $ z_0  > 1 \text{ mm}$ and $ d_0  > 0.2 \text{ mm}$
Bad muons	Events must not contain muons, before overlap removal, with $\sigma(q/p)/ q/p  > 0.2$
Bad jets	Reject events with jets fulfilling any of the <i>Loose-Bad</i> criteria of reference [193]
Jet Vertex Tagger	Reject events when there is a jet with $50 < p_T < 70 \text{ GeV}$ , $ \eta  < 2.4$ , $JVT < 0.64$ and with $\Delta\phi(\text{jet}, E_T^{\text{miss}}) > 2.2$
Bad Tile Cells	Reject events most affected by not-operational Tile calorimeter cells
LAr, Tile and SCT errors	Events with known errors in the LAr or Tile calorimeter or the SCT are vetoed

**Table 5.2.:** Summary of the event cleaning and data quality cuts.

are rejected. Events affected by the recovery procedure of the SCT from single-event upsets are also removed.

**Dead Tile cells** Some events have objects falling within non-operational tile calorimeter cells, which gives rise to fake  $E_T^{\text{miss}}$ . In particular of all jets with  $p_T > 50 \text{ GeV}$  and  $|\eta| < 2.0$ , if the jet with the smallest  $\Delta\phi$  between the jet and  $E_T^{\text{miss}}$  is in the dead tile region ( $0.1 < |\eta| < 1.0$ ,  $0.8 < \phi < 1.1$ ) then the event is vetoed. The kinematic requirements on the jets reflect those in the signal regions. The dead tile region was not simulated in MC, and so events satisfying the above selection were rejected in both data and MC.

### 5.3.5. Event selection

The final selection on events forms the signal regions. These are regions of kinematic space optimised to be enriched in the signal processes of interest, whilst simultaneously being as free from Standard Model background as possible. Once defined, the background composition is carefully estimated before making a comparison with the data yield. Any significant deviation of the data from the background prediction will be evidence for new physics.

The baseline selection was inspired by the 2012 version of this analysis, which used  $20.3 \text{ fb}^{-1}$  of 8 TeV data [4]. The 2012 analysis was split into two streams: the “flavour stream” and the “ $M_J^\Sigma$  stream”. Both streams required events with high jet multiplicity and a cut on  $E_T^{\text{miss}}/\sqrt{H_T}$ , but with differing cuts on other variables – the flavour stream selected events with various  $b$ -jet multiplicities and the “ $M_J^\Sigma$ ” stream sub-divided the analysis signal regions according to  $M_J^\Sigma > 340 \text{ GeV}$  and  $M_J^\Sigma > 420 \text{ GeV}$ . A re-optimised version of the flavour stream was performed with the  $3.2 \text{ fb}^{-1}$  of 13 TeV data collected in 2015, and published in reference [4], which left the  $M_J^\Sigma$  stream to be re-investigated with a larger dataset.

The increase of centre-of-mass energy from 8 to 13 TeV brought with it an increase in the production cross-section of not only the signal processes, but also the background processes too. This meant that even with less data ( $18.2 \text{ fb}^{-1}$  of 13 TeV data versus  $20.3 \text{ fb}^{-1}$  of 8 TeV data) re-optimisation of the signal regions was necessary. Firstly, several other transverse-mass variables (such as those described in reference [195]) were investigated as potential replacements to  $M_J^\Sigma$ , however studies performed by collaborators found  $M_J^\Sigma$  to be the most effective. Thus, the basic outline of the selection cuts remained broadly the same as in 2012 with some specific optimisations.

The optimisation procedure itself was performed with restricted access to the data. Data was not added to potential signal regions (*i.e.* high jet multiplicity regions with large  $E_T^{\text{miss}}/\sqrt{H_T}$ ) until the development stage was over and the background estimate was satisfactory. The procedure is usually referred to as *blinding* and is employed to remove any potential human bias in the design of the selection.

The signal regions used in this analysis are defined by a series of cuts on the objects and variables described in section 5.3.2 and section 5.3.3. Selections are made on the number of jets,  $M_J^\Sigma$  and finally  $E_T^{\text{miss}}/\sqrt{H_T}$  to define a total of six signal regions. The signal regions are also required to have no baseline leptons. The optimisation and definition of the specific cuts are described below, and summarised in table 5.3.

### Preliminary selection

The preliminary selection used for this analysis is the logical AND of the following:

1. Pass the Good Runs List selection.
2. Pass the triggers selection, which requires at least six jets each with  $p_T > 45 \text{ GeV}$  and  $|\eta| < 2.4$ .
3. Pass the event cleaning, described in section 5.3.4.

This preliminary selection applies to all events, not just those entering the signal region.

### Jets selection

The selection on the number of jets is one of the defining features of this search. The selection is designed to enhance the signal significance in the signal regions and ensure that the event selection is fully efficient with respect to the trigger. One can see immediately from figure 5.7(a) and (b) that the signal models have higher jet multiplicity than background processes. The jet multiplicity,  $n_{50}$  is defined as the number of signal jets with  $p_T > 50 \text{ GeV}$  and  $|\eta| < 2.0$ . The  $p_T$  threshold is motivated by the trigger selection and is as loose as possible without incurring trigger inefficiencies. Lower jet  $p_T$  thresholds are useful in searching for SUSY scenarios where the gluino and LSP are compressed and there is little phase space for the decay, resulting in lower jet  $p_T$ . The  $|\eta|$  restriction is designed to exploit two features of SUSY decays that are present in the pMSSM-slice and two-step models. Firstly, the fact that the massive gluino (or some other massive new particle) is likely to be produced close to threshold means it will have little momentum in the lab frame and hence will produce more central jets, whereas

the main backgrounds originate from much lighter progenitors that are more likely to be boosted longitudinally, giving rise to less-central jets. Secondly, SUSY production is dominated by  $s$ -channel processes, while for example  $t\bar{t}$ +ISR is predominantly produced through  $t$ -channel processes. Typically,  $s$ -channel processes have lower  $\Delta\eta$  between the jets. This also results in the  $p_T$  of jets produced from SUSY decays to be harder than their Standard Model counterparts. The fact that jets from SUSY decays are typically more central than from background processes and that they have a harder  $p_T$  spectrum can be seen in figures 5.7(c)–(f). The harder  $p_T$  spectrum at first implies that gains in sensitivity could be made from a higher threshold on the jet  $p_T$ . However the peak of the  $p_T$  distribution of the signal jets decreases with increasing jet multiplicity, and so for regions with a very high jet count, a tight  $p_T$  cut would be too aggressive and reduce the significance of the signal, as can be seen in figure 5.8.

Three separate thresholds are required on  $n_{50^\circ}$ :  $\geq 8$ ,  $\geq 9$  and  $\geq 10$ , which are further divided by cuts on  $M_J^\Sigma$ , described next.

### $M_J^\Sigma$ selection

The size of the background from  $t\bar{t}$  decays is second only to the multijet background. The selection on  $E_T^{\text{miss}}/\sqrt{H_T}$ , described next, is able to tackle most of the multijet background and so optimisation is possible by attempting to remove some of the remaining  $t\bar{t}$  background. The discriminating power of this variable is displayed in figure 5.9, showing the  $M_J^\Sigma$  distribution for signal processes and  $t\bar{t}$  background. Optimisation studies performed with collaborators found that harsher cuts on  $M_J^\Sigma$  improved the sensitivity of the analysis to models with larger gluino masses, but simultaneously reduced the sensitivity to models with larger neutralino masses. As a result, two cuts were chosen,  $M_J^\Sigma > 340 \text{ GeV}$  and  $M_J^\Sigma > 500 \text{ GeV}$ , the former to maintain sensitivity to models with large neutralino mass, and the latter to improve sensitivity to models with larger gluino mass.



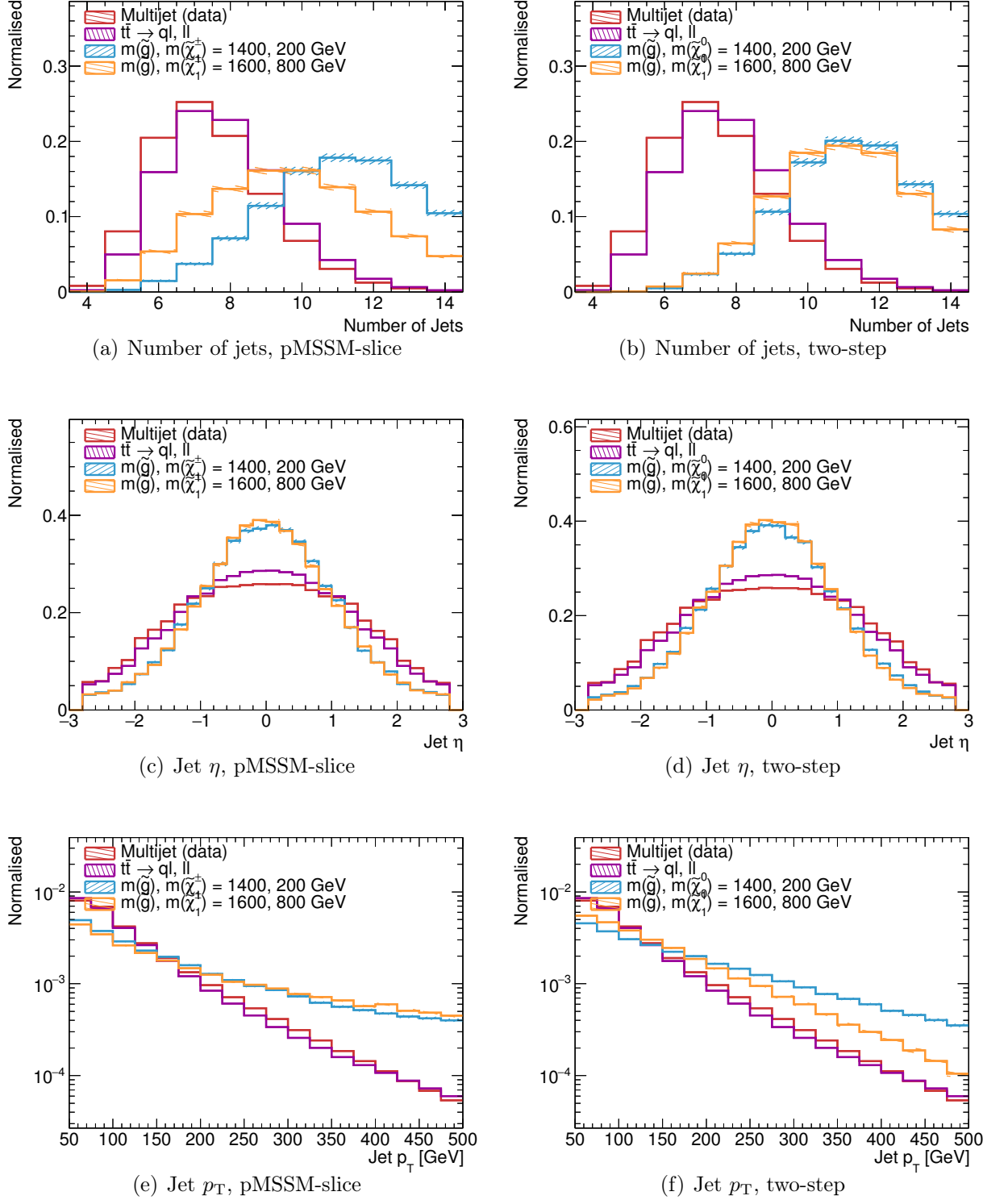


**Figure 5.7.:** Normalised distributions of  $\eta$ ,  $p_T$  and multiplicity of jets for a set of pMSSM-slice (left) and two-step (right) benchmark points. The jets have  $p_T > 20$  GeV,  $|\eta| < 2.8$  and pass the signal criteria described in section 5.3.2, and events pass the preliminary selection described in the text. The signal distributions and  $t\bar{t}$  background are from Monte Carlo simulation, whereas the Multijet component has come from data (with an additional selection requiring  $E_T^{\text{miss}}/\sqrt{H_T} < 3 \text{ GeV}^{1/2}$ ).

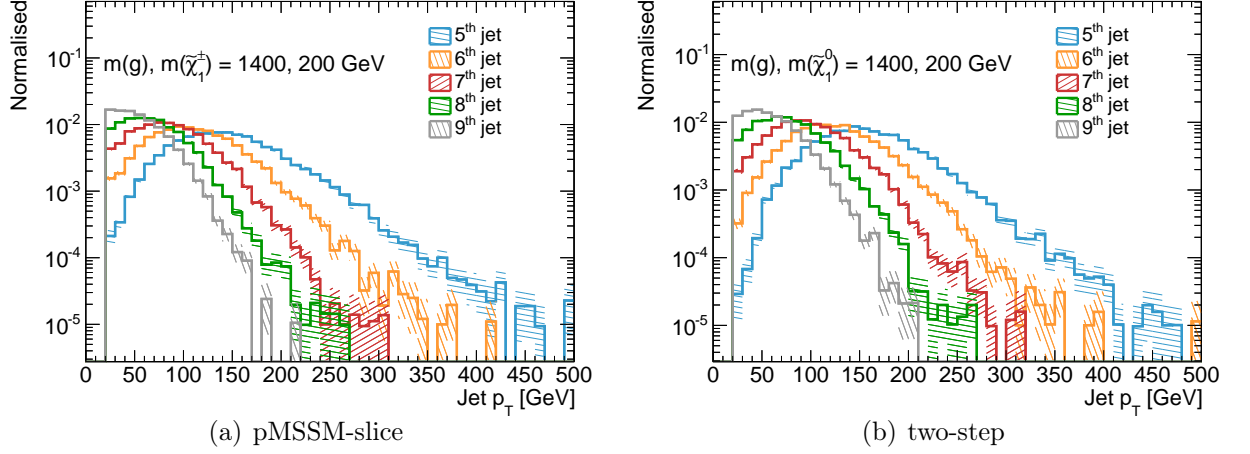


**Figure 5.8.:** Normalised  $p_T$  distributions of the 5<sup>th</sup>–9<sup>th</sup> jet for a benchmark pMSSM-slice model (left) and two-step model (right). Other details are as in figure 5.7.

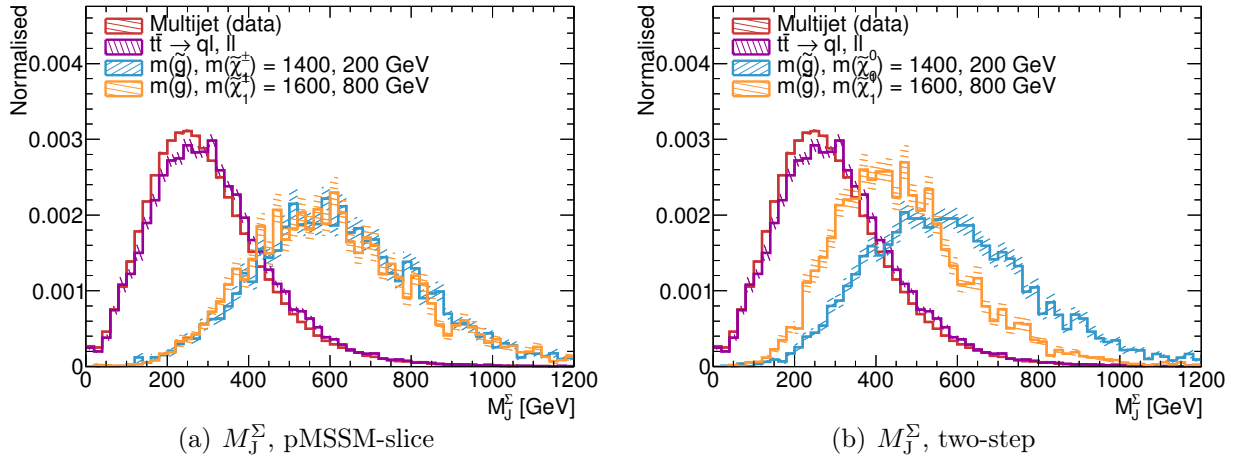


**Figure 5.9.:** Normalised distributions of  $M_J^\Sigma$  for a set of pMSSM-slice (left) and two-step (right) benchmark points. Events are selected after pre-selection and  $n_{50} \geq 8$ . The signal distributions and  $t\bar{t}$  background are from Monte Carlo simulation, whereas the Multijet component has come from data (with an additional selection requiring  $E_T^{\text{miss}}/\sqrt{H_T} < 3 \text{ GeV}^{1/2}$ ).

### $E_T^{\text{miss}}/\sqrt{H_T}$ selection

Even after requiring large jet multiplicity the QCD multijet background is still dominant. QCD multijet events typically have low  $E_T^{\text{miss}}$ , whereas the signal models both have a certain amount of  $E_T^{\text{miss}}$  from the non-interacting  $\tilde{\chi}_1^0$  and  $Z \rightarrow \nu\nu$  decays. Simply cutting on  $E_T^{\text{miss}}$  would therefore seem a good candidate to remove the multijet background however, multijet production is modelled too poorly in high jet multiplicity events to reliably calculate background rejection rates for given signal efficiency<sup>3</sup>. Furthermore, directly cutting on  $E_T^{\text{miss}}$  would reduce the sensitivity of the search to any  $R$ -parity violating scenarios. That multijet production cannot be well modelled by Monte Carlo methods also rules out cutting on any other variable to reduce the QCD backgrounds. The exception is  $E_T^{\text{miss}}/\sqrt{H_T}$ , as the shape of this variable can be used in a data-driven way to estimate the multijet background (as described in section 5.5). For signal regions, a value of  $E_T^{\text{miss}}/\sqrt{H_T} > 4 \text{ GeV}^{1/2}$  is required – providing a good balance between background rejection and signal efficiency.

### Summary of event selection

Cuts are made on jet multiplicity,  $M_J^\Sigma$  and  $E_T^{\text{miss}}/\sqrt{H_T}$  to define a total of six signal regions, as described above. The signal regions are summarised in table 5.3. Throughout this chapter, signal regions will be denoted by a short-hand nomenclature, such as SR-9j50-MJ340, which represents the signal region with at least 9 jets each with  $p_T > 50 \text{ GeV}$  and  $M_J^\Sigma > 340 \text{ GeV}$ . Signal regions only differ in the jet multiplicity and  $M_J^\Sigma$  cuts and so only these two values change in the short-hand string.

## 5.4. Leptonic background estimation

Standard Model multijet processes that also produce one or more leptons can contaminate the signal regions under certain circumstances. These backgrounds are collectively referred

---

<sup>3</sup>For an excellent discussion on this, see section 5.4 of reference [196].

Identifier	8j50	9j50	10j50
Jet $ \eta $	$< 2.0$	$< 2.0$	$< 2.0$
Jet $p_T$	$> 50 \text{ GeV}$	$> 50 \text{ GeV}$	$> 50 \text{ GeV}$
Jet Count	$\geq 8$	$\geq 9$	$\geq 10$
$M_J^\Sigma \text{ [GeV]}$	$> 340$ and $> 500$ for each case		
$E_T^{\text{miss}}/\sqrt{H_T}$	$> 4 \text{ GeV}^{1/2}$	$> 4 \text{ GeV}^{1/2}$	$> 4 \text{ GeV}^{1/2}$

**Table 5.3.:** Summary of the selection cuts defining the 6 signal regions.

to as *leptonic*, and events containing these processes can enter the signal regions if they somehow pass the lepton veto, as well as producing high jet multiplicity and  $E_T^{\text{miss}}$ . There are several cases where events including leptons can pass the lepton veto:

1. As only electrons and muons are rejected by the lepton veto, hadronically decaying  $\tau$  leptons, from top or  $W$  boson decays, can contribute to the signal regions. The  $\tau$  is treated as a jet, increasing the jet multiplicity and the  $\nu_\tau$  contributes to the  $E_T^{\text{miss}}$ .
2. Cases where electrons and muons are produced out of the detector acceptance. The missed lepton can contribute to the  $E_T^{\text{miss}}$ .
3. Events with electrons or muons that are mis-reconstructed. The missed lepton can contribute to the  $E_T^{\text{miss}}$ .
4. Decays of  $Z \rightarrow \nu\nu$ , where the  $Z$  boson is produced in association with jets. The neutrinos contribute to the  $E_T^{\text{miss}}$ .

Two processes dominate the leptonic background contribution to this analysis: partially leptonic decays of  $t\bar{t}$  and leptonically decaying  $W$  bosons produced in association with jets (henceforth “ $W$ +jets”). The contribution of these two processes to the signal regions is initially estimated with Monte Carlo simulation which is then improved by a global fit to data in dedicated control regions. The control regions are defined in section 5.4.3, and the fitting procedure in section 5.6.1. Other, subdominant processes that contribute to the leptonic background considered in this analysis are leptonically decaying  $Z$  bosons produced in association with jets (“ $Z$ +jets”), single top production, diboson production

( $WW$ ,  $WZ$  or  $ZZ$ ), and the production of  $t\bar{t}$  pairs in association with additional heavy particles – comprising three-top, four-top,  $t\bar{t} + W$ ,  $t\bar{t} + Z$ ,  $t\bar{t} + H$  and  $t\bar{t} + WW$  – collectively referred as “ $t\bar{t} + X$ ”. The contribution of these backgrounds to the signal region is determined solely from Monte Carlo simulation. The Monte Carlo simulation for all of the leptonic backgrounds is described in section 5.4.2. Systematic uncertainties on the backgrounds are also described in this section. These uncertainties can arise from two sources. On the one hand, there are uncertainties that may arise from the different theoretical approaches and approximations used to estimate the backgrounds. On the other hand, there are uncertainties related to the experimental measurement of objects and how well these are described by the simulations. These uncertainties are described in section 5.4.4 and section 5.4.5 respectively.

### 5.4.1. Description of the leptonic $t\bar{t}$ and $W + \text{jets}$ backgrounds

#### Top pair production

Leptonically decaying  $t\bar{t}$  pairs are the largest of the leptonic backgrounds. This is due to the large production cross-section of around 816 pb at  $\sqrt{s} = 13$  TeV [197] and the large number of jets produced from top decays. At the LHC around 90% of  $t\bar{t}$  pairs are produced from  $gg \rightarrow t\bar{t}$  processes and the remaining 10% from  $q\bar{q} \rightarrow t\bar{t}$ , for which the Feynman diagrams are shown in figure 5.10.

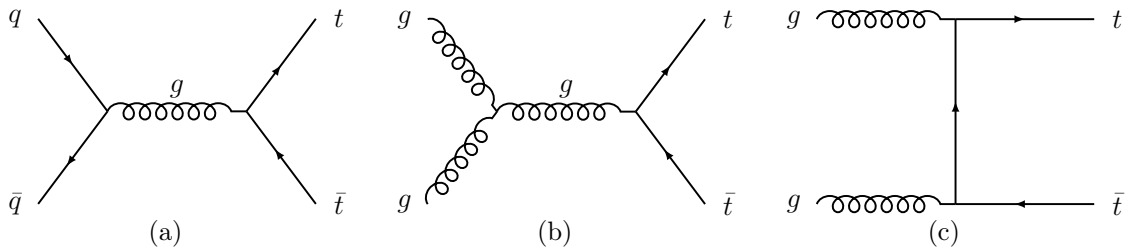


**Figure 5.10.:** Leading order Feynman diagrams for the production of  $t\bar{t}$  pairs.

The top quark decays almost exclusively to a  $W$  boson and a down-type quark (96% of the time this is a  $b$  quark [34] as the magnitudes of the  $V_{ts}$  and  $V_{td}$  elements of the CKM matrix are small). As the  $W$  boson can decay either hadronically to quark pairs or

leptonically, the decays of  $t\bar{t}$  pairs are categorised by the  $W$  boson decay and are divided into three classes:

Fully hadronic	$t\bar{t} \rightarrow W^+ b W^- \bar{b} \rightarrow q \bar{q}' b q'' \bar{q}''' \bar{b}$	45.7%
Semileptonic	$t\bar{t} \rightarrow W^+ b W^- \bar{b} \rightarrow q \bar{q}' b \ell^- \bar{\nu}_\ell \bar{b}$ or $\ell^+ \nu_\ell b q'' \bar{q}''' \bar{b}$	43.8%
Dileptonic	$t\bar{t} \rightarrow W^+ b W^- \bar{b} \rightarrow \ell^+ \nu_\ell b \ell' \bar{\nu}_{\ell'} \bar{b}$	10.5%

where the percentages indicate the branching fractions assuming lepton universality. The fully hadronic case is subsumed into the multijet background, described in section 5.5 and will not be commented upon further here. To a good approximation, the quarks produced in the semileptonic and dileptonic cases will each produce one jet, meaning these decays will produce 4 jets + 1 lepton and 2 jets + 2 leptons respectively. The loosest signal region requires at least 8 jets, and so several extra jets are required. These extra jets can come from ISR, FSR or fully hadronic decays of  $\tau$  leptons. Given that each extra jet from ISR or FSR occurs with a probability of order  $\alpha_s$  (about 0.1), it becomes clear why hadronic  $\tau$  decays from  $t\bar{t}$  production is one of the major sources of background. Even though the probability of the  $W$  boson producing a  $\tau$  that decays hadronically ( $\frac{\Gamma(W \rightarrow \tau \nu)}{\Gamma(W \rightarrow \ell \nu)} \times \text{BR}(\tau \rightarrow q \bar{q}' \nu) \approx 1/3 \times 0.65 \approx 0.2$ ) is only roughly twice that of  $\alpha_s$ , if an electron or muon are produced, or the  $\tau$  decays leptonically then those leptons must pass the lepton veto to remain in the signal region. A rough estimate of the number of  $t\bar{t}$  events with 8 jets  $N_{t\bar{t}}^{8 \text{ jets}}$  can be made. Considering the semileptonic mode will be dominant over the dileptonic mode and both (a) a  $\tau$  lepton is produced which decays hadronically or (b) all four extra jets being produced via ISR/FSR we find,

$$\begin{aligned}
N_{t\bar{t}}^{8 \text{ jets}} &\sim \sigma_{t\bar{t}} \cdot \mathcal{L}_{int} \cdot \text{BR}(t\bar{t} \rightarrow \text{semileptonic}) \cdot \alpha_s^3 \left[ \frac{\Gamma(W \rightarrow \tau \nu)}{\Gamma(W \rightarrow \ell \nu)} \cdot \text{BR}(\tau \rightarrow \nu q \bar{q}') + \alpha_s \right] \\
&\sim \mathcal{O}(10^3)
\end{aligned}$$

for an integrated luminosity  $\mathcal{L}_{int} = 18.2 \text{ fb}^{-1}$ . This estimate ignores detector acceptance effects and the analysis selection.

### **$W$ boson production in association with jets**

The second most-significant of the leptonic background is the production of  $W$  bosons in association with jets. The Feynman diagrams for the production of  $W + \text{jets}$  at leading order are shown in figure 5.11 and we see that only one jet is produced in association with the  $W$ . This means at least 7 extra jets must be produced in order for this process to contaminate the 8-jet signal region. Again these extra jets can be produced from ISR or FSR, or possibly from the hard splitting of the gluon in diagram 5.11(b). Given that each extra jet occurs with a probability of order  $\alpha_s$ , requiring at least 7 extra jets is an extreme region of phase space. However, the large production cross-section at  $\sqrt{s} = 13 \text{ TeV}$ ,  $\sigma_{W+\text{jets}} \approx 20000 \text{ pb}$  means we can still expect

$$\sigma_{W+\text{jets}} \cdot \mathcal{L}_{\text{int}} \cdot \alpha_s^7 \sim \mathcal{O}(10)$$

events with 8 jets, for  $\mathcal{L}_{\text{int}} = 18.2 \text{ fb}^{-1}$ . Again this approximation ignores detector and selection effects, but shows that this background can pollute the signal region in principle. Again, the extra jet produced from a hadronic  $\tau$  decay increases the above estimate as one fewer jet from ISR or FSR is required.

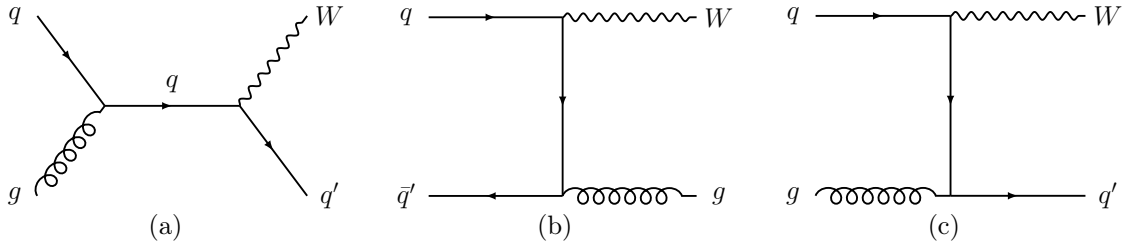


**Figure 5.11.:** Leading order Feynman diagrams for the production of a  $W$  boson in association with jets.

#### **5.4.2. Monte Carlo simulation**

Monte Carlo simulations are employed to aid in the estimation of the Standard Model background and predict signals, both for optimisation and limit-setting purposes. A different sample was used for each of the distinct backgrounds, and not always the same Monte Carlo generator was used for each. The simulations are discussed briefly here, and

specific details of the PDF sets, generators used and settings are described in reference [3]. In all cases, the response of the detector to particles is modelled with an simulation of the ATLAS detector [198], either based fully on **Geant4** [199] or in the case of signal models a fast simulation based on a parametrisation of the performance of the ATLAS electromagnetic and hadronic calorimeter [200].

As the average number of interactions per bunch crossing in the 2016 data taking was 24 (with a maximum around 50), it is important to take this into account, as the additional hadronic activity can degrade the measurement of jet energies and  $E_{\text{T}}^{\text{miss}}$ , reducing the effectiveness of vertex finding and directly generate extra jets [107]. The effect of multiple  $pp$  interactions (pile-up) is not included in Monte Carlo generation and so pile-up was taken into account by overlaying each event with multiple  $pp$  collisions simulated with soft QCD processes. Furthermore, out-of-time pile-up is modelled in the simulation by overlaying soft QCD processes in previous bunch crossings.

During data-taking, computing resources are insufficient to generate all of the Monte Carlo needs of the collaboration, therefore simulation is completed before the start of data-taking. This means the pile-up distribution is not known at the time of generation, and a best-guess is made based on predictions of the LHC performance. The simulations are then weighted post facto such that the pile-up conditions match those of the data.

Seven distinct groups of leptonic background relevant to this analysis were simulated:  $t\bar{t}$ ,  $W + \text{jets}$ ,  $Z + \text{jets}$ , diboson processes, single top production,  $t\bar{t} + X$  and  $t\bar{t} + h$ , and are described below.

- The production of  $t\bar{t}$  pairs (both semileptonic and dileptonic), was simulated using **Powheg** [201,202] interfaced with **Pythia6** [203].
- The production of  $W + \text{jets}$  and  $Z + \text{jets}$  were both simulated with **Sherpa 2.2** [204].
- Diboson processes, including the production of  $WW$ ,  $ZZ$  and  $WZ$  pairs were simulated with **Sherpa 2.1**.
- Single top-quark production was simulated using **Powheg** [201,202] interfaced with **Pythia6** [203].



- Events containing  $t\bar{t}$  and additional heavy particles – collectively referred to as  $t\bar{t} + X$  – comprising three-top, four-top,  $t\bar{t} + W$ ,  $t\bar{t} + Z$  and  $t\bar{t} + WW$  production are simulated at leading order using **MadGraph5** [205] with up to two additional partons in the matrix element, and interfaced to **Pythia8**.
- In addition to  $t\bar{t} + X$ ,  $t\bar{t} + h$  events are simulated at next-to leading order using **MadGraph5\_aMC@NLO** [205] interfaced with **Pythia8**. This background could have been subsumed into the  $t\bar{t} + X$  category above, but was treated separately in the analysis.

### 5.4.3. Control regions

The Monte Carlo prediction of the major backgrounds can be improved through the use of a simultaneous fit to data. This fit is performed in a series of control regions which are designed to be kinematically close to the signal regions yet free from signal processes, and the normalisation factors derived from the fit are carried over to the signal regions. Control regions must therefore be designed to be enriched in one of the background processes of interest, and have data and Monte Carlo yields large enough to provide good statistical precision.

For each signal region two control regions are designed, one each to control the  $t\bar{t}$  and  $W + \text{jets}$  backgrounds separately, denoted **CRT** and **CRW** respectively. Each control region is designed to be as close to signal region that it controls, and so the kinematic selection is similar. The control regions require the same event cleaning and pre-selection as events entering the signal regions (including the same trigger selection) but require exactly one lepton (electron or muon), where the “signal” definitions of the leptons from section 5.3.2 is used. To mimic the signal regions, the leptons are treated as jets – that is, they are included in the calculation of  $H_T$  (and therefore also  $E_T^{\text{miss}}/\sqrt{H_T}$ ) and the jet count if the leptons pass the same kinematic criteria as the jets. The jet  $p_T$  and  $|\eta|$  requirements are the same as the signal regions. In order to remove signal contamination an additional  $m_T < 120 \text{ GeV}$  cut is applied, as shown in figure 5.12. The  $M_J^\Sigma$  cut is the same as the signal regions. The jet multiplicity requirement (potentially including a lepton)

is one fewer than the signal region, and the requirement on  $E_T^{\text{miss}}/\sqrt{H_T}$  is relaxed to  $E_T^{\text{miss}}/\sqrt{H_T} > 3 \text{ GeV}$  – both of these are designed to increase the data yield in the control regions. Finally, the control regions are then split by requiring exactly 0  $b$ -jets for the  $W + \text{jets}$  region, and at least one  $b$ -jet for the  $t\bar{t}$  region. This resulted in a total of 12 control regions, which are summarised in table 5.4. Distributions of the number of jets in some of the control regions are shown in figure 5.13. The purity of  $W + \text{jets}$  in the CRW regions is low due to the  $t\bar{t}$  contamination. The simultaneous fit to the control regions takes this into account, and also normalises the  $t\bar{t}$  component in the CRW regions.

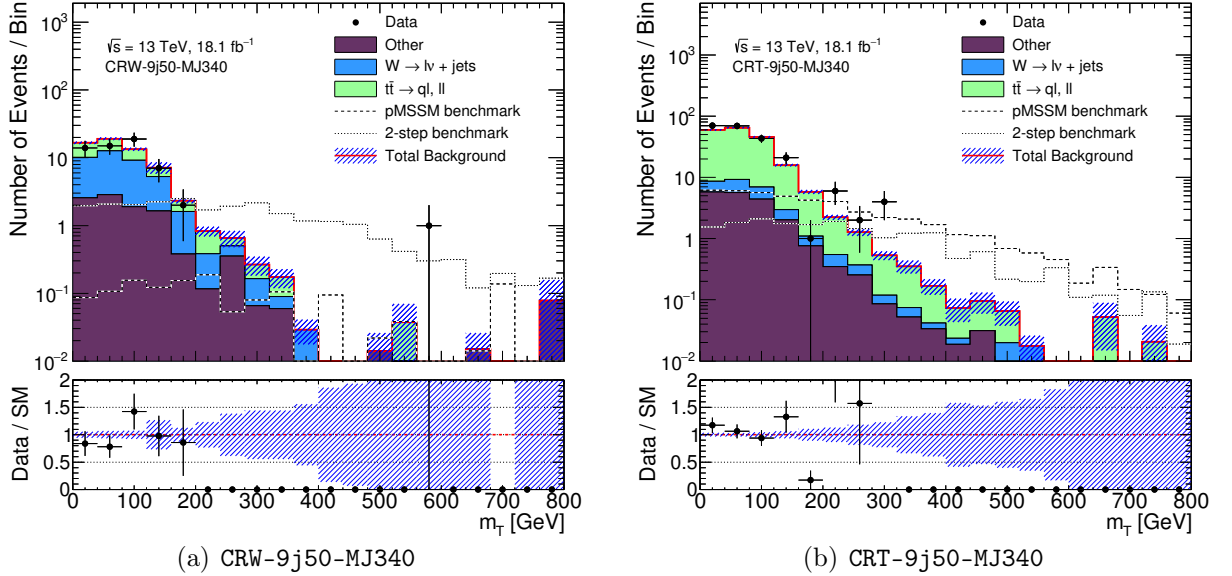


**Figure 5.12.:** Transverse mass distribution in the 9-jet  $W + \text{jets}$  (left) and  $t\bar{t}$  (right) control regions, before applying the  $m_T < 120 \text{ GeV}$  requirement.

#### 5.4.4. Theoretical systematic uncertainties

Uncertainties in Monte Carlo modelling, otherwise known as theoretical systematic uncertainties, can be determined through comparing samples produced with alternative generators and or generator settings. A symmetrical systematic uncertainty was extracted by comparing the yields from different generators. Note these were derived by a collaborator. This was done for  $t\bar{t}$ , which is by far the most important of the leptonic

Control Region Selection	
Trigger	HLT_6j45_0eta240
Lepton $p_T$	$> 20 \text{ GeV}$
Lepton $ \eta $	$e: < 2.47, \mu: < 2.5$
Lepton multiplicity	Exactly one, $\ell \in e \mu$
$m_T$	$< 120 \text{ GeV}$
Jet $p_T$	$> 50 \text{ GeV}$
Jet $ \eta $	$< 2.0$
Number of jets including lepton	$N_{SR} - 1$
$b$ -jet multiplicity	$= 0 (W) \text{ or } \geq 1 (t\bar{t})$
$M_J^\Sigma$	Same as SR
$E_T^{\text{miss}}/\sqrt{H_T}$	$> 3 \text{ GeV}^{1/2}$

**Table 5.4.:** Definition of the leptonic control regions, used to normalise the  $t\bar{t}$  and  $W + \text{jets}$  backgrounds. In the control regions, the lepton is recast as a jet if it passes the same kinematic criteria as the jets. Such leptons contribute to the  $E_T^{\text{miss}}/\sqrt{H_T}$  (through the  $H_T$ ) and also  $M_J^\Sigma$ .

backgrounds. Several alternatives were considered and compared to the nominal Powheg + Pythia6 sample, specifically Powheg interfaced with Herwig++ [206] and Madgraph5 interfaced with Pythia8 were used to cover differences in the shower modelling, while MadGraph5\_amc@NLO interfaced with Herwig++ was used as an alternative matrix element generator. Additionally, samples produced with more/less radiation tunes of the parton shower [207] were also compared. Table 5.5 shows these uncertainties for the SR-8j50-MJ340 signal region and its corresponding leptonic control regions. A full list of the  $t\bar{t}$  theory systematics are tabulated in appendix B.1. The dominant uncertainty comes from the different radiation tunes.

For the  $W + \text{jets}$  background, it was found that (prior to the fit) there was an over-prediction from the Monte Carlo that particularly affected the  $W + \text{jets}$  control regions (those selecting exactly 0  $b$ -jets). This was traced to an asymmetry between electrons

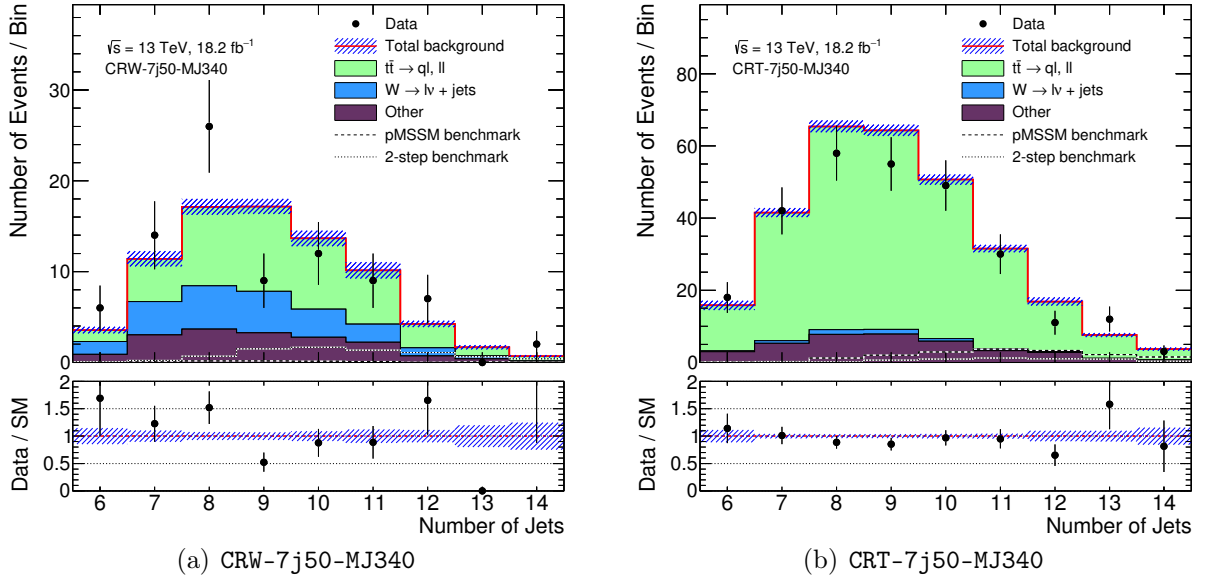


**Figure 5.13.:** Distribution of the number of jets in the control regions for the 7-jet  $W + \text{jets}$  (left) and  $t\bar{t}$  (right) control regions. Leptons are treated as jets, hence entries in the 6-jet bin. All other control regions are subsets of these, with tighter jet or  $M_J^\Sigma$  thresholds.

Region	Powheg	amc@NLO	Madgraph	Rad.	Rad.
	Herwig++	Herwig++	Pythia8	Up	Down
SR-8j50-MJ340	-1.4 %	-12.0 %	-20.0 %	72.0 %	-43.0 %
CRW-7j50-MJ340	4.3 %	12.0 %	-21.0 %	45.0 %	-52.0 %
CRT-7j50-MJ340	-2.9 %	1.0 %	-8.0 %	46.0 %	-32.0 %

**Table 5.5.:** Theoretical systematic uncertainties, in percent, for the 8j50-MJ340 signal region and the corresponding leptonic control regions. “Rad. Up” and “Rad. Down” refer to the radiation tunes of the parton shower.

and muons, in that the Monte Carlo predicted more muon events than were seen in data. As a result, an additional 10% uncertainty was included for the  $W + \text{jets}$  background for every region.

For other backgrounds, for which variations were either not available or severely statistically limited, a global, symmetrical uncertainty is taken – drawn from the recommendations of the ATLAS physics modelling group – as follows:

- diboson: 50%.
- $Z + \text{jets}$ : 40%.
- Single top: 30%.
- $t\bar{t} + X$ : 30%.

#### 5.4.5. Experimental systematic uncertainties

Experimental uncertainties include those related to the measurement of physics objects or the simulation of the ATLAS detector itself. In most cases, these uncertainties were calculated by re-computing the Monte Carlo predictions after altering parameters such as object calibration by an amount reflecting the uncertainty on that parameter. The yields were then compared to the nominal to derive the uncertainty.

The uncertainties were evaluated only for the  $t\bar{t}$ ,  $W + \text{jets}$  and single top backgrounds, due to constraints on available computation power, with the values for other Monte Carlo-determined backgrounds assumed to be smaller than the global uncertainties listed in section 5.4.4. Since these other backgrounds are a very small fraction of the total, and since their uncertainties are mostly dominated by Monte Carlo statistics, any falsities inherent in this approximation will have a negligible impact on the final result.

In the signal regions, the dominant uncertainties are those on the jet energy scale (JES) and resolution (JER), and the measurement of the luminosity which are described below. Several other sources of uncertainty were calculated, including those related to  $b$ -tagging, lepton and photon measurement,  $E_{\text{T}}^{\text{miss}}$  calculation and pile-up reweighting of Monte Carlo. Due to the lepton veto in the signal regions, systematics on the lepton efficiencies and

lepton energy scales and resolution enter either through the control-region measurement of the backgrounds or via small changes in yields in the signal regions due to changing numbers of baseline leptons, and were found to be sub-dominant. This is also the case for  $b$ -tagging efficiencies as no selection on  $b$ -jets is made in the signal regions. Other uncertainties were also found to be sub-dominant.

**Jet energy scale** As part of jet energy calibration, the jet energy scale (JES) correction attempts to correct the jet energy to the scale of the parton that initiated it. The calibration procedure, which is described in reference [106], relies partly on Monte Carlo simulation, and partly on data. The calibration in data is performed by studying the momentum balance between a well-measured reference object and the recoiling jet(s). Consequently, the associated systematic uncertainties originate both from the Monte Carlo (differences between Monte Carlo generators, physics modelling, etc) and from experimental aspects and assumptions made in the data analysis (jet flavour, trigger inefficiencies, pile-up, etc). In addition, uncertainties from the calibration of the reference objects used in the data-based jet calibration are also propagated. The result is a set of 60 nuisance parameters which could each be varied individually, but were combined (by collaborators) into 3 asymmetric terms by grouping together terms and simplifying assumptions about the correlations between these parameters. Jet energies are then varied up and down in a correlated manner by these 3 nuisance parameters, and the change in yield is used to derive a systematic uncertainty for each parameter. The first of these parameters was the dominant detector systematic, with an uncertainty ranging between 4–9% depending on the signal region.

**Jet energy resolution** The JES calibration takes the average measured jet energy back to the Monte Carlo value at hadron level. Since it is a correction on the average, there is still a spread of reconstructed jet energies around the true one; this spread is characterised by the jet energy resolution (JER). A single nuisance parameter is assigned, and evaluated by smearing the jet energies by a Gaussian, whose width is determined from the difference between the jet resolutions measured in Monte Carlo and data in order to account for the difference. The difference in yields was treated

as a symmetric systematic uncertainty, which varied from 0.1 – 9% depending on the signal region.

**Luminosity** The uncertainty on the 2016 integrated luminosity is 3.7%. It is derived, following a methodology similar to that detailed in reference [208], from a preliminary calibration of the luminosity scale using  $x$ - $y$  beam-separation scans performed in May 2016.

## 5.5. Multijet background estimation

The dominant background contaminating the signal regions in this analysis cannot be estimated with Monte Carlo techniques and so a data-driven method, the *template method*, is employed. The technique relies on the observed properties of the  $E_T^{\text{miss}}/\sqrt{H_T}$  variable:

- (i) The distribution of  $E_T^{\text{miss}}/\sqrt{H_T}$  is invariant under changes in jet multiplicity in events where the  $E_T^{\text{miss}}$  is dominated by jet mis-measurement.
- (ii) Multijet background events dominate the low values of  $E_T^{\text{miss}}/\sqrt{H_T}$ , whereas signal events typically occupy the higher values.

The latter point motivates cutting on this variable to remove background.

The template method is an “ABCD” method, so called because four non-overlapping regions are defined and the shape of a distribution is estimated in a particular region of phase space, D, using information from regions A, B and C. The four regions are defined in terms of two uncorrelated variables, in the case of this analysis  $E_T^{\text{miss}}/\sqrt{H_T}$  and jet multiplicity. The method is used to estimate the contribution of fully-hadronic processes in which there should be negligible genuine  $E_T^{\text{miss}}$ , yet still have large  $E_T^{\text{miss}}/\sqrt{H_T}$  due to one or more jets being significantly mismeasured.

### 5.5.1. Description of the background

The “multijet” background collectively categorises all fully-hadronic Standard Model processes that enter the signal regions. The dominant process is QCD multijet production where either the hard scatter or quark or gluon splitting can produce a large number of jets. The probability of each extra jet decreases by about  $\alpha_s$  per jet, and so events with 8 or more jets constitute a tiny fraction of QCD multijet events. However, the enormous cross-section for QCD dijet production ensures this process dominates the background contribution to this analysis.



Several other processes that augment the total multijet background include the fully-hadronic decays of  $t\bar{t}$  and  $W + \text{jets}$ , and to a lesser extent single top,  $Z + \text{jets}$ , diboson and  $t\bar{t} + X$  processes – these being the lepton-free analogues of the leptonic backgrounds discussed in section 5.4.

### 5.5.2. The template method

This method exploits the invariance of the  $E_T^{\text{miss}}/\sqrt{H_T}$  distribution for events where the  $E_T^{\text{miss}}$  is dominated by jet mismeasurement. Firstly, a series of template regions (TR) are built using the same kinematic requirements as in the signal regions, except with exactly 6 jets. A *template* is then formed by performing a bin-by-bin subtraction of the contribution from the leptonic backgrounds, the contribution being estimated with Monte Carlo and in the cases of  $t\bar{t}$  and  $W + \text{jets}$  further modified by fits to the control region as described in section 5.6.1. This subtraction removes the contribution from events with real  $E_T^{\text{miss}}$  which are not expected to be invariant under changes in jet multiplicity. The remaining shape – the template – is then extrapolated to the signal region jet multiplicity and normalised in the region  $E_T^{\text{miss}}/\sqrt{H_T} < 1.5 \text{ GeV}^{1/2}$ , which is expected to have negligible signal contamination. A separate template is built for each of the  $M_J^\Sigma$  thresholds defining the signal regions, meaning a total of two templates are created. Plots of the template regions are shown in figure 5.14(a) and (b).

The procedure can be summarised as follows. For each bin  $i$  in  $S_T^{\text{miss}} = E_T^{\text{miss}}/(\sqrt{H_T} \cdot \text{GeV}^{1/2})$ , the multijet prediction  $Y_i$  for a region with  $n$  jets is given by:

$$Y_i^{n \text{ jet}} = \left( N_i^{6 \text{ jet, data}} - N_i^{6 \text{ jet, lept.}} \right) \times \left[ \frac{\sum_k^{\forall k \in S_T^{\text{miss}} < 1.5} \left( N_k^{n \text{ jet, data}} - N_k^{n \text{ jet, lept.}} \right)}{\sum_k^{\forall k \in S_T^{\text{miss}} < 1.5} \left( N_k^{6 \text{ jet, data}} - N_k^{6 \text{ jet, lept.}} \right)} \right] \quad (5.8)$$

where  $N_i^{n \text{ jet, type}}$  is the number of events with  $n$  jets in  $E_T^{\text{miss}}/\sqrt{H_T}$  bin  $i$  from data or the leptonic background prediction. The term in the square brackets is the normalisation used

to extrapolate from 6-jets to the jet multiplicity of the signal region. It is possible that the multijet background prediction can be negative for a given bin if  $N_i^{6 \text{ jet, data}} < N_i^{6 \text{ jet, lept.}}$ .

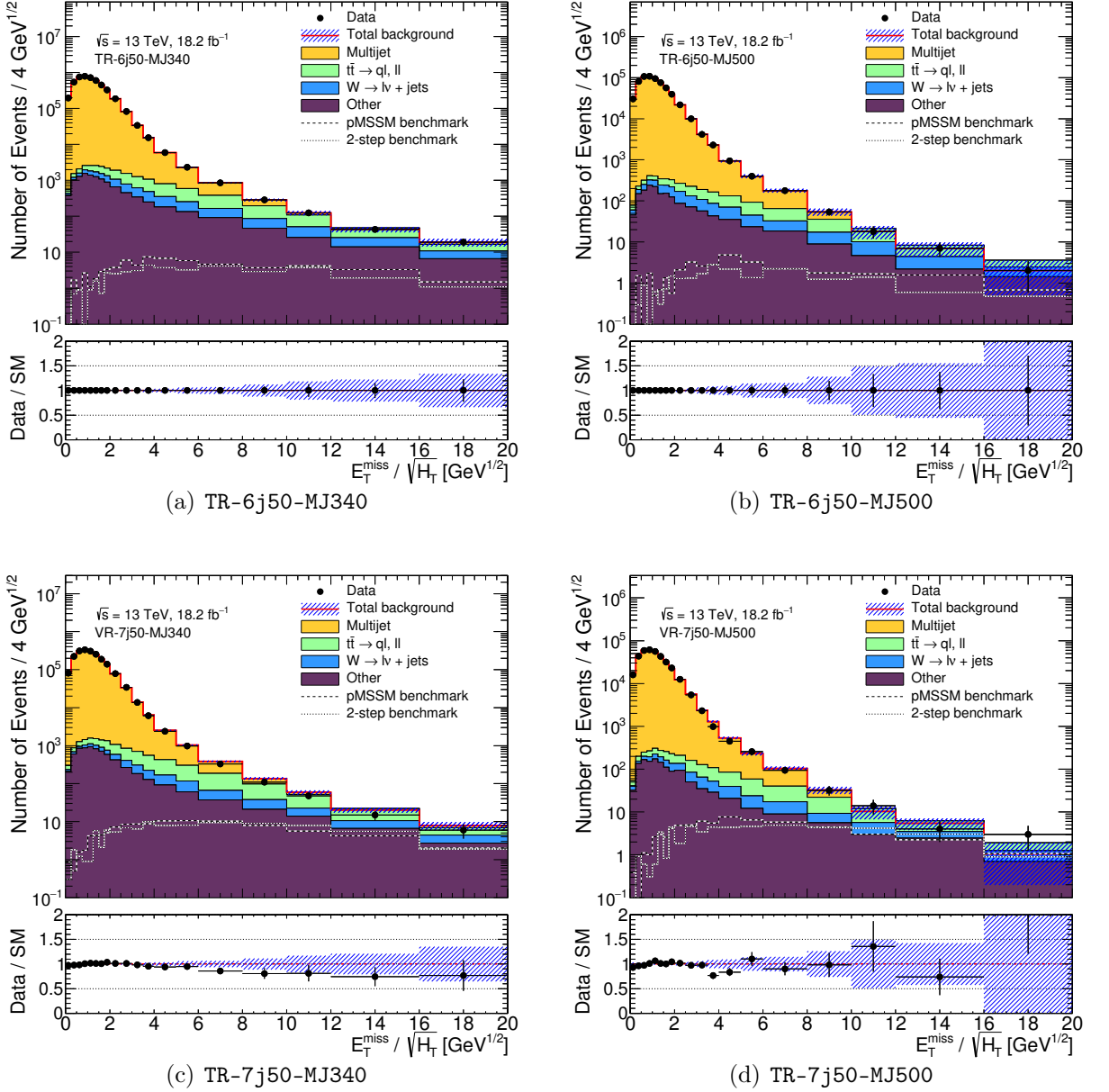


**Figure 5.14.:** The  $E_T^{\text{miss}} / \sqrt{H_T}$  distribution in the 6 jet template regions (upper panels) and the 7 jet validation regions (lower panels) for the  $M_J^\Sigma > 340 \text{ GeV}$  (left) and  $M_J^\Sigma > 500 \text{ GeV}$  (right) regions. The blue hatched band shows the statistical uncertainty on the background prediction. Note that in these plots the Monte Carlo backgrounds have not been modified by the fit.

### 5.5.3. Closure tests of the template method

The dominant systematic uncertainty on the template method as described above is quantified from the degree to which the method is observed to work in regions where little signal is expected. The template prediction is said to “close” if there is agreement between the prediction and data in a series of validation regions (VR). The template is checked in bins of  $E_T^{\text{miss}}/\sqrt{H_T}$  in-between the template normalisation region and the signal region in the ranges 1.5–2.0, 2.0–2.5 and 2.5–3.0  $\text{GeV}^{1/2}$  for each of the signal region jet multiplicities and separately for each of the  $M_J^\Sigma$  thresholds. Additionally, a further validation region is defined with exactly 7 jets in which the above  $E_T^{\text{miss}}/\sqrt{H_T}$  bins are tested as well as the signal region-like bin  $E_T^{\text{miss}}/\sqrt{H_T} > 4.0 \text{ GeV}^{1/2}$ . The jet selection is exclusive such that the signal regions remain blind. For each  $M_J^\Sigma$  threshold, this corresponds to a total of 13 validation regions.

The (symmetrical) systematic uncertainty for a particular signal region is then defined as the maximal deviation in any of the closure validation regions with jet multiplicity less than or equal to that specific signal region, and the same  $M_J^\Sigma$  cut. For example, the systematic uncertainty in for the region SR-9j50-MJ500 is given by considering all of the 7ej50-MJ500, 8j50-MJ500 and 9j50-MJ500 validation regions, but not any of the 10j50-MJ500 regions or any of the MJ340 regions.

Table 5.6 summarises the values extracted from this procedure, and this is also shown graphically in figure 5.15. The end-result of the template method applied to the validation regions is shown in figure 5.14(c) and (d).

### 5.5.4. Heavy-flavour systematic

The heavy-flavour systematic is included to account for the possibility that the assumptions made to build the templates break down at higher jet multiplicities due to the differing proportion of  $b$ -jets.

$n_{50}(\text{MJ340})$	$E_{\text{T}}^{\text{miss}}/\sqrt{H_{\text{T}}}$ range [ $\text{GeV}^{1/2}$ ]				Total
	[1.5, 2.0]	[2.0, 2.5]	[2.5, 3.0]	[4.0, $\infty$ ]	
$= 7$	-0.8%	1.2%	1.8%	7.7%	—
$\geq 8$	-1.2%	4.7%	7.3%	(blinded)	7.3%
$\geq 9$	2.8%	4.7%	13.0%	(blinded)	13.0%
$\geq 10$	2.4%	4.9%	12.1%	(blinded)	13.0%

$n_{50}(\text{MJ500})$	$E_{\text{T}}^{\text{miss}}/\sqrt{H_{\text{T}}}$ range [ $\text{GeV}^{1/2}$ ]				Total
	[1.5, 2.0]	[2.0, 2.5]	[2.5, 3.0]	[4.0, $\infty$ ]	
$= 7$	-0.2%	-2.3%	3.7%	4.6%	—
$\geq 8$	-2.0%	0.4%	7.0%	(blinded)	7.0%
$\geq 9$	2.3%	2.3%	16.2%	(blinded)	16.2%
$\geq 10$	6.8%	-0.8%	4.3%	(blinded)	16.2%

**Table 5.6.:** The degree of closure observed in the multijet validation regions. The bracketed ranges indicate the  $E_{\text{T}}^{\text{miss}}/\sqrt{H_{\text{T}}}$  interval considered, in  $\text{GeV}^{1/2}$ . Cells highlighted in blue indicate validation regions, signal regions are in red and green indicates the closure systematic used for the respective signal region. The upper table is for the  $M_{\text{J}}^{\Sigma} > 340 \text{ GeV}$  regions and the lower table for the  $M_{\text{J}}^{\Sigma} > 500 \text{ GeV}$  regions. The closure is calculated as  $(\text{observation} - \text{prediction})/(\text{prediction})$ , where the prediction is given as the sum of the fitted leptonic backgrounds and the multijet estimation from the template.

The  $b$ -quark decays via the emission of a  $W$  boson and either a  $c$  or  $u$  quark. The  $W$  boson subsequently decays either leptonically or hadronically and in the leptonic case a neutrino is produced. This effectively turns  $b$ -jets into a genuine source of  $E_T^{\text{miss}}$ , albeit a small one. The effect on the template is demonstrated in figure 5.16, where the nominal template is compared with a template built from events with exactly no  $b$ -jets (**0eb**) and another built from events with at least 1  $b$ -jet (**1ib**). We see that with increasing numbers of  $b$ -jets the template shape broadens, due to the additional  $E_T^{\text{miss}}$ .

Figure 5.17 shows the number of  $b$ -jets is roughly constant as the number of jets increases, the average number of  $b$ -jets being around 0.85 per event. Therefore,  $b$ -jets make up a smaller proportion of the total number of jets in the signal regions than in the template region, which in turn implies a different shape of the multijet background. It is expected that the shape of the  $E_T^{\text{miss}}/\sqrt{H_T}$  for the multijet background for 10-jet events would be narrower than for 6-jet events.

To take this effect into account, the following uncertainty was derived. This method was implemented with a collaborator and so only brief details are included here. A new template definition was created by taking a linear combination of the nominal “flavour-blind” (**0ib**) template and the “flavour-split” (**0eb** + **1ib**) templates, denoted  $F_b$  and  $F_s$  respectively. Here, these  $F$ -values are a total background estimate, being the number of events predicted by the respective template, added to the total contribution from the leptonic backgrounds. The final background estimate,  $\mathcal{T}$ , is then:

$$\mathcal{T} = fF_b + (1 - f)F_s, \quad (5.9)$$

where  $f \in [0, 1]$ . The same set of validation regions used for the closure systematic, described above, are used. For each, a  $\chi^2$  minimisation is performed to find an optimal  $f$  value. The standard  $\chi^2$  is used, for  $E$  observed data in the validation region

$$\chi^2 = \frac{(E - \mathcal{T})^2}{\sigma^2}, \quad (5.10)$$

where  $\sigma^2$  represents the quadratic sum of the statistical uncertainties on the data and background prediction.

$n_{50}$	$M_J^\Sigma$ threshold [GeV]	
	340	500
$\geq 8$	0.2%	2.1%
$\geq 9$	0.8%	2.7%
$\geq 10$	3.3%	8.3%

**Table 5.7.:** Uncertainties on the multijet prediction derived from heavy-flavour effects.

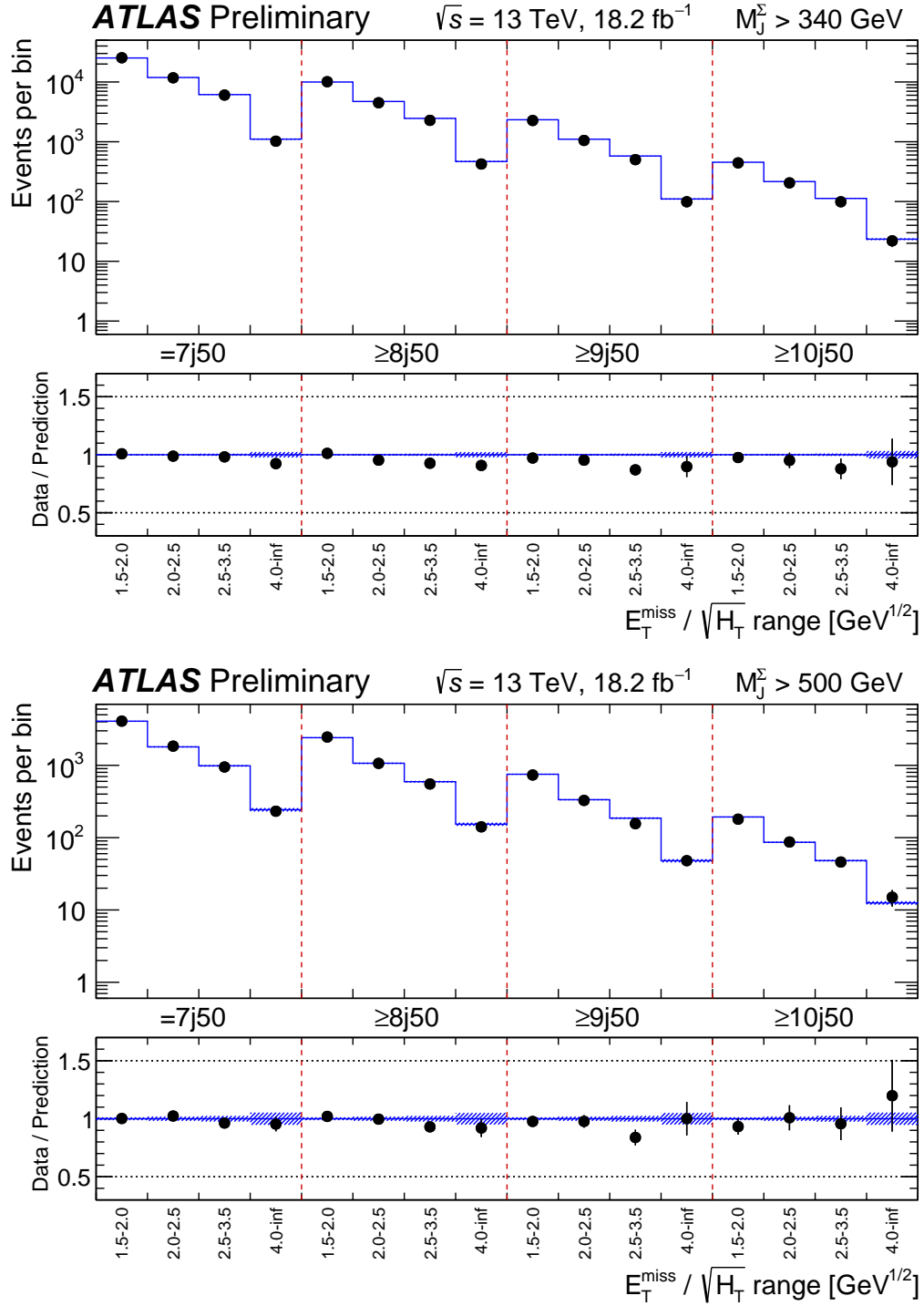
The systematic uncertainty for a given signal region is then defined in a similar way to the closure systematic, being the maximal deviation from the nominal ( $f = 1$ ) background prediction and the  $\mathcal{T}$  prediction in any of the validation regions with the same  $M_J^\Sigma$  cut, and with jet multiplicity less than or equal to the jet multiplicity of the signal region. The final uncertainties are summarised in table 5.7.

### 5.5.5. Additional systematic uncertainties

In the previous iteration of this analysis it was found that the  $E_T^{\text{miss}}/\sqrt{H_T}$  distribution was not invariant under changes in jet multiplicity for events with  $H_T \lesssim 1$  TeV. This was a result of using a  $E_T^{\text{miss}}$  definition built from inner-detector tracks to evaluate the soft term, the so called “track soft term”  $E_T^{\text{miss}}$ .<sup>4</sup> Since the soft term is generated from tracks, there is intrinsic  $E_T^{\text{miss}}$  in all events from soft forward particles outside the inner-detector acceptance, and from central neutral particles that leave no tracks. This intrinsic  $E_T^{\text{miss}}$  breaks the invariance of the  $E_T^{\text{miss}}/\sqrt{H_T}$  distribution for events with low  $H_T$ . This issue was previously resolved by binning the template in slices of  $H_T$ . However, the  $M_J^\Sigma$  variable is correlated with  $H_T$ , and a minimum threshold on  $M_J^\Sigma$  imposes a threshold on  $H_T$ :  $M_J^\Sigma > 340$  (500) GeV corresponding to roughly  $H_T > 400$  (500) GeV. The  $M_J^\Sigma$  cut therefore removes events with low  $H_T$  and restores the closure of the template without the need for binning, partly demonstrated by the successful background prediction in

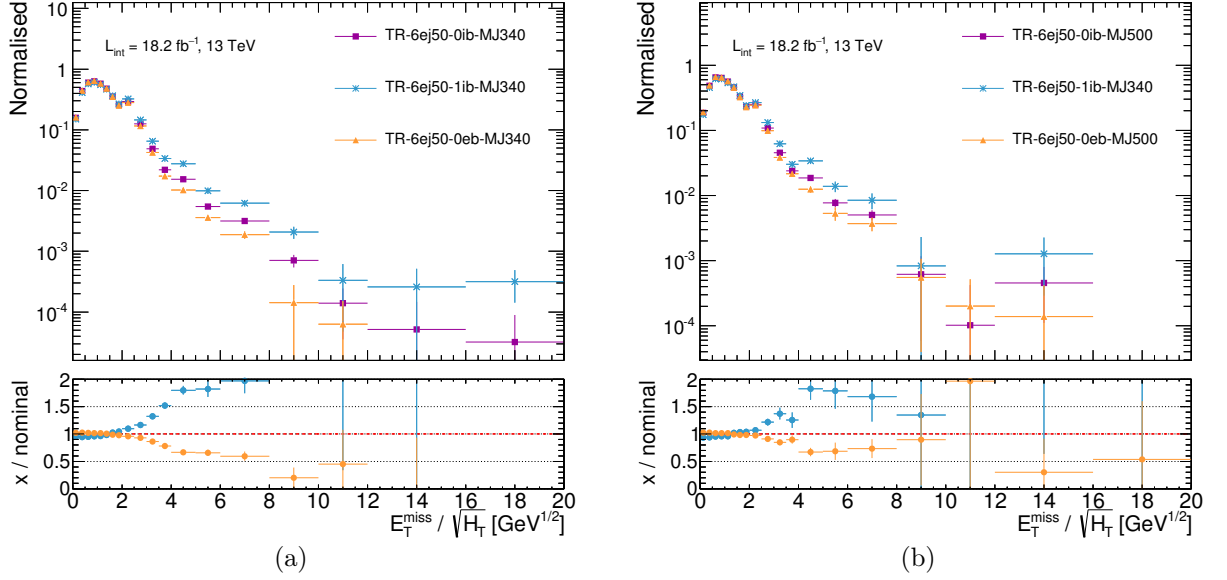
<sup>4</sup>The alternative definition is the “calorimeter soft term”, used in Run-1. However, this was sensitive to pileup and so was discarded due to the increased pileup conditions in Run-2.

figure 5.14. However, is possible for some residual  $H_T$  dependence of the template to remain, and therefore an additional 5% systematic uncertainty was applied to the MJ340 regions. Additional studies into  $H_T$  binning the template are show in appendix B.2.



**Figure 5.15.:** The degree of closure observed in the various multijet validation regions with  $M_J^\Sigma > 340 \text{ GeV}$  (upper panel) and  $M_J^\Sigma > 500 \text{ GeV}$  (lower panel). The solid lines are the predicted numbers of events and the points are the observed data. The signal regions are also included in the plot (4.0– $\infty$ ) for the 8, 9 and 10 jet regions, but these are not included in the calculation of the systematic uncertainty. The blue bands indicate the statistical uncertainties on the total background prediction.





**Figure 5.16.:** These plots show the multijet template extracted from the “nominal” template region (with no  $b$ -jet requirement) and the alternative “flavour” template regions with either at least 1  $b$ -jet or exactly 0  $b$ -jets. The histograms have been normalised and rebinned – the spike around  $E_T^{\text{miss}} / \sqrt{H_T} = 2 \text{ GeV}^{1/2}$  being an artefact of the increased bin width. The lower pad shows the ratio of each of the templates to the nominal.

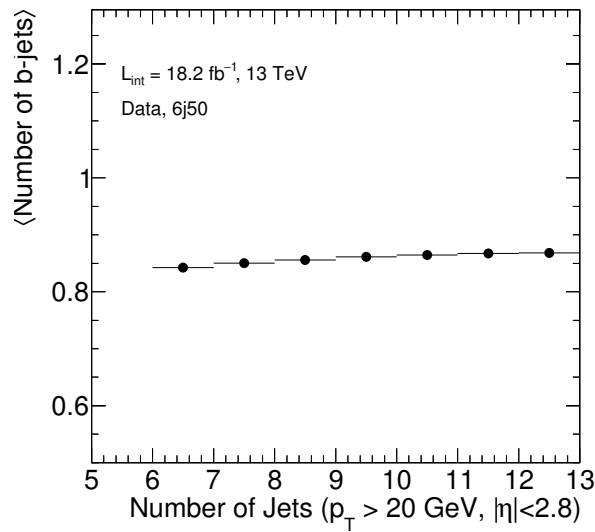


**Figure 5.17.:** The average number of  $b$ -jets versus the number of jets in data. All cleaning cuts have been applied, as well a lepton veto and a 6 jet selection.

## 5.6. Results and interpretation

The final test for new physics is to compare the data and the Standard Model background prediction in the signal regions. However, before doing this, the individual components of the background and their uncertainties are fitted in order to improve the background prediction. This is done in a process known as the “background-only” fit, which combines information in the control regions to improve the background prediction in the signal region. In this analysis, a scale factor for  $t\bar{t}$  and  $W + \text{jets}$  background is extracted via a simultaneous fit to the control regions. These scale factors, denoted  $\mu_{t\bar{t}}$  and  $\mu_{W+\text{jets}}$  are multiplicative factors that modify the size of the respective background in the signal region. The total uncertainty, after taking into account any correlations between systematic uncertainties is also calculated by this fit, and the end result is a total background prediction with its uncertainty for a given signal region. Only from this result can the statistical significance of any excess be calculated, and the question “is there any new physics in the data” be answered. The full fitting procedure is described in section 5.6.1.

Distributions of the  $E_{\text{T}}^{\text{miss}}/\sqrt{H_{\text{T}}}$  in the signal regions, complete with the template prediction of the multijet background and the leptonic background modified by the fitting procedure outlined above, are shown in figure 5.18 and figure 5.19. Unfortunately, there is no obvious excess of the data over the Standard Model prediction. As a result, exclusion limits can be set on new phenomena. This can be done in two ways, which will first be briefly described here and then in detail in the following sections.

**Model-independent limits** The data in a given signal region and the corresponding background prediction from the background-only fit are used to give an estimate of the minimum number of signal events that *any* new physics scenario should predict in order to be excluded by that signal region. This number can also be translated into a cross-section upper limit, given the luminosity of the data. The fit includes one signal region at a time, along with all the corresponding control regions; the possible signal contamination in the control regions is neglected; and it is assumed that the signal events have no systematic uncertainties. A scan is performed over all possible values of the signal strength, until the  $p$ -value of the signal plus background

hypothesis is smaller than 0.05, or conventionally excluded at the 95% confidence level. As no particular model is assumed when deriving this upper limit, this result is often used for reinterpretation, and can be used to exclude any new physics model. Model-independent limits of Run-1 new physics searches were used for the study described in chapter 4. A more detailed description of this kind of fit is given in section 5.6.2.

**Model-dependent limits** As the name suggests, a particular signal model is considered in the fit. The contribution of the signal model to all of the control regions and signal regions are accounted for, including statistical uncertainties and systematic uncertainties that may be correlated with those of the background. The background estimate in the signal region is then recalculated in a similar way to what is done for the background-only fit, except that the signal contamination in the control region is accounted for. The  $p$ -value of the background plus signal hypothesis is then calculated and translated into a confidence level. A more detailed description is given in section 5.6.3.

The author calculated all of the inputs to the fit, save the systematics explicitly mentioned in the previous section, ran the fitting algorithms, and produced the tables of results and plots. All of the fits are implemented with the `HistFitter` package [209].

### 5.6.1. The background only fit

The purpose of this fit strategy is to estimate the Standard Model background in a given region of phase space without making assumptions on any signal model. For this analysis, this is done by the extraction of the two scale factors  $\mu_{t\bar{t}}$  and  $\mu_{W+\text{jets}}$  via the frequentist parameter extraction method known as maximum likelihood estimation. The likelihood function is constructed containing the estimated rates of all background processes in all regions, all sources of systematic uncertainty, and the data (except in the signal region). In this section, the construction of the likelihood function will be described by first building a simple likelihood and sequentially increasing the complexity. The notation is defined such that Roman characters correspond to observable quantities,

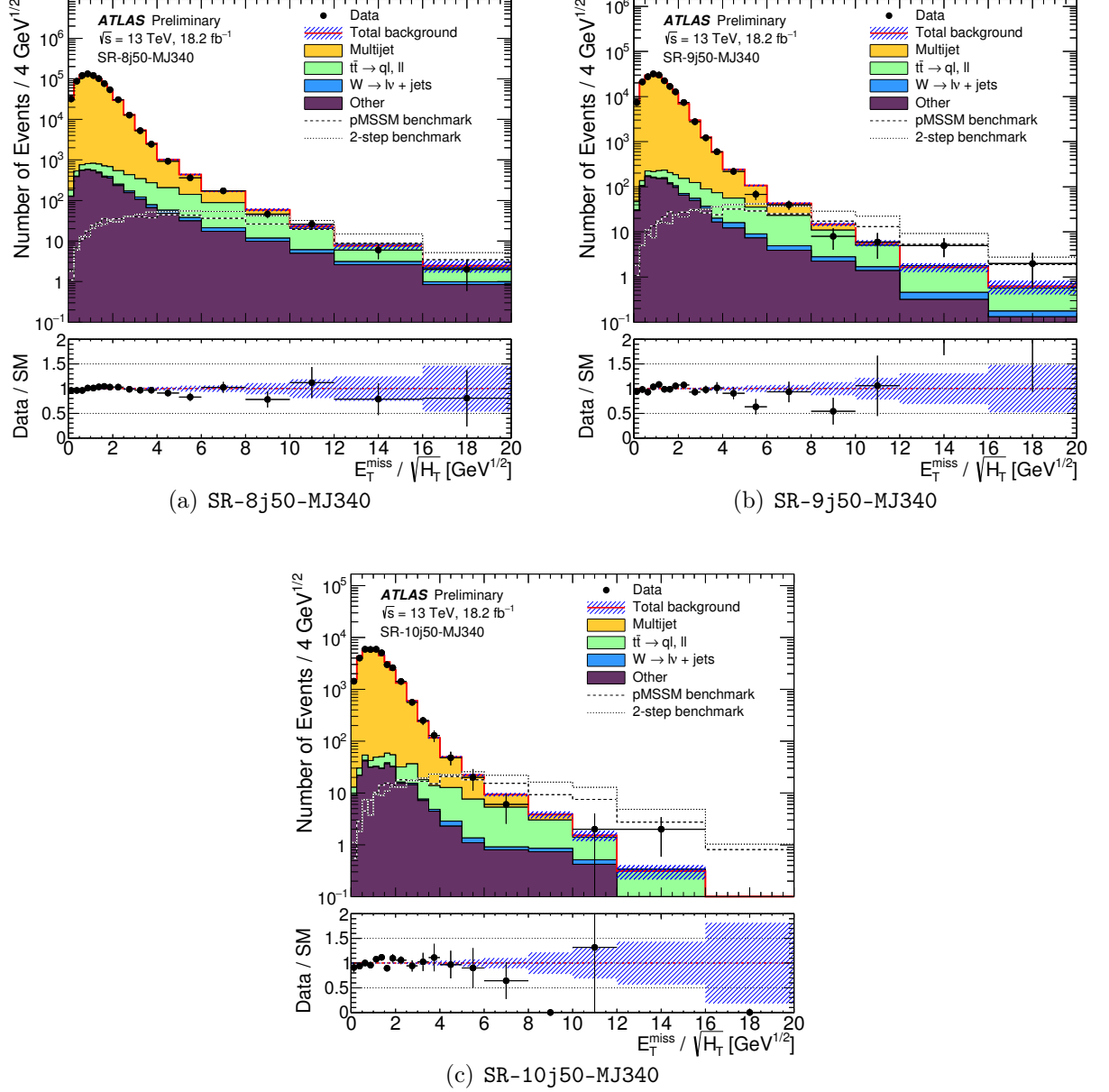


**Figure 5.18.:**  $E_T^{\text{miss}} / \sqrt{H_T}$  distributions for the signal regions with  $M_J^\Sigma > 340$  GeV for at least 8, 9 and 10 jets (a, b and c respectively). Note the  $t\bar{t}$  and  $W + \text{jets}$  backgrounds have been modified from the raw MC prediction by the scale factors from the background-only fit.

while Greek characters correspond to parameters of the statistical model. The likelihood is constructed with the `HistFactory` [210] package, through `HistFitter`.

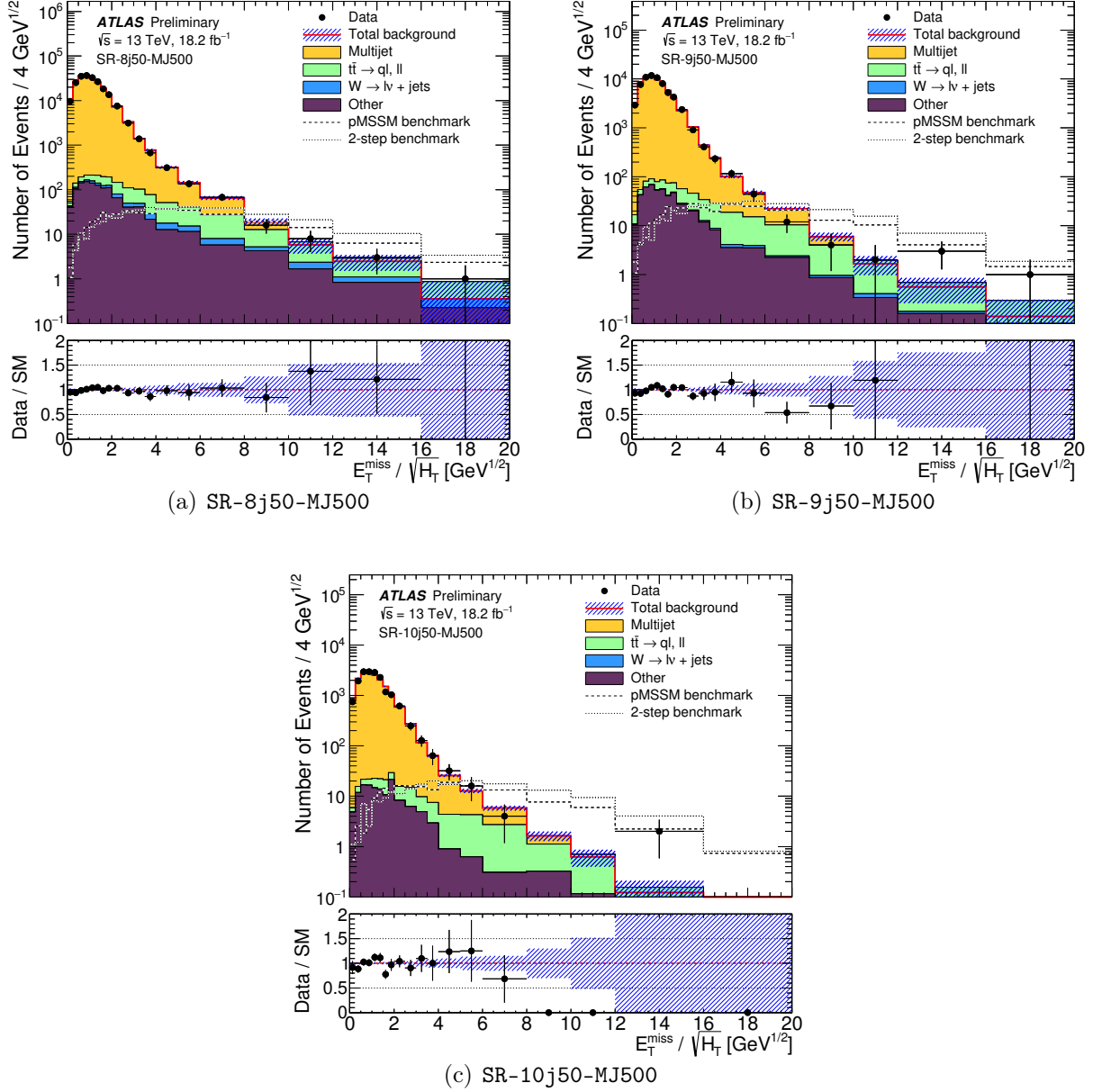


**Figure 5.19.:**  $E_T^{\text{miss}} / \sqrt{H_T}$  distributions for the signal regions with  $M_J^\Sigma > 500$  GeV for at least 8, 9 and 10 jets (a, b and c respectively). Note the  $t\bar{t}$  and  $W + \text{jets}$  backgrounds have been modified from the raw Monte Carlo prediction by the scale factors from the background-only fit.

## Event counts

For this analysis three channels are used for the background-only fit, *channel* being an umbrella term for distinct regions of phase space defined by event selection criteria,

corresponding to the signal region and two control regions. Each channel consists of a simple event count – the data and predictions of the rate of a Standard Model process with the associated uncertainties.<sup>5</sup> In an abstract sense, each channel contains many *samples*, corresponding to different background processes (and principally also the signal). To build the likelihood function, we will start a simple example: a single channel with  $s \in \{\text{bkg}_1, \text{bkg}_2, \dots\}$  samples each with a nominal expected event count  $\nu_s$ , all of which are known to perfect accuracy except  $\nu_1$  from  $\text{bkg}_1$ . The expected event yield for all other background processes is fixed in the statistical model (we assume that all these backgrounds present in the data are accounted for and known exactly). However, the number of events from  $\text{bkg}_1$  observed data is not known a priori and so must be allowed to float in the statistical model. This freedom is included by introducing the parameter ( $\mu$ ) which gives the yield of the sample in question relative to the theoretically predicted number of events. The total background prediction,  $\nu$  is then given by

$$\nu = \mu\nu_1 + \sum_{\forall s \neq 1} \nu_s. \quad (5.11)$$

where the sum runs over all of the background samples  $s$  except  $\nu_1$ . With a statistical model defined, the relation of the data to the model can now be incorporated – the probability density function (pdf) must be defined.

Given we are searching for new physics, the signal channels typically have small event counts as they are on the edges of accessible phase space. An appropriate choice of pdf for such a counting experiment is the Poisson distribution, abbreviated to  $\text{Pois}(n | \nu)$  where

$$\text{Pois}(n | \nu) = \frac{\nu^n e^{-\nu}}{n!} \quad (5.12)$$

for  $n$  data events. The probability distribution can be reinterpreted as a likelihood, which in our specific example becomes:

$$\mathcal{L}(\mu | n) = \text{Pois}(n | \nu) = \text{Pois}\left(n \left| \mu\nu_1 + \sum_{\forall s \neq 1} \nu_s \right.\right). \quad (5.13)$$

---

<sup>5</sup>Alternatively, a channel could instead be a binned histogram of an observable, however this technique was not used in this analysis.

The best estimate for  $\mu$  (denoted  $\hat{\mu}$ ) given the data  $n$  and the  $\nu_s$  is extracted by maximising the likelihood. For this example,  $\hat{\mu}$  can be extracted analytically yielding  $\hat{\mu} = \frac{n - \sum_{s \neq 1} \nu_s}{\nu_1}$  as expected from the definition of  $\mu$ . The likelihood function can then be extended consider an arbitrary number of channels  $c$  as follows:

$$\mathcal{L}(\boldsymbol{\mu} \mid \mathbf{n}) = \prod_c \text{Pois}(n_c \mid \nu_c) \quad (5.14)$$

where  $\boldsymbol{\mu} = \{\mu_1, \mu_2, \dots\}$  is the set of scale factors to be extracted,  $\mathbf{n} = \{n_1, n_2, \dots\}$  is the measured data in each channel and  $\nu_c$  is the generalised form of eq. (5.12) for a channel  $c$ .

### Adding uncertainties

In reality, the nominal statistical model is not known perfectly. There will be uncertainties originating from various sources. Additional parameters must be included in the likelihood to account for these uncertainties.

Certain parameters are constrained by previous measurements, which means that they are free to float but are bounded by some pdf so that the statistical model is penalised if a constrained parameter moves too far from its expectation. Measurements of calibrations and efficiencies, as well as theoretical predictions, are known as *sources* and have such constraints. A particular experiment will measure the values of sources as auxiliary measurements,  $a \in \{a_1, \dots, a_N\}$ , with some uncertainty. However, the experiment is only run once, and future experiments may observe different values of those auxiliary measurements. Therefore, the true mean values of the sources,  $\alpha \in \{\alpha_1, \dots, \alpha_N\}$ , are not known a priori and they must be extracted from the statistical model. If enough information is included in the statistical model, then the data can be used to constrain the true value of each  $\alpha$  and its uncertainty  $\Delta_\alpha$ .

Other parameters are unconstrained, and are allowed to float freely (within some predefined range).

Four types of parameter are used in this analysis. In the language of `HistFactory`, these are: `NormFactor`, `ShapeSys`, `Luminosity` and `OverallSys`, which will be described below –

others are possible (see reference [210]) but are not used in this analysis and therefore are not discussed here.

**NormFactor:** These are unconstrained normalisations of the (background) samples, denoted  $\mu_s$ , relative to the nominal number of events in the input model. The signal strength  $\mu_{\text{sig}}$  is a special case of such a parameter and will be discussed in later sections (it is not used in the background-only fit). These normalisations are parameters of interest, and in this analysis two are extracted:  $\mu_{t\bar{t}}$  and  $\mu_{W+\text{jets}}$ .

**ShapeSys:** Statistical uncertainties from limited Monte Carlo event counts are taken into account by scale factors  $\gamma_c$ , which is a shared parameter for all samples in the channel. These are generally constrained by Poisson distributions.

**Luminosity:** The luminosity  $\lambda_s$ , enters the fit as a Gaussian constraint for any sample that is normalised directly according to the theoretical prediction within a given channel. This corresponds to the channels that do not have a NormFactor.<sup>6</sup> This is a common luminosity parameter  $G(\lambda_s | L_0, \Delta_L)$  centred at the measured luminosity value  $L_0$  and with width  $\Delta_L$  representative of the uncertainty of the measurement. For samples with an associated NormFactor, the nominal luminosity  $L_0$  is used.

**OverallSys:** These parameters, denoted  $\eta_s(\alpha)$ , correspond to an overall shift up or down in the normalisation of a sample, and are used to account for systematic uncertainties in the analysis. For each systematic  $p$ ,  $\alpha_p = 0$  corresponds to the nominal case and  $\alpha_p = \pm 1$  corresponds to the  $\pm 1\sigma$  variations of the systematic (as measured by the relevant ATLAS performance group, or extracted from theory variations). The values  $\eta_s(-1)$  and  $\eta_s(+1)$  are the relative values of the sample event yields ( $\nu_s$ ) with respect to the  $\alpha_p = 0$  case (for which  $\eta_s(0) = 1$ ), and are obtained empirically by running the analysis with the nominal calibration and then repeating this with the  $\pm 1\sigma$  calibrations. For intermediate values of  $\alpha_p$ ,  $\eta_s$  is interpolated following a procedure defined in reference [210], which guarantees that  $\eta_s(\alpha_p) > 0$ .

Auxiliary measurements constrain the extent by which a systematic can vary and any deviation of the  $\alpha_p$  parameter too far from the auxiliary measurement is constrained.

---

<sup>6</sup>Except if this is applied to a signal sample, in which case both a Gaussian constraint for the luminosity and a NormFactor are used.



This is achieved by introducing Gaussian constraints  $P_p(a_p \mid \alpha_p)$  with  $a_p$  being the value of the calibration measured in the auxiliary measurement of the source. A mapping is used such that  $a_p \equiv 0$  and the constraint term on the true value of the calibration,  $\alpha_p$ , is a Gaussian centred at 0 and with width 1. In the case in which a background process has a floating normalisation (NormFactor), and a source of systematic uncertainty is fully correlated between the channels, the uncertainty can be factorised in an overall normalisation factor and a residual term. The overall normalisation factor is absorbed in the floating  $\mu_s$  parameter, thus effectively reducing the impact of the uncertainty source.

The background prediction in eq. (5.12) is then extended to include all uncertainty parameters,

$$\nu_c(\boldsymbol{\mu}, \boldsymbol{\alpha}) = \sum_s \lambda_s \gamma_c \mu_s \eta_{s,c}(\boldsymbol{\alpha}). \quad (5.15)$$

The likelihood (eq. (5.14)) is also modified for the effect of the uncertainty parameters as follows:

$$\mathcal{L}(\boldsymbol{\mu}, \boldsymbol{\alpha} \mid \mathbf{n}, \mathbf{a}) = \prod_c \text{Pois}(n_c \mid \nu_c) \cdot G(L_0 \mid \lambda, \Delta_L) \cdot \prod_p P_p(a_p \mid \alpha_p). \quad (5.16)$$

By maximising the likelihood function,  $\mu_{t\bar{t}}$  and  $\mu_{W+\text{jets}}$  can be extracted. This is the background-only fit.

### Results of the background only fit

The resulting background predictions and the associated scale factors are summarised in table 5.8 for all signal regions. The data are also included and no significant excess above the Standard Model prediction is observed. Figure 5.20 displays the same information graphically. The dominant sources of systematic uncertainty in each of the signal regions is shown in table 5.9 and table 5.10. These uncertainties are dominated by theoretical uncertainties on  $t\bar{t}$  modelling, the closure of the multijet template, and the jet energy scale. A complete breakdown of the yields for each background, both pre- and post-fit are given in the appendix B.3.

	8j50			9j50			10j50		
	MJ340	MJ500	MJ340	MJ340	MJ500	MJ340	MJ340	MJ500	MJ500
Observed	424	141	99	48	22	15			
Expected	$467.2 \pm 29.3$	$153.3 \pm 8.7$	$110.3 \pm 10.5$	$48.0 \pm 5.7$	$23.4 \pm 2.3$	$12.5 \pm 1.7$			
<i>Fitted</i>									
Multijet	$312.1 \pm 28.7$	$107.4 \pm 7.7$	$72.7 \pm 10.2$	$33.4 \pm 5.4$	$14.1 \pm 2.0$	$8.6 \pm 1.4$			
$t\bar{t}$	$108.0 \pm 6.2$	$29.2 \pm 3.9$	$28.7 \pm 2.5$	$11.2 \pm 1.9$	$7.2 \pm 1.2$	$3.2 \pm 0.9$			
$W + \text{jets}$	$12.5 \pm 3.1$	$5.0 \pm 2.1$	$1.9 \pm 0.8$	$0.7 \pm 0.6$	$0.7 \pm 0.5$	$0.1 \pm 0.2$			
Other	$34.6 \pm 0.1$	$11.7 \pm 0.1$	$7.0 \pm 0.0$	$2.7 \pm 0.0$	$1.5 \pm 0.0$	$0.6 \pm 0.0$			
<i>Scale Factors</i>									
$\mu_{t\bar{t}}$	$0.91 \pm 0.05$	$0.79 \pm 0.10$	$0.87 \pm 0.08$	$0.85 \pm 0.14$	$0.92 \pm 0.15$	$0.83 \pm 0.23$			
$\mu_{W+\text{jets}}$	$0.54 \pm 0.15$	$0.48 \pm 0.21$	$0.54 \pm 0.24$	$0.30 \pm 0.30$	$0.66 \pm 0.51$	$0.16 \pm 0.65$			
<i>Pre-fit</i>									
Multijet	312.1	107.4	72.7	33.4	14.1	8.6			
$t\bar{t}$	119.0	37.0	32.9	13.2	7.8	3.9			
$W + \text{jets}$	22.9	10.4	3.6	2.1	1.0	0.6			
Other	34.6	11.7	7.0	2.7	1.5	0.6			

**Table 5.8.:** Data yields and the Standard Model expectation for each signal region, both before and after the background-only fit. The uncertainties reflect the combination of statistical and systematic sources. The normalisation on the  $W + \text{jets}$  background is typically around 0.5 or smaller, demonstrating that the Monte Carlo does not describe data well for the yield of  $W + \text{jets}$  in high jet multiplicity events.

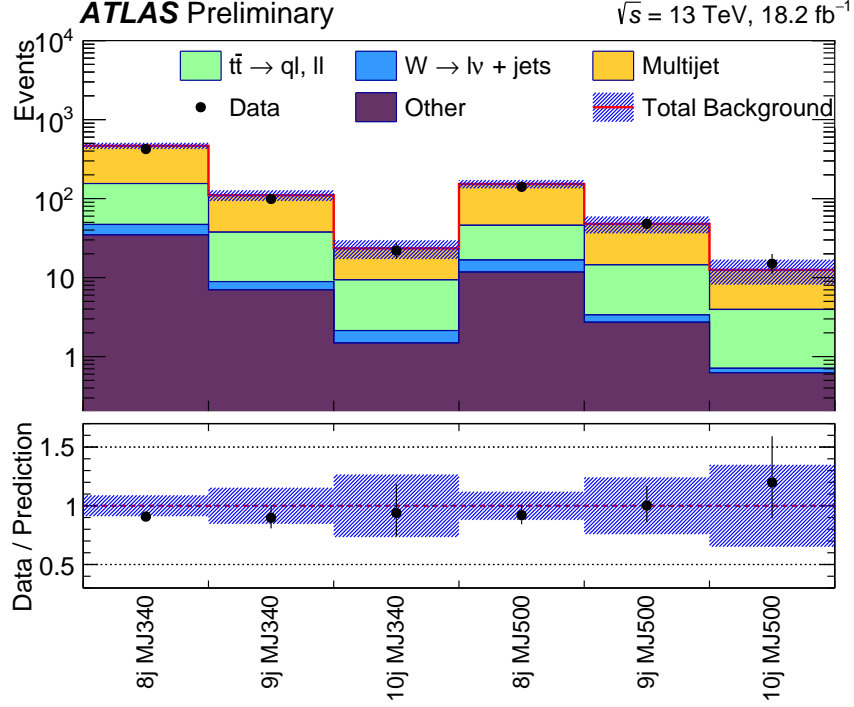


**Figure 5.20.:** A summary of the data and Standard Model prediction for the 6 signal regions. The blue band shows the combined statistical and systematic uncertainty on the Standard Model predictions after the background fit.

Region	SR-8j50-MJ340	SR-9j50-MJ340	SR-10j50-MJ340
Total background expectation	467.14	110.33	23.44
Total statistical	4.6%	9.5%	21%
Total systematic	8.5%	15%	26%
$t\bar{t}$ theory – radiation	13%	23%	40%
$t\bar{t}$ normalisation uncertainty	9.9%	15%	23%
Template closure	5.1%	8.6%	7.8%
JES	4.4%	5.7%	6.1%
$t\bar{t}$ theory – parton shower choice	0.32%	3.1%	15%
JER	0.34%	4.6%	9.2%
$t\bar{t}$ theory – generator choice	4.6%	4.6%	7.6%

**Table 5.9.:** Dominant ( $> 5\%$  in any region) systematic uncertainties for the MJ340 regions. Uncertainties are correlated so may add to more than the totals quoted. The  $t\bar{t}$  normalisation uncertainty corresponds to the uncertainty on the  $t\bar{t}$  scale factor, and is related to both the statistical and systematic uncertainties in the control regions.

Region	SR-8j50-MJ500	SR-9j50-MJ500	SR-10j50-MJ500
Total background expectation	153.28	47.89	12.52
Total statistical	8.1%	14%	28%
Total systematic	11%	23%	33%
$t\bar{t}$ theory – radiation	17%	30%	45%
$t\bar{t}$ normalisation uncertainty	11%	15%	20%
Template closure	4.9%	11%	11%
JES	4.1%	6.1%	5.8%
$t\bar{t}$ theory – generator choice	4.6%	6%	13%
$t\bar{t}$ theory – parton shower choice	0.91%	0.86%	7.2%
Template flavour	2.6%	2.6%	5.7%

**Table 5.10.:** Dominant ( $> 5\%$  in any region) systematic uncertainties for the MJ500 regions. Uncertainties are correlated so may add to more than the totals quoted. The  $t\bar{t}$  normalisation uncertainty corresponds to the uncertainty on the  $t\bar{t}$  scale factor, and is related to both the statistical and systematic uncertainties in the control regions.

### 5.6.2. Model-independent fit

As no significant excess of events is observed in any signal region, upper limits on the number of BSM events can be derived for each signal region. The expected number of events in eq. (5.15) is modified by adding a signal with one event in the signal regions with a normalisation factor  $\mu_{\text{sig}}$ , which will be referred to as the signal strength parameter. To remain as model-independent as possible, no assumptions are made about the source of the signal: no signal contamination is permitted in the control regions and no systematic uncertainties are assigned. From now onwards, the sole parameter of interest is  $\mu_{\text{sig}}$ , which will be relabelled as  $\mu$ . All other parameters (including the background normalisation factors) are considered as nuisance parameters  $\boldsymbol{\theta}$ . We then re-write the likelihood as  $\mathcal{L}(\boldsymbol{\mu}, \boldsymbol{\alpha} \mid \boldsymbol{n}, \boldsymbol{a}) \rightarrow \mathcal{L}(\mu, \boldsymbol{\theta})$ . A test statistic known as the profile log-likelihood ratio is used, which is derived from the profile likelihood ratio:

$$\lambda(\mu) = \frac{\mathcal{L}(\mu, \hat{\boldsymbol{\theta}}(\mu))}{\mathcal{L}(\hat{\mu}, \hat{\boldsymbol{\theta}})} \quad (5.17)$$

where  $\hat{\mu}$  and  $\hat{\boldsymbol{\theta}}$  are the maximum likelihood estimators (values of  $\mu$  and  $\boldsymbol{\theta}$  that maximise  $\mathcal{L}$ ) and  $\hat{\boldsymbol{\theta}}(\mu)$  is a curve with the maximum value of  $\mathcal{L}$  for a given  $\mu$ . The value of  $\hat{\mu}$  is forced to be positive so that only physical regions can be tested. By definition, we see that  $0 \leq \lambda(\mu) \leq 1$ , with  $\lambda(\mu)$  near 1 implying good agreement between the data and the hypothesis value of  $\mu$ .

The profile log-likelihood is then:

$$q_{\mu} = \begin{cases} -2 \ln \lambda(\mu) & \mu \geq \hat{\mu}; \\ 0 & \mu < \hat{\mu}, \end{cases} \quad (5.18)$$

where the requirement  $\mu \geq \hat{\mu}$  is made because when setting an upper limit one would not regard data with  $\mu < \hat{\mu}$  as representing less compatibility with  $\mu$  than the data obtained, and therefore this is not taken as part of the rejection region of the test. In order to calculate a  $p$ -value the pdf of the test statistic,  $f(q_{\mu} | \mu)$  must be calculated. An approximation to this can be made analytically for large numbers of observed events [211], or alternatively if the number of observed events is small an MC technique is used in which many pseudo-datasets are sampled from the model pdf in eq. (5.16) and the value of the test statistic is calculated for each one. The  $p$ -value for the model-independent signal+background hypothesis is

$$p_{s+b} = \int_{q_{\mu, \text{obs}}}^{\infty} f(q_{\mu} | \mu) dq_{\mu}. \quad (5.19)$$

The value of  $\mu$  is scanned over until  $p_{s+b} < 0.05$ , which corresponds to 95% confidence level exclusion on the signal+background hypothesis with signal strength  $\mu$ . As only 1 signal event was injected into the signal region, the value of  $\mu$  for which  $p_{s+b} = 0.05$  gives the 95% CL upper limit on the number of signal events in the signal region, denoted  $S_{\text{obs}}^{95}$ . An example of the scan is shown in figure 5.21. This upper limit can also be interpreted as the upper limit on the visible cross-section,  $\langle \epsilon \sigma \rangle_{\text{obs}}^{95} = S_{\text{obs}}^{95} / \mathcal{L}_{\text{int}}$ , where  $\epsilon$  is the fraction of the total cross-section to which the signal region is sensitive. Observed upper limits on the number of signal events and on the visible cross section are given in table 5.11 for each signal region. The expected upper-limit,  $S_{\text{exp}}^{95}$  is also tabulated,

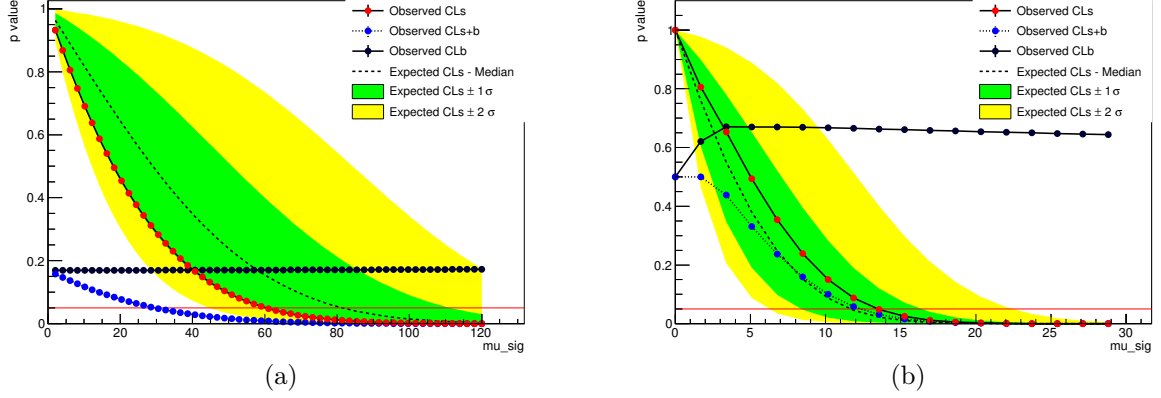


**Figure 5.21.:** The distribution of  $p$ -values for the  $CL_s$ ,  $CL_{s+b}$  and  $CL_b$  hypotheses as a function of the signal strength parameter in the SR-8j50-MJ340 region (left) and the SR-10j50-MJ500 region (right).

which is calculated assuming the background-only hypothesis and can be compared to the observed upper-limits.

The background-only hypothesis, specifically  $\mu = 0$  is calculated in a similar manner to the above. Here, the test statistic used is:

$$q_0 = \begin{cases} -2 \ln \lambda(0) & \hat{\mu} \geq 0; \\ 0 & \hat{\mu} < 0. \end{cases} \quad (5.20)$$

Note here that only non-negative values of  $\hat{\mu}$  are allowed. Although  $\hat{\mu} < 0$  may provide evidence against the background-only hypothesis, we specifically assume the signal will contribute to the event count. An under-fluctuation in data would cause  $\hat{\mu} < 0$ , but this does not show that the data contains any signal. The  $p$ -value is computed in a similar manner to the above:

$$p_0 = \int_{q_{0,\text{obs}}}^{\infty} f(q_0 | 0) dq_0, \quad (5.21)$$

and by convention we define  $p_b = 1 - p_0$ . The corresponding  $CL_B$  values are given in table 5.11.

It is the convention in ATLAS to assume that a signal can only lead to a positive enhancement of event counts in the signal region, and that a negative contribution

Signal channel	$\langle\epsilon\sigma\rangle_{\text{obs}}^{95}[\text{fb}]$	$S_{\text{obs}}^{95}$	$S_{\text{exp}}^{95}$	$CL_B$
SR-8j50-MJ340	3.3	60	$82_{-22}^{+30}$	0.17
SR-9j50-MJ340	1.6	29	$35_{-9}^{+13}$	0.28
SR-10j50-MJ340	0.78	14	$15_{-4}^{+6}$	0.43
SR-8j50-MJ500	1.8	33	$39_{-11}^{+15}$	0.28
SR-9j50-MJ500	1.4	25	$25_{-6}^{+9}$	0.50
SR-10j50-MJ500	0.74	14	$12_{-3}^{+5}$	0.66

**Table 5.11.:** Left to right: 95% CL upper limits on the visible cross section ( $\langle\epsilon\sigma\rangle_{\text{obs}}^{95}$ ) and on the number of signal events ( $S_{\text{obs}}^{95}$ ). The third column ( $S_{\text{exp}}^{95}$ ) shows the 95% CL upper limit on the number of signal events, given the expected number (and  $\pm 1\sigma$  excursions on the expectation) of background events. The last column indicates the  $CL_B$  value, i.e. the confidence level observed for the background-only hypothesis.

is unphysical. The presence of new physics is then consistent only with an excess of events. Conversely, one would not wish to exclude a new physics scenario on the grounds that fewer events were seen than predicted. In the case there is an under-fluctuation in the data, it is possible to exclude the background-only hypothesis at 95% CL, and therefore also exclude any signal model, even if the search has no sensitivity to it<sup>7</sup>. In order to protect against this, the convention in ATLAS is to adopt the conservative  $CL_s$  prescription [212], in which the  $p$ -value for the signal plus background hypothesis is normalised by the  $p$ -value for the background-only hypothesis:

$$CL_s = \frac{p_{s+b}}{1 - p_b}. \quad (5.22)$$

Notice that while the  $CL_s$  is not a true  $p$ -value, it is always larger than  $CL_{s+b}$ . Both the model-independent limits presented in table 5.11 and the model-dependent limits in the following section are calculated using  $CL_s$  values.

<sup>7</sup>Consider a scenario in which  $p_b < 0.05$ , then it is also true that  $p_{s+b} < 0.05$  for all  $s$ , including  $s = 0$ .

### 5.6.3. Model-dependent limits

The results are also interpreted in the context of the SUSY models described in section 5.2. For each of these models, a grid of points is generated by varying two of the parameters of the model. For the pMSSM case, the gluino mass and Higgsino mass parameters are varied, for the two-step case it is the gluino mass and lightest neutralino mass that are varied. The expected number of events from each of these points is calculated in the signal and control regions. The model-dependent limits are then calculated with the same likelihood function and test statistic as for the model independent limits, except that the particular signal yield is used and signal contamination in the control regions is also accounted for. Furthermore, systematic uncertainties on the signal are also incorporated into the likelihood. For each model point, the observed and expected upper limits at 95%  $\text{CL}_s$  are calculated in each signal region.

For each signal grid, an interpolated curve is drawn between the  $\text{CL}_s$  values (both observed and expected, separated) for each point from the signal region with the highest expected  $\text{CL}_s$  value. The result is shown in figure 5.22 for the pMSSM grid, and figure 5.23 for the two-step grid. The location of each signal point, and which signal region had the largest expected  $\text{CL}_s$  is shown in figure 5.24 for both pMSSM and two-step grids.

### 5.6.4. Comparison with the CMS experiment

The CMS collaboration also produce a suite of searches for SUSY, and some of these may also be sensitive to the models used in this search. Some care must be taken when making a comparison with the CMS searches, as different analysis strategies are typically employed. Furthermore, none of the CMS searches use the models described in this thesis to optimise or interpret their searches. Nonetheless some comparison is possible. The most similar CMS search that targets high jet multiplicity final states is documented in reference [213], which has signal regions with some similarity to those in this analysis, for example regions requiring no leptons and at least 9 jets. However, all signal regions in the CMS search require  $H_{\text{T}}^{\text{miss}} > 300 \text{ GeV}$ , where  $H_{\text{T}}^{\text{miss}}$  is the magnitude of the negative vector sum of the jet momenta in the event. This will be roughly equivalent to  $E_{\text{T}}^{\text{miss}}$  in



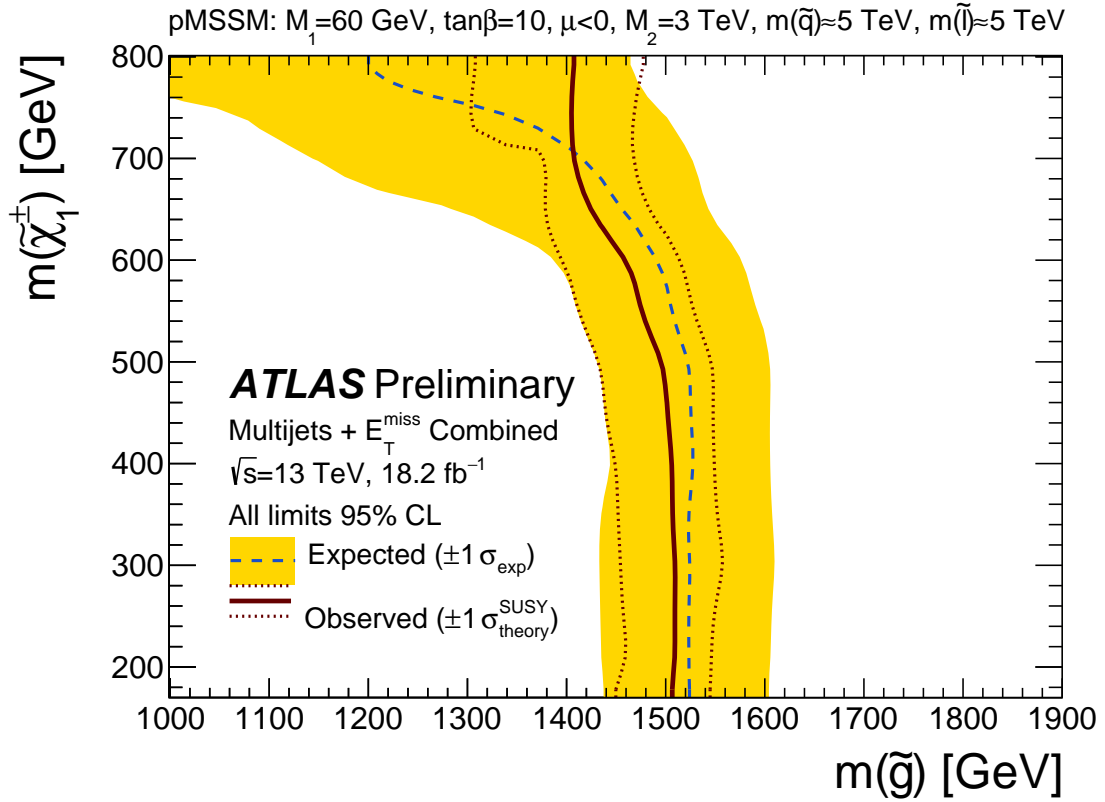


**Figure 5.22.:** 95% exclusion curve for the pMSSM-slice model. The solid red and dashed blue curves show the 95% CL observed and expected limits, respectively, including all uncertainties except the theoretical signal cross-section uncertainty (PDF and scale). The dotted red lines bracketing the observed limit represent the result produced when moving the signal cross-section by  $\pm 1\sigma$  (as defined by the PDF and scale uncertainties). The shaded yellow band around the expected limit shows the  $\pm 1\sigma$  variation of the expected limit.

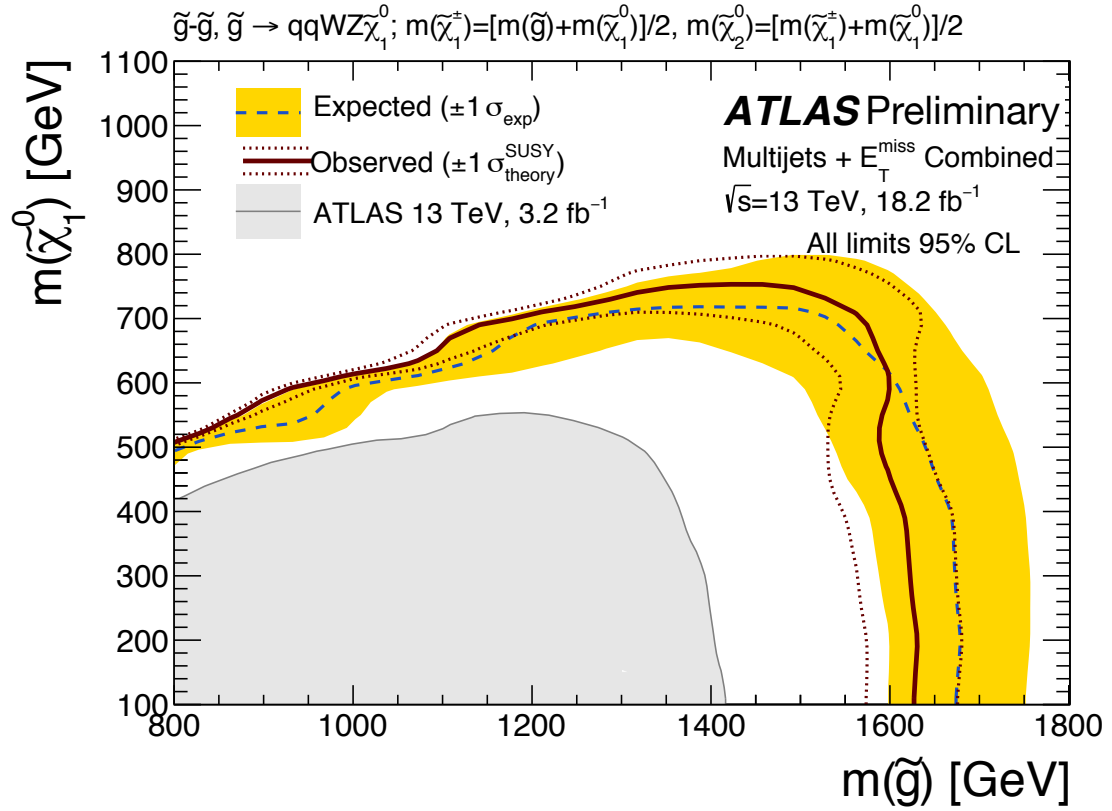


**Figure 5.23.:** 95% exclusion curve for the two-step simplified model. The shaded grey area shows the observed exclusion from a previous iteration of the analysis [4]. Other details are as described in figure 5.22.

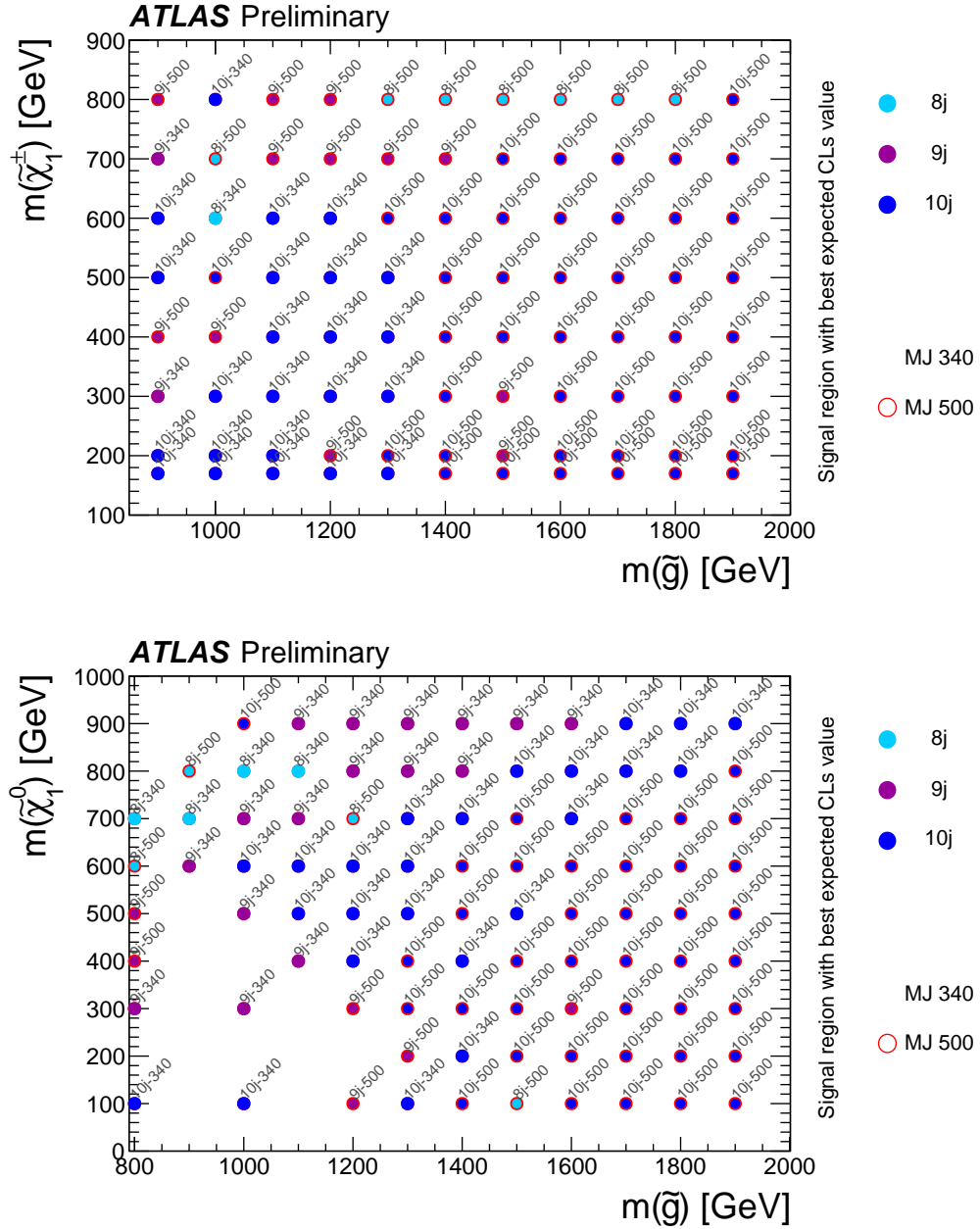


**Figure 5.24.:** Location of model points for the pMSSM (left) and two-step (right) grids, with the signal region yielding the largest expected  $CL_s$  value indicated on the point.

ATLAS, as the jet mismeasurement dominates the  $E_T^{\text{miss}}$  in high jet multiplicity events. Only 18% of events in the SR-9j50-MJ340 region had  $E_T^{\text{miss}} > 300$  GeV, and removing the  $M_J^\Sigma$  or  $E_T^{\text{miss}}/\sqrt{H_T}$  requirements only reduces this percentage. This illustrates that there is a small overlap with this search and those performed by CMS but their approach may have sensitivity to the models considered in this chapter.

## 5.7. Conclusions

This chapter has presented a search for new phenomena in events with high jet multiplicities using  $18.2\text{ fb}^{-1}$  of data collected by the ATLAS detector at the LHC. Key to this search was the  $E_T^{\text{miss}}/\sqrt{H_T}$  variable, whose properties were utilised in the estimation of the dominant multijet background. The other backgrounds were estimated with Monte Carlo simulation, and the predictions from the largest two of these backgrounds were improved via a fit to dedicated control regions. Furthermore, the variable  $M_J^\Sigma$  was utilised, for the first time by a Run-2 SUSY search, making use of jet-substructure techniques to optimise the signal significance in the signal regions. The two aforementioned variables, as well as a selection on the number of jets, was used to define six signal regions in which the Standard Model background was estimated. This followed an optimisation procedure in which two SUSY models were used: the pMSSM and two-step models described in section 5.2.

After performing a background-only fit, the data were found to agree with the Standard Model prediction within one standard deviation of the uncertainty on the background prediction in all signal regions, meaning no statistically significant excess was found. As a result, both model-independent and model-dependent limits were set on new physics models. In the latter case, the two signal grids used for optimisation studies were also used for the interpretation of results. This search extended the exclusion of gluinos by around 100 GeV in mass for both signal models, compared to previous results.

## 6 | Summary and outlook

So far, the LHC programme has been very successful. During the 8 TeV Run-1 of the LHC programme the Higgs boson was discovered, completing the Standard Model. As I write this thesis, we are in the midst of Run-2 and data are currently being collected by the LHC experiments at a centre of mass energy of 13 TeV. My time as a DPhil student began at the intersection of these two periods, during the long shutdown of the LHC between Run-1 and Run-2, which is reflected in this thesis.

The first analysis, described in chapter 4, presents a summary of the impact of Run-1 ATLAS SUSY searches on the pMSSM. The approach used attempts to address the problems with interpreting the null results of searches for SUSY, which is challenging given there are over 100 free parameters in the ordinary MSSM. The interplay between ATLAS searches and other constraints on SUSY (from Dark Matter experiments, heavy flavour results and precision electroweak measurements) were also explored, showing a complementarity between the approaches. The results also showed there were no “gaping holes” left by the Run-1 ATLAS searches, but certain corners of phase space were found to be untouched. This led to new search strategies being developed during Run-2 to specifically target these areas.

One search that benefited was also the second analysis described in this thesis, which is a direct search for new physics with 13 TeV data. Final states with large jet multiplicity were targeted, which are difficult to calculate theoretically, making it a challenge to estimate the Standard Model background. The challenge was addressed by employing a powerful data-driven technique to estimate the background – the template method – based on the properties of the  $E_T^{\text{miss}}/\sqrt{H_T}$  variable. The search excludes gluinos with

masses below 1.6 TeV in a simplified model where they decay via  $\tilde{g} \rightarrow qqWZ\tilde{\chi}_1^0$ . The results provided world-leading sensitivity to the simplified SUSY scenarios employed, but have now been superseded by an updated analysis that I also led [2].

Although no physics beyond the Standard Model has been found, the LHC is collecting yet more data that will allow further tests of the Standard Model and searches for new physics. The ever increasing integrated luminosity will allow more precise measurements to be made, and new areas of phase space to be explored. Ultimately, this will bring us closer to answering that fundamental question: what is the universe made of?



# A | Additional theoretical background

## A.1. Quantum Electrodynamics

Quantum electrodynamics, or QED, can be used as a starting point to describe some of the relevant symmetry principles in the Standard Model. We start with the Dirac Lagrangian, describing a fermion field  $\psi$  with mass  $m$ :

$$\mathcal{L}_{\text{Dirac}} = \bar{\psi}(i\partial_\mu\gamma^\mu - m)\psi, \quad (\text{A.1})$$

where  $\gamma^\mu$  are the Dirac matrices. As is, eq. (A.1) is not invariant under the U(1) local gauge transformation,  $\psi \rightarrow e^{i\alpha(x)}\psi$ . To restore the invariance, the covariant derivative  $\partial_\mu$  is replaced with the gauge covariant derivative:

$$D_\mu = \partial_\mu - ieA_\mu, \quad (\text{A.2})$$

where  $A_\mu$  is a new field in the theory (that we have added), which couples to the Dirac field  $\psi$  with strength equal to  $-e$  and transforms under U(1) as  $A_\mu \rightarrow A_\mu + \frac{1}{e}\partial_\mu\alpha$ . The replacement of  $\partial_\mu$  with  $D_\mu$  is equivalent to adding a new field with an interaction term of the form  $e\bar{\psi}\gamma^\mu A_\mu\psi$  to the Dirac Lagrangian. We can say that the Lagrangian gained an interaction term by demanding local gauge invariance, an important result exemplifying how *symmetry* is related to *dynamics*.

Adding the Lagrangian for the  $A_\mu$  field then completes the description of a charged fermion field interacting with a Maxwell field, and we have

$$\mathcal{L}_{\text{QED}} = \bar{\psi}(i\gamma^\mu D_\mu - m)\psi - \frac{1}{4}F_{\mu\nu}F^{\mu\nu}. \quad (\text{A.3})$$



QED is currently the most precisely verified theory, currently to within 1 part in  $10^8$ .

As an aside, applying the Euler-Lagrange equation for  $A_\mu$  to  $\mathcal{L}_{\text{QED}}$ , one obtains:

$$\partial_\mu \left( \frac{\partial \mathcal{L}_{\text{QED}}}{\partial (\partial_\nu A_\mu)} \right) = \frac{\partial \mathcal{L}_{\text{QED}}}{\partial A_\mu} \quad (\text{A.4})$$

$$\partial_\nu F^{\mu\nu} = e\bar{\psi}\gamma^\mu\psi \quad (\text{A.5})$$

$$\partial_\nu \partial^\nu A^\mu = -e\bar{\psi}\gamma^\mu\psi \text{ in the Lorentz gauge, } \partial_\mu A^\mu = 0, \quad (\text{A.6})$$

which is a wave equation for the electromagnetic field, equivalent to the one obtainable from the classical Maxwell equations. In fact, all of Maxwell's equations can be extracted from eq. (A.6).

This same idea can be generalised by noting that imposing gauge invariance on a free Lagrangian leads to the appearance of interacting gauge bosons. The fundamental difference between this example and the other more complicated gauge theories is that the symmetry transformations may involve more than one state or field at a time, instead of just one as is the case here. Consequently, the phase factors  $\alpha(x)$  become  $n \times n$  matrices, where  $n$  is the dimension of the group representation.

## A.2. Quark mixing and CP-violation

Experimentally we observe decays such as  $\Lambda \rightarrow pe^-\bar{\nu}_e$ , which involves cross-generation transitions of quarks (in this case  $s \rightarrow u$ ). We also observe the mixing between neutral mesons, which also includes cross-generation transitions of quarks. All of these transitions are mediated by the weak force, which leads us to the conclusion that the weak eigenstates must be a superposition of the mass (or physical) eigenstates. The weak eigenstates can therefore be written as

$$\begin{pmatrix} U_f \\ V_{ff'} D_{f'} \end{pmatrix} \quad \text{where } f, f' = 1, 2, 3 \quad (\text{A.7})$$

with  $U_1 = u$ ,  $D_1 = d$  et cetera and  $V_{ff'}$  denoting the Cabibbo-Kobayashi-Maskawa (CKM) matrix, a  $3 \times 3$  unitary matrix. Each element  $ij$  of this matrix describes the coupling

of a  $j \rightarrow i$  quark transition via a  $W$  boson. The CKM matrix has a single, irreducible complex phase, which accounts for CP-violation in the Standard Model. Furthermore, the unitary nature of the matrix forbids flavour changing neutral currents at the tree-level.

CP-violation can manifest itself in three ways: the asymmetrical mixing of neutral mesons, where one direction is favoured over another; directly, if a given decay occurs more frequently than its CP-mirror decay; and also by the interference of the above two effects for example when a meson and antimeson decay to the same final state. Via these mechanisms, matter can be preferentially produced over antimatter that, in principle, can give rise to the matter-dominated universe we observe today. However, there is not enough CP-violation in the Standard Model to account for the matter density currently observed.

### A.3. Higgs vacuum and cosmology

The minimum value of the Higgs potential (eq. (2.14)), is given by

$$V_{min} = -\frac{\lambda v^4}{4}. \quad (\text{A.8})$$

With  $v \approx 246 \text{ GeV}$  [34], one finds  $V_{min} \approx -10^9 \lambda \text{ GeV}^4$ . From cosmological observations, the total energy density of the universe is known to be rather small, of the order  $10^{-4} \text{ GeV}/\text{cm}^{-3}$ . After making the substitution  $1 \text{ GeV}^3 = 1.3 \times 10^{41} \text{ cm}^{-3}$  (when  $\hbar = c = 1$ ), one finds a huge value  $V_{min} \approx -10^{50} \lambda \text{ GeV}/\text{cm}^{-3}$ . Choosing a reasonable value for  $\lambda$ ,  $\lambda = 0.1$  (0.001), one obtains a contribution to the total energy density of the universe  $10^{54}$  ( $10^{52}$ ) times larger than the observed energy density of the universe.

This problem has a simple solution: to add a constant term to the Higgs potential, for example

$$V(\Phi) = \frac{\lambda}{4}(\Phi\Phi^\dagger - v^2)^2, \quad (\text{A.9})$$

which has a minimum value of  $V_{min} = 0$  by construction.

However, this can be seen as something of a fine-tuning problem. For the Higgs vacuum energy to be in accordance with the total energy density of the universe it requires an adjustment of the constant term in the potential to an accuracy of around  $10^{-54}$ . Furthermore, this has consequences for the space-time geometry of the universe, but hints that the spontaneous symmetry breaking mechanism of the universe may be connected with gravity.

## A.4. The WIMP Miracle

In the early universe, dark matter particles could pair-annihilate to Standard Model particles and vice versa. If the annihilation rate,  $\Gamma$  of the dark matter particles  $\chi\bar{\chi}$  is lower than the instantaneous expansion rate of the universe (the Hubble “constant” at that time)  $H$ , then the annihilation of  $\chi$ ’s freezes out. The dark matter relic density is then expected to be

$$\Omega_\chi h^2 \sim \frac{10^{-26} \text{ cm}^3/\text{s}}{\langle\sigma_{Av}\rangle}. \quad (\text{A.10})$$

Taking the velocity-weighted mean annihilation cross-section as  $\langle\sigma_{Av}\rangle \sim \alpha^2/m_\chi^2$ , where  $\alpha$  is the weak coupling constant and  $m_\chi$  the dark matter mass, eq. (A.10) can be written suggestively as

$$\Omega_\chi h^2 \sim 0.1 \left(\frac{0.01}{\alpha}\right)^2 \left(\frac{m_\chi}{100 \text{ GeV}}\right)^2. \quad (\text{A.11})$$

Assuming a weakly-interacting dark matter particle with coupling  $\alpha \sim 0.01$  and mass  $m_\chi \sim 100 \text{ GeV}$  gives the correct order of magnitude abundance today as measured by Planck,  $\Omega_\chi = 0.1188 \pm 0.0010$  [47]. This coincidence is known as the “WIMP miracle”.

## A.5. Particle masses in unbroken supersymmetry

If the fermion and boson states  $|f\rangle$  and  $|b\rangle$  are members of the same supermultiplet then by definition  $|f\rangle$  is proportional to some combination of  $Q$  and  $Q^\dagger$ , where  $Q$  are the generators of the SUSY transformation defined in section 2.3.1 (note spinor indices

have been suppressed). Let us choose  $Q|b\rangle = |f\rangle$ , then since  $P^\mu P_\mu|b\rangle = m_b^2|b\rangle$  and  $P^\mu P_\mu|f\rangle = m_f^2|f\rangle$

$$P^\mu P_\mu Q|b\rangle = P^\mu P_\mu|f\rangle = m_f^2|f\rangle \quad (\text{A.12})$$

$$= QP^\mu P_\mu|b\rangle = m_b^2 Q|b\rangle = m_b^2|b\rangle, \quad (\text{A.13})$$

where we have used the commutation relation  $[P_\mu, Q] = 0$  from which one infers  $[P_\mu P^\mu, Q] = 0$ . Hence,  $m_b = m_f$  for particles in the same supermultiplet. This symmetry is not observed in nature, meaning supersymmetry must be broken.

## B | Additional multijet systematic uncertainties

### B.1. Leptonic theory systematics

A full list of the  $t\bar{t}$  theory systematics is given in table B.1. See section 5.4.4 for further details.

### B.2. $H_T$ binning of the template

In the previous (2015) multijet analysis [4], the template method was binned in  $H_T$  to account for events with low  $H_T$  where the  $E_T^{\text{miss}}$  is not necessarily dominated by jet mis-measurement. As described in section 5.5.5,  $M_J^\Sigma$  and  $H_T$  are correlated, so by applying a cut of  $M_J^\Sigma > 340$  GeV we are applying a cut of approximately  $H_T > 500$  GeV (and  $M_J^\Sigma > 500$  GeV corresponds to approximately  $H_T > 800$  GeV), and so such low  $H_T$  event should be removed. However, it is not *necessarily* true that there is no longer any  $H_T$  dependence on the template.

In order to test this, the template was split into two bins in  $H_T$ :  $H_T < 1200$  GeV and  $H_T > 1200$  GeV. The two templates were calculated separately and then combined. This was then compared to the nominal template, and the comparison is shown in table B.2. The simplest conclusion is that for the  $M_J^\Sigma > 500$  GeV regions (which are shown in the lower part of the table), there is no significant difference between using the  $H_T$

Region	Powheg	amc@NLO	Madgraph	Rad.	Rad.
	Herwig++	Herwig++	Pythia8	Up	Down
SR-8j50-MJ340	-1.4 %	-12.0 %	-20.0 %	72.0 %	-43.0 %
CRW-7j50-MJ340	4.3 %	12.0 %	-21.0 %	45.0 %	-52.0 %
CRT-7j50-MJ340	-2.9 %	1.0 %	-8.0 %	46.0 %	-32.0 %
SR-9j50-MJ340	12.0 %	11.0 %	-18.0 %	130.0 %	-50.0 %
CRW-8j50-MJ340	48.0 %	14.0 %	-25.0 %	110.0 %	-42.0 %
CRT-8j50-MJ340	0.1 %	-7.0 %	-14.0 %	67.0 %	-37.0 %
SR-10j50-MJ340	49.0 %	12.0 %	-25.0 %	190.0 %	-71.0 %
CRW-9j50-MJ340	57.0 %	17.0 %	-46.0 %	85.0 %	-60.0 %
CRT-9j50-MJ340	16.0 %	2.7 %	-18.0 %	87.0 %	-43.0 %
SR-8j50-MJ500	-4.8 %	-15.0 %	-24.0 %	130.0 %	-46.0 %
CRW-7j50-MJ500	-28.0 %	-23.0 %	-45.0 %	52.0 %	-62.0 %
CRT-7j50-MJ500	8.3 %	-30.0 %	-21.0 %	55.0 %	-28.0 %
SR-9j50-MJ500	-3.7 %	1.4 %	-26.0 %	200.0 %	-59.0 %
CRW-8j50-MJ500	-28.0 %	-32.0 %	-55.0 %	120.0 %	-66.0 %
CRT-8j50-MJ500	-0.6 %	-29.0 %	-25.0 %	65.0 %	-35.0 %
SR-10j50-MJ500	28.0 %	1.6 %	-52.0 %	290.0 %	-56.0 %
CRW-9j50-MJ500	-83.0 %	-6.5 %	-63.0 %	140.0 %	-48.0 %
CRT-9j50-MJ500	26.0 %	-11.0 %	-29.0 %	99.0 %	-14.0 %

**Table B.1.:** Theoretical systematic uncertainties, in percent, for the 8j50-MJ340 signal region and the corresponding leptonic control regions. “Rad. Up” and “Rad. Down” refer to the radiation radiation tunes of the parton shower.

binned templates and the nominal template. Less clear is the case for the  $M_J^\Sigma > 340$  GeV regions. For SR-8j50-MJ340, the  $H_T$  binned template typically has better closure than the nominal template method, particularly in the  $2.5 < E_T^{\text{miss}}/\sqrt{H_T} < 3.5$  GeV<sup>1/2</sup> regions.

In order to keep the analysis simple, a flat 5% systematic will be applied to the  $M_J^\Sigma > 340$  GeV regions in order to account for possible  $H_T$  dependence.

### B.3. Complete breakdown of SR and CR yields

Tables B.3 to B.8 show a breakdown of pre- and post-fit yields for each of the background processes. The total background estimate is also shown, as well as the observed number of events in data.

Region	$E_{\text{T}}^{\text{miss}}/\sqrt{H_{\text{T}}}$ bin [ $\text{GeV}^{1/2}$ ]	Data	Nominal		$H_{\text{T}}$ binned		Prediction Diff. (%)
			Prediction	Deviation (%)	Prediction	Deviation (%)	
7	(1.5, 2.0)	16739	16670.23 $\pm$ 83.53	-0.41	16501.33 $\pm$ 83.21	-1.44	1.01
7	(2.0, 2.5)	7712	7802.76 $\pm$ 56.98	1.16	7686.10 $\pm$ 56.50	-0.34	1.50
7	(2.5, 3.5)	3944	4031.92 $\pm$ 42.02	2.18	3965.56 $\pm$ 41.82	0.54	1.65
7	(4.0, -1)	679	736.47 $\pm$ 19.41	7.80	741.06 $\pm$ 19.94	8.37	-0.62
8	(1.5, 2.0)	6675	6578.36 $\pm$ 32.85	-1.47	6389.92 $\pm$ 33.55	-4.46	2.86
8	(2.0, 2.5)	2929	3088.24 $\pm$ 22.55	5.16	2958.27 $\pm$ 22.74	0.99	4.21
8	(2.5, 3.5)	1475	1613.79 $\pm$ 17.32	8.60	1539.83 $\pm$ 17.62	4.21	4.58
9	(1.5, 2.0)	1490	1532.11 $\pm$ 7.74	2.75	1465.10 $\pm$ 8.27	-1.70	4.37
9	(2.0, 2.5)	689	720.26 $\pm$ 5.28	4.34	674.05 $\pm$ 5.55	-2.22	6.42
9	(2.5, 3.5)	335	377.87 $\pm$ 4.35	11.35	351.58 $\pm$ 4.58	4.72	6.96
10	(1.5, 2.0)	283	298.76 $\pm$ 1.60	5.27	281.89 $\pm$ 1.79	-0.39	5.65
10	(2.0, 2.5)	135	140.90 $\pm$ 1.17	4.19	129.27 $\pm$ 1.27	-4.44	8.25
10	(2.5, 3.5)	67	73.57 $\pm$ 0.84	8.93	66.95 $\pm$ 0.93	-0.07	9.00
7	(1.5, 2.0)	2680	2682.32 $\pm$ 38.64	0.09	2678.02 $\pm$ 38.60	-0.07	0.16
7	(2.0, 2.5)	1230	1170.23 $\pm$ 25.71	-5.11	1167.79 $\pm$ 25.67	-5.33	0.21
7	(2.5, 3.5)	635	643.63 $\pm$ 18.91	1.34	642.49 $\pm$ 18.90	1.17	0.18
7	(4.0, -1)	149	167.87 $\pm$ 10.10	11.24	168.26 $\pm$ 10.12	11.45	-0.23
8	(1.5, 2.0)	1590	1566.61 $\pm$ 22.55	-1.49	1559.07 $\pm$ 22.55	-1.98	0.48
8	(2.0, 2.5)	673	686.42 $\pm$ 14.95	1.96	682.15 $\pm$ 14.94	1.34	0.62
8	(2.5, 3.5)	361	388.38 $\pm$ 11.98	7.05	386.84 $\pm$ 12.00	6.68	0.40
9	(1.5, 2.0)	473	485.57 $\pm$ 7.04	2.59	481.83 $\pm$ 7.07	1.83	0.77
9	(2.0, 2.5)	212	213.70 $\pm$ 4.66	0.80	211.58 $\pm$ 4.68	-0.20	0.99
9	(2.5, 3.5)	101	121.02 $\pm$ 3.91	16.54	120.30 $\pm$ 3.93	16.04	0.60
10	(1.5, 2.0)	115	124.48 $\pm$ 1.85	7.62	123.20 $\pm$ 1.87	6.66	1.03
10	(2.0, 2.5)	55	55.18 $\pm$ 1.30	0.33	54.46 $\pm$ 1.31	-1.00	1.31
10	(2.5, 3.5)	29	30.96 $\pm$ 0.93	6.34	30.72 $\pm$ 0.94	5.60	0.78

**Table B.2.:** Results showing the difference between the nominal template, and the  $H_{\text{T}}$  binned template (as described in the text). The deviation is calculated as (data-prediction)/prediction. The difference in the predictions is calculated as (nominal - HT template)/nominal. The upper set of regions correspond to  $M_{\text{J}}^{\Sigma} > 340$  GeV and the lower regions correspond to  $M_{\text{J}}^{\Sigma} > 500$  GeV.



Region	SR-8j50-MJ340	CRW-7j50-MJ340	CRT-7j50-MJ340
Observed data events	424	173	604
Fitted bkg events	$467.14 \pm 39.74$	$172.76 \pm 13.15$	$604.07 \pm 24.62$
Fitted $t\bar{t} + h$ events	$1.68 \pm 0.50$	$0.71 \pm 0.21$	$6.72 \pm 2.01$
Fitted $t\bar{t} + X$ events	$8.88 \pm 2.65$	$3.10 \pm 0.93$	$22.71 \pm 6.78$
Fitted diboson events	$4.95 \pm 2.46$	$17.04 \pm 8.48$	$4.98 \pm 2.48$
Fitted single top events	$9.65 \pm 4.27$	$6.73 \pm 2.38$	$32.80 \pm 11.18$
Fitted $Z + \text{jets}$ events	$9.49 \pm 3.77$	$3.30 \pm 1.31$	$1.16 \pm 0.46$
Fitted $W + \text{jets}$ events	$12.41 \pm 5.15$	$61.10 \pm 25.03$	$23.49 \pm 9.92$
Fitted $t\bar{t}$ events	$107.99 \pm 28.79$	$80.78 \pm 18.63$	$512.21 \pm 31.05$
Fitted multijet events	$312.10 \pm 28.71$	$0.00 \pm 0.00$	$0.00 \pm 0.00$
Exp. Standard Model events	488.62	232.67	676.12
MC exp. $t\bar{t} + h$ events	1.68	0.71	6.72
MC exp. $t\bar{t} + X$ events	8.88	3.10	22.71
MC exp. diboson events	4.95	17.04	4.98
MC exp. single top events	9.65	6.73	32.79
MC exp. $Z + \text{jets}$ events	9.49	3.30	1.16
MC exp. $W + \text{jets}$ events	22.91	112.78	43.36
MC exp. $t\bar{t}$ events	118.98	89.01	564.40
Exp. multijet events	312.10	0.00	0.00

**Table B.3.:** Breakdown of pre- and post-fit yields for the SR-8j50-MJ340 region and its corresponding control regions.

Region	SR-9j50-MJ340	CRW-8j50-MJ340	CRT-8j50-MJ340
Observed data events	99	57	210
Fitted bkg events	$110.33 \pm 16.11$	$57.05 \pm 7.55$	$209.94 \pm 14.51$
Fitted $t\bar{t} + h$ events	$0.46 \pm 0.14$	$0.21 \pm 0.06$	$2.61 \pm 0.78$
Fitted $t\bar{t} + X$ events	$2.95 \pm 0.88$	$1.21 \pm 0.36$	$10.25 \pm 3.06$
Fitted diboson events	$0.50 \pm 0.25$	$7.23 \pm 3.60$	$2.22 \pm 1.10$
Fitted single top events	$1.35 \pm 1.15$	$1.87 \pm 0.72$	$11.40 \pm 4.06$
Fitted $Z + \text{jets}$ events	$1.75 \pm 0.69$	$1.15 \pm 0.46$	$0.21 \pm 0.08$
Fitted $W + \text{jets}$ events	$1.91^{+2.50}_{-1.91}$	$19.45 \pm 18.29$	$4.73 \pm 4.60$
Fitted $t\bar{t}$ events	$28.67 \pm 13.21$	$25.93 \pm 15.99$	$178.53 \pm 16.41$
Fitted multijet events	$72.75 \pm 10.20$	$0.00 \pm 0.00$	$0.00 \pm 0.00$
Exp. Standard Model events	116.18	77.65	240.47
MC exp. $t\bar{t} + h$ events	0.46	0.21	2.61
MC exp. $t\bar{t} + X$ events	2.95	1.21	10.25
MC exp. diboson events	0.50	7.23	2.22
MC exp. single top events	1.34	1.86	11.39
MC exp. $Z + \text{jets}$ events	1.75	1.15	0.21
MC exp. $W + \text{jets}$ events	3.56	36.22	8.80
MC exp. $t\bar{t}$ events	32.89	29.78	204.99
Exp. multijet events	72.75	0.00	0.00

**Table B.4.:** Breakdown of pre- and post-fit yields for the SR-9j50-MJ340 region and its corresponding control regions.

Region	SR-10j50-MJ340	CRW-9j50-MJ340	CRT-9j50-MJ340
Observed data events	22	15	64
Fitted bkg events	$23.44 \pm 6.06$	$14.99 \pm 3.76$	$63.99 \pm 8.01$
Fitted $t\bar{t} + h$ events	$0.08 \pm 0.02$	$0.04 \pm 0.01$	$0.69 \pm 0.21$
Fitted $t\bar{t} + X$ events	$0.74 \pm 0.22$	$0.32 \pm 0.10$	$3.60 \pm 1.08$
Fitted diboson events	$0.00 \pm 0.00$	$1.85 \pm 0.93$	$0.86 \pm 0.43$
Fitted single top events	$0.41 \pm 0.30$	$0.27 \pm 0.20$	$3.17 \pm 1.07$
Fitted $Z + \text{jets}$ events	$0.26 \pm 0.10$	$0.20 \pm 0.08$	$0.03 \pm 0.01$
Fitted $W + \text{jets}$ events	$0.65^{+0.66}_{-0.65}$	$5.60 \pm 5.49$	$1.57^{+1.58}_{-1.57}$
Fitted $t\bar{t}$ events	$7.21 \pm 5.84$	$6.72 \pm 3.81$	$54.07 \pm 8.57$
Fitted multijet events	$14.09 \pm 2.06$	$0.00 \pm 0.00$	$0.00 \pm 0.00$
Exp. Standard Model events	24.38	18.48	69.39
MC exp. $t\bar{t} + h$ events	0.08	0.04	0.69
MC exp. $t\bar{t} + X$ events	0.74	0.32	3.60
MC exp. diboson events	0.00	1.85	0.86
MC exp. single top events	0.41	0.27	3.17
MC exp. $Z + \text{jets}$ events	0.26	0.20	0.03
MC exp. $W + \text{jets}$ events	0.99	8.52	2.39
MC exp. $t\bar{t}$ events	7.81	7.28	58.65
Exp. multijet events	14.09	0.00	0.00

**Table B.5.:** Breakdown of pre- and post-fit yields for the SR-10j50-MJ340 region and its corresponding control regions.

Region	SR-8j50-MJ500	CRW-7j50-MJ500	CRT-7j50-MJ500
Observed data events	141	40	107
Fitted bkg events	$153.28 \pm 16.99$	$39.99 \pm 6.32$	$107.07 \pm 10.35$
Fitted $t\bar{t} + h$ events	$0.42 \pm 0.12$	$0.08 \pm 0.02$	$0.94 \pm 0.28$
Fitted $t\bar{t} + X$ events	$3.14 \pm 0.94$	$0.73 \pm 0.22$	$5.27 \pm 1.57$
Fitted diboson events	$1.27 \pm 0.63$	$4.74 \pm 2.37$	$2.09 \pm 1.04$
Fitted single top events	$3.48 \pm 1.48$	$1.26 \pm 0.70$	$7.98 \pm 3.16$
Fitted $Z + \text{jets}$ events	$3.44 \pm 1.37$	$0.74 \pm 0.30$	$0.24 \pm 0.09$
Fitted $W + \text{jets}$ events	$4.95 \pm 3.12$	$17.41 \pm 10.48$	$4.60 \pm 2.83$
Fitted $t\bar{t}$ events	$29.21 \pm 15.74$	$15.04 \pm 7.73$	$85.94 \pm 11.79$
Fitted multijet events	$107.38 \pm 8.69$	$0.00 \pm 0.00$	$0.00 \pm 0.00$
Exp. Standard Model events	166.49	63.02	135.02
MC exp. $t\bar{t} + h$ events	0.42	0.08	0.94
MC exp. $t\bar{t} + X$ events	3.14	0.73	5.27
MC exp. diboson events	1.27	4.74	2.09
MC exp. single top events	3.48	1.26	7.98
MC exp. $Z + \text{jets}$ events	3.44	0.74	0.24
MC exp. $W + \text{jets}$ events	10.36	36.42	9.62
MC exp. $t\bar{t}$ events	37.01	19.06	108.87
Exp. multijet events	107.38	0.00	0.00

**Table B.6.:** Breakdown of pre- and post-fit yields for the SR-8j50-MJ500 region and its corresponding control regions.

Region	SR-9j50-MJ500	CRW-8j50-MJ500	CRT-8j50-MJ500
Observed data events	48	16	56
Fitted bkg events	$47.89 \pm 11.17$	$15.98 \pm 3.42$	$55.92 \pm 7.52$
Fitted $t\bar{t} + h$ events	$0.14 \pm 0.04$	$0.04 \pm 0.01$	$0.49 \pm 0.15$
Fitted $t\bar{t} + X$ events	$1.33 \pm 0.40$	$0.39 \pm 0.12$	$3.10 \pm 0.93$
Fitted diboson events	$0.07 \pm 0.04$	$2.73 \pm 1.38$	$1.65 \pm 0.82$
Fitted single top events	$0.49^{+0.61}_{-0.49}$	$0.66 \pm 0.24$	$2.57 \pm 1.43$
Fitted $Z + \text{jets}$ events	$0.69 \pm 0.27$	$0.35 \pm 0.14$	$0.04 \pm 0.01$
Fitted $W + \text{jets}$ events	$0.65^{+1.22}_{-0.65}$	$4.57^{+5.47}_{-4.57}$	$1.07^{+1.39}_{-1.07}$
Fitted $t\bar{t}$ events	$11.11 \pm 10.04$	$7.24 \pm 4.83$	$47.00 \pm 8.18$
Fitted multijet events	$33.41 \pm 5.57$	$0.00 \pm 0.00$	$0.00 \pm 0.00$
Exp. Standard Model events	51.48	27.87	66.94
MC exp. $t\bar{t} + h$ events	0.14	0.04	0.49
MC exp. $t\bar{t} + X$ events	1.33	0.39	3.10
MC exp. diboson events	0.07	2.73	1.65
MC exp. single top events	0.49	0.66	2.57
MC exp. $Z + \text{jets}$ events	0.69	0.35	0.04
MC exp. $W + \text{jets}$ events	2.15	15.14	3.55
MC exp. $t\bar{t}$ events	13.20	8.56	55.55
Exp. multijet events	33.41	0.00	0.00

**Table B.7.:** Breakdown of pre- and post-fit yields for the SR-9j50-MJ500 region and its corresponding control regions.

Region	SR-10j50-MJ500	CRW-9j50-MJ500	CRT-9j50-MJ500
Observed data events	15	5	22
Fitted bkg events	$12.52 \pm 4.19$	$5.00 \pm 2.08$	$22.01 \pm 4.70$
Fitted $t\bar{t} + h$ events	$0.01 \pm 0.00$	$0.01 \pm 0.00$	$0.16 \pm 0.05$
Fitted $t\bar{t} + X$ events	$0.47 \pm 0.14$	$0.16 \pm 0.05$	$1.40 \pm 0.42$
Fitted diboson events	$0.00 \pm 0.00$	$1.33 \pm 0.68$	$0.81 \pm 0.40$
Fitted single top events	$0.00 \pm 0.00$	$0.14 \pm 0.12$	$1.54 \pm 0.52$
Fitted $Z + \text{jets}$ events	$0.14 \pm 0.05$	$0.11 \pm 0.05$	$0.02 \pm 0.01$
Fitted $W + \text{jets}$ events	$0.09^{+0.56}_{-0.09}$	$0.61^{+3.89}_{-0.61}$	$0.17^{+1.09}_{-0.17}$
Fitted $t\bar{t}$ events	$3.24^{+4.03}_{-3.24}$	$2.63^{+3.39}_{-2.63}$	$17.91 \pm 5.07$
Fitted multijet events	$8.57 \pm 1.59$	$0.00 \pm 0.00$	$0.00 \pm 0.00$
Exp. Standard Model events	13.65	8.83	26.59
MC exp. $t\bar{t} + h$ events	0.01	0.01	0.16
MC exp. $t\bar{t} + X$ events	0.47	0.16	1.40
MC exp. diboson events	0.00	1.33	0.81
MC exp. single top events	0.00	0.14	1.54
MC exp. $Z + \text{jets}$ events	0.14	0.11	0.02
MC exp. $W + \text{jets}$ events	0.55	3.90	1.08
MC exp. $t\bar{t}$ events	3.90	3.17	21.58
Exp. multijet events	8.57	0.00	0.00

**Table B.8.:** Breakdown of pre- and post-fit yields for the SR-10j50-MJ500 region and its corresponding control regions.



# Colophon

This thesis was made in  $\text{\LaTeX} 2_{\epsilon}$  using the “hepthesis” class [214].



# Bibliography

- [1] ATLAS Collaboration, *Search for new phenomena with large jet multiplicities and missing transverse momentum using large-radius jets and flavour-tagging at ATLAS in 13 TeV pp collisions*, JHEP **12** (2017) 034, [arXiv:1708.02794](#) [hep-ex].
- [2] ATLAS Collaboration, *Search for new phenomena with large jet multiplicities and missing transverse momentum using large-radius jets and flavour-tagging at ATLAS in 13 TeV pp collisions*, ATLAS-CONF-2017-033.  
<https://cds.cern.ch/record/2265802>.
- [3] ATLAS Collaboration, *Pursuit of new phenomena in final states with high jet multiplicity, high jet masses and missing transverse momentum with ATLAS at  $\sqrt{s} = 13$  TeV*, ATLAS-CONF-2016-095.  
<https://cds.cern.ch/record/2212161/>.
- [4] ATLAS Collaboration, *Search for new phenomena in final states with large jet multiplicities and missing transverse momentum with ATLAS using  $\sqrt{s} = 13$  TeV proton–proton collisions*, Phys. Lett. B **757** (2016) 334, [arXiv:1602.06194](#) [hep-ex].
- [5] ATLAS Collaboration, *Search for new phenomena in final states with large jet multiplicities and missing transverse momentum with ATLAS using  $\sqrt{s} = 13$  TeV proton–proton collisions*, ATLAS-CONF-2015-077.  
<https://cds.cern.ch/record/2114849>.
- [6] ATLAS Collaboration, *Summary of the ATLAS experiment’s sensitivity to*

- supersymmetry after LHC Run 1 – interpreted in the phenomenological MSSM*, JHEP **10** (2015) 134, [arXiv:1508.06608 \[hep-ex\]](#).
- [7] I. J. R. Aitchison and A. J. G. Hey, *Gauge Theories in Particle Physics: A Practical Introduction, Volume 1*. CRC Press, 2012.
- [8] I. J. R. Aitchison and A. J. G. Hey, *Gauge Theories in Particle Physics: A Practical Introduction, Volume 2*. CRC Press, 2012.
- [9] V. A. Bednyakov, N. D. Giokaris, and A. V. Bednyakov, *On Higgs mass generation mechanism in the Standard Model*, Phys. Part. Nucl. **39** (2008) 13–36, [arXiv:hep-ph/0703280 \[HEP-PH\]](#).
- [10] S. P. Martin, *A Supersymmetry primer*, [arXiv:hep-ph/9709356 \[hep-ph\]](#). [Adv. Ser. Direct. High Energy Phys.18,1(1998)].
- [11] P. Binetruy, *Supersymmetry: Theory, experiment and cosmology*. 2006.
- [12] E. D. Bloom, D. H. Coward, H. DeStaebler, et al., *High-Energy Inelastic  $e$ - $p$  Scattering at  $6^\circ$  and  $10^\circ$* , Phys. Rev. Lett. **23** (1969) 930–934. <https://link.aps.org/doi/10.1103/PhysRevLett.23.930>.
- [13] M. Breidenbach, J. I. Friedman, H. W. Kendall, et al., *Observed Behavior of Highly Inelastic Electron-Proton Scattering*, Phys. Rev. Lett. **23** (1969) 935–939. <https://link.aps.org/doi/10.1103/PhysRevLett.23.935>.
- [14] J. E. Augustin, A. M. Boyarski, M. Breidenbach, et al., *Discovery of a Narrow Resonance in  $e^+e^-$  Annihilation*, Phys. Rev. Lett. **33** (1974) 1406–1408. <https://link.aps.org/doi/10.1103/PhysRevLett.33.1406>.
- [15] J. J. Aubert, U. Becker, P. J. Biggs, et al., *Experimental Observation of a Heavy Particle  $J$* , Phys. Rev. Lett. **33** (1974) 1404–1406. <https://link.aps.org/doi/10.1103/PhysRevLett.33.1404>.
- [16] S. W. Herb, D. C. Hom, L. M. Lederman, et al., *Observation of a Dimuon Resonance at 9.5 GeV in 400-GeV Proton-Nucleus Collisions*, Phys. Rev. Lett. **39** (1977) 252–255. <https://link.aps.org/doi/10.1103/PhysRevLett.39.252>.

- [17] CDF Collaboration, *Observation of Top Quark Production in  $\bar{p}p$  Collisions with the Collider Detector at Fermilab*, Phys. Rev. Lett. **74** (1995) 2626–2631.  
<https://link.aps.org/doi/10.1103/PhysRevLett.74.2626>.
- [18] DØ Collaboration, *Search for High Mass Top Quark Production in  $p\bar{p}$  Collisions at  $\sqrt{s} = 1.8$  TeV*, Phys. Rev. Lett. **74** (1995) 2422–2426.  
<https://link.aps.org/doi/10.1103/PhysRevLett.74.2422>.
- [19] J. J. Thomson, *XL. Cathode Rays*, Philosophical Magazine Series 5 **44** no. 269, (1897) 293–316. <http://dx.doi.org/10.1080/14786449708621070>.
- [20] F. Reines and C. L. Cowan, *The Neutrino*, Nature **178** no. 4531, (1956) 446–449.  
<http://dx.doi.org/10.1038/178446a0>.
- [21] C. D. Anderson and S. H. Neddermeyer, *Cloud Chamber Observations of Cosmic Rays at 4300 Meters Elevation and Near Sea-Level*, Phys. Rev. **50** (1936) 263–271.  
<https://link.aps.org/doi/10.1103/PhysRev.50.263>.
- [22] J. C. Street and E. C. Stevenson, *New Evidence for the Existence of a Particle of Mass Intermediate Between the Proton and Electron*, Phys. Rev. **52** (1937) 1003–1004. <https://link.aps.org/doi/10.1103/PhysRev.52.1003>.
- [23] G. Danby, J.-M. Gaillard, K. Goulianos, et al., *Observation of High-Energy Neutrino Reactions and the Existence of Two Kinds of Neutrinos*, Phys. Rev. Lett. **9** (1962) 36–44. <https://link.aps.org/doi/10.1103/PhysRevLett.9.36>.
- [24] M. L. Perl, G. S. Abrams, A. M. Boyarski, et al., *Evidence for Anomalous Lepton Production in  $e^+ - e^-$  Annihilation*, Phys. Rev. Lett. **35** (1975) 1489–1492.  
<https://link.aps.org/doi/10.1103/PhysRevLett.35.1489>.
- [25] DONUT Collaboration, K. Kodama et al., *Observation of tau neutrino interactions*, Phys. Lett. **B504** (2001) 218–224, [arXiv:hep-ex/0012035](https://arxiv.org/abs/hep-ex/0012035) [hep-ex].
- [26] A. H. Compton, *A Quantum Theory of the Scattering of X-rays by Light Elements*, Phys. Rev. **21** (1923) 483–502.  
<https://link.aps.org/doi/10.1103/PhysRev.21.483>.

- [27] UA1 Collaboration, *Experimental observation of isolated large transverse energy electrons with associated missing energy at  $\sqrt{s} = 540$  GeV*, Physics Letters B **122** no. 1, (1983) 103 – 116.  
<http://www.sciencedirect.com/science/article/pii/0370269383911772>.
- [28] UA2 Collaboration, *Observation of single isolated electrons of high transverse momentum in events with missing transverse energy at the CERN pp collider*, Physics Letters B **122** no. 5, (1983) 476 – 485.  
<http://www.sciencedirect.com/science/article/pii/0370269383916052>.
- [29] UA1 Collaboration, *Experimental observation of lepton pairs of invariant mass around 95 GeV/c<sup>2</sup> at the CERN SPS collider*, Physics Letters B **126** no. 5, (1983) 398 – 410.  
<http://www.sciencedirect.com/science/article/pii/0370269383901880>.
- [30] UA2 Collaboration, *Evidence for  $Z^0 \rightarrow e^+e^-$  at the CERN pp collider*, Physics Letters B **129** no. 1, (1983) 130 – 140.  
<http://www.sciencedirect.com/science/article/pii/037026938390744X>.
- [31] P. Söding, *On the discovery of the gluon*, The European Physical Journal H **35** no. 1, (2010) 3–28. <http://dx.doi.org/10.1140/epjh/e2010-00002-5>.
- [32] ATLAS Collaboration, *Observation of a new particle in the search for the Standard Model Higgs boson with the ATLAS detector at the LHC*, Phys. Lett. B **716** (2012) 1, arXiv:1207.7214 [hep-ex].
- [33] CMS Collaboration, *Observation of a new boson at a mass of 125 GeV with the CMS experiment at the LHC*, Phys. Lett. B **716** (2012) 30, arXiv:1207.7235 [hep-ex].
- [34] Particle Data Group, *Review of Particle Physics*, Chinese Physics C **40** no. 100001, (2016).
- [35] R. Davis, D. S. Harmer, and K. C. Hoffman, *Search for Neutrinos from the Sun*, Phys. Rev. Lett. **20** (1968) 1205–1209.  
<https://link.aps.org/doi/10.1103/PhysRevLett.20.1205>.

- [36] Super-Kamiokande Collaboration, *Evidence for Oscillation of Atmospheric Neutrinos*, Phys. Rev. Lett. **81** (1998) 1562–1567.  
<https://link.aps.org/doi/10.1103/PhysRevLett.81.1562>.
- [37] SNO Collaboration, *Direct evidence for neutrino flavor transformation from neutral current interactions in the Sudbury Neutrino Observatory*, Phys. Rev. Lett. **89** (2002) 011301, [arXiv:nuc1-ex/0204008](https://arxiv.org/abs/nuc1-ex/0204008) [nuc1-ex].
- [38] SNO Collaboration, *Measurement of the Rate of  $\nu_e + d \rightarrow p + p + e^-$  Interactions Produced by  $^8\text{B}$  Solar Neutrinos at the Sudbury Neutrino Observatory*, Phys. Rev. Lett. **87** (2001) 071301.  
<https://link.aps.org/doi/10.1103/PhysRevLett.87.071301>.
- [39] KamLAND Collaboration, *First results from KamLAND: Evidence for reactor anti-neutrino disappearance*, Phys. Rev. Lett. **90** (2003) 021802, [arXiv:hep-ex/0212021](https://arxiv.org/abs/hep-ex/0212021) [hep-ex].
- [40] E. Majorana, *Teoria simmetrica dell’elettrone e del positrone*, Il Nuovo Cimento (1924-1942) **14** no. 4, (2008) 171. <http://dx.doi.org/10.1007/BF02961314>.
- [41] LHCb Collaboration, *Observation of  $J/\psi p$  Resonances Consistent with Pentaquark States in  $\Lambda_b^0 \rightarrow J/\psi K^- p$  Decays*, Phys. Rev. Lett. **115** (2015) 072001. <https://link.aps.org/doi/10.1103/PhysRevLett.115.072001>.
- [42] E. Noether, *Invariant variation problems*, Transport Theory and Statistical Physics **1** no. 3, (1971) 186–207. <http://dx.doi.org/10.1080/00411457108231446>.  
Translated from *Invariante Variationsprobleme*, Nachr. d. König. Gesellsch. d. Wiss. zu Göttingen, Math-phys. (1918).
- [43] F. Englert and R. Brout, *Broken Symmetry and the Mass of Gauge Vector Mesons*, Phys. Rev. Lett. **13** (1964) 321–323.  
<https://link.aps.org/doi/10.1103/PhysRevLett.13.321>.
- [44] P. W. Higgs, *Broken Symmetries and the Masses of Gauge Bosons*, Phys. Rev. Lett. **13** (1964) 508–509.  
<https://link.aps.org/doi/10.1103/PhysRevLett.13.508>.

- 
- [45] G. S. Guralnik, C. R. Hagen, and T. W. B. Kibble, *Global Conservation Laws and Massless Particles*, Phys. Rev. Lett. **13** (1964) 585–587.  
<https://link.aps.org/doi/10.1103/PhysRevLett.13.585>.
- [46] M. McIrvin, *Renormalization in QED*,  
<https://commons.wikimedia.org/w/index.php?curid=1008752>.
- [47] Planck Collaboration, *Planck 2015 results. XIII. Cosmological parameters*, Astron. Astrophys. **594** (2016) A13, [arXiv:1502.01589](https://arxiv.org/abs/1502.01589) [astro-ph.CO].
- [48] T. Blum, A. Denig, I. Logashenko, et al., *The Muon ( $g-2$ ) Theory Value: Present and Future*, [arXiv:1311.2198](https://arxiv.org/abs/1311.2198) [hep-ph].
- [49] G. Bertone and D. Hooper, *A History of Dark Matter*, Submitted to: Rev. Mod. Phys. (2016), [arXiv:1605.04909](https://arxiv.org/abs/1605.04909) [astro-ph.CO].
- [50] K. Garrett and G. Duda, *Dark Matter: A Primer*, Adv. Astron. **2011** (2011) 968283, [arXiv:1006.2483](https://arxiv.org/abs/1006.2483) [hep-ph].
- [51] N. Arkani-Hamed, S. Dimopoulos, and G. R. Dvali, *The Hierarchy problem and new dimensions at a millimeter*, Phys. Lett. **B429** (1998) 263–272,  
[arXiv:hep-ph/9803315](https://arxiv.org/abs/hep-ph/9803315) [hep-ph].
- [52] G. 't Hooft, *Naturalness, chiral symmetry, and spontaneous chiral symmetry breaking*, NATO Sci. Ser. B **59** (1980) 135–157.
- [53] S. R. Coleman and J. Mandula, *All Possible Symmetries of the S Matrix*, Phys. Rev. **159** (1967) 1251–1256.
- [54] R. Haag, J. T. Lopuszanski, and M. Sohnius, *All Possible Generators of Supersymmetries of the s Matrix*, Nucl. Phys. **B88** (1975) 257.
- [55] A. H. Chamseddine, R. Arnowitt, and P. Nath, *Locally Supersymmetric Grand Unification*, Phys. Rev. Lett. **49** (1982) 970–974.  
<https://link.aps.org/doi/10.1103/PhysRevLett.49.970>.
- [56] M. Dine and W. Fischler, *A Phenomenological Model of Particle Physics Based on Supersymmetry*, Phys. Lett. **B 110** (1982) 227.

- [57] L. Alvarez-Gaume, M. Claudson, and M. B. Wise, *Low-Energy Supersymmetry*, Nucl. Phys. **B 207** (1982) 96.
- [58] C. R. Nappi and B. A. Ovrut, *Supersymmetric Extension of the  $SU(3)\times SU(2)\times U(1)$  Model*, Phys. Lett. **B 113** (1982) 175.
- [59] L. Randall and R. Sundrum, *Out of this world supersymmetry breaking*, Nucl. Phys. **B557** (1999) 79–118, [arXiv:hep-th/9810155](https://arxiv.org/abs/hep-th/9810155) [hep-th].
- [60] G. F. Giudice, M. A. Luty, H. Murayama, and R. Rattazzi, *Gaugino mass without singlets*, JHEP **12** (1998) 027, [arXiv:hep-ph/9810442](https://arxiv.org/abs/hep-ph/9810442) [hep-ph].
- [61] Super-Kamiokande Collaboration, *Search for Proton Decay via  $p \rightarrow e^+\pi^0$  and  $p \rightarrow \mu^+\pi^0$  in a Large Water Cherenkov Detector*, Phys. Rev. Lett. **102** (2009) 141801. <https://link.aps.org/doi/10.1103/PhysRevLett.102.141801>.
- [62] Super-Kamiokande Collaboration, *Search for Nucleon Decay into Charged Anti-lepton plus Meson in Super-Kamiokande I and II*, Phys. Rev. **D85** (2012) 112001, [arXiv:1203.4030](https://arxiv.org/abs/1203.4030) [hep-ex].
- [63] H. K. Dreiner, *Comments on a Massless Neutralino*, AIP Conf. Proc. **1200** (2010) 73–80, [arXiv:0910.1509](https://arxiv.org/abs/0910.1509) [hep-ph].
- [64] H. Georgi and S. L. Glashow, *Unity of All Elementary-Particle Forces*, Phys. Rev. Lett. **32** (1974) 438–441. <https://link.aps.org/doi/10.1103/PhysRevLett.32.438>.
- [65] H. E. Haber, R. Hempfling, and A. H. Hoang, *Approximating the radiatively corrected Higgs mass in the minimal supersymmetric model*, Z. Phys. **C75** (1997) 539–554, [arXiv:hep-ph/9609331](https://arxiv.org/abs/hep-ph/9609331) [hep-ph].
- [66] M. Papucci, J. T. Ruderman, and A. Weiler, *Natural SUSY Endures*, JHEP **09** (2012) 035, [arXiv:1110.6926](https://arxiv.org/abs/1110.6926) [hep-ph].
- [67] R. Barbieri and G. Giudice, *Upper bounds on supersymmetric particle masses*, Nucl. Phys. **B306** (1988) 63.

- [68] C. Borschensky, M. Krämer, A. Kulesza, et al., *Squark and gluino production cross sections in pp collisions at  $\sqrt{s} = 13, 14, 33$  and 100 TeV*, Eur. Phys. J. **C74** no. 12, (2014) 3174, arXiv:1407.5066 [hep-ph].
- [69] ATLAS Collaboration, *The ATLAS Experiment at the CERN Large Hadron Collider*, JINST **3** (2008) S08003.
- [70] L. Evans and P. Bryant, *LHC Machine*, Journal of Instrumentation **3** no. 08, (2008) S08001. <http://stacks.iop.org/1748-0221/3/i=08/a=S08001>.
- [71] D. C. Hall, *Discovery and measurement of the Higgs boson in the WW decay channel*. DPhil thesis, University of Oxford, August, 2014. CERN-THESIS-2014-130.
- [72] CMS Collaboration, *The CMS Experiment at the CERN LHC*, JINST **3** (2008) S08004.
- [73] LHCb Collaboration, *The LHCb Detector at the LHC*, JINST **3** (2008) S08005.
- [74] ALICE Collaboration, *The ALICE experiment at the CERN LHC*, JINST **3** no. 08, (2008) S08002. <http://stacks.iop.org/1748-0221/3/i=08/a=S08002>.
- [75] ATLAS Collaboration, *Characterization of Interaction-Point Beam Parameters Using the pp Event-Vertex Distribution Reconstructed in the ATLAS Detector at the LHC*, Tech. Rep. ATLAS-CONF-2010-027, CERN, Geneva, May, 2010. <http://cds.cern.ch/record/1277659>.
- [76] L. Evans and P. Bryant, *LHC Machine*, Journal of Instrumentation **3** no. 08, (2008) S08001. <http://stacks.iop.org/1748-0221/3/i=08/a=S08001>.
- [77] ATLAS Collaboration, *Luminosity Public Results*,. <https://twiki.cern.ch/twiki/bin/view/AtlasPublic/LuminosityPublicResults>.
- [78] ATLAS Collaboration, *Luminosity Public Results in Run-2*,. <https://twiki.cern.ch/twiki/bin/view/AtlasPublic/LuminosityPublicResultsRun2>.



- [79] J. J. Goodson, *Search for Supersymmetry in States with Large Missing Transverse Momentum and Three Leptons including a Z-Boson*. PhD thesis, Stony Brook University, May, 2012. CERN-THESIS-2012-053.
- [80] The ATLAS Pixel Collaboration, *ATLAS pixel detector electronics and sensors*, JINST **3** (2008) P07007.
- [81] ATLAS Collaboration, *The ATLAS Insertable B-Layer: from construction to operation*, JINST **11** no. 12, (2016) C12036, [arXiv:1610.01994 \[physics.ins-det\]](#).
- [82] M. Capeans, G. Darbo, K. Einsweiler, et al., *ATLAS Insertable B-Layer Technical Design Report*, Tech. Rep. CERN-LHCC-2010-013. ATLAS-TDR-19, Sep, 2010. <http://cds.cern.ch/record/1291633>.
- [83] ATLAS Collaboration, *Operation and performance of the ATLAS semiconductor tracker*, Journal of Instrumentation **9** no. 08, (2014) P08009. <http://stacks.iop.org/1748-0221/9/i=08/a=P08009>.
- [84] The ATLAS TRT Collaboration, *The ATLAS TRT Barrel Detector*, Journal of Instrumentation **3** no. 02, (2008) P02014. <http://stacks.iop.org/1748-0221/3/i=02/a=P02014>.
- [85] The ATLAS TRT Collaboration, *The ATLAS TRT end-cap detectors*, Journal of Instrumentation **3** no. 10, (2008) P10003. <http://stacks.iop.org/1748-0221/3/i=10/a=P10003>.
- [86] The ATLAS TRT Collaboration, *The ATLAS Transition Radiation Tracker (TRT) proportional drift tube: design and performance*, Journal of Instrumentation **3** no. 02, (2008) P02013. <http://stacks.iop.org/1748-0221/3/i=02/a=P02013>.
- [87] N. Nikiforou, *Performance of the ATLAS Liquid Argon Calorimeter after three years of LHC operation and plans for a future upgrade*, in *Proceedings, 3rd International Conference on Advancements in Nuclear Instrumentation Measurement Methods and their Applications (ANIMMA 2013): Marseille, France*,

- June 23-27, 2013*. 2013. [arXiv:1306.6756](#) [physics.ins-det].  
<https://inspirehep.net/record/1240499/files/arXiv:1306.6756.pdf>.
- [88] ATLAS Collaboration, *Readiness of the ATLAS Tile Calorimeter for LHC collisions*, Eur. Phys. J. **C70** (2010) 1193–1236, [arXiv:1007.5423](#) [physics.ins-det].
- [89] A. Artamonov, D. Bailey, G. Belanger, et al., *The ATLAS Forward Calorimeter*, Journal of Instrumentation **3** no. 02, (2008) P02010.  
<http://stacks.iop.org/1748-0221/3/i=02/a=P02010>.
- [90] ATLAS Collaboration, *Electron and photon energy calibration with the ATLAS detector using LHC Run 1 data*, Eur. Phys. J. **C74** no. 10, (2014) 3071, [arXiv:1407.5063](#) [hep-ex].
- [91] M. Aharrouche, J. Colas, L. D. Ciaccio, et al., *Energy linearity and resolution of the ATLAS electromagnetic barrel calorimeter in an electron test-beam*, Nuclear Instruments and Methods in Physics Research Section A: Accelerators, Spectrometers, Detectors and Associated Equipment **568** no. 2, (2006) 601 – 623.  
<http://www.sciencedirect.com/science/article/pii/S0168900206013222>.
- [92] ATLAS Collaboration, *Charged-particle distributions in  $\sqrt{s} = 13$  TeV pp interactions measured with the ATLAS detector at the LHC*, Phys. Lett. **B758** (2016) 67–88, [arXiv:1602.01633](#) [hep-ex].
- [93] W. J. Stirling. Private communication.
- [94] ATLAS Collaboration, *Performance of the ATLAS Trigger System in 2010*, Eur. Phys. J. **C72** (2012) 1849, [arXiv:1110.1530](#) [hep-ex].
- [95] ATLAS Collaboration, *Performance of the ATLAS Trigger System in 2015*, Eur. Phys. J. **C77** no. 5, (2017) 317, [arXiv:1611.09661](#) [hep-ex].
- [96] R. Achenbach, P. Adragna, V. Andrei, et al., *The ATLAS Level-1 Calorimeter Trigger*, Journal of Instrumentation **3** no. 03, (2008) P03001.  
<http://stacks.iop.org/1748-0221/3/i=03/a=P03001>.

- 
- [97] ATLAS Collaboration, *Performance of the ATLAS muon trigger in pp collisions at  $\sqrt{s} = 8$  TeV*, Eur. Phys. J. **C75** (2015) 120, [arXiv:1408.3179 \[hep-ex\]](#).
- [98] ATLAS Collaboration, *Topological cell clustering in the ATLAS calorimeters and its performance in LHC Run 1*, [arXiv:1603.02934 \[hep-ex\]](#).
- [99] ATLAS Collaboration, *Measurement of the muon reconstruction performance of the ATLAS detector using 2011 and 2012 LHC proton-proton collision data*, The European Physical Journal C **74** no. 11, (2014) 3130.  
<http://dx.doi.org/10.1140/epjc/s10052-014-3130-x>.
- [100] ATLAS Collaboration, *Electron reconstruction and identification efficiency measurements with the ATLAS detector using the 2011 LHC proton-proton collision data*, Eur. Phys. J. **C74** no. 7, (2014) 2941, [arXiv:1404.2240 \[hep-ex\]](#).
- [101] ATLAS Collaboration, *Measurement of the photon identification efficiencies with the ATLAS detector using LHC Run-1 data*, Eur. Phys. J. **C76** no. 12, (2016) 666, [arXiv:1606.01813 \[hep-ex\]](#).
- [102] M. Cacciari, G. P. Salam, and G. Soyez, *The Anti- $k(t)$  jet clustering algorithm*, JHEP **04** (2008) 063, [arXiv:0802.1189 \[hep-ph\]](#).
- [103] M. Cacciari and G. P. Salam, *Dispelling the  $N^3$  myth for the  $k_t$  jet-finder*, Phys. Lett. **B641** (2006) 57–61, [arXiv:hep-ph/0512210 \[hep-ph\]](#).
- [104] G. C. Blazey et al., *Run II jet physics*, [arXiv:hep-ex/0005012 \[hep-ex\]](#).  
[http://lss.fnal.gov/cgi-bin/find\\_paper.pl?conf-00-092](http://lss.fnal.gov/cgi-bin/find_paper.pl?conf-00-092).
- [105] ATLAS Collaboration, *Jet energy measurement with the ATLAS detector in proton-proton collisions at  $\sqrt{s} = 7$  TeV*, Eur. Phys. J. **C73** no. 3, (2013) 2304, [arXiv:1112.6426 \[hep-ex\]](#).
- [106] ATLAS Collaboration, *Jet energy scale measurements and their systematic uncertainties in proton-proton collisions at  $\sqrt{s} = 13$  TeV with the ATLAS detector*, [arXiv:1703.09665 \[hep-ex\]](#).

- [107] ATLAS Collaboration, *Performance of pile-up mitigation techniques for jets in pp collisions at  $\sqrt{s} = 8$  TeV using the ATLAS detector*, Eur. Phys. J. **C76** no. 11, (2016) 581, [arXiv:1510.03823 \[hep-ex\]](#).
- [108] ATLAS Collaboration, *Commissioning of the ATLAS high-performance b-tagging algorithms in the 7 TeV collision data*, Tech. Rep. ATLAS-CONF-2011-102, CERN, Geneva, Jul, 2011. <https://cds.cern.ch/record/1369219>.
- [109] ATLAS Collaboration, *Performance of b-Jet Identification in the ATLAS Experiment*, JINST **11** no. 04, (2016) P04008, [arXiv:1512.01094 \[hep-ex\]](#).
- [110] ATLAS Collaboration, *Identification and energy calibration of hadronically decaying tau leptons with the ATLAS experiment in pp collisions at  $\sqrt{s}=8$  TeV*, Eur. Phys. J. **C75** no. 7, (2015) 303, [arXiv:1412.7086 \[hep-ex\]](#).
- [111] J. Alwall, M.-P. Le, M. Lisanti, and J. G. Wacker, *Searching for Directly Decaying Gluinos at the Tevatron*, Phys. Lett. **B666** (2008) 34–37, [arXiv:0803.0019 \[hep-ph\]](#).
- [112] J. Alwall, P. Schuster, and N. Toro, *Simplified models for a first characterization of new physics at the LHC*, Phys. Rev. **D79** (2009) 075020, [arXiv:0810.3921 \[hep-ph\]](#).
- [113] D. Alves et al., *Simplified Models for LHC New Physics Searches*, J. Phys. G: Nucl. Part. Phys. **39** (2012) 105005, [arXiv:1105.2838 \[hep-ph\]](#).
- [114] MSSM Working Group Collaboration, A. Djouadi et al., *The Minimal supersymmetric standard model: Group summary report*, in *GDR (Groupement De Recherche) - Supersymetrie Montpellier, France, April 15-17, 1998*. 1998. [arXiv:hep-ph/9901246 \[hep-ph\]](#).  
[https://inspirehep.net/record/481987/files/arXiv:hep-ph\\_9901246.pdf](https://inspirehep.net/record/481987/files/arXiv:hep-ph_9901246.pdf).
- [115] C. F. Berger, J. S. Gainer, J. L. Hewett, and T. G. Rizzo, *Supersymmetry without prejudice*, JHEP **0902** (2009) 023, [arXiv:0812.0980 \[hep-ph\]](#).

- [116] Y. Amhis et al., *Averages of  $b$ -hadron,  $c$ -hadron, and  $\tau$ -lepton properties as of summer 2016*, arXiv:1612.07233 [hep-ex].
- [117] G. D'Ambrosio, G. Giudice, G. Isidori, and A. Strumia, *Minimal flavor violation: An Effective field theory approach*, Nucl. Phys. **B645** (2002) 155–187, arXiv:hep-ph/0207036 [hep-ph].
- [118] J. D. Wells, *Implications of supersymmetry breaking with a little hierarchy between gauginos and scalars*, in *11th International Conference on Supersymmetry and the Unification of Fundamental Interactions (SUSY 2003) Tucson, Arizona, June 5-10, 2003*. 2003. arXiv:hep-ph/0306127 [hep-ph].
- [119] N. Arkani-Hamed and S. Dimopoulos, *Supersymmetric unification without low energy supersymmetry and signatures for fine-tuning at the LHC*, JHEP **06** (2005) 073, arXiv:hep-th/0405159 [hep-th].
- [120] G. F. Giudice and A. Romanino, *Split supersymmetry*, Nucl. Phys. **B699** (2004) 65–89, arXiv:hep-ph/0406088 [hep-ph]. [Erratum: Nucl. Phys.B706,487(2005)].
- [121] G. Belanger, F. Boudjema, A. Pukhov, and A. Semenov, *micrOMEGAs3: A program for calculating dark matter observables*, Comput. Phys. Commun. **185** (2014) 960–985, arXiv:1305.0237 [hep-ph].
- [122] S. Heinemeyer, W. Hollik, and G. Weiglein, *FeynHiggs: A Program for the calculation of the masses of the neutral CP even Higgs bosons in the MSSM*, Comput. Phys. Commun. **124** (2000) 76–89, arXiv:hep-ph/9812320 [hep-ph].
- [123] M. Baak, M. Goebel, J. Haller, et al., *The Electroweak Fit of the Standard Model after the Discovery of a New Boson at the LHC*, Eur. Phys. J. **C72** (2012) 2205, arXiv:1209.2716 [hep-ph].
- [124] Heavy Flavor Averaging Group, *Averages of  $B$ -Hadron,  $C$ -Hadron, and tau-lepton properties as of early 2012*, arXiv:1207.1158 [hep-ex].
- [125] K. De Bruyn, R. Fleischer, R. Knegjens, et al., *Probing new physics via the  $B_s^0 \rightarrow \mu^+ \mu^-$  Effective Lifetime*, Phys. Rev. Lett. **109** (2012) 041801, arXiv:1204.1737 [hep-ph].

- 
- [126] CMS and LHCb Collaborations, *Observation of the rare  $B_s^0 \rightarrow \mu^+ \mu^-$  decay from the combined analysis of CMS and LHCb data*, Nature **522** (2015) 68–72, [arXiv:1411.4413 \[hep-ex\]](#).
- [127] F. Mahmoudi, *SuperIso v2.3: A Program for calculating flavor physics observables in Supersymmetry*, Comput. Phys. Commun. **180** (2009) 1579–1613, [arXiv:0808.3144 \[hep-ph\]](#).
- [128] BaBar Collaboration, *A Search for  $B^+ \rightarrow \ell^+ \nu_\ell$  Recoiling Against  $B^- \rightarrow D^0 \ell^- \bar{\nu} X$* , Phys. Rev. **D81** (2010) 051101, [arXiv:0912.2453 \[hep-ex\]](#).
- [129] Belle Collaboration, *Evidence for  $B^- \rightarrow \tau^- \bar{\nu}$  with a Semileptonic Tagging Method*, Phys. Rev. **D82** (2010) 071101, [arXiv:1006.4201 \[hep-ex\]](#).
- [130] Belle Collaboration, I. Adachi et al., *Evidence for  $B^- \rightarrow \tau^- \bar{\nu}_\tau$  with a Hadronic Tagging Method Using the Full Data Sample of Belle*, Phys. Rev. Lett. **110** no. 13, (2013) 131801, [arXiv:1208.4678 \[hep-ex\]](#).
- [131] BaBar Collaboration, *Evidence of  $B^+ \rightarrow \tau^+ \nu$  decays with hadronic  $B$  tags*, Phys. Rev. **D88** no. 3, (2013) 031102, [arXiv:1207.0698 \[hep-ex\]](#).
- [132] CKMfitter Group, *CP violation and the CKM matrix: Assessing the impact of the asymmetric  $B$  factories*, Eur. Phys. J. **C41** (2005) 1–131, [arXiv:hep-ph/0406184 \[hep-ph\]](#). Updated result as of summer 2014 from <http://ckmfitter.in2p3.fr>.
- [133] T. Aoyama, M. Hayakawa, T. Kinoshita, and M. Nio, *Complete tenth-order QED contribution to the muon  $g-2$* , Phys. Rev. Lett. **109** (2012) 111808, [arXiv:1205.5370 \[hep-ph\]](#).
- [134] K. Hagiwara, R. Liao, A. D. Martin, D. Nomura, and T. Teubner,  *$(g-2)_\mu$  and  $\alpha(M_Z^2)$  re-evaluated using new precise data*, J. Phys. **G38** (2011) 085003, [arXiv:1105.3149 \[hep-ph\]](#).
- [135] A. Nyffeler, *Hadronic light-by-light scattering in the muon  $g-2$ : A New short-distance constraint on pion-exchange*, Phys. Rev. **D79** (2009) 073012, [arXiv:0901.1172 \[hep-ph\]](#).

- 
- [136] A. Czarnecki, W. J. Marciano, and A. Vainshtein, *Refinements in electroweak contributions to the muon anomalous magnetic moment*, Phys. Rev. **D67** (2003) 073006, [arXiv:hep-ph/0212229](#) [hep-ph]. [Erratum: Phys. Rev. **D73**, 119901 (2006)].
- [137] Muon g-2 Collaboration, *Measurement of the Negative Muon Anomalous Magnetic Moment to 0.7 ppm*, Phys. Rev. Lett. **92** (2004) 161802, [arXiv:hep-ex/0401008](#) [hep-ex].
- [138] Muon g-2 Collaboration, *Final report of the E821 muon anomalous magnetic moment measurement at BNL*, Phys. Rev. D **73** (2006) 072003, [arXiv:hep-ex/0602035](#) [hep-ex].
- [139] P. J. Mohr, B. N. Taylor, and D. B. Newell, *CODATA recommended values of the fundamental physical constants: 2006\**, Rev. Mod. Phys. **80** (2008) 633–730, [arXiv:0801.0028](#) [physics.atom-ph].
- [140] B. L. Roberts et al., *Status of the Fermilab muon ( $g - 2$ ) experiment*, Chinese Physics C **34** no. 6, (2010) 741, [arXiv:1001.2898](#) [hep-ex].
- [141] LUX Collaboration, *First results from the LUX dark matter experiment at the Sanford Underground Research Facility*, Phys. Rev. Lett. **112** (2014) 091303, [arXiv:1310.8214](#) [astro-ph.CO].
- [142] COUPP Collaboration, *First Dark Matter Search Results from a 4-kg CF<sub>3</sub>I Bubble Chamber Operated in a Deep Underground Site*, Phys. Rev. **D86** (2012) 052001, [arXiv:1204.3094](#) [astro-ph.CO].
- [143] XENON100 Collaboration, *Limits on spin-dependent WIMP-nucleon cross-sections from 225 live days of XENON100 data*, Phys. Rev. Lett. **111** no. 2, (2013) 021301, [arXiv:1301.6620](#) [astro-ph.CO].
- [144] T. Hahn, S. Heinemeyer, W. Hollik, H. Rzehak, and G. Weiglein, *High-precision predictions for the light CP-even Higgs Boson Mass of the MSSM*, Phys. Rev. Lett. **112** (2014) 141801, [arXiv:1312.4937](#) [hep-ph].

- [145] ALEPH, DELPHI, L3, OPAL, SLD, LEP Electroweak Working Group, SLD Electroweak Group, SLD Heavy Flavour Group, *Precision electroweak measurements on the Z resonance*, Phys. Rept. **427** (2006) 257–454, [arXiv:hep-ex/0509008](#) [hep-ex].
- [146] “The LEP SUSY Working Group and the ALEPH, DELPHI, L3 and OPAL experiments, note LEPSUSYWG/01-03.1.”  
<http://lepsusy.web.cern.ch/lepsusy>.
- [147] N. Arkani-Hamed, A. Delgado, and G. Giudice, *The well-tempered neutralino*, Nucl. Phys. **B741** (2006) 108–130, [arXiv:hep-ph/0601041](#) [hep-ph].
- [148] ATLAS Collaboration, *Search for squarks and gluinos with the ATLAS detector in final states with jets and missing transverse momentum using  $\sqrt{s} = 8$  TeV proton–proton collision data*, JHEP **1409** (2014) 176, [arXiv:1405.7875](#) [hep-ex].
- [149] ATLAS Collaboration, *Search for new phenomena in final states with large jet multiplicities and missing transverse momentum at  $\sqrt{s} = 8$  TeV proton-proton collisions using the ATLAS experiment*, JHEP **10** (2013) 130, [arXiv:1308.1841](#) [hep-ex].
- [150] ATLAS Collaboration, *Search for squarks and gluinos in events with isolated leptons, jets and missing transverse momentum at  $\sqrt{s} = 8$  TeV with the ATLAS detector*, JHEP **1504** (2015) 116, [arXiv:1501.03555](#) [hep-ex].
- [151] ATLAS Collaboration, *Search for supersymmetry in events with large missing transverse momentum, jets, and at least one tau lepton in  $20 \text{ fb}^{-1}$  of  $\sqrt{s} = 8$  TeV proton-proton collision data with the ATLAS detector*, JHEP **1409** (2014) 103, [arXiv:1407.0603](#) [hep-ex].
- [152] ATLAS Collaboration, *Search for supersymmetry at  $\sqrt{s} = 8$  TeV in final states with jets and two same-sign leptons or three leptons with the ATLAS detector*, JHEP **1406** (2014) 035, [arXiv:1404.2500](#) [hep-ex].



- [153] ATLAS Collaboration, *Search for strong production of supersymmetric particles in final states with missing transverse momentum and at least three  $b$ -jets at  $\sqrt{s} = 8$  TeV proton-proton collisions with the ATLAS detector*, JHEP **1410** (2014) 24, [arXiv:1407.0600 \[hep-ex\]](#).
- [154] ATLAS Collaboration, *Search for new phenomena in final states with an energetic jet and large missing transverse momentum in  $pp$  collisions at  $\sqrt{s} = 8$  TeV with the ATLAS detector*, Eur. Phys. J. **C75** no. 7, (2015) 299, [arXiv:1502.01518 \[hep-ex\]](#).
- [155] ATLAS Collaboration, *Search for direct pair production of the top squark in all-hadronic final states in proton-proton collisions at  $\sqrt{s} = 8$  TeV with the ATLAS detector*, JHEP **1409** (2014) 015, [arXiv:1406.1122 \[hep-ex\]](#).
- [156] ATLAS Collaboration, *Search for top squark pair production in final states with one isolated lepton, jets, and missing transverse momentum in  $\sqrt{s} = 8$  TeV  $pp$  collisions with the ATLAS detector*, JHEP **11** (2014) 118, [arXiv:1407.0583 \[hep-ex\]](#).
- [157] ATLAS Collaboration, *Search for direct top-squark pair production in final states with two leptons in  $pp$  collisions at  $\sqrt{s} = 8$  TeV with the ATLAS detector*, JHEP **1406** (2014) 124, [arXiv:1403.4853 \[hep-ex\]](#).
- [158] ATLAS Collaboration, *Search for pair-produced third-generation squarks decaying via charm quarks or in compressed supersymmetric scenarios in  $pp$  collisions at  $\sqrt{s} = 8$  TeV with the ATLAS detector*, Phys. Rev. D **90** (2014) 052008, [arXiv:1407.0608 \[hep-ex\]](#).
- [159] ATLAS Collaboration, *Search for direct top squark pair production in events with a  $Z$  boson,  $b$ -jets and missing transverse momentum in  $\sqrt{s} = 8$  TeV  $pp$  collisions with the ATLAS detector*, Eur. Phys. J. **C74** no. 6, (2014) 2883, [arXiv:1403.5222 \[hep-ex\]](#).
- [160] ATLAS Collaboration, *Search for direct third-generation squark pair production in final states with missing transverse momentum and two  $b$ -jets in  $\sqrt{s} = 8$  TeV  $pp$*

- collisions with the ATLAS detector*, JHEP **1310** (2013) 189, [arXiv:1308.2631](#) [hep-ex].
- [161] ATLAS Collaboration, *ATLAS Run 1 searches for direct pair production of third-generation squarks at the Large Hadron Collider*, Eur. Phys. J. **C75** no. 10, (2015) 510, [arXiv:1506.08616](#) [hep-ex]. [Erratum: Eur. Phys. J. **C76**, no. 3, 153 (2016)].
- [162] ATLAS Collaboration, *Search for direct pair production of a chargino and a neutralino decaying to the 125 GeV Higgs boson in  $\sqrt{s} = 8$  TeV pp collisions with the ATLAS detector*, Eur. Phys. J. **C75** no. 5, (2015) 208, [arXiv:1501.07110](#) [hep-ex].
- [163] ATLAS Collaboration, *Search for direct production of charginos, neutralinos and sleptons in final states with two leptons and missing transverse momentum in pp collisions at  $\sqrt{s} = 8$  TeV with the ATLAS detector*, JHEP **05** (2014) 071, [arXiv:1403.5294](#) [hep-ex].
- [164] ATLAS Collaboration, *Search for the direct production of charginos, neutralinos and staus in final states with at least two hadronically decaying taus and missing transverse momentum in pp collisions at  $\sqrt{s} = 8$  TeV with the ATLAS detector*, JHEP **10** (2014) 96, [arXiv:1407.0350](#) [hep-ex].
- [165] ATLAS Collaboration, *Search for direct production of charginos and neutralinos in events with three leptons and missing transverse momentum in  $\sqrt{s} = 8$  TeV pp collisions with the ATLAS detector*, JHEP **1404** (2014) 169, [arXiv:1402.7029](#) [hep-ex].
- [166] ATLAS Collaboration, *Search for supersymmetry in events with four or more leptons in  $\sqrt{s} = 8$  TeV pp collisions with the ATLAS detector*, Phys. Rev. **D90** no. 5, (2014) 052001, [arXiv:1405.5086](#) [hep-ex].
- [167] ATLAS Collaboration, *Search for charginos nearly mass degenerate with the lightest neutralino based on a disappearing-track signature in pp collisions at  $\sqrt{s} = 8$  TeV with the ATLAS detector*, Phys. Rev. **D88** no. 11, (2013) 112006, [arXiv:1310.3675](#) [hep-ex].

- [168] ATLAS Collaboration, *Searches for heavy long-lived sleptons and R-Hadrons with the ATLAS detector in pp collisions at  $\sqrt{s} = 7$  TeV*, Phys. Lett. **B720** (2013) 277–308, [arXiv:1211.1597 \[hep-ex\]](#).
- [169] ATLAS Collaboration, *Searches for heavy long-lived charged particles with the ATLAS detector in proton-proton collisions at  $\sqrt{s} = 8$  TeV*, JHEP **1501** (2015) 068, [arXiv:1411.6795 \[hep-ex\]](#).
- [170] ATLAS Collaboration, *Search for neutral Higgs bosons of the minimal supersymmetric standard model in pp collisions at  $\sqrt{s} = 8$  TeV with the ATLAS detector*, JHEP **1411** (2014) 056, [arXiv:1409.6064 \[hep-ex\]](#).
- [171] T. Rizzo, *Private Communication*.
- [172] J. Ellis, T. Falk, and K. A. Olive, *Neutralino-stau coannihilation and the cosmological upper limit on the mass of the lightest supersymmetric particle*, Physics Letters B **444** no. 3–4, (1998) 367–372.  
<http://www.sciencedirect.com/science/article/pii/S0370269398013926>.
- [173] ATLAS Collaboration, *Constraints on new phenomena via Higgs boson couplings and invisible decays with the ATLAS detector*, [arXiv:1509.00672 \[hep-ex\]](#).
- [174] ATLAS Collaboration, *Measurements of the Higgs boson production and decay rates and coupling strengths using pp collision data at  $\sqrt{s} = 7$  and 8 TeV in the ATLAS experiment*, Eur. Phys. J. **C76** no. 1, (2016) 6, [arXiv:1507.04548 \[hep-ex\]](#).
- [175] M. W. Cahill-Rowley, J. L. Hewett, A. Ismail, and T. G. Rizzo, *The Higgs Sector and Fine-Tuning in the pMSSM*, Phys. Rev. **D86** (2012) 075015, [arXiv:1206.5800 \[hep-ph\]](#).
- [176] A. Buckley, *PySLHA: a Pythonic interface to SUSY Les Houches Accord data*, Eur. Phys. J. **C75** no. 10, (2015) 467, [arXiv:1305.4194 \[hep-ph\]](#).
- [177] T. Li, J. A. Maxin, D. V. Nanopoulos, and J. W. Walker, *The Ultra-High Jet Multiplicity Signal of Stringy No-Scale F–SU(5) at the  $\sqrt{s} = 7$  TeV LHC*, Phys. Rev. **D84** (2011) 076003, [arXiv:1103.4160 \[hep-ph\]](#).

- 
- [178] D. Feldman, G. Kane, E. Kuflik, and R. Lu, *A new (string motivated) approach to the little hierarchy problem*, Phys. Lett. **B704** (2011) 56–61, [arXiv:1105.3765 \[hep-ph\]](#).
- [179] P. Svantesson, A. Belyaev, J. P. Hall, and S. F. King, *E6SSM vs MSSM Gluino Phenomenology*, EPJ Web Conf. **28** (2012) 12014, [arXiv:1201.5141 \[hep-ph\]](#).
- [180] ATLAS Collaboration, *Search for new phenomena in final states with large jet multiplicities and missing transverse momentum using  $\sqrt{s} = 7$  TeV pp collisions with the ATLAS detector*, JHEP **11** (2011) 099, [arXiv:1110.2299 \[hep-ex\]](#).
- [181] ATLAS Collaboration, *Hunt for new phenomena using large jet multiplicities and missing transverse momentum with ATLAS in  $4.7 \text{ fb}^{-1}$  of  $\sqrt{s} = 7$  TeV proton–proton collisions*, JHEP **07** (2012) 167, [arXiv:1206.1760 \[hep-ex\]](#).
- [182] ATLAS Collaboration, *Performance of b-Jet Identification in the ATLAS Experiment*, JINST **11** (2016) P04008, [arXiv:1512.01094 \[hep-ex\]](#).
- [183] ATLAS Collaboration, *Optimisation of the ATLAS b-tagging performance for the 2016 LHC Run*, ATL-PHYS-PUB-2016-012.
- [184] ATLAS Collaboration, *Electron reconstruction and identification efficiency measurements with the ATLAS detector using the 2011 LHC proton–proton collision data*, Eur. Phys. J. C **74** (2014) 2941, [arXiv:1404.2240 \[hep-ex\]](#).
- [185] ATLAS Collaboration, *Electron efficiency measurements with the ATLAS detector using the 2015 LHC proton-proton collision data*, ATLAS-CONF-2016-024.
- [186] ATLAS Collaboration, *Muon reconstruction performance of the ATLAS detector in proton-proton collision data at  $\sqrt{s} = 13$  TeV*, Eur. Phys. J. **C76** no. 5, (2016) 292, [arXiv:1603.05598 \[hep-ex\]](#).
- [187] ATLAS Collaboration, *Search for new phenomena using large jet multiplicities and missing transverse momentum with ATLAS in  $5.8 \text{ fb}^{-1}$  of  $\sqrt{s} = 8$  TeV proton–proton collisions*, ATLAS-CONF-2012-103.
- [188] B. Nachman and C. G. Lester, *Significance Variables*, Phys. Rev. **D88** no. 7, (2013) 075013, [arXiv:1303.7009 \[hep-ph\]](#).

- [189] ATLAS Collaboration, *Performance of missing transverse momentum reconstruction in proton–proton collisions at  $\sqrt{s} = 7$  TeV with ATLAS*, Eur. Phys. J. C **72** (2012) 1844, [arXiv:1108.5602 \[hep-ex\]](#).
- [190] M. Ackermann et al., *Detection of the Characteristic Pion-Decay Signature in Supernova Remnants*, Science **339** no. 6121, (2013) 807–811.
- [191] H.E.S.S. Collaboration, *Acceleration of petaelectronvolt protons in the Galactic Centre*, Nature **531** (2016) 476, [arXiv:1603.07730 \[astro-ph.HE\]](#).
- [192] ATLAS Collaboration, *Studies of the performance of the ATLAS detector using cosmic-ray muons*, Eur. Phys. J. **C71** (2011) 1593, [arXiv:1011.6665 \[physics.ins-det\]](#).
- [193] ATLAS Collaboration, *Selection of jets produced in 13 TeV proton-proton collisions with the ATLAS detector*, ATLAS-CONF-2015-029.
- [194] ATLAS Collaboration, *Tagging and suppression of pileup jets with the ATLAS detector*, ATLAS-CONF-2014-018.
- [195] A. J. Barr, T. J. Khoo, P. Konar, et al., *Guide to transverse projections and mass-constraining variables*, Phys. Rev. **D84** (2011) 095031, [arXiv:1105.2977 \[hep-ph\]](#).
- [196] C. W. Kalderon, *Searches for Scharms and Gluinos with the ATLAS Detector*. DPhil thesis, University of Oxford, April, 2016. CERN-THESIS-2016-076.
- [197] M. Czakon, P. Fiedler, and A. Mitov, *Total Top-Quark Pair-Production Cross Section at Hadron Colliders Through  $\mathcal{O}(\alpha_S^4)$* , Phys. Rev. Lett. **110** (2013) 252004. <http://link.aps.org/doi/10.1103/PhysRevLett.110.252004>.
- [198] ATLAS Collaboration, *The ATLAS Simulation Infrastructure*, Eur. Phys. J. **C70** (2010) 823–874, [arXiv:1005.4568 \[physics.ins-det\]](#).
- [199] S. Agostinelli et al., *Geant4 – a simulation toolkit*, Nuclear Instruments and Methods in Physics Research Section A: Accelerators, Spectrometers, Detectors and Associated Equipment **506** no. 3, (2003) 250 – 303. <http://www.sciencedirect.com/science/article/pii/S0168900203013688>.

- 
- [200] ATLAS Collaboration, *The ATLAS Simulation Infrastructure*, Eur. Phys. J. C **70** (2010) 823, [arXiv:1005.4568 \[hep-ex\]](#).
- [201] S. Alioli, P. Nason, C. Oleari, and E. Re, *A general framework for implementing NLO calculations in shower Monte Carlo programs: the POWHEG BOX*, JHEP **06** (2010) 043, [arXiv:1002.2581 \[hep-ph\]](#).
- [202] H.-L. Lai, M. Guzzi, J. Huston, et al., *New parton distributions for collider physics*, Phys. Rev. **D82** (2010) 074024, [arXiv:1007.2241 \[hep-ph\]](#).
- [203] T. Sjostrand, S. Mrenna, and P. Z. Skands, *PYTHIA 6.4 Physics and Manual*, JHEP **05** (2006) 026, [arXiv:hep-ph/0603175 \[hep-ph\]](#).
- [204] T. Gleisberg et al., *Event generation with SHERPA 1.1*, JHEP **02** (2009) 007, [arXiv:0811.4622 \[hep-ph\]](#).
- [205] J. Alwall, R. Frederix, S. Frixione, et al., *The automated computation of tree-level and next-to-leading order differential cross sections, and their matching to parton shower simulations*, JHEP **07** (2014) 079, [arXiv:1405.0301 \[hep-ph\]](#).
- [206] M. Bahr et al., *Herwig++ Physics and Manual*, Eur. Phys. J. **C58** (2008) 639–707, [arXiv:0803.0883 \[hep-ph\]](#).
- [207] ATLAS Collaboration, *Comparison of Monte Carlo generator predictions from Powheg and Sherpa to ATLAS measurements of top pair production at 7 TeV*, ATL-PHYS-PUB-2015-011.
- [208] ATLAS Collaboration, *Luminosity determination in pp collisions at  $\sqrt{s} = 8$  TeV using the ATLAS detector at the LHC*, Eur. Phys. J. **C76** no. 12, (2016) 653, [arXiv:1608.03953 \[hep-ex\]](#).
- [209] M. Baak, G. J. Besjes, D. Côté, et al., *HistFitter software framework for statistical data analysis*, Eur. Phys. J. **C75** (2015) 153, [arXiv:1410.1280 \[hep-ex\]](#).
- [210] Krammer, K. and Lewis, G. and Moneta, L. and Shibata, A. and Verkerke, W., *HistFactory: A tool for creating statistical models for use with RooFit and RooStats*, CERN-OPEN-2012-016.

- 
- [211] G. Cowan, K. Cranmer, E. Gross, and O. Vitells, *Asymptotic formulae for likelihood-based tests of new physics*, The European Physical Journal C **71** no. 2, (2011) 1554. <http://dx.doi.org/10.1140/epjc/s10052-011-1554-0>.
- [212] A. L. Read, *Presentation of search results: the CL<sub>s</sub> technique*, Journal of Physics G: Nuclear and Particle Physics **28** no. 10, (2002) 2693. <http://stacks.iop.org/0954-3899/28/i=10/a=313>.
- [213] CMS Collaboration, *Search for supersymmetry in events with jets and missing transverse momentum in proton-proton collisions at 13 TeV*, Tech. Rep. CMS-PAS-SUS-16-014, CERN, Geneva, 2016. <https://cds.cern.ch/record/2205158>.
- [214] A. Buckley, *The hepthesis Latex class*. <https://www.ctan.org/pkg/hepthesis>.

# List of figures

2.1.	Feynman diagrams showing the interactions between fermions and bosons.	6
2.2.	Feynman diagrams representing self-interactions between gauge bosons. $V$ and $V'$ correspond to any two gauge bosons such that the total electric charge is conserved. . . . .	7
2.3.	Feynman diagrams for the interaction of the Higgs boson with the gauge bosons, and also the self-interactions of the Higgs boson. $V$ and $V'$ correspond to any two gauge bosons such that the total electric charge is conserved. . . . .	7
2.4.	A photon–fermion interaction at tree-level (left) and one-loop (right). As long as momentum is conserved at each vertex and $q = p' - p$ , the momenta around the loop $k$ and $k'$ are unconstrained. Diagrams from [46]. . . . .	17
2.5.	Renormalisation group evolution of the inverse gauge couplings $\alpha^{-1}$ as a function of the energy scale $Q$ in the Standard Model (dashed lines) and the MSSM (solid lines). In the MSSM case, the sparticle masses are treated as a common threshold varied between 500 GeV and 1.5 TeV, and $\alpha_S(m_Z)$ is varied between 0.117 and 0.121 giving rise to the red and blue solid lines. Image taken from reference [10]. . . . .	20
2.6.	Corrections to the Higgs mass from (a) fermions, (b) gauge bosons and (c) scalars at 1-loop. . . . .	22
2.7.	Example of a Feynman diagram depicting proton decay, in the case non-zero $R$ -parity violating couplings. . . . .	27



2.8.	Sparticle pair-production cross-sections at 13 TeV as a function of sparticle mass, calculated from ref. [68]. The gluino cross-section assumes all squarks are decoupled, the squark cross-section assumes the gluino and the stop are decoupled with the remaining squarks degenerate (meaning a 10-fold squark degeneracy), and the stop/sbottom cross-section assumes the gluino and the first and second generation squarks are decoupled. . . . .	35
2.9.	Feynman diagrams for strong production of SUSY particles. . . . .	35
3.1.	A schematic of the LHC ring and accelerator complex at CERN. The successively higher energy accelerators are: Linear Accelerator 2 (LINAC 2), Proton Synchrotron Booster, Proton Synchrotron (PS), Super Proton Synchrotron (SPS) and finally the Large Hadron Collider. Image reproduced with permission from [71]. . . . .	39
3.2.	Distribution of the mean number of proton-proton interactions per bunch crossing, commonly referred to as in-time pile-up, for the Run-1 (left) and Run-2 (right) datasets, taken from reference [77] and reference [78] respectively. . . . .	41
3.3.	A cut-away drawing of the ATLAS detector at the LHC, showing the separate subsystems. Image from reference [69]. Note that LUCID and the other forward detectors are not pictured. . . . .	44
3.4.	A schematic of the ATLAS magnet system. Image taken from reference [79].	46
3.5.	A cut-away view of the ATLAS inner detector used in Run-1. The Insertable B-Layer was added in-between Run-1 and Run-2 and is not shown here. Image taken from reference [69]. . . . .	47
3.6.	Cross-sectional views of the ATLAS inner detector. The end caps are shown in the upper panel, and the barrel is shown in the lower panel. Images taken from reference [69]. . . . .	48
3.7.	A cut-away diagram of the ATLAS calorimeter system. Image taken from reference [69]. . . . .	52
3.8.	A cut-away diagram of the ATLAS muon spectrometer. Image taken from reference [69]. . . . .	56

3.9. Inclusive cross-section values for several important processes as a function of centre of mass energy. The right vertical axis reports the number of events for an instantaneous luminosity of $L = 10^{33} \text{ cm}^{-2} \text{ s}^{-1}$ . The cross-sections on the left hand side of the discontinuity at $\sqrt{s} = 4 \text{ TeV}$ are calculated for the proton-antiproton initial state, while the cross-sections on the right hand side are calculated for the proton-proton initial state. Image from reference [93]. . . . .	61
3.10. Jets clustered with the anti- $k_t$ algorithm with radius parameter $R = 1$ . Image from reference [102]. . . . .	70
4.1. Distributions of the gluino (left) and LSP (right) masses, shown separately for models with a bino-like (dotted red), wino-like (dashed blue) or Higgsino-like (solid green) LSP. The constraints listed in table 4.3 have been applied, but not the constraints from the ATLAS searches. The distributions are normalised to unit area. The inset in the plot on the right shows in more detail the region of low neutralino mass for the models with bino-like LSP. . . . .	89
4.2. Normalised distribution of sparticle masses for the lightest stop (solid red), sbottom (dashed blue), first- or second-generation squark (dashed green) and stau (dot-dashed black) for all LSP types combined. The constraints listed in table 4.3 have been applied, but not the constraints from the ATLAS searches. . . . .	90
4.3. Distributions of all simulated pMSSM models before and after the combination of ATLAS searches for gluinos (left) and the lightest squark (right). The ratio plot shows the fraction of models excluded by the searches. . .	94

- 4.4. Fraction of pMSSM points excluded by the combination of 8 TeV ATLAS searches in the (a)  $\tilde{g}$ - $\tilde{\chi}_1^0$  and (b) the  $\tilde{q}$ - $\tilde{\chi}_1^0$  mass planes. These plots are binned projections of the pMSSM onto a 2D plane. Many models may populate each bin, and the colour scale indicates the fraction of models excluded, with black squares indicating 100% of model points being excluded. The white regions indicate places where no model points were sampled, due to the constraints of table 4.2 and table 4.3. In both cases, the solid white lines overlaid are observed simplified-model limits from the 0-lepton + 2–6 jets +  $E_T^{\text{miss}}$  search [148] at 95% CL. In the  $\tilde{g}$ - $\tilde{\chi}_1^0$  case, the simplified-model limit is set assuming direct production of gluino pairs and that the squarks are decoupled, with gluino decaying to quarks and a neutralino,  $\tilde{g} \rightarrow q\bar{q}\tilde{\chi}_1^0$ . In the  $\tilde{q}$ - $\tilde{\chi}_1^0$  plane, both lines are drawn assuming directly produced first/second-generation squark pairs, with each squark decaying to a quark and a neutralino,  $\tilde{q} \rightarrow q\tilde{\chi}_1^0$ . The solid line corresponds to the case where all eight squarks from the first two generations are assumed to be mass degenerate. The dashed line has the squark production cross-section scaled down by a factor of four to emulate the effect of only two of those eight squarks being kinematically accessible. 96
- 4.5. Fraction of pMSSM points excluded in the  $\tilde{g}$ - $\tilde{q}$  mass plane, where  $\tilde{q}$  represents the lightest squark from the first two generations. The overlaid line shows a limit for a simplified model from the 0-lepton + 2–6 jets +  $E_T^{\text{miss}}$  search [148] which assumes strong production of gluinos and eight-fold degenerate first- and second-generation squarks, with direct decays to quarks and massless neutralinos. . . . . 97
- 4.6. Distribution of the mass of the lightest stop (left) and sbottom (right) before and after the combined ATLAS searches. . . . . 98

- 4.7. Fraction of pMSSM points excluded in the  $\tilde{t}_1$ - $\tilde{\chi}_1^0$  plane in various cases. The top two plots show the full model set, with impact of all searches on the left and only the third-generation searches on the right. The bottom row of plots separates the models according to whether the  $\tilde{t}_1$  is either mostly (c)  $\tilde{t}_L$  or (d)  $\tilde{t}_R$ . There are relatively few pMSSM points at low  $\tilde{t}_1$  mass for the reasons described in the text. Three simplified-model limits are overlaid [156, 161]. The solid line represents the limit set assuming directly produced top squark pairs, with each decaying to a top quark and neutralino,  $\tilde{t}_1 \rightarrow t\tilde{\chi}_1^0$ . The dashed and dotted lines correspond to limits assuming decays of  $\tilde{t}_1 \rightarrow \tilde{\chi}_1^\pm b$  with the chargino decaying via an off- or on-shell  $W$  to the neutralino, respectively. . . . . 99
- 4.8. Fraction of pMSSM points excluded in the  $\tilde{b}_1$ - $\tilde{\chi}_1^0$  plane after the combination of all ATLAS searches (a) and just the third generation searches (b). In both cases, the white line corresponds to the simplified model limit from [160] which assumes direct production of sbottom pairs, with the decay  $\tilde{b} \rightarrow b\tilde{\chi}_1^0$ . The bottom row of plots separates the models according to whether the  $\tilde{b}_1$  is either mostly (c)  $\tilde{b}_L$  or (d)  $\tilde{b}_R$ . . . . . 102
- 4.9. Fraction of pMSSM points excluded in the  $\tilde{\ell}$ - $\tilde{\chi}_1^0$  plane after the combination of all ATLAS searches (a) and just the electroweak searches (b). Here  $\tilde{\ell}$  corresponds to the lightest of any first or second generation slepton or sneutrino. In both cases, the white line corresponds to the simplified model limit from [163] which assumes direct production of slepton pairs assuming that the left- and right-handed selectrons (or smuons) are mass-degenerate and that each decays via  $\tilde{\ell} \rightarrow \ell\tilde{\chi}_1^0$ . . . . . 104
- 4.10. Fraction of pMSSM points excluded in the  $\tilde{\ell}_L$ - $\tilde{\chi}_1^0$  plane (left) and  $\tilde{\ell}_R$ - $\tilde{\chi}_1^0$  plane (right) after the combination of the electroweak searches as defined in table 4.5. The simplified model limit in the  $\tilde{\ell}_L$  ( $\tilde{\ell}_R$ ) case is set assuming directly pair-produced left (right) handed selectrons/smuons, decaying to an electron/muon and neutralino [163]. . . . . 104
- 4.11. Distribution of the total production cross-section for the production of SUSY particles before and after the combined ATLAS searches. . . . . 105

- 4.12. Examples of annihilation and co-annihilation mechanisms that can reduce the dark matter relic density. Diagram (a) typically occurs for models with a wino- or Higgsino-dominated LSP as these naturally have a chargino that is degenerate with the neutralino, whereas diagram (b) is only possible for models with a bino-dominated LSP (with some Higgsino component) in the  $Z/h$  funnel. Diagram (c) is an example of stau co-annihilation, which may occur if the stau is sufficiently close in mass to the neutralino. Similar diagrams exist where the stau is replaced with another sfermion. . . . . 107
- 4.13. The density of pMSSM points projected onto the plane of dark matter relic density versus LSP mass, before and after the constraints from the ATLAS searches. The colours code the dominant LSP type, as defined in table 4.4. . . . . 108
- 4.14. The density of pMSSM points with a bino-dominated LSP projected onto the plane of dark matter relic density versus LSP mass, before and after the constraints from the ATLAS searches. The colours code the annihilation mechanism as described in the text. ‘Gaugino’ refers to electroweak gaugino coannihilation, while ‘Light Flavour’ refers to coannihilation either against squarks of the first two generations or against gluinos. . . . . 108
- 4.15. The mass distribution of the lightest neutralino (the dark matter candidate) before and after the ATLAS searches. . . . . 109
- 4.16. Impact of the combined ATLAS searches on observables relating to the decays of the Higgs boson. The branching ratio of the Higgs boson to a pair of neutralinos is shown in (a), and (b) shows the Higgs  $b$ -quark coupling ratio  $\kappa_b$ . Only models with a bino-dominated LSP and  $m(\tilde{\chi}_1^0) < 65$  GeV are included in (a), whereas all models are included in (b). The dashed lines show the observed and expected upper bounds of the 95% confidence limits on those parameters. . . . . 111

4.17. Distributions of model points before and after applying ATLAS searches for various precision observables. Figure (a) shows the mass of the light (SM-like) Higgs boson, $m(h)$ , (b) shows the branching ratio of $B_s \rightarrow \mu + \mu$ , (c) is the branching ratio of $b \rightarrow s + \gamma$ and (d) is the branching ratio of $B \rightarrow \tau \nu$ . . . . .	113
4.18. Distribution of model points in the plane of the mass of the lightest left- or right-handed smuon versus $\Delta(g_\mu - 2)$ . The experimental measurement is overlaid as the hatched band [133]. . . . .	114
4.19. Fine-tuning, before and after ATLAS exclusion. The second pad shows the ratio between the two histograms. . . . .	116
4.20. Distribution of pMSSM points in the plane showing fine-tuning versus $\mu^2$ for all models (left) and Higgsino-LSP models (right). The wino- and bino-LSP models have similar distribution to one another and make up the difference between the two plots. . . . .	117
4.21. Distribution of pMSSM points in the plane showing fine-tuning versus $A_t^2$ for all models (left) and Higgsino-LSP models (right). The wino- and bino-LSP models have similar distribution to one another and make up the difference between the two plots. . . . .	117
4.22. Particle spectra for models with low fine-tuning that evaded the ATLAS searches. Figures produced using PySHLA [176]. . . . .	118
4.23. Particle spectra for models with low fine-tuning that evaded the ATLAS searches. Figures produced using PySHLA [176]. . . . .	119

- 4.24. The fraction of models excluded for each sparticle in the pMSSM, as a (binned) function of sparticle mass. The combination of models is shown (all LSP types), weighted as described in the text. One interesting feature that can be seen in the case of the  $\tilde{\chi}_1^\pm$ , where the fraction of model points decreases to almost 0 at 1 TeV and then increases again at around 1.5 TeV. This is because the chargino mass and neutralino mass are near degenerate in wino and Higgsino-LSP models, and so a heavy  $\tilde{\chi}_1^\pm$  means a heavy LSP. The decrease in sensitivity to the chargino mass around 1 TeV is an artefact of weighting the bino model points by a factor of 1/24, because in bins around this region there are relatively few bino-LSP model points and so their contribution to the fraction of model points excluded is negligible. As the chargino mass increases, there are fewer model points with wino or Higgsino LSPs and so the fraction of model points excluded is then only representative of the bino-LSP models. . . . . 121
- 5.1. Ratio of the gluino production cross-section from 8 to 13 TeV. Cross-sections calculated from reference [68]. . . . . 123
- 5.2. Pseudo-Feynman diagrams showing benchmark signal processes used for interpretation and optimisation. No attempt is made to distinguish particles and their corresponding anti-particles. Diagram (a) was produced by collaborators. . . . . 125
- 5.3. Distributions of the number of jets versus (a) the number of baseline leptons, and (b) the number of  $b$ -jets from a benchmark two-step model with  $(m(\tilde{g}), m(\tilde{\chi}_1^0)) = (1400, 200)$  GeV. Basic event cleaning has been applied. 126
- 5.4. The particle spectra for a pair of models taken from the pMSSM study described in chapter 4 and reference [6]. Particles with mass greater than 1.8 TeV are not shown, and decays with branching fraction  $< 0.1$  are not shown. Figures produced using PySLHA [176]. . . . . 128
- 5.5. Distributions of the number of jets versus (a) the number of baseline leptons, and (b) the number of  $b$ -jets from a benchmark pMSSM model with  $(m(\tilde{g}), m(\tilde{\chi}_1^\pm)) = (1400, 200)$  GeV. Basic event cleaning has been applied. . . . . 129

- 5.6. Cumulative efficiency curves for HLT\_6j45\_0eta240, shown as a function of jet  $p_T$  for various jet multiplicities. The top-left panel shows the sixth leading jet, the top-right panel shows the seventh, and the lower panel shows the eighth. The offline jet  $p_T$  threshold used in the analysis is shown by the vertical dashed line. The efficiencies were derived by . . . . . 131
- 5.7. Normalised distributions of  $\eta$ ,  $p_T$  and multiplicity of jets for a set of pMSSM-slice (left) and two-step (right) benchmark points. The jets have  $p_T > 20$  GeV,  $|\eta| < 2.8$  and pass the signal criteria described in section 5.3.2, and events pass the preliminary selection described in the text. The signal distributions and  $t\bar{t}$  background are from Monte Carlo simulation, whereas the Multijet component has come from data (with an additional selection requiring  $E_T^{\text{miss}}/\sqrt{H_T} < 3 \text{ GeV}^{1/2}$ ). . . . . 143
- 5.8. Normalised  $p_T$  distributions of the 5<sup>th</sup>–9<sup>th</sup> jet for a benchmark pMSSM-slice model (left) and two-step model (right). Other details are as in figure 5.7. . . . . 144
- 5.9. Normalised distributions of  $M_J^\Sigma$  for a set of pMSSM-slice (left) and two-step (right) benchmark points. Events are selected after pre-selection and  $n_{50} \geq 8$ . The signal distributions and  $t\bar{t}$  background are from Monte Carlo simulation, whereas the Multijet component has come from data (with an additional selection requiring  $E_T^{\text{miss}}/\sqrt{H_T} < 3 \text{ GeV}^{1/2}$ ). . . . . 144
- 5.10. Leading order Feynman diagrams for the production of  $t\bar{t}$  pairs. . . . . 147
- 5.11. Leading order Feynman diagrams for the production of a  $W$  boson in association with jets. . . . . 149
- 5.12. Transverse mass distribution in the 9-jet  $W + \text{jets}$  (left) and  $t\bar{t}$  (right) control regions, before applying the  $m_T < 120$  GeV requirement. . . . . 152
- 5.13. Distribution of the number of jets in the control regions for the 7-jet  $W + \text{jets}$  (left) and  $t\bar{t}$  (right) control regions. Leptons are treated as jets, hence entries in the 6-jet bin. All other control regions are subsets of these, with tighter jet or  $M_J^\Sigma$  thresholds. . . . . 154



- 5.14. The  $E_T^{\text{miss}}/\sqrt{H_T}$  distribution in the 6 jet template regions (upper panels) and the 7 jet validation regions (lower panels) for the  $M_J^\Sigma > 340$  GeV (left) and  $M_J^\Sigma > 500$  GeV (right) regions. The blue hatched band shows the statistical uncertainty on the background prediction. Note that in these plots the Monte Carlo backgrounds have not been modified by the fit. . . . . 160
- 5.15. The degree of closure observed in the various multijet validation regions with  $M_J^\Sigma > 340$  GeV (upper panel) and  $M_J^\Sigma > 500$  GeV (lower panel). The solid lines are the predicted numbers of events and the points are the observed data. The signal regions are also included in the plot  $(4.0-\infty)$  for the 8, 9 and 10 jet regions, but these are not included in the calculation of the systematic uncertainty. The blue bands indicate the statistical uncertainties on the total background prediction. . . . . 166
- 5.16. These plots show the multijet template extracted from the “nominal” template region (with no  $b$ -jet requirement) and the alternative “flavour” template regions with either at least 1  $b$ -jet or exactly 0  $b$ -jets. The histograms have been normalised and rebinned – the spike around  $E_T^{\text{miss}}/\sqrt{H_T} = 2$  GeV<sup>1/2</sup> being an artefact of the increased bin width. The lower pad shows the ratio of each of the templates to the nominal. . . . . 167
- 5.17. The average number of  $b$ -jets versus the number of jets in data. All cleaning cuts have been applied, as well a lepton veto and a 6 jet selection. 167
- 5.18.  $E_T^{\text{miss}}/\sqrt{H_T}$  distributions for the signal regions with  $M_J^\Sigma > 340$  GeV for at least 8, 9 and 10 jets (a, b and c respectively). Note the  $t\bar{t}$  and  $W + \text{jets}$  backgrounds have been modified from the raw MC prediction by the scale factors from the background-only fit. . . . . 170
- 5.19.  $E_T^{\text{miss}}/\sqrt{H_T}$  distributions for the signal regions with  $M_J^\Sigma > 500$  GeV for at least 8, 9 and 10 jets (a, b and c respectively). Note the  $t\bar{t}$  and  $W + \text{jets}$  backgrounds have been modified from the raw Monte Carlo prediction by the scale factors from the background-only fit. . . . . 171
- 5.20. A summary of the data and Standard Model prediction for the 6 signal regions. The blue band shows the combined statistical and systematic uncertainty on the Standard Model predictions after the background fit. . . . . 177

- 5.21. The distribution of  $p$ -values for the  $\text{CL}_s$ ,  $\text{CL}_{s+b}$  and  $\text{CL}_b$  hypotheses as a function of the signal strength parameter in the SR-8j50-MJ340 region (left) and the SR-10j50-MJ500 region (right). . . . . 180
- 5.22. 95% exclusion curve for the pMSSM-slice model. The solid red and dashed blue curves show the 95% CL observed and expected limits, respectively, including all uncertainties except the theoretical signal cross-section uncertainty (PDF and scale). The dotted red lines bracketing the observed limit represent the result produced when moving the signal cross-section by  $\pm 1\sigma$  (as defined by the PDF and scale uncertainties). The shaded yellow band around the expected limit shows the  $\pm 1\sigma$  variation of the expected limit. . . . . 183
- 5.23. 95% exclusion curve for the two-step simplified model. The shaded grey area shows the observed exclusion from a previous iteration of the analysis [4]. Other details are as described in figure 5.22. . . . . 184
- 5.24. Location of model points for the pMSSM (left) and two-step (right) grids, with the signal region yielding the largest expected  $\text{CL}_s$  value indicated on the point. . . . . 185

# List of tables

2.1.	The known fundamental particles comprising the Standard Model and some of their properties. Not listed in the table are the antiparticles of the quarks and leptons, which have identical mass and opposite electric charge. Furthermore, for each flavour of quark there are 3 colour versions, and there are 8 different coloured gluons. Masses are from the Review of Particle Physics [34]. . . . .	5
2.2.	The fermion content of the Standard Model with their associated charges. There are three generations of both right- and left-handed quarks and leptons. $Q$ refers to the electric charge, $Y$ to the weak hypercharge, and $I$ and $I_3$ to isospin and the third component of isospin respectively. They are related by $Y = 2(Q - I_3)$ . Right-handed neutrinos are not present in the Standard Model and so are not included. . . . .	10
2.3.	Particle content of the MSSM before electroweak symmetry breaking. . .	29
2.4.	The undiscovered particle content of the MSSM (with the exception of $h^0$ ), before and after electroweak symmetry breaking. Mixing within the first two generations is assumed to be negligible. . . . .	32
3.1.	Summary of LHC beam parameters through the major data-taking years to-date, and also the design specification. Data were also recorded in 2011 and 2015, however these years provided a significantly smaller fraction of the total data recorded. . . . .	40
4.1.	The definition of the 19 pMSSM parameters, in addition to those of the Standard Model. LH and RH refer to left- and right-handed respectively.	80

4.2.	Scan ranges used for each of the 19 pMSSM parameters (as defined in table 4.1). Where the parameter is written with a modulus sign both the positive and negative values are permitted. . . . .	83
4.3.	Constraints on acceptable pMSSM points from considerations of precision electroweak and flavour results, dark matter relic density, and other collider measurements. A long dash (—) indicates that no requirement is made. Further details may be found in the text. . . . .	84
4.4.	Categorisation of the 310,327 model points by the type of the LSP (assumed to be the $\tilde{\chi}_1^0$ ) according to the neutralino mixing matrix parameters $N_{ij}$ , where the first index indicates the neutralino mass eigenstate and the second indicates its nature in the lexicographical order $(\tilde{B}^0, \tilde{W}^0, \tilde{H}_u^0, \tilde{H}_d^0)$ . For example, $N_{12}$ is the amplitude for the LSP to be $\tilde{W}^0$ . The final two columns indicate the total number of viable models in each of the LSP categories, and the fraction relative to the total 310,327 models. . . . .	88
4.5.	The 22 different ATLAS searches considered. The term ‘lepton’ ( $\ell$ ) refers specifically to $e^\pm$ and $\mu^\pm$ states, except in the cases of the electroweak 3-leptons and 4-leptons analyses where $\tau$ leptons are also included. . . .	92
5.1.	The jet $p_T$ threshold at which the trigger HLT_6j45_0eta240 becomes 90, 95, 99 and 99.5% efficient for the sixth, seventh and eighth leading jet. .	132
5.2.	Summary of the event cleaning and data quality cuts. . . . .	139
5.3.	Summary of the selection cuts defining the 6 signal regions. . . . .	146
5.4.	Definition of the leptonic control regions, used to normalise the $t\bar{t}$ and $W + \text{jets}$ backgrounds. In the control regions, the lepton is recast as a jet if it passes the same kinematic criteria as the jets. Such leptons contribute to the $E_T^{\text{miss}}/\sqrt{H_T}$ (through the $H_T$ ) and also $M_J^\Sigma$ . . . . .	153
5.5.	Theoretical systematic uncertainties, in percent, for the 8j50-MJ340 signal region and the corresponding leptonic control regions. “Rad. Up” and “Rad. Down” refer to the radiation tunes of the parton shower. . . . .	154

- 5.6. The degree of closure observed in the multijet validation regions. The bracketed ranges indicate the  $E_T^{\text{miss}}/\sqrt{H_T}$  interval considered, in  $\text{GeV}^{1/2}$ . Cells highlighted in blue indicate validation regions, signal regions are in red and green indicates the closure systematic used for the respective signal region. The upper table is for the  $M_J^\Sigma > 340 \text{ GeV}$  regions and the lower table for the  $M_J^\Sigma > 500 \text{ GeV}$  regions. The closure is calculated as  $(\text{observation} - \text{prediction})/(\text{prediction})$ , where the prediction is given as the sum of the fitted leptonic backgrounds and the multijet estimation from the template. . . . . 162
- 5.7. Uncertainties on the multijet prediction derived from heavy-flavour effects. 164
- 5.8. Data yields and the Standard Model expectation for each signal region, both before and after the background-only fit. The uncertainties reflect the combination of statistical and systematic sources. The normalisation on the  $W + \text{jets}$  background is typically around 0.5 or smaller, demonstrating that the Monte Carlo does not describe data well for the yield of  $W + \text{jets}$  in high jet multiplicity events. . . . . 176
- 5.9. Dominant ( $> 5\%$  in any region) systematic uncertainties for the MJ340 regions. Uncertainties are correlated so may add to more than the totals quoted. The  $t\bar{t}$  normalisation uncertainty corresponds to the uncertainty on the  $t\bar{t}$  scale factor, and is related to both the statistical and systematic uncertainties in the control regions. . . . . 177
- 5.10. Dominant ( $> 5\%$  in any region) systematic uncertainties for the MJ500 regions. Uncertainties are correlated so may add to more than the totals quoted. The  $t\bar{t}$  normalisation uncertainty corresponds to the uncertainty on the  $t\bar{t}$  scale factor, and is related to both the statistical and systematic uncertainties in the control regions. . . . . 178

5.11. Left to right: 95% CL upper limits on the visible cross section ( $\langle\epsilon\sigma\rangle_{obs}^{95}$ ) and on the number of signal events ( $S_{obs}^{95}$ ). The third column ( $S_{exp}^{95}$ ) shows the 95% CL upper limit on the number of signal events, given the expected number (and $\pm 1\sigma$ excursions on the expectation) of background events. The last column indicates the $CL_B$ value, i.e. the confidence level observed for the background-only hypothesis. . . . .	181
B.1. Theoretical systematic uncertainties, in percent, for the 8j50-MJ340 signal region and the corresponding leptonic control regions. “Rad. Up” and “Rad. Down” refer to the radiation radiation tunes of the parton shower. . . . .	196
B.2. Results showing the difference between the nominal template, and the $H_T$ binned template (as described in the text). The deviation is calculated as (data-prediction)/prediction. The difference in the predictions is calculated as (nominal - HT template)/nominal. The upper set of regions correspond to $M_J^\Sigma > 340$ GeV and the lower regions correspond to $M_J^\Sigma > 500$ GeV. . . . .	198
B.3. Breakdown of pre- and post-fit yields for the SR-8j50-MJ340 region and its corresponding control regions. . . . .	199
B.4. Breakdown of pre- and post-fit yields for the SR-9j50-MJ340 region and its corresponding control regions. . . . .	200
B.5. Breakdown of pre- and post-fit yields for the SR-10j50-MJ340 region and its corresponding control regions. . . . .	201
B.6. Breakdown of pre- and post-fit yields for the SR-8j50-MJ500 region and its corresponding control regions. . . . .	202
B.7. Breakdown of pre- and post-fit yields for the SR-9j50-MJ500 region and its corresponding control regions. . . . .	203
B.8. Breakdown of pre- and post-fit yields for the SR-10j50-MJ500 region and its corresponding control regions. . . . .	204